Mode-matching techniques for the modeling of rotor-stator wake-interaction noise, with emphasis on the effects of vane camber

Leo Girier

N° d'ordre NNT: 2022LYSEC003

THÈSE de DOCTORAT DE L'UNIVERSITÉ DE LYON
opérée au sein de l'École Centrale de Lyon

École Doctorale N° 162
Mécanique Énergétique Génie Civil Acoustique

Spécialité de doctorat : Acoustique

Soutenue publiquement le 31/01/2022, par

Léo GIRIER

Mode-matching techniques for the modeling of rotor-stator wake-interaction tonal noise, with emphasis on the effects of vane camber

---

Devant le jury composé de :

Pr.	Auregan, Yves	Le Mans Université	Examinateur
Pr.	Grace, Sheryl	Boston University	Rapporteure
Dr.	Ingenito, Johanna	Horizon Orientation	Examinatrice
Pr.	Joseph, Phillip	University of Southampton	Examinateur
Dr.	Lafitte, Anthony	Safran Aircraft Engines	Invité
Pr.	Moreau, Stéphane	Université de Sherbrooke	Président du jury
Dr.	Posson, Hélène	Safran Aircraft Engines	Examinatrice
Pr.	Roger, Michel	École Centrale de Lyon	Directeur de thèse
Pr.	Schram, Christophe	Von Karman Institute	Rapporteur

À ma mémé Paulette,
ton petit coquelicot a finalement éclos.

Abstract

The present work is devoted to the modeling of noise generated by the impingement of fan wakes on outlet guide vanes in turbofan engines, which has been acknowledged as one of the most important contribution to aircraft noise. Modern fan stages display a high number of blades/vanes, resulting in strong cascade effect. For such configurations, the mode-matching technique chosen in this thesis shown promising capabilities to better understand and predict noise generation and propagation. This is why an extension of this technique to more realistic vane geometries is proposed, with the addition of camber in two dimensions.

Accounting for camber has a twofold impact on sound propagation through the inter-vane channels: curvature of the center line, and expansion of the cross-section. The latter is introduced by means of a multiple-scale analysis, relying on slow variations along the channel, while the former is added by formulating the wave equation in curvilinear coordinates. The channel expansion plays a significant role on sound transmission and reflection phenomena at all frequencies. It also generates cut-on/cut-off transitions of channel modes, which can drastically change the acoustic behavior. A detailed study of this mechanism has been carried out. On the other hand, it has been observed that curvature only matters above the first cut-off frequency of the channels, for typical outlet guide vane geometries.

Concerning the wakes evolution through the cascade of cambered vanes, only the expansion effect has been modeled. This allows one to recover the wakes slicing and tilting observed in numerical simulations. However, the missing curvature effects proved to be limiting to address noise prediction in realistic configurations. They should be added to ensure reliable results.

Throughout this work, emphasis was also placed on acoustic resonances. Parametric studies have been performed on the influence of vane design parameters and incident perturbation on the prediction of resonant frequencies. The modulation of the resonance pattern by an incident acoustic wave in non-ideal conditions has been explained, as well as the crucial role of cut-on/cut-off transitions at certain frequencies. The influence of acoustic resonances triggered by wake impingement was also studied. It appeared that their occurrence can either reduce or amplify noise.

Keywords: Aeroacoustics, rotor-stator wake-interaction noise, camber, mode-matching, multiple-scale analysis, cut-on/cut-off transition, acoustic resonance

Résumé

Ce travail est consacré à la modélisation du bruit d'impact des sillages de la soufflante sur les aubes de redresseur du flux secondaire d'un turboréacteur, qui est reconnu comme l'une des contributions majeures au bruit d'un avion civil moderne. Les étages de soufflante modernes présentent un nombre élevé de pales/aubes, ce qui entraîne un fort effet de grille. Pour de telles configurations, la technique de raccordement modal retenue pour cette thèse a montré des capacités prometteuses pour mieux comprendre et prédire la génération et propagation du bruit. C'est pourquoi une extension de cette technique à des géométries d'aube plus réalistes est proposée, avec l'ajout de la cambrure en deux dimensions.

La prise en compte de la cambrure a un double impact sur la propagation du son dans les canaux inter-aubes : la courbure de la ligne centrale et l'évasement de la section transverse. L'effet d'évasement est introduit au moyen d'une analyse multi-échelle, en supposant des variations lentes du canal, tandis que les effets de courbure sont ajoutés en formulant l'équation d'onde en coordonnées curvilignes. L'évasement du canal joue un rôle significatif sur la transmission et la réflexion du son à toutes les fréquences. Il génère également des transitions de mode coupé/passant dans les canaux, ce qui peut changer radicalement le comportement acoustique de la grille. D'autre part, il a été observé que la courbure n'a d'importance qu'au-dessus de la première fréquence de coupure des canaux, pour des géométries d'aube classiques.

Concernant l'évolution des sillages à travers la grille d'aubes cambrées, seul l'effet d'évasement a été modélisé. Cela a permis de prendre en compte le découpage et l'inclinaison des sillages observés dans les simulations numériques. Cependant, les effets de courbure semblent nécessaires pour prédire correctement le contenu modal généré dans des configurations réalistes. Ils devront être ajoutés pour garantir la fiabilité des résultats.

Au cours de ce travail, l'accent a aussi été mis sur les résonances acoustiques. Des études paramétriques ont été réalisées sur l'influence des paramètres géométriques des aubes et de la perturbation incidente. La modulation du motif de résonance par une onde acoustique incidente dans des conditions de résonance non idéales a été expliquée, ainsi que le rôle crucial des transitions. L'influence des résonances acoustiques déclenchées par l'impact des sillages a également été étudiée. Il apparaît que la résonance de la grille peut soit réduire, soit amplifier le bruit généré, en fonction de son motif.

Mots-clés: Aéroacoustique, bruit d'interaction de sillage, cambrure, raccordement modal, analyse multi-échelle, transition coupé/passant, résonance acoustique

Remerciements

Cette thèse de doctorat a débuté en février 2018 à l'aide du dispositif Cifre : avec la collaboration de l'entreprise Safran Aircraft Engines et du Laboratoire de Mécanique des Fluides et d'Acoustique (LMFA, UMR CNRS 5509), à cheval sur les chaires industrielles ADOPSYS (ANR-13-CHIN-0001) et ARENA (ANR-18-CHIN-0004). Elle a aussi bénéficié du soutien financier et de l'environnement fournis par le Labex CeLyA (Centre Lyonnais d'Acoustique) de la COMUE Université de Lyon, au sein du programme "Investissement d'Avenir" (ANR-10-LABX-0060/ANR-16-IDEX-0005) géré par l'Agence Nationale de la Recherche. J'ai ainsi passé du temps à la fois sur le site de l'entreprise à Villaroche et sur le site de l'École Centrale de Lyon, où se trouve le Centre Acoustique du LMFA, avec quelques passages dans les différents sites de la COMUE pour ma formation doctorale avec l'ED 162 MEGA. Je passe un petit clin d'œil au National Institute of Standards and Technology (anciennement National Bureau of Standards) qui a publié le fameux Handbook of Mathematical Functions (aka Abramowitz & Stegun), ainsi qu'au site web WolframAlpha, créé par Stephen Wolfram, sans quoi les thèses analytiques n'existeraient plus.

Je tiens à exprimer toute ma gratitude à mes encadrants qui m'ont soutenu et guidé avec une incroyable bienveillance pendant ces quatre années. Merci à toi, Michel, de m'avoir permis de suivre tes pas tout en me laissant trouver ma voie. Comme beaucoup j'admire à la fois le chercheur que tu es et l'humain au quotidien, humble et proche des gens. J'espère qu'un jour j'aurais l'occasion d'aller à l'ISROMAC avec toi. Merci à toi, Anthony-b, pour tes conseils et ta bonne humeur. Je me rends compte de la chance que j'ai d'avoir eu un encadrant comme toi, qui sait ce qu'est une thèse et aime la recherche. Ça va faire 5 ans que tu subis mes premiers jets de rapport écrit, depuis mon stage de fin d'étude, mais promis je vais redoubler d'effort pendant le post-doc !

I would also like to thank all my jury members for agreeing to attend my defense and to review my work, and especially my reviewers Sheryl Grace and Christophe Schram, who were quiet flattering despite the short amount of time given for their task. I hope to have the opportunity to meet you in person and perhaps even collaborate as I just begin my life as an aeroacoustics researcher.

Merci aux personnes qui m'ont formé des bancs de la fac au diplôme d'ingénieur, dont une grande partie est au LMFA. Coïncidence ? Je ne crois pas... J'en profite pour en remercier certaines qui m'ont particulièrement marqué. Merci à Marc Jacob, qui m'a initié à l'acoustique et a accepté d'écrire ma lettre de recommandation pour Centrale. Je ne devais pas être un élève trop casse-pieds, ma foi. Merci à Gilles Robert, dont j'admire le travail pédagogique. Merci à Christophe Bailly, un excellent professeur comme un excellent directeur de laboratoire, proche et à l'écoute. Merci à Lionel Soulhac, qui fut un tuteur PCP bienveillant, même si j'ai préféré m'orienter

vers l'acoustique plutôt que la dispersion atmosphérique. D'ailleurs, je n'ai toujours pas changé ma photo de CV/mariage... Merci à Édouard Salze, qui avait moins de barbe à l'époque mais était tout aussi gentil. Tu as changé ma vie avec tes schémas faits sous Inkscape, même si la team TikZ prend de l'ampleur #TikZProject. Merci à Stéphane, qui m'a accueilli à bras ouverts au pays de la poutine et m'a permis de faire mes premiers pas dans le monde de la recherche. Merci à Vincent Clair, dévoué à coder de super cas-tests illustratifs pour ses élèves et toujours de bonne compagnie pour une dernière bière (même celles qui piquent en Belgique). Merci à Didier Dragna pour sa patience exemplaire face à un groupe de jeunes centraliens démunis devant l'équation de Helmholtz en 2D un matin à 8h (sûrement un vendredi...). Merci à Fred (alias Frédéric Sturm), toujours une espièglerie en tête et le sourire aux coins des lèvres, grâce à qui je peux faire semblant de comprendre la parabolique quand je discute avec les gens faisant de la propa. Un laboratoire, ce n'est évidemment pas que des enseignants. Je voudrais remercier également Simon Bouley d'avoir écrit un manuscrit d'une telle clarté qu'il m'a guidé tout au long de ma thèse, et parfois encore aujourd'hui (non, je ne dors pas avec). Merci à Carine Zambardi et Agnès Delebassee-Nabet pour l'organisation du côté du LabEx CeLyA. Un immense merci à Marie-Gabrielle Perriaux, Marie-Noëlle Pailhès et Fatima El Boukhrissi, ainsi qu'à tout le SAF, pour leur travail précieux. Merci à Laurent Pouilloux, l'homme qui vit plus vite que son ombre, et Matteo Camier le prodige de l'info pour le SIC. Merci à Marie-Annick Galland pour la relance des cafés scientifiques. Merci à Louis Gostiaux pour son enthousiasme contagieux qui n'a d'égal que sa passion pour l'informatique libre. Merci également à lui et Wouter Bos pour l'organisation des séminaires du vendredi et leur reprise post-covid. Je remercie aussi Christophe Corre, qui m'a fait confiance pour les TP/BE de l'UE FLE (même si j'ai regretté quelques instants en voyant le nombre de slides à lire), et toute l'équipe pédagogique pour ces moments de partage et d'enrichissement. Merci à Michel Tessieux pour son humanité, toujours une ristourne en poche quand arrive le printemps du cinéma. Enfin, merci à tout le personnel (permanent et non-permanent) qui fait vivre le laboratoire. Je me rappelle que le point majeur qui était ressorti du sondage auprès des doctorant·e·s et post-doctorant·e·s était la qualité de l'environnement humain. Je plussoie cette conclusion mille fois !

Un grand merci également du côté de Safran à toute l'équipe YX-je-sais-plus-quoi-ça-change-tout-le-temps, en particulier à Mathieu Gruber, mon ancien tuteur de stage puis chef pendant la thèse. J'ai sincèrement apprécié toutes ces discussions que l'on a pu avoir, notamment sur la vision de l'encadrement qui est un sujet qui me tient à cœur. Je voudrais aussi remercier spécialement Hélène de Laborderie, qui a suivi en partie ma thèse et a toujours répondu présente pour m'aider si j'en avais besoin. Enfin, merci à William Roussel, anciennement connu comme l'expert python chez les stagiaires, maintenant chef d'équipe. Je vous retrouve en septembre, en espérant que le badge de prestataire externe ait aussi l'élastique !

Ma vie au Centre Acoustique s'est également enrichie de rencontres inoubliables, rythmées par les barbecues (team barbecue), raclettes, congrès, sorties, pauses café et baby-foot (le KCA indéniablement meilleure équipe de baby-foot du labo, no rage). En première place dans mon petit ~~foie~~ cœur tout mou, la team dont on taira le nom, avec Danny au poste de pilier, le gars sur qui on peut toujours compter en soirée comme en amitié. Attention Paris les beaux quartiers, ça va dannyraper ! Elina la trobairitz qui fait tout pour me remettre au sport afin de recommencer les sessions run&potins. Vivement qu'on se retrouve à Villaroche avé quelques chocos sorties d'une

poche. Ariane la ministre de la danse et son unité irlando-bretonne de température que personne ne comprend. Hâte de découvrir Fontainebleau avec mon crash pad pour moult sessions d'escalade. Yann le barman, que celui ou celle qui n'a jamais succombé à ses cocktails, me lance la première badiane. Je suis content d'incrémenter ton compteur de potes débiles, ne sachant pas faire la roulade de manière habile. Et finalement, Pierre notre soleil, qui en connaît un rayon en bicyclette chouette ! A bientôt sur Paris pour se faire coucou dans la vrai vie. Spéciale casse-dédi à deux autres joyeux lurons : Miguel et David, la soirée innellea n'était qu'un échauffement. Grazzie Gabriele, sans ton sourire les plantes ne poussent plus au bureau. Le destin nous a déjà rassemblé, je suis curieux de voir où est-ce qu'on va se retrouver. Merci à mon co-bureau préféré Jean, futur sénior/dictateur du bureau, pour m'avoir rappelé comment barrer un mot sous LaTeX. Merci à Mohcene, le meilleur skieur algérien du bureau avec qui j'ai enfin pu discuter de raccordement modal. Merci à Simon 1er du nom, nouveau membre de la team Roger, enfin un vrai acousticien ! Merci à Étienne, développeur de BATMAN, dont la passion pour les vieilles choses me dépasse tout autant que son intellect. Merci à Vathieu qui me fait maré avec ses jeux de mots. Tchin Fadlalah et la team LTDS oubliée dans le H10, les habitués des 3B. Merci à la génération terrible : Igor avec son style vestimentaire aussi décontracté que sa grimpe (et Florence pour ses délicieuses confitures), Estelle biceps qu'aucun dévers n'arrête, Alexandre l'homme mystérieux aux multiples noms de scène (certains l'appellent même Loïc), Jules #leJU le maître du TikZProject, Simon à la couleur de cheveux parfois surprenante, et Simon le photographe des lumières. Merci à Laura qui nous rappelle l'importance de la photosynthèse, à Arthur pour son style dans les calanques avec ses lunettes de soleil, à Codor l'incarnation de Jimmy Neutron, toujours le cerveau en éruption, à Hugo qui donne tout au marathon, à Alexis la machine, à Courtney et ses délicieux gâteaux, à Daniel et ses choix de musiques latines un peu douteux en fin de soirée, à Amal pour sa curiosité, à Emanuele et à Hemant les petits nouveaux. Merci à Jérôme pour ses coups droits bien liftés, à Wesley et les compères de l'équipe TI qui font des trucs trop savants pour que des acousticiens puissent comprendre. Merci aux sportifs de l'équipe TM : Aurélien, Majid et Anne-Lise, ainsi qu'à Florent, avec qui j'ai passé beaucoup trop d'heures à faire du PowerPoint. Merci à Marie, coach de danse, Andréa, qui déteste le baby-foot depuis son arrivée au labo, et tout le quartier de Little Italy (euh... FCT pardon !). Merci aussi aux anciens et anciennes : Giorgos, Vianney, Bertrand, Marion, Paul, Justine, Damien, Raffael, YuanYuan, Sarah, Maria, Petr, Antoni, Daher, Nacho, Thomas, Achraf l'inoubliable, Antoine le poilu, Maxime (car ce running gag doit persister), et toutes celles et ceux que j'oublie !

J'ai également une pensée pour tous mes amis de longue date, dont certains sont même venus écouter 45 min de charabia, sans qui rien ne serait possible. Il en va évidemment de même pour ma famille qui s'est déplacée en nombre pour ma soutenance. Merci papa, maman, Clément, Marion, Matthieu, Benoît, Annie, Gilbert, Yvan et Yenn (en visio à 5h du mat' !), Pierre et Paulette, qui aura vu tous ses petits enfants aller au bout de leurs études, dont deux docteurs ! Si c'est pas les gènes de la mémé ça !

Contents

List of Figures

List of Tables

Nomenclature

Abbreviations

ACARE	Aviation Research and Innovation in Europe
BPF	Blade Passing Frequency
CAA	Computational AeroAcoustics
DNS	Direct Numerical Simulation
FEM	Finite Element Method
HP	High-Pressure
ICAO	International Civil Aviation Organization
IGV	Internal Guide Vanes
LBM	Lattice-Boltzmann Method
LE	Leading Edge
LES	Large Eddy Simulation
LMFA	Laboratoire de Mécanique des Fluides et d'Acoustique
LP	Low-Pressure
MMBCW	Mode Matching for Bifurcated Curved Wave-guides
MMBW	Mode Matching for Bifurcated Wave-guides
OGV	Outlet Guide Vanes
PML	Perfectly Matched Layers
RANS	Reynolds-Averaged Navier-Stokes
TE	Trailing Edge
URANS	Unsteady Reynolds-Averaged Navier-Stokes

Greek Letters

$(\mathbf{u}^*, \mathbf{U}, \mathbf{u})$	total, mean and fluctuating velocity	[m/s]
$(\mathcal{A}, \mathcal{B})$	projection coefficients from cos to ψ and vice versa	
(ρ^*, D, ρ)	total, mean and fluctuating density	[kg/m^3]
(ζ, η, z)	staggered vane-related system of coordinates at LE	[m]
(c^*, C, c)	total, mean and fluctuating sound speed	[m/s]
(p^*, P, p)	total, mean and fluctuating pressure	[kg $\cdot$ m/s^2]
$\alpha_{j,p,q}$	transverse wavenumber	[m^{-1}]
β	Prandtl–Glauert factor	
Δ	relative error	
$\delta_{\nu,q}$	Kronecker delta	
ϵ	slow expansion parameter	
Γ	vector of conservative variables	
γ	parameter angle	

γ^*	ratio of specific heats	
$\Gamma_{1,2}$	conservative variable	
$\hat{\phi}$	generalized velocity potential accounting for transition	$[\mathrm{m}^2/\mathrm{s}]$
κ	curvature	$[\mathrm{m}^{-1}]$
$\mathcal{F}_q$	amplitude and phase relative coefficient of the reflected part of a cut-off mode undergoing transition	
$\mathcal{K}$	modified staggered wavenumber relative to the modified velocity	$[\mathrm{m}^{-1}]$
$\mathcal{L}$	wave operator	
$\mathfrak{I}$	inner product related to the annular modal basis	[m]
$\mathfrak{J}$	inner product related to the channel modal basis	[m]
$\mathfrak{K}$	modified staggered wavenumber relative to the modified enthalpy	$[\mathrm{m}^{-1}]$
μ	slowly-varying axial wavenumber	$[\mathrm{m}^{-1}]$
ν	integer related to an inner product	
ω	angular frequency	[rad/s]
Ω_R	shaft-rotation rate	[rad/s]
Φ	reduced slowly-varying velocity potential	$[\mathrm{m}^2/\mathrm{s}]$
ϕ	velocity potential	$[\mathrm{m}^2/\mathrm{s}]$
Ψ	camber angle	
ψ	normalized modal shape (duct eigenfunction)	$[\mathrm{m}^{-1/2}]$
Ψ_s	stagger angle	
σ	reduced axial wavenumber	
τ	generalized axial wavenumber	$[\mathrm{m}^{-1}]$
θ	slowly-varying transverse wavenumber	$[\mathrm{m}^{-1}]$
$\tilde{\phi}$	velocity potential in the Prandtl-Glauert space	$[\mathrm{m}^2/\mathrm{s}]$
Υ	stream-wise variation function	
ς	generalized reduced axial wavenumber	
Ξ	generalized stream-wise variation function accounting for transition	

Latin Letters

$(\mathrm{A_i}, \mathrm{B_i})$	Airy function of the first and second kind	
(J, Y)	Bessel function of the first and second kind	
$(\tilde{x}, \tilde{y})$	system of coordinates in the Prandtl-Glauert space	[m]
(A_q, B_q)	modal coefficients related to downstream- and upstream-propagating channel modes	$[\mathrm{m}^2/\mathrm{s}]$
(j, p, q)	integers relative to the incident, annular and channel modes	
(R_p, T_p)	modal coefficients related to reflected and transmitted annular modes	$[\mathrm{m}^2/\mathrm{s}]$
(s, n, z)	curved-channel system of coordinates	[m]
(x', y', z)	annular system of coordinates attache to TE	[m]
(x, y, z)	annular system of coordinates attache to LE	[m]
$\bar{a}$	exact channel inlet height	[m]
$\bar{k}$	propagative part of the total wavenumber	$[\mathrm{m}^{-1}]$
$\bar{R}_c$	channel center line curvature radius	[m]
e	exponential function	
$\mathrm{F_{BA}} \equiv \frac{1}{2}(\mathrm{B_i} + \mathrm{iA_i})$	composition of Airy functions	

i	imaginary unit	
$\mathbf{n}$	normal unit vector	
$\mathcal{P}$	acoustic power	[W]
$\tilde{k}$	total wavenumber in the Prandtl-Glauert space	[m^{-1}]
a	approximate channel inlet height	[m]
A_q^R	modal coefficients of the vortical channel modes	[m/s]
$A_q^{\pm\pm}$	staggered transverse wavenumber	[m^{-1}]
B	number of blades	
b	vane spacing	[m]
C_p	heat capacity at constant pressure	
F_j^R	vortical phase shift between LE and TE	
H	enthalpy	
h	channel height	[m]
$k = \omega/C$	total wavenumber	[m^{-1}]
$K_q^{\pm\pm}$	staggered axial wavenumber	[m^{-1}]
$k_{j,p,q}$	axial wavenumber	[m^{-1}]
l	chord length	[m]
l_c	inter-vane channel length, from interface BC to TE	[m]
$M = U/C$	Mach number	
n_j	collocation points	[m]
R	radius of the unwrapped cut	[m]
r	dimensionless inner coordinate (4.28)	
R_c	vane curvature radius	[m]
$S = \epsilon s$	slow curvilinear coordinate	[m]
T	temperature	
t	time	[s]
T_m	Chebyshev polynomials of the first kind	
T_p^R	modal coefficients of the vortical transmitted modes	[m/s]
V	number of vanes	
w_j	modal coefficients of the vortical incident modes	[m/s]
$X = \epsilon x$	slow axial coordinate	[m]
Z	acoustic impedance	[$kg/m^2/s$]

Superscripts

γ	Order of magnitude of the inner function expansion
R	relative to the vortical field
0	relative to either the initial iteration or an inner product with $\Psi = 0$
g	relative to the g^{th} iteration

Subscripts

(x, y, s, n)	relative to the component associated with the coordinate
$+$	relative to downstream propagation
$+\infty$	relative to the downstream annular domain
$-$	relative to upstream propagation
$-\infty$	relative to the upstream annular domain
γ	relative to either i, r, t, d or u)
d	relative to the downstream-propagating channel field

i	relative to the incident annular field
ps	relative to the pressure side
r	relative to the reflected annular field
ss	relative to the suction side
t	relative to the point $x = x_t$
t	relative to the transmitted annular field
u	relative to the upstream-propagating channel field
0,1,2	relative to the order in the power series

Introduction

General Context

With the exponential growth of air traffic, aircraft noise pollution has become a real societal problem. To remedy this, an international specialized agency, known as the International Civil Aviation Organization (ICAO), has emerged from the Chicago Convention in the late 1940s. Its role is to provide standards and recommended practices to manage aircraft noise pollution at an international level. One of the most important pillars of the balanced approach adopted by the ICAO is the reduction of noise at its source. To this end, noise limits have been imposed for aircraft since the 1970s. Since then, the ICAO noise standards, known as chapters, continue to evolve and are applied through the ICAO certification. The ICAO policy on that matter is "*to ensure that the latest available noise reduction technology is incorporated into aircraft design and that this is demonstrated by procedures that are relevant to day-to-day operations.*"[1]. Aircraft manufacturers are forced to pass this certification process with each of their airplanes for it to be allowed to fly. Also, the Advisory Council for Aviation Research and Innovation in Europe (ACARE) has set several objectives for the continent, as a reduction of 65% of the noise emissions for airplanes in 2050, compared to airplanes from the 2000s[2].

Aircraft noise can emerge from a variety of sources that are always related to some sort of flow unsteadiness. They can be split into two categories: sources related to the engine and sources related to the airframe. The engine is a complex system that generates sound in several ways internally, and by turbulent mixing within the hot jet flow downstream (shown in red in Figure 1). The airframe elements generate noise due to their interactions with the ambient flow during flight (shown in green in Figure 1). Moreover, sources can interact with each others, typically the jet flow with wing elements, as shown in blue in Figure 1.

Though all sources indicated in Figure 1 might be relevant for on-board noise, the present work focuses on noise pollution for people living near airports. To this end, the relative efficiency of each noise source is estimated on the ground through the certification process defined by the ICAO. The measurements are done during two main flight procedures: approach and take-off, as depicted in Figure 2. The approach procedure is basically a landing operation, so the engines run at the lowest

[1] International Civil Aviation Organization. [Online]. Available: https://www.icao.int/environmental-protection/Pages/Reduction-of-Noise-at-Source.aspx

[2] Advisory Council for Aviation Research and Innovation in Europe. [Online]. Available: https://www.acare4europe.org/sria/flightpath-2050-goals/protecting-environment-and-energy-supply-0

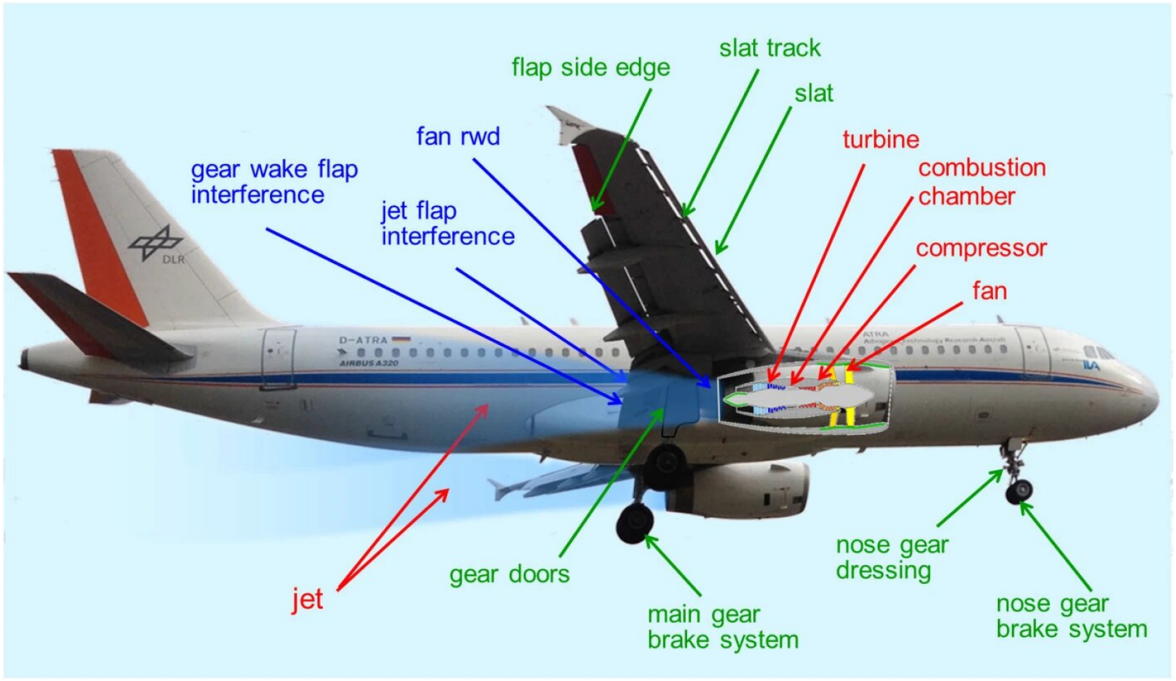

Figure 1: List of the most relevant noise sources and interactions, ©Henri Siller and Jan Delfs, DLR, 2019.

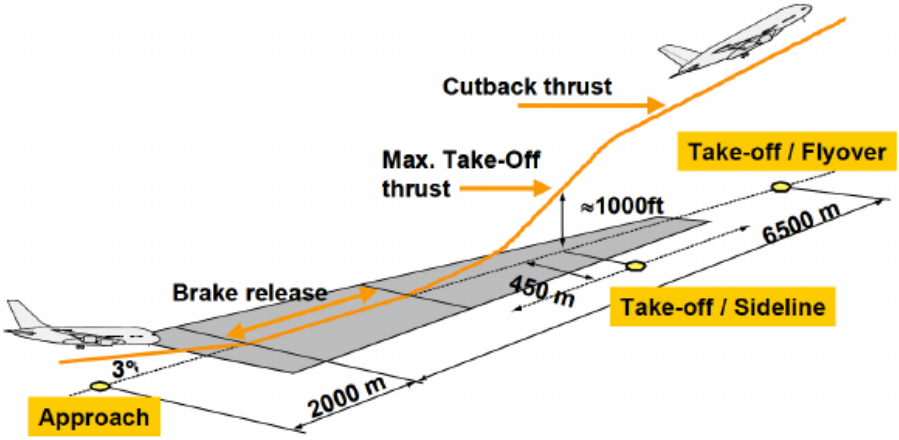

Figure 2: Noise certification flight paths and control points.

power/thrust of the certification. Noise is measured at a point directly below the flight path. During the take-off procedure, two sets of noise measurements are done. One lateral measurement (called sideline) during the first part of the take-off, where the engines are operated at full power/thrust, and another measurement below the flight path (called flyover/cutback) after the engines have been reduced to cutback power/thrust, ensuring a minimum climb gradient.

A study made in the early century, on typical long-range four-engine aircraft [50], pointed out that the airframe and engine noises are both crucial in approach condition whereas the engine noise is always significant and especially dominant during take-off, with emphasis on jet- and fan-related noise (see Figure 3). Reducing fan-related noise then appears as one of the main lever to reduce the overall aircraft noise emission. Therefore, this work focuses on the modeling of fan-related noise.

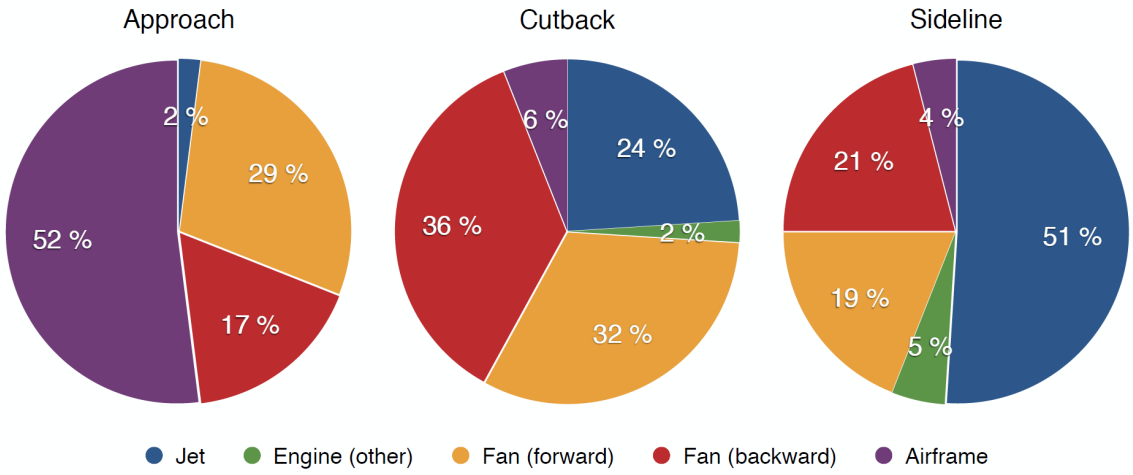

Figure 3: Example of noise source contributions for typical long-range four-engine aircraft, at the three certification points [50].

Thesis Aim

In order to reduce fan-related noise, aircraft engine manufacturers have two options: apply acoustic liners inside the engine to absorb noise, and optimize the design of the fan stage to directly reduce noise generation. The present work is concerned with the latter. Accurate and efficient predictive tools are then needed in optimization strategies at each step of the design (pre-design, design, ...). In this context, the mode-matching technique described in Bouley et al. [12] showed promising capabilities as a tool for fan stage acoustic pre-design, especially to further understand acoustic transmission and reflection phenomena. Safran Aircraft Engines, as an aircraft engine manufacturer, and the Laboratoire de Mécanique des Fluides et d'Acoustique (LMFA) in Lyon want to further improve this model and to include as many realistic design parameters as possible while preserving analytical tractability, so that fast computations are ensured when used in optimization loops and/or for broadband noise predictions. For this purpose, the present thesis proposes an extension of the model of Bouley et al. [12] by taking into account the effects of vane camber. Results are focused on tonal noise predictions but the model can be applied to broadband predictions as shown by François et al. [34].

Outline of Contents

The outline of the manuscript is as follows. Chapter 1 is dedicated to a literature review on the most important noise sources present in the fan stage, and the tools that are currently available to study and predict them. The general principles of the mode-matching technique are then explained. Finally, a particular attention is paid to the influence of vane camber on noise generation, that is yet to be fully understood.

Chapters 2 to 4 are devoted to the modeling and study of the transmission and reflection phenomena in a cascade of cambered vanes. In Chapter 2, the system of mode-matching equations is first detailed for a linear cascade of flat vanes. A first extension to account for the effects of camber is then proposed, based on a multiple-scale analysis. This first extension is fully analytical but is limited to relatively low

frequencies. The results obtained with the extended model are compared to highly accurate numerical results, which are used as a reference to validate the model. Chapter 3 presents an alternative extension of the initial model, which allows one to take into account the effects of vane camber at higher frequencies. This extension relies on a pseudo-spectral method to solve an eigenvalue problem, and is therefore qualified as semi-analytical. Comparisons with numerical results are presented to validate the model with and without the presence of a mean flow. The validity range of the low-frequency model is also assessed and parametric studies are conducted to investigate the effects of camber on sound transmission and reflection, with emphasis on the resonance phenomenon. Chapter 4 tackles the delicate phenomenon of cut-on/cut-off transition of acoustic modes, which can happen in the inter-vane channels due to camber. An extension of the multiple-scale analysis is explained, based on some form of matched asymptotic expansion, which allows one to account for the fast variations of sound encountered in the vicinity of the transition location. This extension is then introduced into the low-frequency mode-matching model, and investigations are performed on the role of the transition, with a particular focus on resonance phenomena.

Finally, Chapter 5 introduces the modeling of sound generation by periodic wake impingement on a linear cascade of cambered vanes. The wake is decomposed into vortical gusts in the frequency domain, and a model of vortical gust evolution through the cascade of cambered vanes is proposed, accounting for the "slicing" induced by the vanes downstream. The vortical gust is introduced into the mode-matching model alongside the acoustic waves and comparisons are made with analytical and numerical results available in the literature for tonal noise prediction. Parametric studies are also conducted to further understand the influence of camber on tonal noise generation.

Chapter 1

State of the Art

Introduction

As mentioned in the previous chapter, the aircraft engine is the main source of noise pollution, especially because of the contributions of the fan stage. The engine architecture is first presented in a simplified manner to better visualize the problem. A literature review is then done on the most important noise sources present in the fan stage in order to point out the key sources that need to be dealt with in the first instance. The tools currently available for studying and predicting noise are also presented, which helps to understand where the current work stands at. The general principles of the mode-matching technique used in this PhD are explained afterward. Finally, the current knowledge on the influence of vane camber on sound generation, which is yet to be fully understood, is presented.

Contents

1.1 Fan Noise Sources

1.1.1 Overview

Figure 1.1 displays a schematic view of the cross-section (called meridian plane) of a modern turbofan engine with its main components: the Low-Pressure (LP) and High-Pressure (HP) compressor/turbine stages and the combustion chamber. The so-called

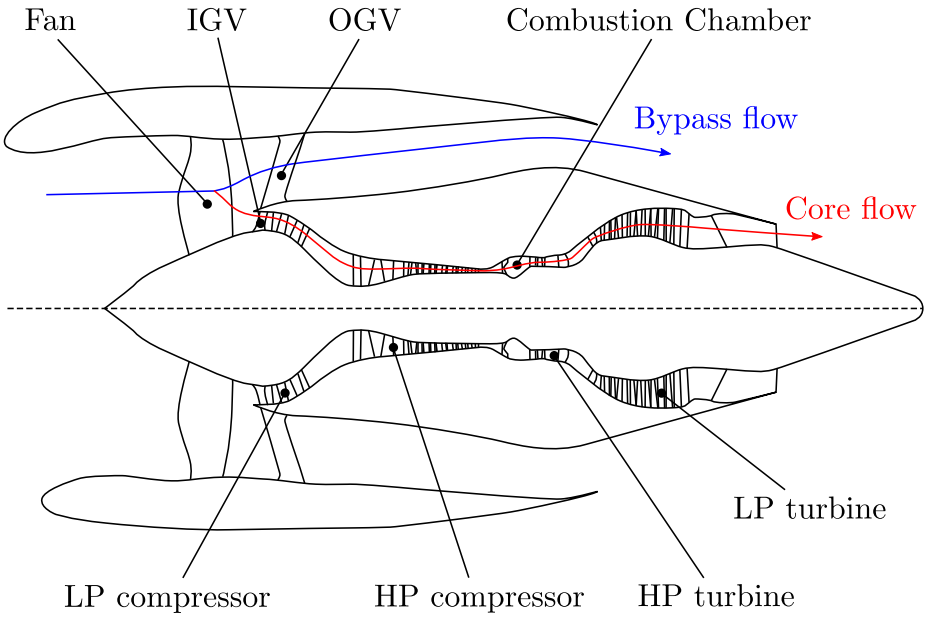

Figure 1.1: Schematic view of a modern turbofan engine.

fan stage is composed of the fan (rotating part) and two sets of guiding vanes (static part) named: Internal Guide Vanes (IGV) in the core duct, and Outlet Guide Vanes (OGV) in the bypass duct. The fan is basically the main component that is seen when standing in front of the engine.

As explained in the Introduction, the noise generated in the fan stage is one of the main contributions to the aircraft noise pollution. In order to predict this noise, the following methodology (see Figure 1.2) can be adopted:

1. Computation of the acoustic sources present in the fan stage;
2. In-duct propagation of sound up to the engine intake and exhaust;
3. Propagation of sound up to the external near-field, accounting for refraction effects at the lip of the air intake and exhaust, as well as the complex interactions with the jet flow;
4. Propagation of sound from the external near-field up to the far-field, where the microphones of the certification process are located, by means of free-field propagation tools.

In this work, only the first two steps are addressed: computation of the acoustic sources and in-duct propagation. The following part presents what sort of acoustic sources exist in the fan stage and how they are produced.

The fan stage of a modern turbofan engine is the home of a variety of noise generation mechanisms. Taking the point of view of a distant observer, the different sources

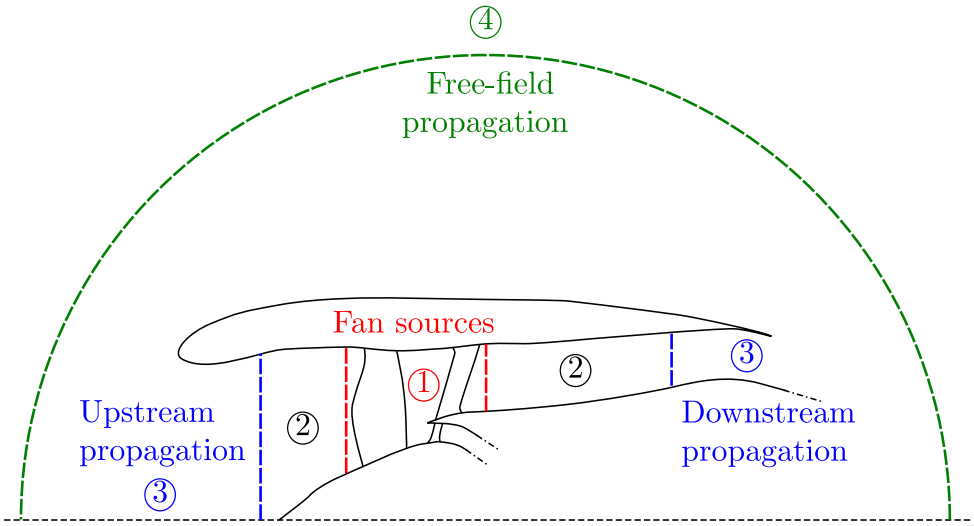

Figure 1.2: Possible noise prediction methodology.

of noise originate from unsteady interactions between the flow and the fan blades or the IGV/OGV. The fundamental analysis of Ffowcs Williams & Hawkings [31] teaches us that the acoustic sources due to a moving surface can be decomposed into three categories, with relative importance based on the Mach number at which the source approaches the observer point:

- thickness noise due to the volume displacement of fluid, mostly significant at high subsonic Mach numbers and for thick-enough bodies;

- loading noise due to the aerodynamic forces exerted by the blade/vane on the fluid, the unsteady part of which is essential at every subsonic Mach numbers on contrary to the steady part that is significant only at higher Mach numbers, similarly to thickness noise;

- flow noise due to unsteady fluctuations and internal stresses inherent to the flow (gathered into the so-called Lighthill's tensor), mostly significant at nearly sonic and supersonic Mach numbers.

Since the fan blades are moving in a non-inertial rotational motion, each aforementioned type of noise can be produced from the point of view of a distant observer. For the stator vanes, however, only unsteady loading can generate noise, since the surface is not moving.

Though the thickness noise, steady loading noise and flow noise can only originate from the rotation of the fan blades, the unsteady loading noise of the blades/vanes has numerous and unavoidable sources. The latter come from unsteady disturbances of the velocity field that flows over the blades/vanes. The main flow interactions that can happen in the fan stage are depicted in Figure 1.3. They can be gathered into two categories from the point of view of the acoustics, depeding on whether they are periodic or random. A periodic interaction will produce sound at the corresponding frequency and its harmonics. A random interaction will produce sound on a broadband spectrum, covering a continuous range of frequencies. A description of the resulting sources of noise is given in the following, according to the review by Peake & Parry [94].

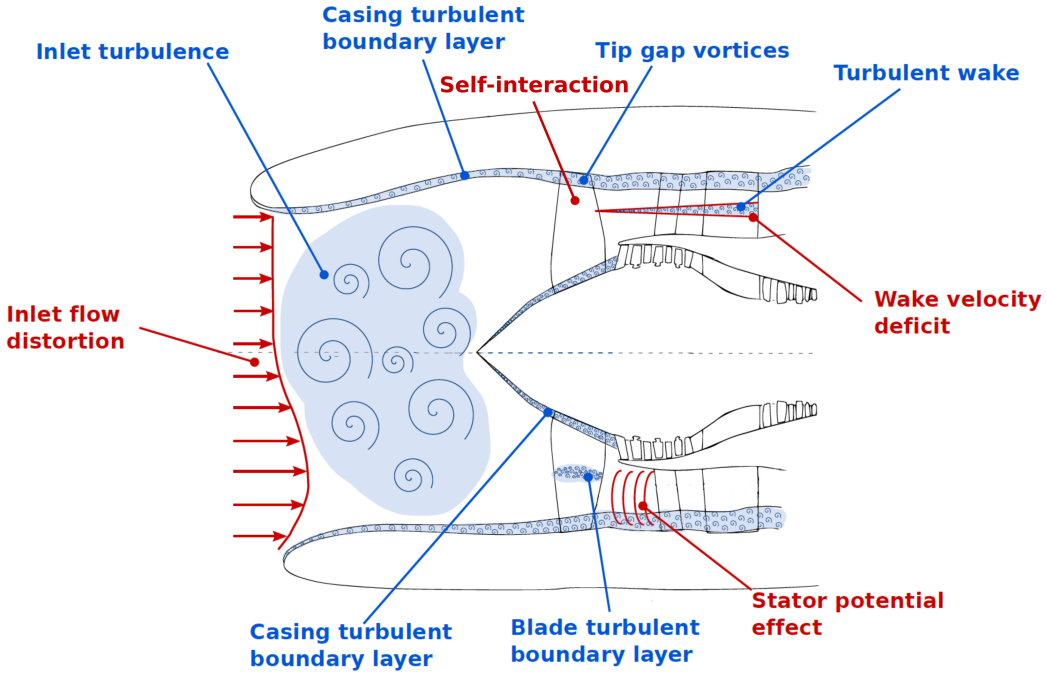

Figure 1.3: Fan noise sources caused by periodic (red) or random (blue) interactions.

1.1.2 Tonal Noise Sources

Fan Self-Interaction

Fan self-interaction mainly describes the fan thickness noise and steady loading noise here, which become significant at high subsonic speeds. Since unsteadiness is needed to produce sound, the steady part of the aerodynamic forces exerted by the blades on the fluid can only generate noise when the blades are in a non-inertial motion, such as a rotating motion. This is the case for the fan blades, the steady loading of which induces an unsteady periodic fluctuation of the fluid at each passage of a blade. Thus, these fluctuations naturally produce noise at harmonics of the Blade Passing Frequency (BPF), which is equal to the number of blades times the shaft-rotation rate Ω_R (in rad/s). In addition, at supersonic blade speeds encountered in take-off condition, shocks start to develop at the blade leading edges. The expected characteristic frequency is also the BPF. However, due to the non-linear behavior of the shocks formation and propagation, the latter are particularly sensitive to small blade-to-blade shape variations, resulting in differences in shock amplitude and azimuthal spacing. The azimuthal symmetry is broken and noise is generated, and radiated, at all multiples of the shaft-rotation frequency, generating what is called multiple pure tones, in contrast with the BPF harmonic tones (see [129]).

Droop-Fan Interaction

If the incoming flow in the air intake is non-uniform in the azimuthal direction, it creates mean distortions that interact with the rotating blades of the fan and generate periodic lift fluctuations. Unsteady loading noise is then produced at harmonics of the BPF. During flight, air is coming in the engine with a slight angle of attack due to the difference between the flight path and the aircraft pitch angles. The air intake is

usually designed to counteract this effect and ensure a uniform mean flow parallel to the fan axis. However, the air intake of modern turbofan engines is shorter and shorter and is usually not circular in cross section to satisfy ground-clearance requirements. It is then difficult to ensure a uniform incoming flow.

Fan-Vane Wake Interaction

The rotating wakes of the fan blades are also a strong source of noise when interacting with the stator vanes downstream. Considering all the fan blades as identical and equivalently distributed along the circumference, the rotating wakes periodically interact with each vane. The wake is characterized by a velocity deficit, the mean part of which generates a periodic variation of the vanes lift, as each wake passes by a given vane. This phenomenon generates an unsteady loading noise at harmonics of the BPF. The wakes velocity deficit is usually larger and stronger at mid-span and above. Consequently, the interaction of the wakes with the OGV is significantly noisier than with the IGV. Fan wake-OGV interaction is considered as the main source of tonal noise for a wide range of engine power regimes in current turbofan engines (except at full power during the sideline measurements, where the dominant noise source is due to the shocks developing at the fan leading edge).

Fan-Vane Potential Interaction

The presence of a thick solid surface in the flow forces the fluid to reorganize itself to bypass the obstacle. This creates a mean loading on the obstacle, which generates a local distortion of the flow, called potential effect. If the distance between the fan and the vanes is short enough, or if the potential effect of the vanes is amplified by the presence of struts, the steady distortion generated by the vanes can interact periodically with the fan blade trailing edges. Inversely, the rotating potential distortion generated by the blades can periodically interact with the vane leading edges. An unsteady loading noise is then produced at harmonics of the BPF. This mechanism is usually of secondary importance in modern turbofan engines, even with the reduction of the fan-OGV distance (see for example [122, 95]).

1.1.3 Broadband Noise Sources

Fan Turbulent Boundary-Layer Interaction

The fan is also responsible for a part of the broadband noise due to the turbulent motion of the flow within the blades boundary layer interacting with their trailing edge. At low Mach numbers, it seems that this contribution is dominated by sound amplification of the quadrupoles near the trailing edge [132]. Also, for off-design operating points such as in approach condition, the blades can operate at a high angle of attack resulting in flow separations or recirculation bubbles on the suction side. These mechanisms can generate large turbulent structures that produce broadband noise when interacting with the trailing edge or even produce noise by their own oscillation in the case of recirculation bubbles. All of these noise mechanisms due to the interaction between a fan blade and the turbulence produced in its own boundary layer and near wake are usually referred to as self-noise, with the addition of tip-gap noise [15].

Inlet Turbulence Ingestion

Atmospheric turbulence can also be responsible for broadband noise production [43, 91]. The interaction of the turbulent velocity field with the fan blades generates random fluctuations of the lift concentrated at the leading edge, thus giving rise to a broadband loading noise.

Fan/OGV Casing Boundary-Layer Interaction

The casing boundary layer is also responsible for turbulent interactions with the fan blades and OGV leading edges. This gives rise to a broadband loading noise. It has been noticeably studied by Stephens & Morris [128] and, even if of secondary importance in the present case, could become a significant mechanism for boundary-layer ingestion propulsion systems.

Fan Tip-Gap Noise

Jacob et al. [54] explain that the tip leakage flow is similar to a cross-jet flow, resulting from the pressure gradient between the fan blades pressure side and suction side. This secondary flow is then deflected by the surrounding flow and rolls up into one or two vortices, called the tip leakage vortex (generated at the leading edge) and the tip separation vortex (generated at mid-chord). The tip vortices then interact with the outer flow or the casing, creating two highly turbulent shear layers identified as major mechanisms for broadband noise production.

Fan-Vane Wake Interaction

The fan wakes also possess a strong turbulent component due to the shear layers developing from the mean velocity gradients. This turbulence then interacts with the OGV and produces broadband loading noise. According to Peake & Parry [94], this represents the strongest source of broadband noise.

The fan-OGV wake-interaction noise is considered as the main source of noise in modern turbofan engines for a wide range of operating conditions, for tonal noise as well as broadband noise. Hence, this work is focused on that particular rotor-stator interaction. It can be achieved by different methods, involving numerical simulation, analytical modeling or a combination of both. A list of the most commonly used tools is given in the following, with the aim of assessing their general pros and cons. This will help understand the goals and limitations of the current work.

Fan Noise Sources — Summary

Different types of noise are generated from the rotating motion of the fan and the unsteady interactions of the flow with the fan and the IGV/OGV. The main source of noise in the fan stage results from the unsteady impingement of the fan wake on the OGV. This interaction is both periodic, via the passage of a periodic mean velocity deficit seen by the OGV, and random, via the chaotic unsteadiness inherent to the turbulent flow. Thus, both tonal and broadband components of noise emerge from this interaction. The fan-OGV wake-interaction noise is therefore a complex noise generation mechanism to study but is also one of the

main lever to reduce the overall engine noise, thus aircraft noise pollution. That is why this thesis focuses on this source.

1.2 Rotor-Stator Wake-Interaction Noise Prediction

1.2.1 Blade/Vane Geometry Definition

To get a grasp of the complexity of the problem, the geometrical design parameters of the blades/vanes, involved in the generation of sound, are described below. Notice that those are simplified representations for the sake of explanation and that, in realistic designs, each parameter might vary from the bottom of the blade/vane to its tip, and even from one vane to another (in presence of struts). In Figure 1.4, from left to right, are represented the sweep angle, defined in the meridian plane, the lean angle, defined in the front view of the stator, and the stagger angle, defined in an unwrapped view of the stator at a given span. When unwrapping the stator in a cascade view as in

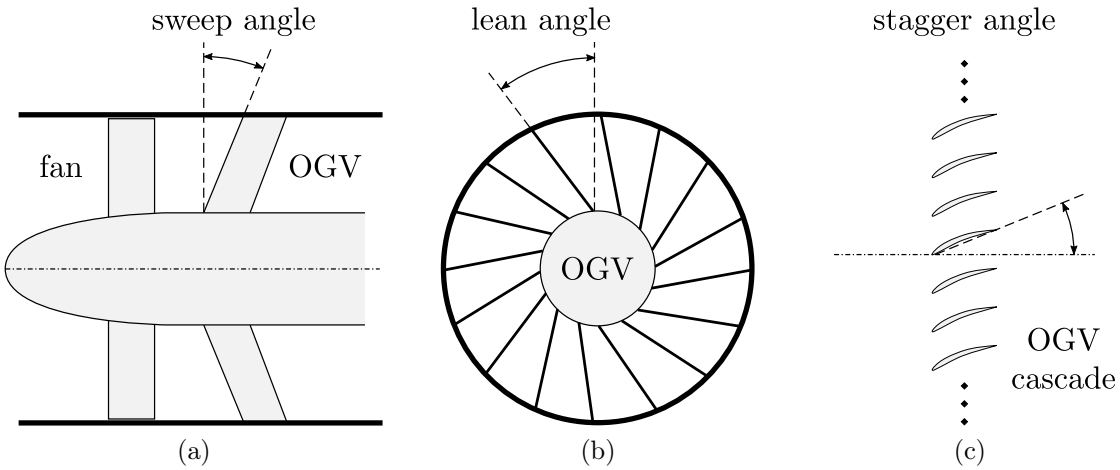

Figure 1.4: Definition of the sweep, lean and stagger angles. Stator in the meridian plane of the bypass duct (a), front view of the stator (b), and unwrapped stator at mid-span (c).

Figure 1.4c, the vane profile is highlighted. The latter also requires some parameters to be defined, which is done in Figure 1.5. The vane profile is defined from a straight line (chord line), the ends of which are called leading edge and trailing edge, respectively. The chord line serves as a reference to define the other parameters, such as the angle of attack of the flow or the stagger angle in Figure 1.4 (c). Then camber and thickness are added. The amount of camber is defined as the inverse of the radius of the smallest circle that fits in the vane (as shown at the leading edge in Figure 1.5), and can vary along the chord line. The thickness is defined as the distance between the upper surface (suction side) and the lower surface (pressure side) following the perpendicular to the chord line. As for camber, the thickness distribution can vary along the vane. Given the distribution of camber and thickness, a new center line, called the camber line, is defined from the upper and lower surfaces of the vane.

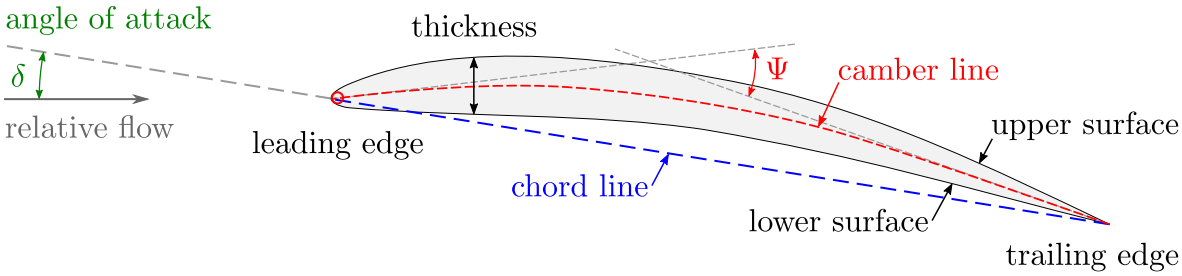

Figure 1.5: Definition of the vane profile.

Now that all the parameters necessary to understand the modeling of fan-OGV wake-interaction have been defined, a literature review of the most commonly used tools currently available to study and predict noise generation is presented.

1.2.2 Numerical Simulation

The study of noise generation through numerical methods is referred to as Computational AeroAcoustics (CAA). When resorting to CAA means, the most general set of equations can be solved while accounting for the real geometry of the problem. This allows a realistic flow description through the fan-OGV stage but is very costly if the whole range of turbulent scales, responsible for the broadband noise, is resolved. Consequently, different types of numerical simulations have been developed, with different levels of accuracy. The turbulent scales can be entirely resolved or only partially, in which case the finer ones are modeled, or even entirely modeled. Modeling the turbulent structures allows one to reduce the computational cost of the simulation by making some assumptions on the turbulence behavior, thus loosing in accuracy. The different approaches are summarized in Figure 1.6 and organized accounting to their relative computational cost and level of modeling [121].

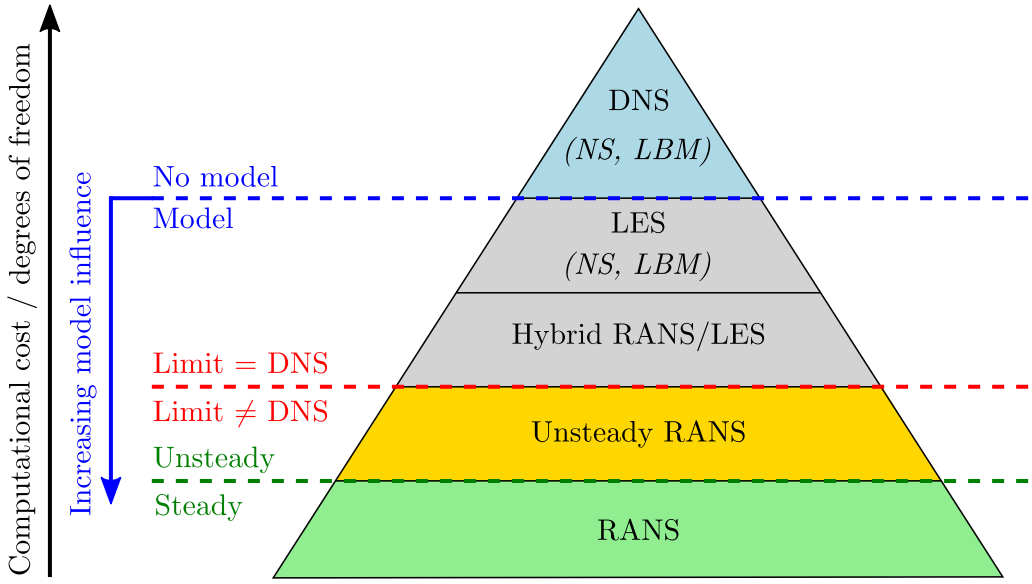

Figure 1.6: Hierarchy of the most commonly used Computational Fluid Dynamics (CFD) methods with different levels of turbulence modeling (from Sagaut et al. [121]).

At the very top, where all the turbulent scales are resolved, seats the Direct Numerical Simulation (DNS). Assuming the underlying equations are exact, only the numerical

configuration is responsible of the accuracy of this method (discretization schemes and boundary conditions). The set of equations used can be either the Navier-Stokes (NS) equations or the Boltzmann equation. The Navier-Stokes equations are the classical equations that describe the motion of Newtonian fluids, developed during the first half of the nineteenth century. The Boltzmann equation takes its roots in the kinetic theory of gases, which describes the gas motion at a smaller scale than classical fluid dynamics and recover the macroscopic fields by statistical means. The Boltzmann equation, after some simplifications, is able to recover the Navier-Stokes equations as a second-order perturbation around a local equilibrium [19]. On the contrary to classical meshes that follow the surface of the blades, the Boltzmann equation is solved on a lattice in which the blades are immersed. The method is therefore referred to as the Lattice-Boltzmann Method (LBM).

The Large Eddy Simulation (LES) is found just below the DNS. In this method, only the larger turbulent scales are resolved, while the finer ones, i.e. the most expensive, are modeled (see Sagaut et al. [121] for more details about the method). This method can also rely on either the NS equations or the LBM. Notice that, in theory, the LES tends to the DNS if the turbulence spectrum tends to be entirely resolved. However, this could cause practical issues due to the classical subgrid-scale models (which model the behavior of the finer turbulence scales) not being fitted for such an extreme use. On the other hand, the LES cost can be reduced by addressing the resolved part of the flow (largest turbulence scales) with a hybrid method. In this case, the resolved part is decomposed into an averaged representation of the flow solved by the Reynolds-Averaged Navier-Stokes (RANS) equations, while the turbulent fluctuations are solved by LES. The RANS method is explained in the following.

The RANS equations can be used in conjunction with LES or alone, to achieve even greater gains in computation time. If used alone, the turbulence is completely modeled, from the largest scales to the smallest ones. This method is based on the Reynolds decomposition (or Favre decomposition for compressible flows), which separates the mean flow part from its fluctuations. Thus, the RANS equations only describe the statistically-averaged part of the flow. A statistical description of the turbulence is still needed though, to get a closed system of equations since the Reynolds-averaged momentum equation involves the fluctuating field, through the so-called Reynolds stress tensor. Due to the use of averaged equations, the unsteady fluctuations are missing. Convergence issues can occur for flows exhibiting an intense unsteadiness, such as vortex shedding. To overcome this issue, an Unsteady-RANS (URANS) approach was developed, which is able to account for periodic and deterministic phenomena happening at a given frequency. Hence, the chaotic unsteadiness related to turbulence is still modeled statistically, but the periodic fluctuations responsible for tonal noise are recovered.

With these numerical tools available, different procedures have been developed for the computation of sound. Colonius & Lele [21] have made a rich review of these methods, highlighting their utility and limitations. They can be separated into two groups: one which directly computes the sound field, and another that separates the calculation of the acoustic sources from the calculation of sound propagation.

Direct Computation of Sound

The direct method numerically computes the unsteady flow and the sound generated by it, by solving compressible flow equations. Depending on the desired level of de-

scription of turbulence, the numerical tool employed is either the DNS, LES or hybrid RANS/LES. In each case, the computational domain needs to be large enough to cover the region of the acoustic sources and the region of the acoustic near-field. Then, if the far-field cannot be directly computed up to the point of interest (the engine intake and exhaust of Figure 1.2), a numerical domain extension or an analytical method is used. In the former, a coarser and better-suited mesh for acoustic propagation is used with simpler equations, such as the linearized Euler equations, whereas the analytical methods rely on a integral formulation of the wave equation. Such methods can be very accurate and account for all types of sources in the fan stage (not only wake interaction), but the drawback is the high computational cost. These methods are then helpful for unraveling the physical mechanisms of sound generation and providing rich databases but are currently restricted to academic problems. Notice that, if only the tonal noise is required, a URANS simulation can be used instead, drastically reducing the computational cost. This latter approach is very attractive in an industrial context.

Hybrid Methods for Noise Prediction

The hybrid methods separate the calculation of the unsteady flow from the calculation of the generated sound field. The sound field is viewed as a post-processing of the unsteady flow computation. This has the advantage of alleviating some of the acoustic requirements on the numerical mesh and schemes, hence reducing the computational cost. The propagation can then either be simulated by analytical or numerical means. A description of the different numerical methods available is given by Colonius & Lele [21]. On the other hand, analytical propagation models can be used in conjunction with either a DNS or LES. The radiated noise is then computed by means of an adequate acoustic analogy (see Goldstein [37]), propagating the numerically computed acoustic sources via a Green's function. The idea of the acoustic analogy is to restate the governing equations of gas dynamics as an equivalent wave equation in an idealized hypothetical medium. It assumes that the aerodynamic fluctuations generating sound are localized in a limited region[1], called the source region, which is described by the right-hand side terms in the equivalent wave equation. This method usually resorts to a linear wave operator, assuming a homogeneous medium at rest or in uniform motion, and thus does not permit any feedback of the acoustic pressure field on the aerodynamic fluctuations, restraining its use to weak pressure fluctuations. An illustrative representation of the principle of acoustic analogy is presented in Figure 1.7, as it was first introduced by Lighthill [66, 67]. Different analogy formulations have then followed, especially to account for the presence of solid surfaces and boundaries that are present in the context of ducted fan noise (see Curle [23], Ffowcs Williams & Hawkings [31] and Goldstein [37]). The fundamental analysis of Ffowcs Williams & Hawkings states that the acoustic sources due to a moving surface can be decomposed into three categories:

- thickness noise equivalent to a surface distribution of monopoles;
- loading noise equivalent to a surface distribution of dipoles;
- flow noise equivalent to a volume distribution of quadrupoles outside the surface.

[1]The ampltiude should decay sufficiently fast toward the boundaries of the numerical domain in order to ensure that most of the noise sources are accounted for.

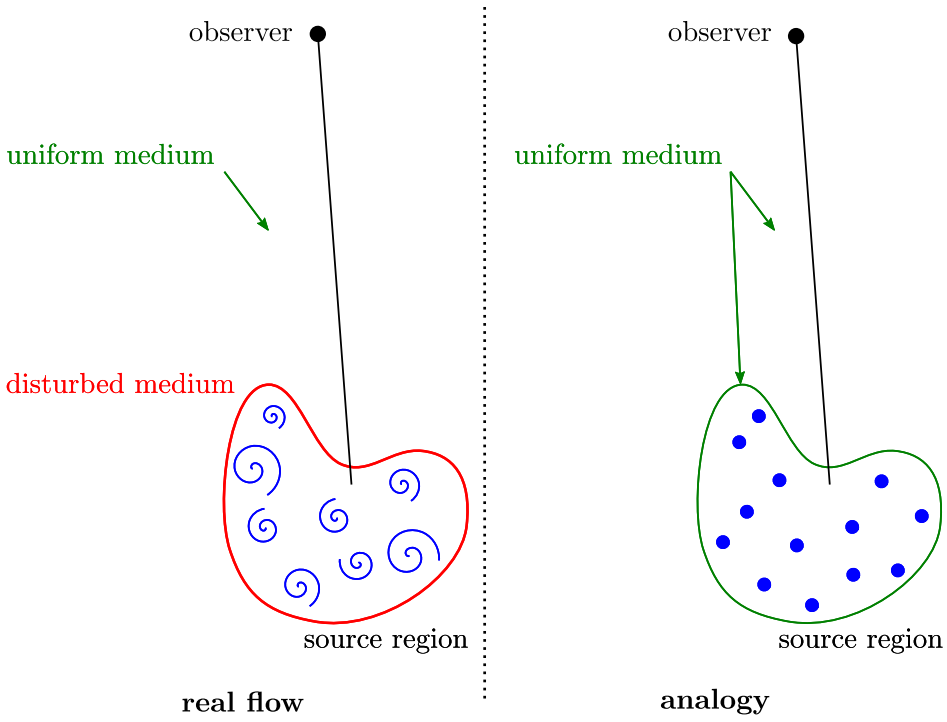

Figure 1.7: Acoustic analogy as introduced by Lighthill [66, 67].

As mentioned earlier, source terms associated to monopoles and quadrupoles can generally be neglected compared to the dipole noise of the wake interaction for low-subsonic fan configurations. Typical fan-OGV interaction noise, in approach condition, is then essentially loading noise due to unsteady pressure-induced forces on the vanes by the passage of the fan wakes. This simplifies the acoustic requirements in the numerical computation since the acoustic sources are supposed to be only on the vanes surface (even if the mesh still needs to be sufficiently refined in the wakes). Note that this simplification is no longer valid at high subsonic Mach numbers, in take-off condition, where the fan quadrupole noise possibly becomes significant and shock waves can appear, generating volume sources of noise by their interactions with vortical structures.

To summarize, hybrid methods are a good trade-off between accuracy and efficiency, compared to direct methods. However, they are generally still too expensive to be used as pre-design tools, especially for preliminary parametric studies or in optimization algorithms. Furthermore, all previous strategies based on numerical simulations require the knowledge of all geometrical details, which makes them unusable at early design stages. That is why aircraft engine manufacturers are interested in the development of a variety of prediction tools: from high accuracy and high computational cost, to low fidelity and low computational cost. For fast and physically consistent predictions, analytical models remain the best option. In each numerically-aided method previously mentioned, the acoustic sources were numerically computed, or at least partially. This is because they represent a crucial and very sensitive part of the noise prediction. In the next section, the analytical modeling is pushed further to tackle this unsteady aerodynamic part, in order to reduce the computational cost even more.

1.2.3 Analytical Modeling

For thin and weakly cambered vanes under small angles of attack, unsteadiness of the total aerodynamic force (composed of lift and drag) is mainly due to fluctuations of the flow angle of attack, thus to fluctuations of the incident velocity component perpendicular to the mean flow direction, called the upwash. This means that drag fluctuations are negligible compared to lift fluctuations in this case. The problem addressed in the following is then the generation of sound due to lift fluctuations only.

The first task is to model the wakes evolution from the rotor trailing edge to the stator leading edge. From the analysis of Chu and Kovásznay [20], if the wake velocity deficit is weak, it can be described at leading order as a pressure-free vortical motion purely convected by the mean flow[2] (frozen). As a consequence, the wake evolution can be described independently of the generated sound field. For tonal noise predictions, only the mean characteristics of the wake are necessary: mean velocity deficit at the wake center and wake width at mid-height. Several semi-empirical models based on the rotor drag coefficient were developed during the twentieth century, with increasing complexity. The most commonly used models are those of Reynolds & Lakshminarayana [102, 103], Majjigi & Gliebe [69], and Philbrick & Topol [96]. Analytical models of the rotor wake also exist, such as the one derived by Cooper & Peake in the early century [22]. For more details, Carazo has made a review of rotor wake models in his PhD thesis in 2012 [17]. Finally, a RANS simulation can also be used to extract the mean wake characteristics at the OGV leading edge[3]. Both modeling and numerical approaches are very affordable in an industrial context. These characteristics are then used to build a periodic Gaussian representation of the wakes velocity deficit, projected onto the direction normal to the mean flow (upwash component). Since the upwash fluctuations at the OGV leading edge are periodic in this case, a Fourier series is applied. Each resulting component in the frequency domain corresponds to a given harmonic of the BPF and is called a gust. The correlation between a given gust and the sound produced at a given harmonic is then straightforward.

For broadband noise predictions, the turbulence evolution is calculated with a RANS simulation. Then, the knowledge of the turbulence statistics at the OGV leading edge allows one to compute the upwash velocity cross correlation, based on a model of upwash turbulent spectrum (usually an isotropic model such as the well-known Liepmann and Von Karman spectra). This cross-correlation function describes the amplitude of each incident gust at each frequency. Comparatively to periodic interactions, a continuous and infinite set of gusts participates to the noise produced at each frequency for turbulent interactions.

Now that the necessary inputs have been defined (either discrete gusts at the BPF harmonics or a continuous gust cross-correlation function), a short survey of the most commonly used analytical models for rotor-stator wake-interaction noise is presented. In order to keep analytical tractability and to better understand the influence of each design parameter on the generated noise, a classical strategy is to start from the sim-

[2]This assumption is valid for a uniform mean flow, as modeled in this work, but is no longer true when accounting for the swirl in the inter-stage [58].

[3]The wake characteristics are, in practice, not directly available at the OGV leading edge due to the use of a mixing plane at the interface between the rotor mesh and the stator mesh. Thus, all fluctuations are lost in the stator domain and an extrapolation strategy is needed from the mixing plane up to the OGV leading edge. The latter is usually done on the wake harmonics, i.e. the Fourier transform of the wake in the azimuthal direction.

plest problem and then, try to alleviate some of the assumptions one by one. That is why the following models have been first derived in two dimensions, before being extended to three dimensions, adding new layers of complexity in the geometry and flow description along the way.

Cascade-Response Based Models

Based on the previous discussion, analytical models were focused on deriving the unsteady lift on the vanes, in order to be used in conjunction with a Green's function within the framework of acoustic analogies. The methodology is summarized synthetically in Figure 1.8, and as follow: the incident gusts generate an unsteady lift distribution along the vanes, then these lift fluctuations are used as an equivalent dipole distribution that generates sound, according to the analysis of Ffowcs Williams & Hawkings [31]. The unsteady lift is computed from the linearized Euler equations,

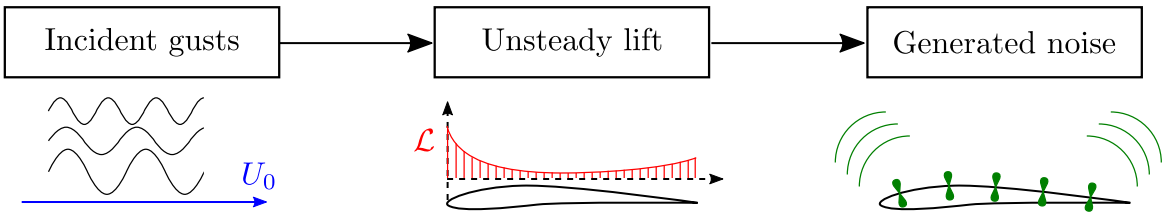

Figure 1.8: Noise prediction methodology scheme.

recast into a wave equation, with boundary conditions ensuring the impermeability of the vanes and a zero pressure jump at the trailing edge (Kutta condition). The resolution of this problem ends up to an integral equation that is solved by different techniques depending on the model considered.

The early developments considered an isolated airfoil modeled as an infinitely thin flat plate immersed in a uniform inviscid flow with zero angle of attack (see Figure 1.9), thus neglecting camber, thickness and mean loading effects. In this context, Sears [125] first derived a model of airfoil response in 1941 for incompressible flows, using the circulation theory. In 1975, Amiet [2] proposed a compressible airfoil response us-

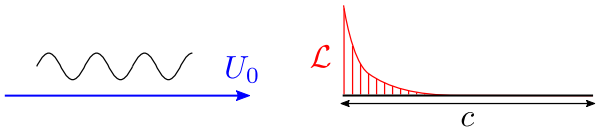

Figure 1.9: Schematic unwrapped representation of the isolated vane problem.

ing Schwarzchild's theorem [124], further extended for finite chord effects in 1976 [3]. These models were then used to deal with trailing-edge noise [4]. More recently, Roger & Moreau [113] and Moreau & Roger [75] proposed an extension of the model for trailing-edge noise by performing a back-scattering iteration. This extension allowed one to account for finite chord effects, which are relevant at low frequencies. In the same time, Moreau et al. [77] and Roger et al. [114] further extended the model to three-dimensional aerodynamic gusts, while also proposing semi-empirical corrections to account for small camber and thickness effects. Finally, Roger & Carazo [112] and Grasso et al. [40] added the effects of vane sweep to the modeling of leading-edge noise

and trailing-edge noise respectively. The stagger angle can then be accounted for by a simple rotation of the vane (polar angle shift in the formulation) and the lean angle by use of a strip theory as in Ref. [114]. However, modern OGV designs display a significant number of vanes with substantial overlapping [76], questioning the isolated vane assumption. In fact, because the equivalent sources are dipoles perpendicular to the vane surface, the interaction with the adjacent vanes is stronger when the overlap d is higher and when the inter-blade spacing a is small (see Figure 1.10). In such a configuration, the influence of the neighboring vanes on the acoustic generation and propagation cannot be neglected anymore.

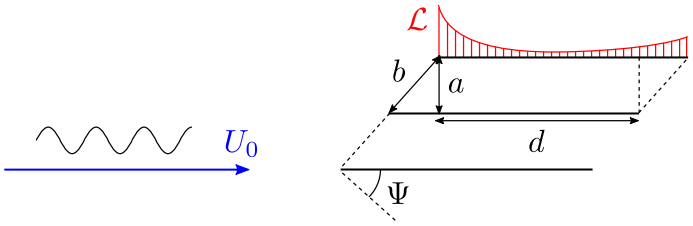

Figure 1.10: Schematic unwrapped representation of the cascade problem.

Cascade response functions have then been developed, accounting for the presence of adjacent vanes on sound generation and propagation, referred to as cascade effect. Different models were developed with increasing complexity and extensions to three-dimensional gusts and three-dimensional cascade responses, relying on the Wiener-Hopf technique (such as Glegg [36], Hanson & Horan [45] or Posson et al. [99]) or a collocation method (such as Ventres [130] and further extensions) to solve the integral equation. The Wiener-Hopf based modeling has then been pusher further, by accounting for the swirling mean flow present in the inter-stage (Posson & Peake [100], Masson et al. [71], Mathews & Peake [72]), or for small camber, thickness and angle of attack of the vanes (Baddoo & Ayton [5]).

These models have enabled a deeper understanding of the relative importance of each geometrical and flow parameter on the noise produced by rotor-stator wake interactions. Yet, artificial resonances between adjacent vanes at each strip, artificially considered parallel, are a concern and the radial scattering is not properly accounted for. An alternative approach for modeling both noise generation and propagation in a blade row has then started to emerge to tackle these issues, based on the mode-matching technique.

Mode-Matching Based Models

Mode-matching based models do not consider the problem as acoustic sources distributed along the vanes. The starting point is still the linearized Euler equations recast into a wave equation but, this time, the problem is seen as a matching problem of vortical and acoustic disturbances at the interfaces of bifurcated wave-guides. This implies that the major boundary value problem is moved from the vanes (impermeability condition) to the inlet and outlet of the wave-guides (continuity equations).

The mode-matching technique was first used for electromagnetic fields by Whitehead [131] and the method was later described in details by Mittra and Lee [73]. In the context of cascade aeroacoustics, Roger et al. [115, 120] and Ingenito et al. [52, 53] started applying the mode-matching technique in the early century to study sound generation and propagation in centrifugal compressors. This approach accounts for a fully

three-dimensional annular duct geometry without resorting to strips, and therefore naturally accounts for the radial scattering. More recently, Bouley et al. [12] developed a two-dimensional model of acoustic generation and transmission for axial-flow turbofan engines. The model is extended to three dimensions for wake-interaction noise in Bouley et al. [11], for trailing-edge noise in Roger et al. [117] and for turbulence impingement noise in François et al. [34]. In the meantime, an alternative mode-matching approach was developed, relying on the edge-dipole theory to recover the sound otherwise produced by the impingement of vortical gusts [13, 118]. The method is also fully explained in the PhD thesis of Bouley [10].

In each of the aforementioned models, the vanes are considered as infinitely thin flat plates with zero stagger, sweep and lean. Returning to two dimensions, extensions have been developed to take into account more realistic vane geometries. To this end, stagger angle was introduced by using Green's second identity, as described by Roger & François [116]. Roger et al. [117] then did a preliminary investigation on the diffuser effect of the OGV row, due to an increasing inter-vane channel cross-section. This effect is introduced when the mean camber is taken into account. To do so, vane profiles have been modeled using circle arcs. Good agreements have been obtained by Roger & Moreau [119] when applying the mode-matching technique with cambered vanes compared to Hixon's results [46] with the NASA Glenn Research Center BASS code, which solves the fully nonlinear Euler equations. A comparative study of two-dimensional sound transmission models in a realistic turbomachinery cascade, involving the mode-matching model [117] and the cascade-response model of Baddoo & Ayton [5], can also be found in Ref. [74], showing good agreement of the mode-matching model with the numerical solution up to a certain frequency. Roger et al. [117] and Roger & François [116] also used Ovenden's solution [86] for the velocity potential to highlight the effect of cut-on/cut-off transition of sound in such cambered inter-vane channels, but did not implement this mechanism in the mode-matching procedure. Meanwhile, Mao et al. [70] derived a mode-matching model with cambered vanes, using a discontinuous representation of a cambered vane in the form of several flat elements. However, the computational efficiency of the model did not seem satisfactory with increasing camber and frequency.

In this context, the mode-matching technique shows promising capabilities and has been chosen for this thesis. The following section explains the general principles of the mode-matching technique applied to a cascade of flat vanes.

Rotor-Stator Wake-Interaction Noise Prediction ——— Summary

Numerical simulations can be very accurate and can account for all types of sources in the fan stage (not only wake interaction), but the drawback is the high computational cost. Furthermore, they require the knowledge of all geometrical details, which makes them unusable at early design stages, when the blade design is not decided yet. The numerical methods are then helpful for unraveling the physical mechanisms of sound generation and provide rich databases but are restricted to more advanced design stages or to academic problems. For fast and physically consistent predictions, analytical models remain the best option. These models rely on stronger assumptions on the flow and the blade geometry, thus being less accurate but usable in early design stages in pre-optimization strategies. In this context, the mode-matching technique shows promising capabilities and has been chosen for this thesis.

1.3 Mode-Matching Technique

1.3.1 General Principle

The mode-matching technique is used to solve boundary value problems with linear frequency-domain differential equations. This technique is well suited when the geometry of the problem can be seen as the junction of multiple sub-regions. Such problems can arise for wave propagation in ducts with liners on specific portions of the wall or for wave scattering through bifurcated channels. In particular, sound propagation through an OGV row seen in a two-dimensional unwrapped cut at a constant radius can be viewed as an example of the latter case. An explanatory scheme is given in Fig. 1.11. An incident acoustic mode, described by its velocity potential ϕ_i, is scattered at the OGV Leading-Edge (LE) interface, generating reflected modes ϕ_r and transmitted modes ϕ_d in the channels. The latter are then scattered at the Trailing-Edge (TE) interface, giving rise to reflected channel modes ϕ_u and transmitted modes ϕ_t. Hard-walled boundary conditions at the walls of the inter-vane channels and periodic boundary conditions in the y-direction are imposed.

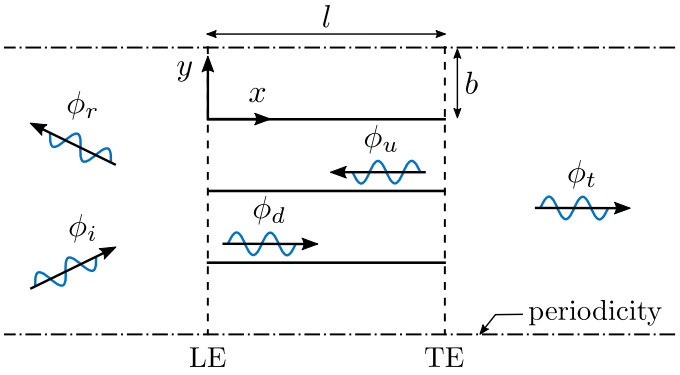

Figure 1.11: Scattering of an incident acoustic wave by a linear cascade of flat vanes.

The mode-matching technique can be described in three steps: partitioning, solving and matching. The partitioning consists in dividing the domain into different sub-domains in which the boundary conditions are uniform, allowing a solution of the wave equation on a local modal basis. In Fig. 1.11, the sub-domains are the upstream medium, each inter-vane channel and the downstream medium. The solving step is self-explanatory and provides the wavenumbers and modal shapes of the scattered waves in each sub-domain, based on an appropriate frequency-domain wave equation. For simple geometries such as in Figure 1.11, these wavenumbers and eigenfunctions are analytically known. Finally, the only remaining unknowns are the modal coefficients of the waves. They are defined by matching the different modal solutions at both leading-edge and trailing-edge interfaces. To do so, continuity equations specific to the problem are used in order to build a set of equations on the modal coefficients, which can be solved by matrix inversion. The equations that need to be satisfied through the OGV row are derived from the classical continuity equations (mass, momentum and energy) applied to an adiabatic lossless turbomachine [28]. The sub-domains solving step and the matching step are then detailed in what follows.

1.3.2 Wave Equation in the Sub-Domains

Consider a compressible inviscid isentropic perfect gas flow. In the following, all variables are made dimensionless in order to write general and concise equations but, notice that dimensional variables are used in all other chapters. The variables are made dimensionless by combinations of the inter-vane spacing b, for length quantities, and the flow fields far upstream of the cascade: density $\rho_{-\infty}$ for mass quantities, and sound speed $c_{-\infty}$ for time quantities. Then, defining the following dimensionless quantities: ρ^* as the density, $\mathbf{u}^*$ as the velocity, c^* as the sound speed, p^* as the pressure and γ^* as the ratio of specific heats, the governing Euler equations and conditions of an isentropic perfect gas are [97]

$$\frac{\partial \rho^*}{\partial t} + \nabla \cdot (\rho^* \mathbf{u}^*) = 0, \tag{1.1a}$$

$$\rho^* \left(\frac{\partial \mathbf{u}^*}{\partial t} + (\mathbf{u}^* \cdot \nabla)\mathbf{u}^* \right) + \nabla p^* = 0, \tag{1.1b}$$

$$\gamma^* p^* = \rho^{*\gamma^*} \quad \text{and} \quad c^{*2} = \frac{\partial p^*}{\partial \rho^*} = \rho^{*\gamma^*-1}. \tag{1.1c}$$

Using the vector identity $(\mathbf{u}^* \cdot \nabla)\,\mathbf{u}^* = \frac{1}{2}\nabla|\mathbf{u}^*|^2 + (\nabla \times \mathbf{u}^*) \times \mathbf{u}^*$, the momentum equation (1.1b) becomes

$$\frac{\partial \mathbf{u}^*}{\partial t} + \frac{1}{2}\nabla|\mathbf{u}^*|^2 + (\nabla \times \mathbf{u}^*) \times \mathbf{u}^* + \frac{1}{\rho^*}\nabla p^* = 0. \tag{1.2}$$

By using the relations between p^*, ρ^* and c^* in (1.1c), it follows that

$$\frac{1}{\rho^*}\nabla p^* = \nabla \left(\frac{\rho^{*\gamma^*-1}}{\gamma^* - 1} \right).$$

Hence, the momentum equation (1.2) is recast into

$$\frac{\partial \mathbf{u}^*}{\partial t} + \nabla \left(\frac{1}{2}|\mathbf{u}^*|^2 + \frac{\rho^{*\gamma^*-1}}{\gamma^* - 1} \right) + (\nabla \times \mathbf{u}^*) \times \mathbf{u}^* = 0. \tag{1.3}$$

The flow is then split up into a steady component (time average) and its fluctuations. The fluctuating part varies harmonically in time, with angular frequency ω, and is assumed to be small enough to allow linearization. Thus, the decomposition reads

$$[\mathbf{u}^*, \rho^*, p^*, c^*] = [\mathbf{U}, D, P, C] + [\mathbf{u}, \rho, p, c]\, \mathrm{e}^{-\mathrm{i}\omega t}. \tag{1.4}$$

The fluctuating velocity $\mathbf{u}$ can be expressed as the sum of independent acoustic and vortical motions according to the analysis of Chu & Kovásznay [20] at leading order. The fundamental theorem of vector calculus states that $\mathbf{u}$ can be decomposed into the sum of an irrotational field $\nabla\phi$ and a solenoidal field $\mathbf{u}^R$, which are associated, in this case, to the acoustic and vortical motions, respectively. Thus, the fluctuating velocity $\mathbf{u}$ reads

$$\mathbf{u} = \nabla\phi + \mathbf{u}^R. \tag{1.5}$$

Substitution into (1.1) and linearization yields:
the mean flow part

$$\nabla \cdot (D\mathbf{U}) = 0, \tag{1.6a}$$

$$\nabla \left(\frac{1}{2}|\mathbf{U}|^2 + \frac{D^{\gamma^*-1}}{\gamma^* - 1} \right) + (\nabla \times \mathbf{U}) \times \mathbf{U} = 0, \tag{1.6b}$$

$$C^2 = \gamma^* P/D = D^{\gamma^*-1}, \tag{1.6c}$$

and the fluctuating flow part

$$-i\omega\rho + \nabla \cdot (D\nabla\phi + \rho\mathbf{U}) = -\nabla \cdot (D\mathbf{u}^R), \tag{1.7a}$$

$$\nabla \left(-i\omega\phi + (\mathbf{U} \cdot \nabla)\phi + \frac{p}{D} \right) + (\nabla \times \mathbf{U}) \times \nabla\phi = -(-i\omega + \mathbf{U} \cdot \nabla)\mathbf{u}^R - (\mathbf{u}^R \cdot \nabla)\mathbf{U}, \tag{1.7b}$$

$$p = C^2\rho. \tag{1.7c}$$

If the mean flow is irrotational, the momentum equation (1.6b) can be integrated to a variant of Bernoulli's equation

$$\frac{1}{2}|\mathbf{U}|^2 + \frac{D^{\gamma^*-1}}{\gamma^* - 1} = E \,(\text{a constant}). \tag{1.8}$$

Otherwise, the above quantity is conserved only along streamlines (E being different for each streamline), which is demonstrated by taking the scalar product of the mean velocity field with the momentum equation: $\mathbf{U}\cdot$ (1.6b). From Goldstein [38], the pressure can be defined as

$$p = -D\left(-\mathrm{i}\omega\phi + \mathbf{U} \cdot \nabla\phi\right), \tag{1.9}$$

without loss of generality. The vortical field $\mathbf{u}^R$ is then uniquely defined by (1.7b) such that

$$\boxed{(-i\omega + \mathbf{U} \cdot \nabla)\mathbf{u}^R + \left(\mathbf{u}^R \cdot \nabla\right)\mathbf{U} = -\left(\nabla \times \mathbf{U}\right) \times \nabla\phi}. \tag{1.10}$$

Subtracting (1.7a) from $D(-\mathrm{i}\omega+\mathbf{U}\cdot\nabla)C^{-2}\times$(1.9), and using relations (1.7c) and (1.6a) finally leads to the following inhomogeneous compressible wave equation

$$\boxed{D(-i\omega + \mathbf{U} \cdot \nabla)\left[\frac{1}{C^2}(-i\omega + \mathbf{U} \cdot \nabla)\phi\right] - \nabla \cdot (D\nabla\phi) = \nabla \cdot (D\mathbf{u}^R)}. \tag{1.11}$$

1.3.3 Jump Conditions at the Interfaces

The mass conservation at an interface between a sub-domain 1 and a sub-domain 2 translates to mass-flow conservation through the interface as

$$[\rho^*\mathbf{u}^*]_1^2 \cdot \mathbf{n} = 0, \tag{1.12}$$

where $[\bullet]_1^2$ represents the jump of the quantity $(\bullet)$ between the domain 1 and 2, and $\mathbf{n}$ is the normal unit vector to the interface. Linearization yields

$$\begin{aligned}&[\rho U_x + D u_x]_1^2 = 0,\\ \Leftrightarrow &\left[\frac{p}{C^2} U_x + D u_x\right]_1^2 = 0.\end{aligned}$$

Finally, multiplying the above expression by the mean velocity U_x, equal at both sides of the interface, and dividing by the mean acoustic impedance of the fluid $Z = DC$, gives

$$\boxed{\left[\frac{p}{Z} M_x^2 + M_x u_x\right]_1^2 = 0}, \tag{1.13}$$

where $M_x = U_x/C$.

Across the stator, no external work acts on the fluid. Since the flow is assumed inviscid and adiabatic, hence isentropic, the conservation of momentum and energy gathered together is equivalent to the conservation of total (or stagnation) enthalpy [28]:

$$\left[H^* + \frac{1}{2}|\mathbf{u}^*|^2\right]_1^2 = 0, \tag{1.14}$$

where

$$|\mathbf{u}^*|^2 = (U_x + u_x)^2 + (U_y + u_y)^2. \tag{1.15}$$

For a perfect gas, the enthalpy can be written as

$$H^* = C_p T + \frac{p}{D}, \tag{1.16}$$

where C_p is the heat capacity at constant pressure. Linearization of (1.14) yields

$$\left[\frac{p}{D} + U_x u_x + U_y u_y\right]_1^2 = 0.$$

Finally, dividing the above equation by the mean sound speed C, identical at both sides of the interface, gives

$$\boxed{\left[\frac{p}{Z} + M_x u_x + M_y u_y\right]_1^2 = 0}. \tag{1.17}$$

Writing U as the norm of the mean velocity and Ψ as the angle with the direction perpendicular to the interface, the x-axis in Figure 1.11, allows one to express the mean velocity components as $U_x = U\cos\Psi$ and $U_y = U\sin\Psi$. The conservation of total enthalpy (1.17) is then recast as

$$\left[\frac{p}{Z} + M_x\left(u_x + u_y \tan\Psi\right)\right]_1^2 = 0. \tag{1.18}$$

Combining equations (1.13) and (1.18) allows one to recover the conservation of the fluctuating pressure p and fluctuating axial velocity u_x, commonly used in mode-matching procedures, but only for the particular case where the mean flow is perfectly perpendicular to the interface, i.e. when $\Psi = 0$. In general, when $\Psi \neq 0$, new variables need to be introduced to ensure the conservation of mass and total enthalpy through the

interface. These new conservative variables are written Γ_1 and Γ_2 in the following, and are gathered into a vector $\Gamma_\gamma = (\Gamma_{1\gamma}, \Gamma_{2\gamma})$, where the index γ stands either for the incident (i), reflected annular (r), transmitted annular (t), downstream-propagating channel (d) or upstream-propagating channel (u) field (see Figure 1.11). The matching equations then read

$$\begin{cases} \Gamma_i + \Gamma_r = \Gamma_d + \Gamma_u & \text{at LE,} \quad (1.19) \\ \Gamma_d + \Gamma_u = \Gamma_t & \text{at TE.} \quad (1.20) \end{cases}$$

Mode-Matching Technique — Summary

The mode-matching technique is used to solve boundary value problems with linear frequency-domain differential equations. This technique is well suited when the geometry of the problem can be seen as the junction of multiple sub-regions, as it is the case for an OGV row (inter-vane channels and annular domains upstream and downstream of the OGV). The mode-matching technique can be described in three steps: partitioning, solving and matching. The partitioning consists in dividing the domain into different sub-domains in which the boundary conditions are uniform. The solving step consists in calculating the eigenfunctions and associated eigenvalues of each sub-domain, if they are not analytically known. Finally, the matching step consists in writing continuity equations specific to the problem at each interface between the sub-domains, in order to build a set of equations on the modal coefficients, which are then solved by matrix inversion. The general wave equation that will be used in each sub-domain in this thesis has been defined, as well as the usual continuity equations at both the leading-edge and trailing-edge interfaces for a lossless adiabatic turbomachine [28], which ensure the conservation of mass and total enthalpy.

1.4 Influence of Vane Camber

Camber seems to play an important role in the generation and propagation of sound in a cascade, yet it remains poorly modeled. Many authors have noted its importance for tonal noise prediction at moderate and high frequency (see Evers & Peake [29], de Laborderie et al. [25, 26, 27] and Baddoo & Ayton [5]). However, it does not significantly affect broadband noise [29, 18, 35]. Accounting for camber has also several benefits in analytical models. When using flat vanes, the choice of an equivalent stagger angle is ambiguous and can have a dramatic impact on noise predictions (see for example the work of Sanjosé et al. [123], Grace [39] or Lewis et al. [65]). This is quite understandable when thinking of an equivalent surface distribution of dipoles, as explained by Ffowcs Williams & Hawkings [31]. The complex interference pattern resulting from the radiation of multiple vanes in a cascade is directly influenced by the orientation of the dipoles. Since the unsteady lift generated by the impingement of wakes on the vanes is mainly concentrated near the leading edge, a proper inclination of the vane leading edges should accurately reproduce the upstream radiation, whereas camber should mainly help to recover the downstream pressure field, as explained by de Laborderie et al. [27]: "*At 2 and 3 BPF the thickness and camber of the vane play a more significant role. Moreover these geometrical parameters seem to influence more*

the downstream propagation. This can be explained by the inter-blade channel geometry controlling the acoustic propagation inside and downstream of the cascade, whereas the upstream radiation is mainly controlled locally by the vane leading edge geometry.". Finally, flat OGV also lead to an ambiguity concerning the mean flow description, which is deviated through the cascade in realistic applications in order to recover the swirl. Hence, the mean flow has to evolve continuously, from upstream to downstream of the OGV, to obtain a relevant sound propagation.

Because of the above considerations, the attention is put on camber and tonal noise modeling in this work. A two-dimensional mode-matching model is proposed to describe sound generation and transmission through a linear cascade of cambered vanes. Neither the thickness nor the angle of attack is considered, and the modeling is limited to two dimensions in order to better understand the effects of camber at first. Note that the introduction of camber should give rise to the question of mean loading effects on sound but has not been introduced in the current model. Investigations on the mean loading effect can be found in Peake & Kerschen [92, 93] and a possible extension of the current model to account for a non-uniform mean flow is presented at the end of Chapter 3.

1.5 Conclusion

The context and limits of the present work have been defined. By view of the literature on fan-related noise, the focus on fan-OGV wake interactions is justified in approach condition of the aircraft, where it might be the dominant source, and even in take-off condition, where it remains significant even if supplemented notably by the generation and interactions of shock waves.

Several methods for simulating noise are available in the literature, from highly accurate but time consuming numerical simulations to approximate analytical solutions, with hybrid methods in the middle. This work focuses on analytical modeling to answer the need of i) fast and reliable prediction tools in the industrial context, and ii) to better understand sound transmission and reflection phenomena in the fan stage. In this context, the mode-matching technique described by Bouley et al. [12] showed promising capabilities to address sound generation and propagation in modern turbofan engines, in which the OGV cascade displays high solidity and overlap. That is why this model has been selected.

The general principles of the mode-matching technique have been explained, as well as all the assumptions made. The model is currently restricted to flat vanes, as are most of the analytical models in the literature. Vane camber remains poorly modeled and has been acknowledged to have a significant impact on wake-interaction tonal noise. Moreover, it has several practical benefits for the analytical modeling, by removing the ambiguity on: the choice of an equivalent stagger angle, and the missing swirl recovery through the OGV. The original contribution of this PhD thesis therefore resides in the addition of vane camber in a two-dimensional mode-matching model for rotor-stator wake-interaction tonal noise prediction.

Chapter 2

Acoustic Scattering by a Linear Cascade of Cambered Vanes at Low Frequency

Introduction

When adding camber to a cascade of vanes, what are the consequences on the scattering of an acoustic wave ? Understanding this is a first step to assess how the noise generated in the rotor-stator stage will propagate and allows one to answer the question of the description of the deviated mean flow. In this chapter, a mode-matching procedure is developed to compute the pressure field and modal content resulting from the scattering of an acoustic wave by a linear cascade of cambered vanes. The mode-matching technique is first explained in detail for flat vanes. Then, a model of acoustic propagation inside cambered inter-vane channels is derived, based on a slowly-varying duct approach. Only the variation of the cross-section is considered and the curvature effects are neglected in the first instance. This propagation model is incorporated in the mode-matching procedure and its validity is assessed with a finite elements numerical code, by comparing qualitative and quantitative results on a set of test cases.

Contents

2.1 Mode-Matching Technique for Flat Vanes

2.1.1 Jump Conditions

The mode-matching technique is first explained in detail with flat vanes, for the problem of acoustic scattering described in Figure 2.1. A set of variables (Γ_1, Γ_2) is sought, the

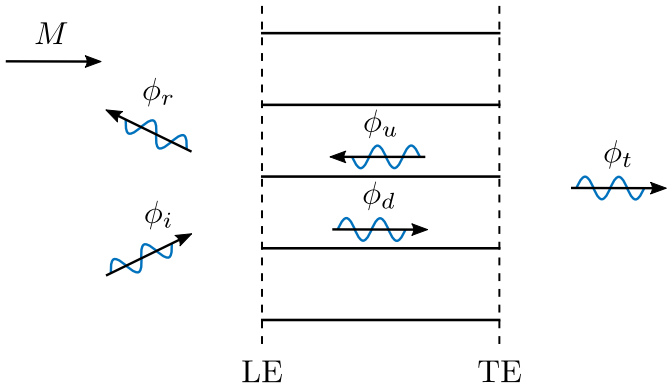

Figure 2.1: Scattering of an incident acoustic wave by a linear cascade.

conservation of which through the leading-edge (LE) and trailing-edge (TE) interfaces ensures the conservation of mass-flow rate (1.13) and total enthalpy (1.17). In this case, both equations involve a combination of the fluctuating pressure p and fluctuating axial velocity u_x. These variables could then be chosen as conservative variables through the interfaces but a few derivations will allow simpler expressions in the mode-matching equations.

Without any vortical perturbations, the fluctuating velocity u is potential:

$$u = \nabla\phi.$$

The pressure field, from (1.9), is given by

$$p = -D\left(-\mathrm{i}\omega + \mathbf{U}\cdot\nabla\right)\phi = \mathrm{i}kZ\phi - ZMu_x,$$

where $k = \omega/C$, $Z = DC$ and $M = U/C$. Thus, the conservation of p and ϕ are equivalent because the conservation of u_x is also enforced. The first conservative variable can be either

$$\boxed{\Gamma_1 = p} \quad \text{or} \quad \boxed{\Gamma_1 = \phi}, \tag{2.1}$$

while the second conservative variable has to be

$$\boxed{\Gamma_2 = u_x}. \tag{2.2}$$

In the following, the velocity potential will be used as the first conservative variable for the sake of simplicity.

In order to solve the continuity equations on ϕ and u_x, the same iterative procedure as in Bouley et al. [12] can be used. It starts with a simplified problem at the leading-edge interface, neglecting any feedback from the trailing-edge scattering. For convenience, ϕ and u_x are gathered into the vector $\Gamma_\gamma = (\phi, u_x)$, where the index γ stands either for the incident (i), reflected annular (r), transmitted annular (t), downstream-propagating channel (d) or upstream-propagating channel (u) field. The initial iteration, indexed by the superscript 0, reads

$$\begin{cases} \Gamma_i + \Gamma_r^0 = \Gamma_d^0, & \text{at LE,} \\ \Gamma_d^0 + \Gamma_u^0 = \Gamma_t^0, & \text{at TE.} \end{cases}$$

This allows one to solve the leading-edge equations independently at first, and get an initial value of the reflected and downstream-propagating modal coefficients. The downstream-propagating modal coefficients are then used to solve the trailing-edge equations and get the transmitted and upstream-propagating modal coefficients. For the next iterations, a correction is made to the leading-edge matching conditions in order to account for trailing-edge back-scattering. The new system is solved iteratively until a convergence is reached on the modal coefficients. The system of equations at the iteration of order $g > 0$ reads

$$\begin{cases} \Gamma_i + \Gamma_r^g = \Gamma_d^g + \Gamma_u^{g-1}, & \text{at LE,} \\ \Gamma_d^g + \Gamma_u^g = \Gamma_t^g, & \text{at TE.} \end{cases}$$

An alternative approach consists of directly solving the whole system of leading-edge and trailing-edge matching equations, which removes the need of an approximate equation at LE but generates a larger system to solve. Both methods have their pros and cons, which are partially discussed in some of the following chapters. In the following, each matching condition is detailed and written in two different ways: one suited for the iterative approach, and another suited for the direct global approach.

2.1.2 Initial Leading-Edge Interface

Acoustic Potentials

The first problem to solve is the scattering of the incident acoustic wave at the leading-edge interface of a periodic cascade of V vanes (Figure 2.2). This will result in scattered modes ϕ_r in the annular domain and ϕ_d in the inter-vane channels. The mean flow is considered uniform and constant through the cascade. From (1.11), each of these acoustic potentials is a solution of the convected Helmholtz equation in its respective sub-domain as

$$\beta^2 \frac{\partial^2 \phi}{\partial x^2} + \frac{\partial^2 \phi}{\partial y^2} + 2\mathrm{i}kM \frac{\partial \phi}{\partial x} + k^2 \phi = 0, \tag{2.3}$$

where $\beta^2 = 1 - M^2$. Using the Reissner transformation [101] allows one to reduce the above equation to the Helmholtz equation in the Prandtl-Glauert space $(x/\beta, y)$, such

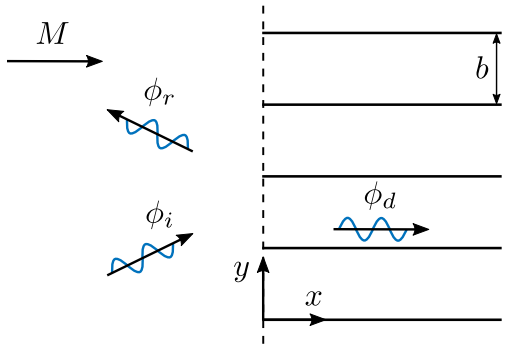

Figure 2.2: Scattering of an incident acoustic wave at the leading-edge interface.

that

$$\frac{\partial^2\tilde{\phi}}{\partial\tilde{x}^2}+\frac{\partial^2\tilde{\phi}}{\partial\tilde{y}^2}+\tilde{k}^2\tilde{\phi}=0, \tag{2.4}$$

where $\tilde{x}=x/\beta$, $\tilde{y}=y$, $\tilde{k}=k/\beta$ and $\tilde{\phi}=\phi\exp(\mathrm{i}kMx/\beta^2)$. By use of separation of variables $\tilde{\phi}(\tilde{x},\tilde{y})=\tilde{\phi}_{\tilde{x}}(\tilde{x})\tilde{\phi}_{\tilde{y}}(\tilde{y})$, equation (2.4) is rewritten as the following set of equations

$$\begin{cases}\partial^2\tilde{\phi}_{\tilde{x}}/\partial\tilde{x}^2+(\tilde{k}^2-\tilde{k}_y^2)\tilde{\phi}_{\tilde{x}}=0,\\ \partial^2\tilde{\phi}_{\tilde{y}}/\partial\tilde{y}^2+\tilde{k}_y^2\tilde{\phi}_{\tilde{y}}=0,\end{cases} \tag{2.5}$$

where $\tilde{k}_y$ is the constant introduced due to the equality of a function dependent on $\tilde{x}$ only with a function dependent on $\tilde{y}$ only, for each $\tilde{x}$ and $\tilde{y}$. The solution of each part is a combination of exponential functions. Introducing the dispersion relation $\tilde{k}_x^2=\tilde{k}^2-\tilde{k}_y^2$, the solution of the convected Helmholtz equation (2.3) in the physical space (x,y) is then

$$\phi(x,y)=\mathrm{e}^{-\mathrm{i}kMx/\beta^2}\left(A_x^+\mathrm{e}^{\mathrm{i}\bar{k}_x x/\beta^2}+A_x^-\mathrm{e}^{-\mathrm{i}\bar{k}_x x/\beta^2}\right)\left(A_y^+\mathrm{e}^{\mathrm{i}k_y y}+A_y^-\mathrm{e}^{-\mathrm{i}k_y y}\right), \tag{2.6}$$

where $(A_x^+,A_x^-,A_y^+,A_y^-)\in\mathbb{C}^4$ are arbitrary constants and $(\bar{k}_x,k_y)\in\mathbb{C}^2$, with $0\leq\arg(\bar{k}_x)\leq\pi/2$ and $0\leq\arg(k_y)\leq\pi/2$, are the axial and azimuthal wavenumbers linked by the dispersion relation $\bar{k}_x^2=k^2-\beta^2k_y^2$. In the following, the convective part $(-kM/\beta^2)$ and the propagative part $(\bar{k}_x/\beta^2)$ of the axial wavenumber are gathered together as

$$k_x^{\pm}=\frac{-kM\pm\bar{k}_x}{\beta^2}. \tag{2.7}$$

The solution (2.6) corresponds to the sum of four plane waves that propagate in each direction in the flow-attached frame of reference. By linearity of the Helmholtz equation, each potential represented in Figure 2.2 can be associated to a subset of these four plane waves and be described individually. The expressions of the incident ϕ_i, reflected ϕ_r and transmitted ϕ_d potentials are now detailed one by one.

In the annular domain, the downstream-propagating incident mode ϕ_i is chosen of unitary amplitude, so that it reads

$$\phi_i(x,y)=\mathrm{e}^{\mathrm{i}\alpha_j y}\mathrm{e}^{\mathrm{i}k_j^+ x},\quad\text{for}\quad-\infty<x\leq0\quad\text{and}\quad0\leq y<2\pi R. \tag{2.8}$$

The periodicity condition in the transverse direction enforces $\phi_i(x,0)=\phi_i(x,2\pi R)$,

which gives

$$\alpha_j = \frac{j}{R}, \quad j \in \mathbb{Z}.$$

The coefficient j represents the azimuthal modal order of the incident mode. Its value corresponds to the number of wavelengths in the transverse direction. Once j is set, the axial wavenumber k_j^+ is given by (2.7) as

$$k_j^+ = \frac{-kM + \sqrt{k^2 - \beta^2\alpha_j^2}}{\beta^2}.$$

It follows that the angle of propagation of the incident mode is set by the combination of the incident mode order j, the wavenumber k and the Mach number M.

The reflected potential ϕ_r is generated by the scattering of ϕ_i by the cascade. By symmetry of the problem, the incident wave is identically scattered by two adjacent vanes with only a constant time delay. This delay can be modeled by a phase shift and, according to the trace-velocity matching principle [97], the resulting scattered waves are structured by the same phase shift. This simply means that the effects (the scattered fields) are generated at each leading edge with the same time delay than the causes (the impact of the incident wave). Hence, the scattered potential is subject to the cascade periodicity through the property

$$\phi_r(x, mb) = \phi_r(x, [m-1]b)\mathrm{e}^{\mathrm{i}\alpha_j b}, \quad \forall m \in [\![1, V]\!], \tag{2.9}$$

which, letting α_p be the reflected transverse wavenumber, is equivalent to $\mathrm{e}^{\mathrm{i}\alpha_p b} = \mathrm{e}^{\mathrm{i}\alpha_j b}$. This leads to writing the reflected potential ϕ_r as the sum of an infinite number of modes, such that

$$\phi_r(x, y) = \sum_{p=-\infty}^{\infty} R_p \mathrm{e}^{\mathrm{i}\alpha_p y}\mathrm{e}^{\mathrm{i}k_p^- x}, \quad \text{for} \quad -\infty < x \leq 0 \quad \text{and} \quad 0 \leq y < 2\pi R, \tag{2.10}$$

where the transverse wavenumbers α_p are given by

$$\alpha_p = \alpha_j + p\frac{2\pi}{b} = \frac{j + pV}{R}, \quad p \in \mathbb{Z},$$

and the axial wavenumbers k_p^- by

$$k_p^- = \frac{-kM - \sqrt{k^2 - \beta^2\alpha_p^2}}{\beta^2}.$$

The expression (2.10) is actually a general mathematical result for periodic functions of the form (2.9) called Floquet modes [32]. It states that any wave propagating in a periodic domain can be described as a sum of plane waves.

In a given inter-vane channel, the downstream-propagating transmitted potential ϕ_d is bounded by hard walls in the transverse direction. This implies that $\partial\phi_d/\partial y = 0$ at $y = 0$ and $y = b$. The solution of the Helmholtz equation in this case is also composed

of an infinite number of modes, which reads

$$\phi_d(x,y) = \sum_{q=0}^{\infty} A_q \cos(\alpha_q y)\, \mathrm{e}^{\mathrm{i}k_q^+ x}, \quad \text{for} \quad 0 \le x < \infty \quad \text{and} \quad 0 \le y \le b, \tag{2.11}$$

where

$$\alpha_q = \frac{q\pi}{b}, \quad q \in \mathbb{N},$$

and

$$k_q^+ = \frac{-kM + \sqrt{k^2 - \beta^2 \alpha_q^2}}{\beta^2}.$$

From the trace-velocity matching principle [97], the value of the potential in the other inter-vane channels is simply given by a phase shift of $\mathrm{e}^{\mathrm{i}\alpha_j m b}$, $m \in [\![1, V-1]\!]$.

Continuity of the Acoustic Potential

Putting (2.8), (2.10) and (2.11) together at $x = 0$, the continuity of the acoustic potential at the leading-edge interface reads

$$\mathrm{e}^{\mathrm{i}\alpha_j y} + \sum_{p=-\infty}^{\infty} R_p \mathrm{e}^{\mathrm{i}\alpha_p y} = \sum_{q=0}^{\infty} A_q \cos(\alpha_q y)\,. \tag{2.12}$$

Since all coefficients R_p and A_q are unknowns, a projection is performed on the modal basis of the reflected waves to decouple them in (2.12), ending up with one equation on each reflected wave due to the property of mode orthogonality. The corresponding operator is

$$\int_0^b (\bullet)\mathrm{e}^{-\mathrm{i}\alpha_\nu y}\,\mathrm{d}y, \quad \text{with} \quad \alpha_\nu = \alpha_j + \nu\frac{2\pi}{b},\ \nu \in \mathbb{Z}. \tag{2.13}$$

This leads to three kinds of integrals in (2.12), namely $\mathfrak{I}_{i,\nu}$, $\mathfrak{I}_{p,\nu}$ and $\mathfrak{I}_{q,\nu}$, such that

$$\mathfrak{I}_{i,\nu} + \sum_{p=-\infty}^{\infty} R_p \mathfrak{I}_{p,\nu} = \sum_{q=0}^{\infty} A_q \mathfrak{I}_{q,\nu}.$$

The integral based on the incident wave is expressed as

$$\mathfrak{I}_{i,\nu} = \int_0^b \mathrm{e}^{\mathrm{i}(\alpha_j - \alpha_\nu)y}\,\mathrm{d}y = \int_0^b \mathrm{e}^{-\mathrm{i}2\pi\nu y/b}\,\mathrm{d}y = \begin{cases} b & \text{if} \quad \nu = 0, \\ 0 & \text{if} \quad \nu \neq 0. \end{cases}$$

Hence, $\mathfrak{I}_{i,\nu} = b\delta_{\nu,0}$ where δ is the Kronecker delta: $\delta_{\nu,0} = 1$ if $\nu = 0$, and $\delta_{\nu,0} = 0$ otherwise. The integral associated with the reflected waves reads

$$\mathfrak{I}_{p,\nu} = \int_0^b \mathrm{e}^{\mathrm{i}(\alpha_p - \alpha_\nu)y}\,\mathrm{d}y = \int_0^b \mathrm{e}^{\mathrm{i}2\pi(p-\nu)y/b}\,\mathrm{d}y = \begin{cases} b & \text{if} \quad \nu = p, \\ 0 & \text{if} \quad \nu \neq p. \end{cases}$$

Hence, $\sum_{p=-\infty}^{\infty} R_p \mathfrak{I}_{p,\nu} = bR_\nu$. Finally, the integral on the transmitted waves in the inter-vane channel yields

$$\mathfrak{I}_{q,\nu} = \int_0^b \cos(\alpha_q y)\, e^{-i\alpha_\nu y}\, \mathrm{d}y = \begin{cases} \dfrac{\mathrm{i}\alpha_\nu}{\alpha_q^2 - \alpha_\nu^2}\left(1 - (-1)^q \mathrm{e}^{-\mathrm{i}\alpha_j b}\right), \\ \dfrac{b}{2}(1 + \delta_{q,0}) \quad \text{if} \quad |\alpha_\nu| = \alpha_q. \end{cases} \tag{2.14}$$

Consequently, the potential continuity at the leading-edge interface is expressed as

$$\boxed{b\left(\delta_{\nu,0} + R_\nu\right) = \sum_{q=0}^{\infty} A_q \mathfrak{I}_{q,\nu}}. \tag{2.15}$$

Continuity of the Acoustic Axial Velocity

The acoustic axial velocity is the derivative of the potential with respect to x. Its continuity at the leading-edge interface reads

$$k_j^+ \mathrm{e}^{\mathrm{i}\alpha_j y} + \sum_{p=-\infty}^{\infty} R_p k_p^- \mathrm{e}^{\mathrm{i}\alpha_p y} = \sum_{q=0}^{\infty} k_q^+ A_q \cos(\alpha_q y) \tag{2.16}$$

Using the same projection method (2.13) gives

$$\boxed{b\left(k_j^+ \delta_{\nu,0} + k_\nu^- R_\nu\right) = \sum_{q=0}^{\infty} k_q^+ A_q \mathfrak{I}_{q,\nu}}, \tag{2.17}$$

where $k_\nu^- = -kM/\beta^2 - \sqrt{k^2 - \beta^2\alpha_\nu^2}/\beta^2$.

Linear System of the Mode-Matching Condition

To solve the problem on the A_q coefficients, the R_ν coefficients are canceled out by subtracting (2.17) to k_ν^- times (2.15). This yields

$$\sum_{q=0}^{\infty} A_q (k_\nu^- - k_q^+) \mathfrak{I}_{q,\nu} = b(k_\nu^- - k_j^+)\delta_{\nu,0}. \tag{2.18}$$

After a modal truncation ($\nu \in [-(N_\nu - 1)/2, (N_\nu - 1)/2]$ and $q \in [0, N_q - 1]$), the matrix form of the linear system of equations reads

$$\underline{\mathbf{M}}^{\mathbf{1}}\mathbf{A} = \mathbf{M_i}, \tag{2.19}$$

where

$$\left[M^1\right]_{\nu,q} = (k_\nu^- - k_q^+)\mathfrak{I}_{q,\nu}, \quad \left[M_i\right]_{\nu,1} = b(k_\nu^- - k_j^+)\delta_{\nu,0}, \quad \text{and} \quad [A]_{q,1} = A_q.$$

This has to be solved numerically using an algorithm based on a direct factorization method, such that the LU decomposition, or an iterative method if necessary. Then the R_ν coefficients can be deduced from either the potential continuity (2.15) or the axial velocity continuity (2.17).

Another possibility is to solve the A_q and R_ν coefficients simultaneously with a global matrix equation of the form

$$\begin{pmatrix} \mathbf{E_1^1} & \mathbf{F_1^1} \\ \underline{\mathbf{E_2^1}} & \underline{\mathbf{F_2^1}} \end{pmatrix} \begin{pmatrix} \mathbf{A} \\ \mathbf{R} \end{pmatrix} = \begin{pmatrix} \mathbf{H_1^1} \\ \mathbf{H_2^1} \end{pmatrix}, \tag{2.20}$$

where

$$\left[E_1^1\right]_{\nu,q} = \mathfrak{I}_{q,\nu}, \quad \left[F_1^1\right]_{\nu,\nu} = -b\delta_{\nu,\nu}, \quad \left[H_1^1\right]_{\nu,1} = b\delta_{\nu,0},$$
$$\left[E_2^1\right]_{\nu,q} = k_q^+\mathfrak{I}_{q,\nu}, \quad \left[F_2^1\right]_{\nu,\nu} = -bk_\nu^-\delta_{\nu,\nu}, \quad \left[H_2^1\right]_{\nu,1} = bk_j^+\delta_{\nu,0},$$
$$[A]_{q,1} = A_q, \quad [R]_{\nu,1} = R_\nu.$$

After solving this system, the A_q coefficients are used for the trailing-edge matching.

2.1.3 Trailing-Edge Interface

Acoustic Potentials

At the trailing-edge interface, the incident potential now corresponds to ϕ_d. Its scattering at the trailing-edges gives rise to reflected scattered modes ϕ_u in the channels and transmitted scattered modes ϕ_t in the annular domain, as shown in Figure 2.3. The

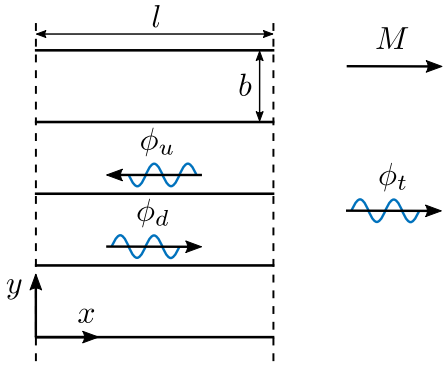

Figure 2.3: Scattering of a channel acoustic wave at the trailing-edge interface.

acoustic potentials are still solution of the convected Helmholtz equation (2.6) with the same boundary conditions. They are expressed in the channels as

$$\phi_d(x,y) = \sum_{q=0}^{\infty} A_q \cos(\alpha_q y)\, \mathrm{e}^{\mathrm{i}k_q^+ x}, \quad \text{for} \quad 0 \le x \le l \quad \text{and} \quad 0 \le y \le b, \tag{2.21}$$

$$\phi_u(x,y) = \sum_{q=0}^{\infty} B_q \cos(\alpha_q y)\, \mathrm{e}^{\mathrm{i}k_q^- (x-l)}, \quad \text{for} \quad 0 \le x \le l \quad \text{and} \quad 0 \le y \le b, \tag{2.22}$$

where

$$k_q^\pm = \frac{-kM \pm \sqrt{k^2 - \beta^2\alpha_q^2}}{\beta^2}, \quad \alpha_q = \frac{q\pi}{b}, \quad q \in \mathbb{N},$$

and in the annular domain as

$$\phi_t(x,y) = \sum_{p=-\infty}^{\infty} T_p \mathrm{e}^{\mathrm{i}\alpha_p y} \mathrm{e}^{\mathrm{i}k_p^+ (x-l)}, \quad \text{for} \quad l \le x < \infty \quad \text{and} \quad 0 \le y < 2\pi R, \tag{2.23}$$

where

$$k_p^+ = \frac{-kM + \sqrt{k^2 - \beta^2\alpha_p^2}}{\beta^2}, \quad \alpha_p = \alpha_j + p\frac{2\pi}{b} = \frac{j + pV}{R}, \quad p \in \mathbb{Z}.$$

Continuity of the Acoustic Potential

Taking the potentials (2.21), (2.22) and (2.23) evaluated at $x = l$ gives

$$\sum_{q=0}^{\infty} \left(A_q \mathrm{e}^{\mathrm{i}k_q^+ l} + B_q \right) \cos\left(\alpha_q y\right) = \sum_{p=-\infty}^{\infty} T_p \mathrm{e}^{\mathrm{i}\alpha_p y}. \tag{2.24}$$

Using the projection (2.13) allows one to write the potential continuity at the trailing-edge interface as

$$\boxed{\sum_{q=0}^{\infty} \left(A_q \mathrm{e}^{\mathrm{i}k_q^+ l} + B_q \right) \mathfrak{I}_{q,\nu} = bT_\nu}, \tag{2.25}$$

where $\mathfrak{I}_{q,\nu}$ is defined by (2.14).

Continuity of the Acoustic Axial Velocity

Taking the derivative of the potentials with respect to x at the trailing-edge interface yields the axial velocity continuity as

$$\sum_{q=0}^{\infty} \left(k_q^+ A_q \mathrm{e}^{\mathrm{i}k_q^+ l} + k_q^- B_q \right) \cos\left(\alpha_q y\right) = \sum_{p=-\infty}^{\infty} k_p^+ T_p \mathrm{e}^{\mathrm{i}\alpha_p y}. \tag{2.26}$$

Hence, using the same projection method as previously gives

$$\boxed{\sum_{q=0}^{\infty} \left(k_q^+ A_q \mathrm{e}^{\mathrm{i}k_q^+ l} + k_q^- B_q \right) \mathfrak{I}_{q,\nu} = bk_\nu^+ T_\nu}, \tag{2.27}$$

where $k_\nu^+ = \frac{-kM + \sqrt{k^2 - \beta^2\alpha_\nu^2}}{\beta^2}$.

Linear System of the Mode-Matching Condition

The T_ν coefficients are now eliminated by subtracting (2.27) to k_ν^+ times (2.25). This yields

$$\sum_{q=0}^{\infty} \left(k_\nu^+ - k_q^- \right) B_q \mathfrak{I}_{q,\nu} = \sum_{q=0}^{\infty} \left(k_q^+ - k_\nu^+ \right) A_q \mathrm{e}^{\mathrm{i}k_q^+ l} \mathfrak{I}_{q,\nu}. \tag{2.28}$$

After a modal truncation ($\nu \in [-(N_\nu - 1)/2, (N_\nu - 1)/2]$ and $q \in [0, N_q - 1]$), the matrix form of the equations to solve is

$$\underline{\mathbf{M}}^{\mathbf{2}}\mathbf{B} = \mathbf{M_d}, \tag{2.29}$$

where

$$\left[M^2\right]_{\nu,q} = \left(k_\nu^+ - k_q^- \right) \mathfrak{I}_{q,\nu}, \quad [M_d]_{\nu,1} = \sum_{q=0}^{\infty} \left(k_q^+ - k_\nu^+ \right) A_q \mathrm{e}^{\mathrm{i}k_q^+ l} \mathfrak{I}_{q,\nu}, \quad \text{and} \quad [B]_{q,1} = B_q.$$

Again, the system of equation can be solved using either a direct factorization method or an iterative method, the latter being generally more robust in this case. Then the T_ν coefficients can be deduced from either the potential continuity (2.25) or the axial velocity continuity (2.27).

Using a global matrix equation instead reads

$$\begin{pmatrix} \mathbf{E_1^2} & \mathbf{F_1^2} \\ \underline{\mathbf{E_2^2}} & \underline{\mathbf{F_2^2}} \end{pmatrix} \begin{pmatrix} \mathbf{B} \\ \mathbf{T} \end{pmatrix} = \begin{pmatrix} \mathbf{H_1^2} \\ \mathbf{H_2^2} \end{pmatrix}, \tag{2.30}$$

where

$$\left[E_1^2\right]_{\nu,q} = \mathfrak{I}_{q,\nu}, \quad \left[F_1^2\right]_{\nu,\nu} = -b\delta_{\nu,\nu}, \quad \left[H_1^2\right]_{\nu,1} = -\sum_{q=0}^{\infty} A_q \mathrm{e}^{\mathrm{i}k_q^+ l}\mathfrak{I}_{q,\nu},$$

$$\left[E_2^2\right]_{\nu,q} = k_q^-\mathfrak{I}_{q,\nu}, \quad \left[F_2^2\right]_{\nu,\nu} = bk_\nu^+\delta_{\nu,\nu}, \quad \left[H_2^2\right]_{\nu,1} = -\sum_{q=0}^{\infty} k_q^+ A_q \mathrm{e}^{\mathrm{i}k_q^+ l}\mathfrak{I}_{q,\nu},$$

$$[B]_{q,1} = A_q, \quad [T]_{\nu,1} = T_\nu.$$

After the first pass of leading-edge matching (2.20) and trailing-edge matching (2.30), an initial value of the B_q coefficients is known. For the next steps in the iterative procedure, the left-running channel modes ϕ_u are added to the leading-edge matching based on the knowledge of the previous iteration. This leads to the correction detailed hereafter.

2.1.4 Correction to the Leading-Edge Interface

The complete mode-matching equations at the leading-edge interface need to account for the left-running modes ϕ_u traveling back from the scattering at the trailing-edge interface. This acts like a feedback from the trailing-edge interface that has been neglected in the first iteration in (2.20). The complete picture of the leading-edge problem is depicted in Figure 2.4. At a given iteration of order $g \geq 1$ the potential

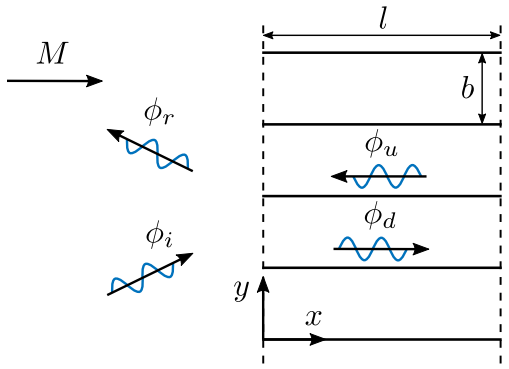

Figure 2.4: Scattering of an incident acoustic wave at the leading-edge interface with feedback from the trailing-edge scattering.

continuity and axial velocity continuity respectively read,

$$\boxed{b\left(\delta_{\nu,0} + R_\nu^g\right) = \sum_{q=0}^{\infty}\left(A_q^g + B_q^{g-1}\mathrm{e}^{-\mathrm{i}k_q^- l}\right)\mathfrak{I}_{q,\nu}}, \tag{2.31}$$

and

$$\boxed{b\left(k_j^+\delta_{\nu,0}+k_\nu^- R_\nu^g\right)=\sum_{q=0}^{\infty}\left(k_q^+A_q^g+k_q^-B_q^{g-1}\mathrm{e}^{-\mathrm{i}k_q^-l}\right)\mathfrak{I}_{q,\nu}}. \tag{2.32}$$

Combining them to cancel out the unknown R_ν^g coefficients yields

$$\sum_{q=0}^{\infty}A_q^g(k_\nu^- - k_q^+)\mathfrak{I}_{q,\nu}=b(k_\nu^- - k_j^+)\delta_{\nu,0}+\sum_{q=0}^{\infty}B_q^{g-1}(k_q^- - k_\nu^-)\mathrm{e}^{-\mathrm{i}k_q^-l}\mathfrak{I}_{q,\nu}. \tag{2.33}$$

After a modal truncation ($\nu\in[-(N_\nu-1)/2,(N_\nu-1)/2]$ and $q\in[0,N_q-1]$), the corrected system of equations at the leading-edge interface is

$$\underline{\mathbf{M}}^{\mathbf{1}}\mathbf{A}=\mathbf{M_i}, \tag{2.34}$$

where

$$\left[M^1\right]_{\nu,q}=(k_\nu^- - k_q^+)\mathfrak{I}_{q,\nu},\quad [M_i]_{\nu,1}=b(k_\nu^- - k_j^+)\delta_{\nu,0}+\sum_{q=0}^{\infty}B_q^{g-1}(k_q^- - k_\nu^-)\mathrm{e}^{-\mathrm{i}k_q^-l}\mathfrak{I}_{q,\nu},$$

$$[A]_{q,1}=A_q^g.$$

The R_ν coefficients are deduced from either (2.31) or (2.32).

The corrected global system of equations at the leading-edge interface is

$$\begin{pmatrix}\underline{\mathbf{E_1^1}} & \underline{\mathbf{F_1^1}}\\ \underline{\mathbf{E_2^1}} & \underline{\mathbf{F_2^1}}\end{pmatrix}\begin{pmatrix}\mathbf{A}\\ \mathbf{R}\end{pmatrix}=\begin{pmatrix}\mathbf{H_1^1}\\ \mathbf{H_2^1}\end{pmatrix}, \tag{2.35}$$

where

$$\left[E_1^1\right]_{\nu,q}=\mathfrak{I}_{q,\nu},\quad \left[F_1^1\right]_{\nu,\nu}=-b\delta_{\nu,\nu},\quad \left[H_1^1\right]_{\nu,1}=b\delta_{\nu,0}-\sum_{q=0}^{\infty}B_q^{g-1}\mathrm{e}^{-\mathrm{i}k_q^-l}\mathfrak{I}_{q,\nu},$$

$$\left[E_2^1\right]_{\nu,q}=k_q^+\mathfrak{I}_{q,\nu},\quad \left[F_2^1\right]_{\nu,\nu}=-bk_\nu^-\delta_{\nu,\nu},\quad \left[H_2^1\right]_{\nu,1}=bk_j^+\delta_{\nu,0}-\sum_{q=0}^{\infty}k_q^-B_q^{g-1}\mathrm{e}^{-\mathrm{i}k_q^-l}\mathfrak{I}_{q,\nu},$$

$$[A]_{q,1}=A_q^g,\quad [R]_{\nu,1}=R_\nu^g.$$

2.1.5 Limitations

The model can be extended to staggered flat vanes using Green's reciprocity theorem, as in Roger & François [116], but a question arises concerning the mean flow description. Adding stagger allows one to be more accurate about acoustic scattering at the leading-edge interface but cannot account for the mean flow deviation through the OGV. Such a model would not be accurate in terms of modal content and sound propagation downstream of the OGV. Some authors [25] used different stagger angles at the leading-edge and trailing-edge interfaces, with an iterative Wiener-Hopf based method, but the equations are somehow ill-posed since this creates a discontinuity in the mean flow field that is not accounted for explicitly. The present work deals with this problem by modeling cambered vanes, allowing a continuous deviation of the mean flow through the cascade. Adding camber should also benefit the noise prediction downstream of the

OGV, due to a more realistic description of sound propagation through the inter-vane channels [29, 27, 26, 25, 5].

The description of the vanes geometry and the mean flow is detailed in the following, with the derivation of slowly-varying acoustic modes in the inter-vane channels and their implementation in the mode-matching technique.

Mode-Matching Technique for Flat Vanes — Summary

The mode-matching technique has first been explained in detail in the simpler case of unstaggered flat vanes, in subsonic flow conditions. The first step consists in defining the set of conservative variables that will be used at the leading-edge and trailing-edge interfaces. These variables are derived from the classical continuity equations (mass, momentum and energy) applied to an adiabatic lossless turbomachine [28]. A wave equation is formulated in each sub-domain (upstream, downstream and between the vanes) and is solved on a local modal basis. The matching equations at the interfaces can then be defined on the modal coefficients of each of these modal solutions. The final step consists in defining an iterative method that solves the leading-edge and trailing-edge mode-matching equations until a sufficient convergence is reached on the modal coefficients.
The validity of this method has been demonstrated by comparing results with the Wiener-Hopf solution in Bouley et al. [12]. The method has also been adapted for staggered flat vanes by Roger & François [116]. Nonetheless, a cascade of flat vanes cannot account for the mean flow deviation occurring through the OGV and thus, is not adapted to the problem of fan-OGV wake-interaction noise. To remedy this problem, the present work extends the mode-matching method to cambered vanes, allowing a continuous deviation of the mean flow through the OGV row. Adding camber also describes more realistically the vanes profile and should benefit tonal noise predictions at high frequency, as noted by many authors [29, 27, 26, 25, 5], especially downstream of the OGV.

2.2 Sound Propagation through Cambered Inter-Vane Channels

2.2.1 Geometry

Circle Arc

The cambered vanes are modeled by circle arcs, which means that a constant curvature distribution along the chord is assumed. Figure 2.5 shows how the stagger angle Ψ_s, the camber angle Ψ and the axial chord length l_x are introduced. Ψ is the angle formed by the tangents to the vane leading edge and trailing edge. Since the OGV trailing edge is aligned with the x-axis, i.e. the turbomachinery axis, the camber angle Ψ is equivalent to the leading-edge slope angle. Furthermore, because the vanes are circle arcs, $\Psi_s = \Psi/2$ and thus $l_x = l\cos\Psi_s = l\cos\Psi/2$.

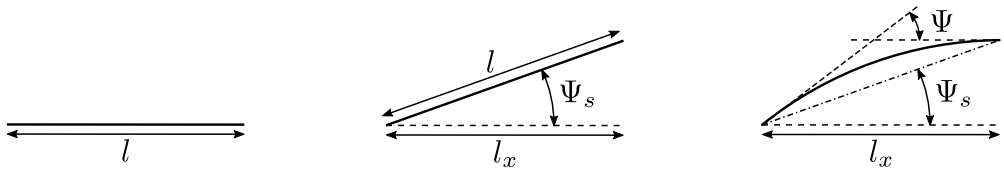

(a) (b) (c)

Figure 2.5: Description of the vanes from flat (a) to staggered (b) and finally curved and staggered (c).

Straight-Channel Approximation

The addition of camber has a twofold impact on sound propagation through the inter-vane channels. Indeed, the channel is curved, but its cross-section also expands from the inlet (leading edge) to the outlet (trailing edge). Both effects are displayed in Figure 2.6. Different authors [25, 51, 119] have found that curvature effects on sound

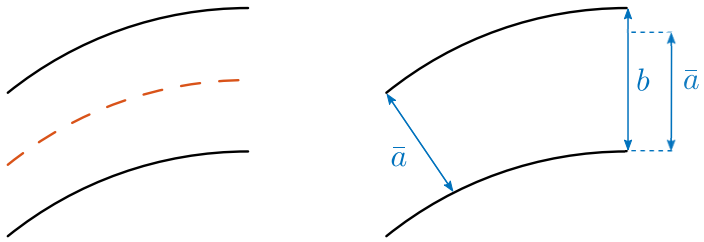

(a) (b)

Figure 2.6: twofold impact of cambered vanes: curvature of the center line (a) and expansion of the cross-section (b).

propagation were only noticeable above a given frequency, depending on the architecture. Below that frequency, the influence of cross-section variations could be dominant. Considering an equivalent straight channel of varying cross-section seems to be a fair first approach to study sound propagation through a cascade of cambered vanes at low frequency, in which the diffuser effect is addressed irrespective of the curvature effect. Furthermore, neglecting the curvature in the first instance will allow to better understand its effects by comparing results with other models accounting for it (see Section 2.4 and Chapter 3).

Geometrical Approximation

From Figure 2.6b, it appears the inter-vane channel is better described in two parts delimited by the measure $\bar{a}$: a semi-open part and then a channel of varying cross-section. A modification is applied to the vanes suction side, depicted in Figure 2.7a, to enable an approximate description of these two parts. The first part of the inter-vane channel is delimited by the triangle ABC. The second part runs from the section BC to the trailing-edge interface and is considered as an equivalent straight channel depicted in Figure 2.7b. Notice that Cartesian coordinates (x, y) will be used when deriving the approximate solution in this second part since it is considered to be straight, and to avoid confusions when curvature effects will be accounted for and curvilinear coordinates (s, n) will be used instead. The point C is where the intersection of the

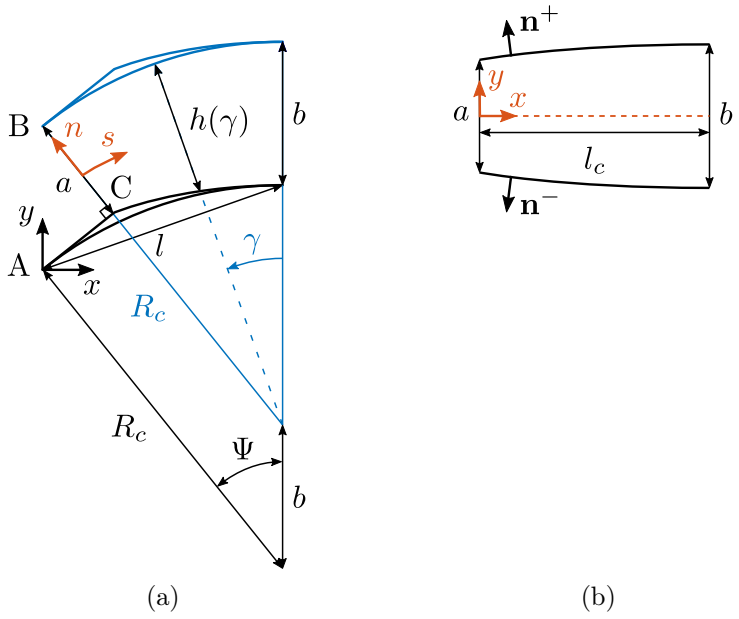

(a) (b)

Figure 2.7: Geometrical approximation of the inter-vane channel (a) and the equivalent straight channel of varying cross-section from section BC to the trailing-edge interface (b).

upper-vane curvature radius R_c (painted in blue in Figure 2.7a) and the lower-vane leading-edge slope (painted in black in Figure 2.7a) makes a right angle. Segment AC is then a straight line whereas the curve from point C to the trailing edge, on the suction side of the vane, is described by the following parametric representation:

$$\begin{cases} x_{ss}(\gamma) = R_c\,(\sin\Psi - \sin\gamma) + b\cos\gamma\sin\gamma, \\ y_{ss}(\gamma) = R_c\,(\cos\gamma - \cos\Psi) + b\sin^2\gamma, \end{cases} \tag{2.36}$$

where $\gamma = 0$ at the outlet and $\gamma = \Psi$ at the inlet (see Figure 2.7a). The upper-vane pressure side that is a circle arc is described by

$$\begin{cases} x_{ps}(\gamma) = R_c\,(\sin\Psi - \sin\gamma)\,, \\ y_{ps}(\gamma) = R_c\,(\cos\gamma - \cos\Psi) + b. \end{cases} \tag{2.37}$$

The parametric representation of the curvilinear abscissa s, along the channel center line, is then

$$\begin{cases} x_s(\gamma) = R_c\,(\sin\Psi - \sin\gamma) + \dfrac{b}{2}\cos\gamma\sin\gamma, \\ y_s(\gamma) = R_c\,(\cos\gamma - \cos\Psi) + b\left(1 - \dfrac{1}{2}\cos^2\gamma\right). \end{cases} \tag{2.38}$$

The exact expression of the channel length l_c in Figure 2.7b is given by

$$l_c = \int_0^{\Psi} \sqrt{\left(\frac{\mathrm{d}x_s}{\mathrm{d}\gamma}\right)^2 + \left(\frac{\mathrm{d}y_s}{\mathrm{d}\gamma}\right)^2}\,\mathrm{d}\gamma, \tag{2.39}$$

but a good approximation is found by considering the curvilinear abscissa as a circle arc with a mean curvature radius. This reads

$$l_c \simeq (R_c - (a+b)/4)\,\Psi = (R_c - b(1+\cos\Psi)/4)\,\Psi. \tag{2.40}$$

The validity of this approximation is shown in Figure 2.8, displaying the relative error $\Delta l_c = (l_c - l_{c,approx})/l_c$ against the camber angle Ψ for different solidity values l/b. Up to about $\Psi = 40°$, the relative error stays below 0.5% for $1 \leq l/b \leq 1.5$.

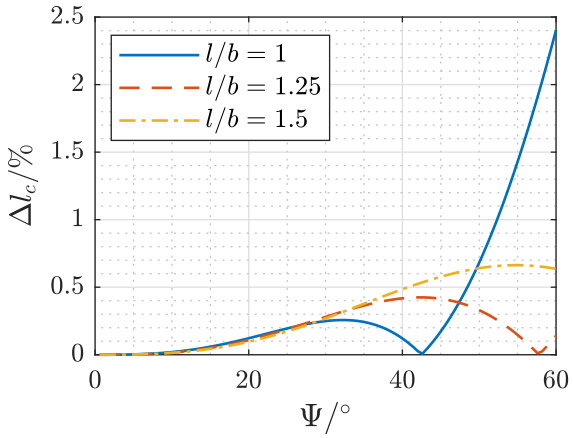

Figure 2.8: Evolution of the channel length relative error $\Delta l_c = (l_c - l_{c,approx})/l_c$ against the camber angle Ψ for different solidity values l/b.

The varying channel height is given by

$$h(\gamma) = b\cos(\gamma), \quad 0 \leq \gamma \leq \Psi. \tag{2.41}$$

As mentioned by Roger et al. [116], the approximate height $a = b\cos\Psi$ of segment BC is lower than the original height $\bar{a}$ between two circle arcs by an error of

$$\frac{\bar{a} - a}{R_c} = 1 - \sqrt{1 - \left(\frac{b}{l}\frac{\sin^2\Psi}{\cos\Psi/2}\right)^2}. \tag{2.42}$$

The error being only dependent on the camber angle Ψ and the solidity l/b, its relative value $\Delta a = (\bar{a} - a)/\bar{a}$ is plotted in Figure 2.9. It shows the error is negligible (less than 2%) for camber angles below 20° but, depending on the solidity value, is equal to 8%, 10% and 12% respectively at $\Psi = 36°$, which is in the range of OGV camber angles. In this case, the difference is not negligible anymore and tends to increase the height expansion of the inter-vane channel. This artificial thickness could have an impact on sound propagation that will be discussed in the next chapter, in Section 3.3.2.

Modal Basis Approximation in the Triangle ABC

In the first part of the inter-vane channel, Whitehead [131] proposed to use Green's reciprocity theorem, based on Green's second identity [41], to link the pressure field from the leading-edge interface to the segment BC in the channel by taking advantage of the absence of acoustic sources. It has been used by Roger & François [116] and could be coupled with Kirchhoff's integral theorem [59] to have access to the pressure field

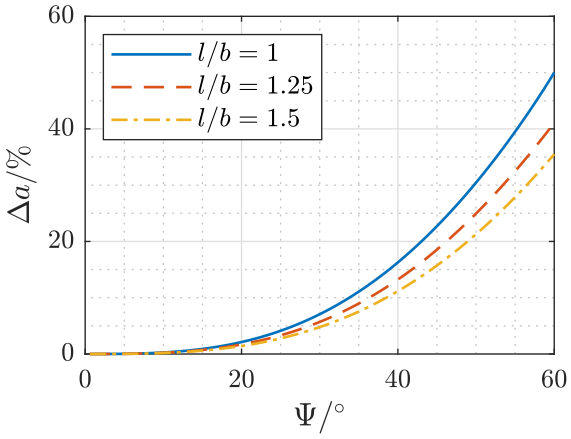

Figure 2.9: Evolution of the inlet height relative error $\Delta a = (\bar{a} - a)/\bar{a}$ against the camber angle Ψ for different solidity values l/b.

inside the triangle ABC, which was missing in Ref. [116]. A convenient approximation has also been proposed by Roger et al. [117] who described the pressure field in this part as if it were a channel of height a and length $b \sin \Psi$. Cosine functions are used as a modal basis and the matching at the leading-edge interface is done classically, considering it as a staggered interface for the channel modes. The authors [117] showed a good agreement between both methods. Consequently, the approximate modal basis is used in the present study for its practicality and will be detailed in Section 2.3.2.

Slowly-Varying Approximation from Section BC to the Trailing Edge

In the varying part of the channel, one last approximation is needed to allow a closed-form solution of sound propagation. Considering the channel center line as a circle arc of modified curvature radius proved to give a good approximation of the channel length in (2.40). In this case, the curvilinear abscissa s is given by

$$s \simeq (R_c - b(1 + \cos \Psi)/4)\, \gamma, \quad 0 \leq \gamma \leq \Psi. \tag{2.43}$$

By unwrapping the curved channel as a straight channel with equivalent length and cross-section variations (Figure 2.7b), the channel height is given in Cartesian coordinates by

$$h(x) \simeq b \cos\left(\Psi - \frac{x}{R_c - b(1 + \cos \Psi)/4}\right), \quad 0 \leq x \leq l_c. \tag{2.44}$$

The maximal value of the cross-section derivative, i.e. the local slope of the channel walls, is

$$\epsilon = \max_{\forall x \in [0, l_c]} \left|\frac{\mathrm{d}h}{\mathrm{d}x}\right| \simeq \frac{b}{R_c - b(1 + \cos \Psi)/4} \sin \Psi = \frac{\sin^2 \Psi}{\dfrac{l}{b} \cos \Psi/2 - \dfrac{1}{4}(1 + \cos \Psi) \sin \Psi}. \tag{2.45}$$

If $\epsilon \ll 1$, the cross-section varies slowly along the channel. In this case, a slowly-varying formalism based on a multiple-scale analysis can be used (see for example [8, 82, 47]) and enables a closed-form solution of sound propagation in the inter-vane channels. The basic idea behind the method of multiple scales is that the variation of cross-section

occurs on a larger scale (hence slower variations) defined by a new and independent coordinate $X = \epsilon x$, called the slow coordinate. Each field is then expanded in a regular asymptotic expansion in powers of ϵ and an approximate solution is found at leading order, accounting for both fast and slow variations. This formalism has been used by many authors in turbomachinery acoustics, e.g. Nayfeh & co-authors [83, 84, 80] or Rienstra [105, 106, 107, 109, 110], and proved its efficiency against numerical results [111]. In the present case, the value of ϵ is plotted against the camber angle for different solidity values in Figure 2.10. ϵ increases with the camber angle Ψ but

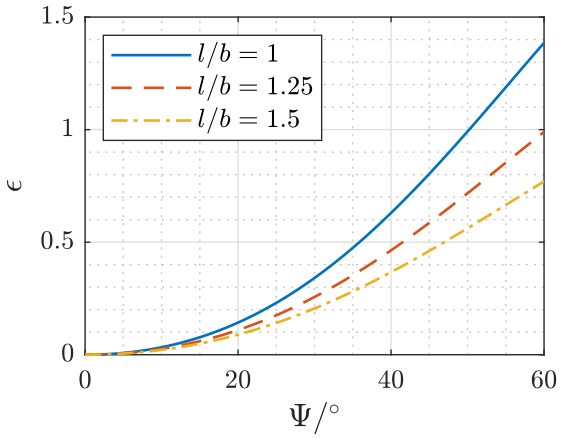

Figure 2.10: Evolution of the cross-section variation parameter ϵ against the camber angle Ψ for different solidity values l/b.

decreases with the solidity value l/b. For typical values of camber angle and solidity of an OGV row, $\epsilon < 1$, which ensures well-ordered expansions in the multiple-scale analysis. Whether or not it is sufficiently small to give accurate results will depend on the problem studied and will be investigated in sections 2.4 and 3.3. Consequently, Figure 2.10 should be used to understand how the validity of the approximation evolves with design parameters, $\partial\epsilon/\partial\Psi$ and $\partial\epsilon/\partial(l/b)$, and not as an absolute criterion to tell whether or not the approximation is valid in a specific case.

In the following, the value of ϵ is assumed to be small enough to consider that the cross-section varies slowly, thus the height h is a function of the slow coordinate X as

$$h(X) = b\cos\left(\Psi - \frac{X}{b\sin\Psi}\right), \quad 0 \leq X \leq L_c = b\Psi\sin\Psi. \tag{2.46}$$

2.2.2 Mean Flow

The incident mean flow is considered uniform and with no angle of incidence, thus being perfectly aligned with the vane leading edges. It is described by

$$\mathbf{U}_{-\infty}(x,y) = U_{-\infty}\cos\Psi\,\mathbf{e}_x + U_{-\infty}\sin\Psi\,\mathbf{e}_y, \quad -\infty \leq x \leq 0 \quad \text{and} \quad 0 \leq y < 2\pi R, \tag{2.47}$$

where the $-\infty$ subscript denotes the fields upstream of the OGV. Beyond the leading-edge interface ($x > 0$), the mean flow enters the inter-vane channels and remains constant in the triangle ABC, then passes through the slowly-varying part. Here, the mean flow is assumed to stay nearly uniform, thus determined by the slowly varying geometry only (dependence in X only). Rewritten in terms of X, the continuity equation

(1.6a) is now

$$\epsilon \frac{\partial D U_x}{\partial X} + \frac{\partial D U_y}{\partial y} = 0. \tag{2.48}$$

It appears that a small axial fluctuation of DU_x can only be balanced by a small transverse fluctuation of DU_y. Consequently $U_y = \mathcal{O}(\epsilon)$ at leading order since U_x is $\mathcal{O}(1)$ by assumption. It follows from equations (1.6b) and (1.6c) that C, D and P are $\mathcal{O}(1)$ at leading order. The variant of Bernoulli's equation (1.6b) indicates that each variable be expanded in powers of ϵ^2. The solution takes the form

$$\mathbf{U}(X, y) = U_{0x}(X)\mathbf{e}_x + \epsilon U_{1y}(X, y)\mathbf{e}_y + \mathcal{O}(\epsilon^2), \tag{2.49a}$$

$$C(X, y) = C_0(X) + \mathcal{O}(\epsilon^2), \tag{2.49b}$$

$$D(X, y) = D_0(X) + \mathcal{O}(\epsilon^2), \tag{2.49c}$$

$$P(X, y) = P_0(X) + \mathcal{O}(\epsilon^2). \tag{2.49d}$$

The value of $U_{0x}(X)$ is given by the conservation of mass-flow rate, i.e. integral version of the mass equation (1.6a), between a given location X and the inlet (interface BC). This reads

$$\int_{-h(X)/2}^{h(X)/2} D_0(X) U_{0x}(X)\, \mathrm{d}y = F_{-\infty} + \mathcal{O}(\epsilon),$$

where $F_{-\infty} = D_{-\infty} U_{-\infty} a$. Hence, the mean velocity at leading order is

$$U_{0x}(X) = U_{-\infty} \frac{D_{-\infty} a}{D_0(X) h(X)}. \tag{2.50}$$

By considering a straight channel, the mean vorticity of the flow is neglected. Thus, from Bernoulli's equation (1.8), it follows that

$$\frac{1}{2} \frac{F_{-\infty}^2}{D_0^2(X) h^2(X)} + \frac{D_0^{\gamma^* - 1}(X)}{\gamma^* - 1} = E_{-\infty} + \mathcal{O}(\epsilon), \tag{2.51}$$

where $E_{-\infty} = U_{-\infty}^2/2 + D_{-\infty}^{\gamma^* - 1}/(\gamma^* - 1)$. Leading-order solutions of equation (2.51) can be viewed as the roots of the polynomial function

$$D_0(X) \mapsto \frac{1}{\gamma^* - 1} D_0^{\gamma^* + 1}(X) - \left(\frac{U_{-\infty}^2}{2} + \frac{D_{-\infty}^{\gamma^* - 1}}{\gamma^* - 1} \right) D_0^2(X) + \frac{1}{2} \left(\frac{D_{-\infty} U_{-\infty} a}{h(X)} \right)^2,$$

where X acts as a parameter. The value of $D_0(X)$ is found by applying Newton-Raphson method (see for example [42]) at each location X with an initial guess equal to $D_{-\infty}$ in order to converge to the desired root. $C_0(X)$ and $P_0(X)$, if needed, are then deduced from the thermodynamics relations (1.6c). Finally, downstream of the OGV, the mean flow exits the channels aligned with the vane trailing edges, hence with the turbomachinery axis. It is described by

$$\mathbf{U}_{+\infty}(x, y) = U_{-\infty} \cos\Psi \frac{D_{-\infty}}{D_{+\infty}} \mathbf{e}_x, \quad l_x \leq x \leq \infty \quad \text{and} \quad 0 \leq y < 2\pi R, \tag{2.52}$$

where the $+\infty$ subscript denotes the fields downstream of the OGV, thus $D_{+\infty} = D_0(L_c)$. The evolution of the mean flow field through the cascade is displayed in

Figure 2.11.

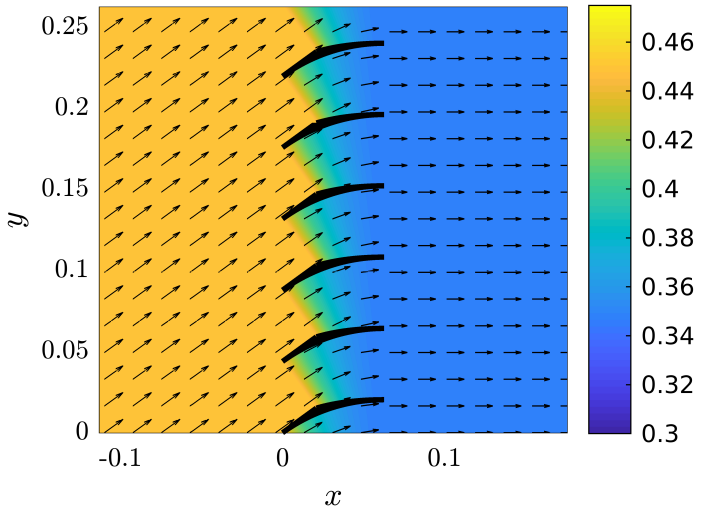

Figure 2.11: Modeled total Mach number and flow angle evolution through a cascade of cambered vanes (geometry and flow conditions from the fourth NASA CAA workshop [24]).

2.2.3 Slowly-Varying Acoustic Modes

Problem Formulation

With the description of the slowly-varying mean flow in (2.49), the compressible convected Helmholtz equation (1.11) can be recast in terms of powers of ϵ. Notice that, in order to avoid a complicated coupling between the two small parameters (ϵ and the acoustic amplitude), the acoustic part will be assumed much smaller than any relevant power of ϵ in all further developments. Consequently, the Helmholtz equation (1.11) in the slowly-varying part of the channel, reads, with a change of Fourier-transform convention to match Rienstra's result [107] (see Appendix A.1.1 for details),

$$\begin{aligned}&\beta^2\frac{\partial^2\phi}{\partial x^2}+\frac{\partial^2\phi}{\partial y^2}-2\mathrm{i}kM\frac{\partial\phi}{\partial x}+k^2\phi\\&+\epsilon\left\{\left[\frac{1}{D_0}\frac{\partial D_0}{\partial X}-U_{0x}\frac{\partial}{\partial X}\left(\frac{M}{C_0}\right)\right]\frac{\partial\phi}{\partial x}-\mathrm{i}\omega U_{0x}\frac{\partial}{\partial X}\left(\frac{1}{C_0^2}\right)\phi-2\mathrm{i}k\frac{U_{1y}}{C_0}\frac{\partial\phi}{\partial y}-2M\frac{U_{1y}}{C_0}\frac{\partial^2\phi}{\partial x\partial y}\right\}\\&+\mathcal{O}(\epsilon^2)=0,\end{aligned}\tag{2.53}$$

where $M=U_{0x}/C_0$, $\beta=\sqrt{1-M^2}$ and $k=\omega/C_0$. At leading order, the Helmholtz equation shows a similar structure in a slowly-varying channel (2.53) than in a straight channel (2.3), the only difference being the non-constant coefficients. The boundary condition for hard walls is written as

$$(\nabla\phi\cdot\mathbf{n})=0,\quad\text{at}\quad y=\pm h(X)/2,\tag{2.54}$$

where $\mathbf{n}$ is the outer normal unit vector to the respective wall, slightly misaligned with $\mathbf{e}_y$ due to the height expansion (Figure 2.7b). The boundary is described from the

center line by $\Sigma^{\pm}(X,y)=0$ where the $\pm$ sign denotes the upper (pressure side) or lower (suction side) boundary, respectively, and

$$\Sigma^{\pm}(X,y)=y\mp\frac{h(X)}{2}.$$

The respective outward-directed normal unit vectors, given by $\nabla\Sigma^{\pm}(X,y)$, are then

$$\mathbf{n}^{+}=\frac{\mathbf{e}_y-\epsilon\dfrac{\sin\left(\Psi-\frac{X}{b\sin\Psi}\right)}{\sin\Psi}\mathbf{e}_x}{\sqrt{1+\epsilon^2\dfrac{\sin^2\left(\Psi-\frac{X}{b\sin\Psi}\right)}{\sin^2\Psi}}},\qquad \mathbf{n}^{-}=-\frac{\mathbf{e}_y+\epsilon\dfrac{\sin\left(\Psi-\frac{X}{b\sin\Psi}\right)}{\sin\Psi}\mathbf{e}_x}{\sqrt{1+\epsilon^2\dfrac{\sin^2\left(\Psi-\frac{X}{b\sin\Psi}\right)}{\sin^2\Psi}}}.$$

This shows that the misalignment between $\mathbf{n}$ and $\mathbf{e}_y$ is, indeed, maximum at $X=0$ where it is given by ϵ, and null at $X=L_c$.

WKB Expansion

The slowly varying acoustic modes are obtained by solving equation (2.53) with the WKB method, which stands for Wentzel–Kramers–Brillouin. The WKB theory is a special case of multiple-scale analysis where the fast variations (dependence in x) are assumed to be exponential (see for example [8, 82, 47]). The asymptotic series expansion of the slowly-varying potential then reads

$$\phi(X,y)=\exp\left(-\frac{\mathrm{i}}{\epsilon}\int^{X}\mu(\xi)\,\mathrm{d}\xi\right)\sum_{m=0}^{\infty}\epsilon^m\Phi_m(X,y),\quad 0\le X\le L_c,\quad -\frac{h(X)}{2}\le y\le\frac{h(X)}{2},\tag{2.55}$$

where $\mu(X)$ is the axial wavenumber that is now able to vary with X. It gives the following derivatives:

$$\epsilon\frac{\partial\phi}{\partial X}(X,y)=\exp\left(-\frac{\mathrm{i}}{\epsilon}\int^{X}\mu(\xi)\,\mathrm{d}\xi\right)\left(-\mathrm{i}\mu+\epsilon\frac{\partial}{\partial X}\right)\sum_{m=0}^{\infty}\epsilon^m\Phi_m(X,y),$$

and

$$\epsilon^2\frac{\partial^2\phi}{\partial X^2}(X,y)=\exp\left(-\frac{\mathrm{i}}{\epsilon}\int^{X}\mu(\xi)\,\mathrm{d}\xi\right)\left(-\mu^2-\mathrm{i}\epsilon\frac{\partial\mu}{\partial X}-2\mathrm{i}\epsilon\mu\frac{\partial}{\partial X}+\epsilon^2\frac{\partial^2}{\partial X^2}\right)\sum_{m=0}^{\infty}\epsilon^m\Phi_m(X,y).$$

Using the above expressions in (2.53) and dividing by the common exponential term (see A.1.2) gives

$$\mathcal{O}(1)\quad \frac{\partial^2\Phi_0}{\partial y^2}+\left(\Lambda^2-\mu^2\right)\Phi_0=0,\tag{2.56a}$$

$$\mathcal{O}(\epsilon)\quad \frac{\partial^2\Phi_1}{\partial y^2}+\left(\Lambda^2-\mu^2\right)\Phi_1=\frac{\mathrm{i}}{D_0\Phi_0}\left\{\frac{\partial}{\partial X}\left[\left(\Lambda M+\mu\right)D_0\Phi_0^2\right]+\frac{\Lambda D_0}{C_0}\frac{\partial}{\partial y}\left(U_{1y}\Phi_0^2\right)\right\},\tag{2.56b}$$

where

$$\Lambda=k-\mu M.$$

The boundary conditions at $y = \pm h(X)/2$ from (2.54) become

$$\mathcal{O}(1) \qquad \left.\frac{\partial \Phi_0}{\partial y}\right|_{y=\pm h(X)/2} = 0, \tag{2.57a}$$

$$\mathcal{O}(\epsilon) \qquad \left.\frac{\partial \Phi_1}{\partial y}\right|_{y=\pm h(X)/2} = \mp \mathrm{i}\mu \frac{\sin\left(\Psi - \frac{X}{b\sin\Psi}\right)}{\sin\Psi}\, \Phi_0|_{y=\pm h(X)/2}\,. \tag{2.57b}$$

The transverse wavenumber θ is introduced through the dispersion relation

$$\theta^2 = \Lambda^2 - \mu^2. \tag{2.58}$$

The leading-order equation (2.56a) with boundary conditions (2.57a) is rewritten as an eigenvalue problem of the operator $-\partial^2/\partial y^2$ in the transverse direction, with eigenvalue θ^2 and eigenfunction ψ, such that

$$-\frac{\partial^2 \psi}{\partial y^2} = \theta^2 \psi, \quad \text{with} \quad \frac{\partial \psi}{\partial y} = 0 \quad \text{at} \quad y = \pm h(X)/2, \tag{2.59}$$

and X acting as a parameter. Following Rienstra [109], a normalization is introduced as

$$\int_{-h(X)/2}^{h(X)/2} \psi^2(X, y)\, \mathrm{d}y = 1. \tag{2.60}$$

The solution of (2.56a) is written as a sum of transverse modes (eigenfunctions) of order $q \in \mathbb{N}$ such that

$$\Phi_0(X, y) = \sum_{q=0}^{\infty} N_q(X) \psi_q(X, y), \tag{2.61}$$

where

$$\psi_q(X, y) = \frac{\cos(\theta_q[y + h(X)/2])}{\sqrt{(1 + \delta_{q,0})h(X)/2}}, \quad \theta_q(X) = \frac{q\pi}{h(X)}, \tag{2.62}$$

where δ is the Kronecker delta: $\delta_{q,0} = 1$ if $q = 0$, and $\delta_{q,0} = 0$ otherwise. The amplitudes $N_q(X)$ are determined by the $\mathcal{O}(\epsilon)$ problem (2.56b), but the latter does not need to be solved. Instead, a solvability condition is used based on the Fredholm alternative (see for example Ref. [82] Chapter 15.4). This states that the $\mathcal{O}(\epsilon)$ problem (2.56b) has a solution if, and only if, its inhomogeneous part (right-hand side) is orthogonal to the solution $\Phi_0^\dagger$ of the adjoint $\mathcal{O}(1)$ problem (2.56a). Since the leading-order homogeneous problem is self-adjoint, $\Phi_0^\dagger = \Phi_0$, the solvability condition is

$$\int_{-h(X)/2}^{h(X)/2} \Phi_0 f_h(\Phi_0)\, \mathrm{d}y = \Phi_0 \left.\frac{\partial \Phi_1}{\partial y}\right|_{y=h(X)/2} - \Phi_0 \left.\frac{\partial \Phi_1}{\partial y}\right|_{y=-h(X)/2}, \tag{2.63}$$

where $f_h(\Phi_0)$ is the inhomogeneous part (right-hand side) of (2.56b). The solvability condition (2.63) reduces to Green's second identity in this case. Notice that, the partial derivative $\partial\Phi_1/\partial y$ evaluated at the boundaries involves only Φ_0 (2.57b). As a consequence, equation (2.63) involves only Φ_0 and so gives the necessary constraint to define the amplitudes N_q. For the sake of clarity, the reduced axial wavenumber is introduced as

$$\sigma_q = \sqrt{1 - \beta^2 \frac{\theta_q^2}{k^2}}. \tag{2.64}$$

After some derivations presented in Appendix A.2, this leads to

$$N_q^2(X) = \frac{Q_q^2}{D_0(X)k(X)\sigma_q(X)}, \tag{2.65}$$

where Q_q are constants to be defined from a known value of $N_q(X)$ at some point (usually the inlet). The axial wavenumber μ is defined through the quadratic equation given by the dispersion relation (2.58) as

$$\mu_q^{\pm} = \frac{-kM \pm k\sigma_q}{\beta^2}, \tag{2.66}$$

where the $\pm$ symbol denotes a wave propagating downstream $(+)$ or upstream $(-)$. Finally, the slowly-varying acoustic potential of the superposition of a downstream-propagating mode of order q and amplitude I, and the opposite upstream-propagating mode of amplitude R, can be approximated at leading order by

$$\begin{aligned}\phi_q(X,y) \sim{}& \frac{Q_q}{\sqrt{D_0(X)k(X)\sigma_q(X)}}\psi_q(X,y)\exp\left(\frac{\mathrm{i}}{\epsilon}\int^X \frac{k(\xi)M(\xi)}{\beta^2(\xi)}\,\mathrm{d}\xi\right)\\ &\times\left[I\exp\left(-\frac{\mathrm{i}}{\epsilon}\int^X \frac{k(\xi)\sigma_q(\xi)}{\beta^2(\xi)}\,\mathrm{d}\xi\right) + R\exp\left(\frac{\mathrm{i}}{\epsilon}\int^X \frac{k(\xi)\sigma_q(\xi)}{\beta^2(\xi)}\,\mathrm{d}\xi\right)\right].\end{aligned} \tag{2.67}$$

Now that a modal solution is known in each subdomain (upstream annular, inter-vane, downstream annular), the mode-matching equations are derived in the following section.

Sound Propagation through Cambered Inter-Vane Channels — Summary

Camber has been introduced by modeling the vanes profile as circle arcs. This has a twofold impact on sound propagation through the inter-vane channels: curvature of the center line and expansion of the cross-section. Different authors found that the curvature effects were negligible at low frequency, where the influence of cross-section variations could be dominant. Thus, a sound propagation model based on straight channels of equivalent cross-section variations has been proposed. Such a problem does not have an exact closed-form solution. A leading-order approximate solution has been derived instead, based on the assumption that the cross-section varies slowly along the channel. This was achieved via the method of multiple scales. An approximation has also been done on the modal basis of the triangle ABC, between the leading-edge interface and the inter-vane channel, using a set of cosine functions. Furthermore, geometrical approximations have been accepted in order to model the inter-vane channel geometry more easily. This results in an artificial thickness of the vane. Finally, the mean flow has been assumed subsonic and to stay nearly uniform through the cascade, while being continuously deviated. All the necessary assumptions of the model are listed below:

- Straight-channel approximation and slowly-varying approach in the inter-vane channel;

- Modal basis approximation in the triangle ABC;
- Geometrical approximation leading to an artificial thickness;
- Nearly uniform mean flow continuously deviated through the cascade.

2.3 Mode-Matching Equations

2.3.1 Jump Conditions

Due to camber, the leading-edge interface is staggered in the vanes reference frame. The oblique mean flow passing through requires a change in the jump conditions seen earlier in 2.1.1. Going back to the conservation of total enthalpy (1.17) leads to

$$[\mathrm{i}k\phi - M_x u_x - M_y u_y + M_x u_x + M_y u_y]_1^2 = [\mathrm{i}k\phi]_1^2 = 0, \tag{2.68}$$

which simply reduces to the conservation of ϕ. The variable Γ_1 is still

$$\boxed{\Gamma_1 = \phi}. \tag{2.69}$$

The conservation of mass-flow rate (1.13) reads

$$\left[\mathrm{i}kM_x^2\phi + \beta_x^2 M_x u_x - M_x^2 M_y u_y\right]_1^2 = 0, \tag{2.70}$$

where $\beta_x^2 = 1 - M_x^2$. Since the potential continuity is already enforced, this equation reduces to the conservation of the following quantity:

$$\boxed{\Gamma_2 = \beta_x^2 u_x - M_x M_y u_y}, \tag{2.71}$$

composed of the fluctuations of axial and tangential velocities. This variable can also be rewritten as

$$\Gamma_2 = \beta_x^2 u_x - M_x^2 u_y \tan\Psi. \tag{2.72}$$

That demonstrates the equivalence of the conservation of Γ_2 and u_x when $\Psi \to 0$ and/or $M \to 0$. In these particular cases, the set of variables (Γ_1, Γ_2) is equivalent to (ϕ, u_x) or (p, u_x) as was previously used for unstaggered flat vanes in 2.1.1. It is important to notice that in general, when $\Psi \neq 0$ and $M \neq 0$, the fluctuating pressure field p cannot be used as a conservative variable through the matching interface.

2.3.2 Initial Leading-Edge Interface

Acoustic Potentials

At this initial step of leading-edge matching, no back-scattering from the trailing-edge interface is accounted for. The slowly-varying formalism is not needed and the only difference with a cascade of flat vanes (Section 2.1.2) is that the matching interface is staggered from the point of view of the channel modes in the triangle ABC (see Figure 2.12). In the annular domain, the mean flow is aligned with the vane leading edges. By noticing that the Helmholtz equation written in the vanes-attached system

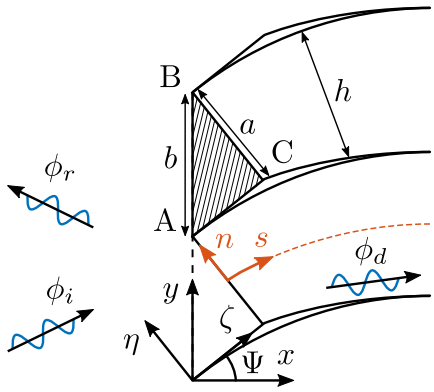

Figure 2.12: Scattering of an incident mode at the staggered leading-edge interface.

of coordinates (ζ, η) is identical to (2.3), a change of variables from (ζ, η) to (x, y) gives

$$\beta^2_{-\infty x}\frac{\partial^2\phi}{\partial x^2}+\beta^2_{-\infty y}\frac{\partial^2\phi}{\partial y^2}-2M_{-\infty x}M_{-\infty y}\frac{\partial^2\phi}{\partial xy}+2\mathrm{i}k_{-\infty}\left(M_{-\infty x}\frac{\partial\phi}{\partial x}+M_{-\infty y}\frac{\partial\phi}{\partial y}\right)+k^2_{-\infty}\phi=0, \tag{2.73}$$

where $M_{-\infty x}=M_{-\infty}\cos\Psi$, $M_{-\infty y}=M_{-\infty}\sin\Psi$, $\beta^2_{-\infty x}=1-M^2_{-\infty x}$, $\beta^2_{-\infty y}=1-M^2_{-\infty y}$. Since each field will be evaluated at the leading-edge interface in this section, the $-\infty$ subscript is not needed and will be dismissed in the following to simplify the notation.

Assuming that equation (2.73) has a solution of the same form as the solution of (2.3), the incident ϕ_i and reflected ϕ_r potentials read

$$\phi_i(x,y)=\mathrm{e}^{\mathrm{i}\alpha_j y}\mathrm{e}^{\mathrm{i}k_j^+ x}, \quad \text{for} \quad -\infty<x\le 0 \quad \text{and} \quad 0\le y<2\pi R, \tag{2.74}$$

where

$$\alpha_j=\frac{j}{R}, \quad k_j^+=-\frac{(k-\alpha_j M_y)M_x}{\beta_x^2}+\frac{\sqrt{k^2-(\beta_x^2-M_y^2)\alpha_j^2-2k\alpha_j M_y}}{\beta_x^2},$$

and

$$\phi_r(x,y)=\sum_{p=-\infty}^{\infty}R_p\mathrm{e}^{\mathrm{i}\alpha_p y}\mathrm{e}^{\mathrm{i}k_p^- x}, \quad \text{for} \quad -\infty<x\le 0 \quad \text{and} \quad 0\le y<2\pi R, \tag{2.75}$$

where

$$\alpha_p=\alpha_j+p\frac{2\pi}{b}, \quad k_p^-=-\frac{(k-\alpha_p M_y)M_x}{\beta_x^2}-\frac{\sqrt{k^2-(\beta_x^2-M_y^2)\alpha_p^2-2k\alpha_p M_y}}{\beta_x^2}.$$

In the triangle ABC, the downstream-propagating transmitted modes are given by the potential ϕ_d as

$$\phi_d(\zeta,\eta)=\sum_{q=0}^{\infty}A_q\cos(\alpha_q\eta)\,\mathrm{e}^{\mathrm{i}k_q^+\zeta}, \quad \text{for} \quad \eta\tan\Psi\le\zeta\le a\tan\Psi \quad \text{and} \quad 0\le\eta\le a, \tag{2.76}$$

where

$$\alpha_q = \frac{q\pi}{a}, \quad k_q^+ = \frac{-kM + \sqrt{k^2 - \beta^2\alpha_q^2}}{\beta^2}.$$

Continuity of the Acoustic Potential

To derive the matching equations, a change of variables is performed on the channel modes to express all potentials in terms of (x, y). It yields

$$\phi_d(x,y) = \frac{1}{2}\sum_{q=0}^{\infty} A_q \left[\mathrm{e}^{\mathrm{i}\left(-\frac{q\pi}{a}\sin\Psi + k_q^+\cos\Psi\right)x} \mathrm{e}^{\mathrm{i}\left(\frac{q\pi}{a}\cos\Psi + k_q^+\sin\Psi\right)y} \right. \\ \left. + \mathrm{e}^{\mathrm{i}\left(\frac{q\pi}{a}\sin\Psi + k_q^+\cos\Psi\right)x} \mathrm{e}^{\mathrm{i}\left(-\frac{q\pi}{a}\cos\Psi + k_q^+\sin\Psi\right)y} \right]. \tag{2.77}$$

The acoustic potential continuity at the leading-edge interface reads

$$\mathrm{e}^{\mathrm{i}\alpha_j y} + \sum_{p=-\infty}^{\infty} R_p \mathrm{e}^{\mathrm{i}\alpha_p y} = \frac{1}{2}\sum_{q=0}^{\infty} A_q \left[\mathrm{e}^{\mathrm{i}\left(\frac{q\pi}{b} + k_q^+\sin\Psi\right)y} + \mathrm{e}^{\mathrm{i}\left(-\frac{q\pi}{b} + k_q^+\sin\Psi\right)y} \right]. \tag{2.78}$$

The same projection on the annular modal basis (2.13), as seen previously for flat vanes, is performed with the operator

$$\int_0^b (\bullet)\mathrm{e}^{-\mathrm{i}\alpha_\nu y}\,\mathrm{d}y, \quad \text{with} \quad \alpha_\nu = \alpha_j + \nu\frac{2\pi}{b},\ \nu \in \mathbb{Z}.$$

This leads to

$$\mathfrak{I}_{i,\nu} + \sum_{p=-\infty}^{\infty} R_p \mathfrak{I}_{p,\nu} = \sum_{q=0}^{\infty} A_q \left(\mathfrak{I}_{q,\nu}^{++} + \mathfrak{I}_{q,\nu}^{-+}\right). \tag{2.79}$$

The first two integrals have been detailed in 2.1.2, whereas the integral on the channel modes is changed due to stagger. It is described by

$$\mathfrak{I}_{q,\nu}^{\pm\pm} = \frac{1}{2}\int_0^b \mathrm{e}^{\mathrm{i}(\pm\frac{q\pi}{b} + k_q^\pm\sin\Psi - \alpha_\nu)y}\,\mathrm{d}y = \frac{b}{2}\frac{\sin\left(\varphi_{q,\nu}^{\pm\pm}\right)}{\varphi_{q,\nu}^{\pm\pm}}\mathrm{e}^{\mathrm{i}\varphi_{q,\nu}^{\pm\pm}},$$

where

$$\varphi_{q,\nu}^{\pm\pm} = \frac{b}{2}\left(\pm\frac{q\pi}{b} + \varphi_{q,\nu}^{\pm}(\Psi)\right) \quad \text{and} \quad \varphi_{q,\nu}^{\pm}(\Psi) = k_q^\pm\sin\Psi - \alpha_\nu.$$

These integrals can also be recast together in the potential continuity equation as

$$\boxed{b\left(R_\nu + \delta_{\nu,0}\right) = \sum_{q=0}^{\infty} A_q \mathfrak{I}_{q,\nu}^{+}}, \tag{2.80}$$

where

$$\mathfrak{I}_{q,\nu}^{+}(\Psi) = \mathfrak{I}_{q,\nu}^{++} + \mathfrak{I}_{q,\nu}^{-+} = \begin{cases} \dfrac{-\mathrm{i}\varphi_{q,\nu}^{+}(\Psi)}{(q\pi/b)^2 - \varphi_{q,\nu}^{+\,2}(\Psi)}\left(1 - (-1)^q\mathrm{e}^{\mathrm{i}b\varphi_{q,\nu}^{+}(\Psi)}\right), \\ \dfrac{b}{2}\left(1 + \delta_{q,0}\right) \quad \text{if} \quad \left|\varphi_{q,\nu}^{+}(\Psi)\right| = \dfrac{q\pi}{b}. \end{cases} \tag{2.81}$$

Continuity of the Modified Acoustic Velocity

To write the continuity equation on the modified acoustic velocity $\beta_x^2 u_x - M_x M_y u_y$, the derivatives of the potential (2.77) with respect to each coordinate are needed. They are derived as

$$\frac{\partial \phi_d}{\partial x} = \frac{\mathrm{i}}{2}\sum_{q=0}^{\infty} A_q \left[\left(-\frac{q\pi}{a}\sin\Psi + k_q^+\cos\Psi\right)\mathrm{e}^{\mathrm{i}\left(-\frac{q\pi}{a}\sin\Psi + k_q^+\cos\Psi\right)x}\mathrm{e}^{\mathrm{i}\left(\frac{q\pi}{a}\cos\Psi + k_q^+\sin\Psi\right)y}\right.$$
$$\left. + \left(\frac{q\pi}{a}\sin\Psi + k_q^+\cos\Psi\right)\mathrm{e}^{\mathrm{i}\left(\frac{q\pi}{a}\sin\Psi + k_q^+\cos\Psi\right)x}\mathrm{e}^{\mathrm{i}\left(-\frac{q\pi}{a}\cos\Psi + k_q^+\sin\Psi\right)y}\right], \tag{2.82}$$

and

$$\frac{\partial \phi_d}{\partial y} = \frac{\mathrm{i}}{2}\sum_{q=0}^{\infty} A_q \left[\left(\frac{q\pi}{a}\cos\Psi + k_q^+\sin\Psi\right)\mathrm{e}^{\mathrm{i}\left(-\frac{q\pi}{a}\sin\Psi + k_q^+\cos\Psi\right)x}\mathrm{e}^{\mathrm{i}\left(\frac{q\pi}{a}\cos\Psi + k_q^+\sin\Psi\right)y}\right.$$
$$\left. + \left(-\frac{q\pi}{a}\cos\Psi + k_q^+\sin\Psi\right)\mathrm{e}^{\mathrm{i}\left(\frac{q\pi}{a}\sin\Psi + k_q^+\cos\Psi\right)x}\mathrm{e}^{\mathrm{i}\left(-\frac{q\pi}{a}\cos\Psi + k_q^+\sin\Psi\right)y}\right]. \tag{2.83}$$

The modified velocity continuity at the leading-edge interface reads

$$(\beta_x^2 k_j^+ - M_x M_y \alpha_j)\mathrm{e}^{\mathrm{i}\alpha_j y} + \sum_{p=-\infty}^{\infty} R_p\left(\beta_x^2 k_p^- - M_x M_y \alpha_p\right)\mathrm{e}^{\mathrm{i}\alpha_p y}$$
$$= \frac{1}{2}\sum_{q=0}^{\infty} A_q\left[\left(\beta_x^2 K_q^{+-} - M_x M_y A_q^{++}\right)\mathrm{e}^{\mathrm{i}A_q^{++}y} + \left(\beta_x^2 K_q^{++} - M_x M_y A_q^{-+}\right)\mathrm{e}^{\mathrm{i}A_q^{-+}y}\right], \tag{2.84}$$

where

$$K_q^{\pm\pm} = k_q^{\pm}\cos\Psi \pm \frac{q\pi}{a}\sin\Psi, \quad A_q^{\pm\pm} = \pm\frac{q\pi}{a}\cos\Psi + k_q^{\pm}\sin\Psi.$$

Using the same projection method as previously gives

$$(\beta_x^2 k_j^+ - M_x M_y \alpha_j)\mathfrak{I}_{i,\nu} + \sum_{p=-\infty}^{\infty} R_p\left(\beta_x^2 k_p^- - M_x M_y \alpha_p\right)\mathfrak{I}_{p,\nu}$$
$$= \frac{1}{2}\sum_{q=0}^{\infty} A_q\left[\left(\beta_x^2 K_q^{+-} - M_x M_y A_q^{++}\right)\mathfrak{I}_{q,\nu}^{++} + \left(\beta_x^2 K_q^{++} - M_x M_y A_q^{-+}\right)\mathfrak{I}_{q,\nu}^{-+}\right]. \tag{2.85}$$

After some algebra, the modified velocity continuity reads

$$\boxed{b\left(\mathcal{K}_j^+\delta_{\nu,0} + \mathcal{K}_\nu^- R_\nu\right) = \sum_{q=0}^{\infty} A_q \mathcal{K}_{q,\nu}^+ \mathfrak{I}_{q,\nu}^+}, \tag{2.86}$$

where

$$\mathcal{K}_j^+ = \beta_x^2 k_j^+ - M_x M_y \alpha_j,$$
$$\mathcal{K}_\nu^- = \beta_x^2 k_\nu^- - M_x M_y \alpha_\nu,$$

$$\mathcal{K}_{q,\nu}^{\pm} = \left(\beta_x^2 \cos\Psi - M_x M_y \sin\Psi\right) k_q^{\pm} + \frac{\tan\Psi}{\varphi_{q,\nu}^{\pm}(\Psi)} \left(\frac{q\pi}{b}\right)^2.$$

Linear System of the Mode-Matching Condition

To solve the problem on the A_q coefficients, the R_ν terms are canceled out by subtracting (2.86) to $\mathcal{K}_\nu^-$ times (2.80). This yields

$$\sum_{q=0}^{\infty} A_q \left(\mathcal{K}_\nu^- - \mathcal{K}_{q,\nu}^+\right) \mathfrak{I}_{q,\nu}^+ = b \left(\mathcal{K}_\nu^- - \mathcal{K}_j^+\right) \delta_{\nu,0}. \tag{2.87}$$

After a modal truncation ($\nu \in [-(N_\nu - 1)/2, (N_\nu - 1)/2]$ and $q \in [0, N_q - 1]$), the matrix form of the equations to solve is

$$\underline{\mathbf{M^1}}\,\mathbf{A} = \mathbf{M_i}, \tag{2.88}$$

where

$$\left[M^1\right]_{\nu,q} = \left(\mathcal{K}_\nu^- - \mathcal{K}_{q,\nu}^+\right) \mathfrak{I}_{q,\nu}^+, \quad \left[M_i\right]_{\nu,1} = b \left(\mathcal{K}_\nu^- - \mathcal{K}_j^+\right) \delta_{\nu,0}, \quad \text{and} \quad [A]_{q,1} = A_q.$$

This is solved by means of an iterative least-squares method. Then the R_ν coefficients can be deduced from either the potential continuity (2.80) or the modified velocity continuity (2.86).

Another possibility is to solve the A_q and R_ν coefficients simultaneously with a global matrix equation of the form

$$\begin{pmatrix} \mathbf{E_1^1} & \mathbf{F_1^1} \\ \underline{\mathbf{E_2^1}} & \underline{\mathbf{F_2^1}} \end{pmatrix} \begin{pmatrix} \mathbf{A} \\ \mathbf{R} \end{pmatrix} = \begin{pmatrix} \mathbf{H_1^1} \\ \mathbf{H_2^1} \end{pmatrix}, \tag{2.89}$$

where

$$\left[E_1^1\right]_{\nu,q} = \mathfrak{I}_{q,\nu}^+, \quad \left[F_1^1\right]_{\nu,\nu} = -b\delta_{\nu,\nu}, \quad \left[H_1^1\right]_{\nu,1} = b\delta_{\nu,0},$$
$$\left[E_2^1\right]_{\nu,q} = \mathcal{K}_{q,\nu}^+ \mathfrak{I}_{q,\nu}^+, \quad \left[F_2^1\right]_{\nu,\nu} = -b\mathcal{K}_\nu^- \delta_{\nu,\nu}, \quad \left[H_2^1\right]_{\nu,1} = b\mathcal{K}_j^+ \delta_{\nu,0},$$
$$[A]_{q,1} = A_q, \quad [R]_{\nu,1} = T_\nu.$$

2.3.3 Trailing-Edge Interface

Acoustic Potentials

At the trailing-edge interface, the acoustic potentials involved are represented in Figure 2.13. Since this interface is not staggered, the continuity of the modified velocity $\beta_x^2 u_x - M_x M_y u_y$ reduces to the continuity of the axial fluctuating velocity u_x, along the continuity of the velocity potential ϕ, which remains unchanged. Downstream of the OGV, the mean flow is axial and the Helmholtz equation is the same as for flat vanes (2.3). The expression of the transmitted acoustic potential ϕ_t is

$$\phi_t(x', y') = \sum_{p=-\infty}^{\infty} T_p \mathrm{e}^{\mathrm{i}\alpha_p y'} \mathrm{e}^{\mathrm{i}k_p^+ x'}, \quad \text{for} \quad 0 \le x' < \infty \quad \text{and} \quad 0 \le y' < 2\pi R, \tag{2.90}$$

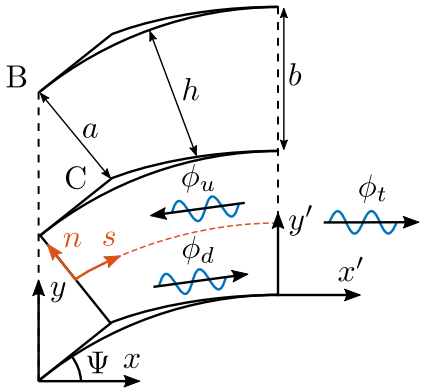

Figure 2.13: Scattering of a downstream-propagating channel mode at the trailing-edge interface.

where

$$x' = x - l_x, \quad y' = y - R_c(1 - \cos\Psi), \quad \alpha_p = \alpha_j + p\frac{2\pi}{b}, \quad k_p^+ = \frac{-kM + \sqrt{k^2 - \beta^2\alpha_p^2}}{\beta^2}.$$

Since all potentials are evaluated at the trailing-edge interface in this section, the $+\infty$ subscript below the mean flow variables is not needed and is dismissed.

In the inter-vane channels, the modes are given by equation (2.67). With the opposite Fourier-transform convention used here, it reads

$$\phi_q(S,n) = \frac{Q_q\sqrt{2/(1+\delta_{q,0})}}{\sqrt{D_0(S)k(S)\sigma_q(S)h(S)}}\cos\left(\theta_q(S)\left[n + \frac{h(S)}{2}\right]\right)\exp\left(\frac{\mathrm{i}}{\epsilon}\int^S \mu_q^{\pm}(\xi)\,\mathrm{d}\xi\right), \tag{2.91}$$

for $0 \le S \le L_c$ and $-h(S)/2 \le n \le h(S)/2$, and where

$$\mu_q^{\pm}(S) = \frac{-k(S)M(S) \pm k(S)\sigma_q(S)}{\beta^2(S)}, \quad \sigma_q(S) = \sqrt{1 - \left(\frac{\beta(S)\theta_q(S)}{k(S)}\right)^2}, \quad \theta_q(S) = \frac{q\pi}{h(S)}.$$

By gathering some constants into the Q_q amplitudes, the potentials ϕ_d and ϕ_u can be expressed in terms of the A_q and B_q modal coefficients. For this purpose, both formulations $\phi_q(S,n)$ (2.91) and $\phi_d(\zeta,\eta)$ (2.76) are matched at the inlet of the slowly-varying channel (segment BC from Figure 2.13). On this interface $h(S=0) = a$, thus

$$\begin{cases} \eta \in [0,a], \\ \zeta = a\tan\Psi, \end{cases} \quad \text{and} \quad \begin{cases} n = \eta - a/2, \\ S = 0. \end{cases}$$

Consequently, the Q_q amplitudes for the downstream-propagating modes are given by

$$Q_q = A_q\frac{\sqrt{D_0(0)k(0)\sigma_q(0)h(0)}}{\sqrt{2/(1+\delta_{q,0})}}\mathrm{e}^{\mathrm{i}k_q^+ a\tan\Psi}.$$

Introducing the stream-wise variation function as

$$\Upsilon_q^+(S) = \sqrt{\frac{D_0(0)k(0)\sigma_q(0)h(0)}{D_0(S)k(S)\sigma_q(S)h(S)}}\exp\left(\frac{\mathrm{i}}{\epsilon}\int_0^S \mu_q^+(\xi)\,\mathrm{d}\xi\right), \tag{2.92}$$

the potential ϕ_d in the slowly-varying channel reads

$$\boxed{\phi_d(S,n) = \sum_{q=0}^{\infty} A_q \Upsilon_q^+(S) \mathrm{e}^{\mathrm{i}k_q^+ a \tan\Psi} \cos\left(\theta_q(S)\left[n + \frac{h(S)}{2}\right]\right)}. \tag{2.93}$$

For the upstream-propagating modes, the matching is done at the trailing-edge interface with a locally constant channel mode. The Q_q amplitudes in this case are given by

$$Q_q = B_q \frac{\sqrt{D_0(L_c)k(L_c)\sigma_q(L_c)h(L_c)}}{\sqrt{2/(1+\delta_{q,0})}}.$$

Hence,

$$\boxed{\phi_u(S,n) = \sum_{q=0}^{\infty} B_q \Upsilon_q^-(S) \cos\left(\theta_q(S)\left[n + \frac{h(S)}{2}\right]\right)}, \tag{2.94}$$

where

$$\Upsilon_q^-(S) = \sqrt{\frac{D_0(L_c)k(L_c)\sigma_q(L_c)h(L_c)}{D_0(S)k(S)\sigma_q(S)h(S)}} \exp\left(\frac{\mathrm{i}}{\epsilon}\int_{L_c}^{S} \mu_q^-(\xi)\,\mathrm{d}\xi\right). \tag{2.95}$$

Continuity of the Acoustic Potential

At the trailing-edge interface, the continuity of the potential reads

$$\sum_{q=0}^{\infty}\left[A_q\Upsilon_q^+(L_c)\mathrm{e}^{\mathrm{i}k_q^+ a\tan\Psi} + B_q\right]\cos\left(\theta_q(L_c)y'\right) = \sum_{p=-\infty}^{\infty} T_p \mathrm{e}^{\mathrm{i}\alpha_p y'}. \tag{2.96}$$

After a projection on the modal basis of the transmitted modes with the operator

$$\int_0^b (\bullet)\mathrm{e}^{-\mathrm{i}\alpha_\nu y'}\,\mathrm{d}y', \quad \text{with} \quad \alpha_\nu = \alpha_j + \nu\frac{2\pi}{b},\ \nu\in\mathbb{Z},$$

the integrals yields

$$\int_0^b \mathrm{e}^{\mathrm{i}(\alpha_p-\alpha_\nu)y'}\,\mathrm{d}y' = b\delta_{\nu,p},$$

and

$$\mathfrak{I}_{q,\nu}^0 = \int_0^b \cos\left(\theta_q(L_c)y'\right)\mathrm{e}^{-\mathrm{i}\alpha_\nu y'}\,\mathrm{d}y' = \begin{cases} \dfrac{\mathrm{i}\alpha_\nu}{(\alpha_q)^2-\alpha_\nu^2}\left[1-(-1)^q\mathrm{e}^{-\mathrm{i}\alpha_j b}\right], \\ \dfrac{b}{2}(1+\delta_{q,0}) \quad \text{if} \quad \alpha_\nu = \dfrac{q\pi}{b}. \end{cases}$$

Notice that $\mathfrak{I}_{q,\nu}^0$ is a particular case of the previously defined inner product $\mathfrak{I}_{q,\nu}^{\pm}(\Psi=0)$ in (2.81) for a zero stagger angle. Compiling these results together yields

$$\boxed{\sum_{q=0}^{\infty}\left[A_q\Upsilon_q^+(L_c)\mathrm{e}^{\mathrm{i}k_q^+ a\tan\Psi} + B_q\right]\mathfrak{I}_{q,\nu}^0 = bT_\nu}. \tag{2.97}$$

Continuity of the Acoustic Axial Velocity

The slowly-varying channel modes ϕ_d and ϕ_u have a slowly varying part (dependence in S) and a rapidly varying part (dependence in s). The small scale variations are given by the exponential term in the stream-wise variation functions $\Upsilon^{\pm}$. Therefore, the derivative of the potentials with respect to s only involves this exponential term at leading order. The acoustic axial velocities are given by

$$\frac{\partial \phi_d}{\partial s}(S,n) = \sum_{q=0}^{\infty} A_q \mathrm{i}\mu_q^+(S)\Upsilon_q^+(S)\mathrm{e}^{\mathrm{i}k_q^+ a\tan\Psi}\cos\left(\theta_q(S)\left[n+\frac{h(S)}{2}\right]\right)+\mathcal{O}(\epsilon), \tag{2.98}$$

and

$$\frac{\partial \phi_u}{\partial s}(S,n) = \sum_{q=0}^{\infty} B_q \mathrm{i}\mu_q^-(S)\Upsilon_q^-(S)\cos\left(\theta_q(S)\left[n+\frac{h(S)}{2}\right]\right)+\mathcal{O}(\epsilon). \tag{2.99}$$

Projecting on the annular modal basis, the axial velocity continuity at the trailing-edge interface reads

$$\boxed{\sum_{q=0}^{\infty}\left[A_q\mu_q^+(L_c)\Upsilon_q^+(L_c)\mathrm{e}^{\mathrm{i}k_q^+ a\tan\Psi}+B_q\mu_q^-(L_c)\right]\mathfrak{I}_{q,\nu}^0 = bk_\nu^+ T_\nu}. \tag{2.100}$$

Linear System of the Mode-Matching Condition

The unknown B_q coefficients are solved by canceling out the T_ν coefficients in (2.97) and (2.100), which gives

$$\sum_{q=0}^{\infty} B_q\left[k_\nu^+-\mu_q^-(L_c)\right]\mathfrak{I}_{q,\nu}^0 = \sum_{q=0}^{\infty} A_q\left[\mu_q^+(L_c)-k_\nu^+\right]\Upsilon^+(L_c)\mathrm{e}^{\mathrm{i}k_q^+ a\tan\Psi}\mathfrak{I}_{q,\nu}^0. \tag{2.101}$$

The modal truncation ($\nu\in[-(N_\nu-1)/2,(N_\nu-1)/2]$ and $q\in[0,N_q-1]$) allows one to numerically compute the B_q coefficients from the linear system of equations

$$\underline{\mathbf{M^2}}\mathbf{B}=\mathbf{M_d}, \tag{2.102}$$

where

$$\left[M^2\right]_{\nu,q}=\left[k_\nu^+-\mu_q^-(L_c)\right]\mathfrak{I}_{q,\nu}^0,\quad \left[M_d\right]_{\nu,1}=\sum_{q=0}^{\infty}A_q\left[\mu_q^+(L_c)-k_\nu^+\right]\Upsilon^+(L_c)\mathrm{e}^{\mathrm{i}k_q^+ a\tan\Psi}\mathfrak{I}_{q,\nu}^0,$$

$$\left[B\right]_{q,1}=B_q.$$

The continuity equation (2.97) or (2.100) can then be used to deduce T_ν.

Finally, the general matrix equation for this interface is

$$\begin{pmatrix}\underline{\mathbf{E_1^2}} & \underline{\mathbf{F_1^2}}\\ \underline{\mathbf{E_2^2}} & \underline{\mathbf{F_2^2}}\end{pmatrix}\begin{pmatrix}\mathbf{B}\\ \mathbf{T}\end{pmatrix}=\begin{pmatrix}\mathbf{H_1^2}\\ \mathbf{H_2^2}\end{pmatrix}, \tag{2.103}$$

where

$$\left[E_1^2\right]_{\nu,q} = \mathfrak{I}^0_{q,\nu}, \quad \left[F_1^2\right]_{\nu,\nu} = -b\delta_{\nu,\nu}, \quad \left[H_1^2\right]_{\nu,1} = -\sum_{q=0}^{\infty} A_q \Upsilon_q^+(L_c) \mathrm{e}^{\mathrm{i}k_q^+ a\tan\Psi} \mathfrak{I}^0_{q,\nu},$$

$$\left[E_2^2\right]_{\nu,q} = \mu_q^-(L_c)\mathfrak{I}^0_{q,\nu}, \quad \left[F_2^2\right]_{\nu,\nu} = -bk_\nu^+\delta_{\nu,\nu}, \quad \left[H_2^2\right]_{\nu,1} = -\sum_{q=0}^{\infty} A_q \mu_q^+(L_c)\Upsilon_q^+(L_c) \mathrm{e}^{\mathrm{i}k_q^+ a\tan\Psi} \mathfrak{I}^0_{q,\nu},$$

$$[B]_{q,1} = A_q, \quad [T]_{\nu,1} = R_\nu.$$

2.3.4 Correction to the Leading-Edge Interface

For the next steps in the iterative procedure, the leading-edge matching (2.89) needs to be modified to account for the upstream scattered modes ϕ_{uq} traveling back from the trailing-edge interface (see Figure 2.14). The potential continuity and modified

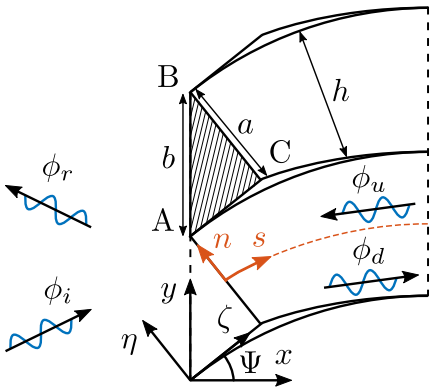

Figure 2.14: Scattering of an incident mode at the staggered leading-edge interface with feedback from the trailing-edge scattering.

velocity continuity read, at the g^{th} iteration,

$$\boxed{\sum_{q=0}^{\infty} A_q^g \mathfrak{I}^+_{q,\nu} + B_q^{g-1}\Upsilon_q^-(0)\mathrm{e}^{-\mathrm{i}k_q^- b\sin\Psi}\mathfrak{I}^-_{q,\nu} = b\left(R_\nu^g + \delta_{\nu,0}\right)}, \tag{2.104}$$

and

$$\boxed{\sum_{q=0}^{\infty} A_q^g \mathcal{K}^+_{q,\nu}\mathfrak{I}^+_{q,\nu} + B_q^{g-1}\Upsilon_q^-(0)\mathrm{e}^{-\mathrm{i}k_q^- b\sin\Psi}\mathcal{K}^-_{q,\nu}\mathfrak{I}^-_{q,\nu} = b\left(\mathcal{K}_\nu^- R_\nu^g + \mathcal{K}_j^+\delta_{\nu,0}\right)}. \tag{2.105}$$

Combining them to cancel out the unknown R_ν^g coefficients yields

$$\sum_{q=0}^{\infty} A_q^g \left(\mathcal{K}_\nu^- - \mathcal{K}^+_{q,\nu}\right)\mathfrak{I}^+_{q,\nu} = b\left(\mathcal{K}_\nu^- - \mathcal{K}_j^+\right)\delta_{\nu,0} - \sum_{q=0}^{\infty} B_q^{g-1}\left(\mathcal{K}_\nu^- - \mathcal{K}^-_{q,\nu}\right)\Upsilon_q^-(0)\mathrm{e}^{-\mathrm{i}k_q^- b\sin\Psi}\mathfrak{I}^-_{q,\nu}. \tag{2.106}$$

After a modal truncation ($\nu \in [-(N_\nu-1)/2, (N_\nu-1)/2]$ and $q \in [0, N_q-1]$), the corrected system of equations at the leading-edge interface is

$$\underline{\mathbf{M}}^{\mathbf{1}}\mathbf{A} = \mathbf{M_i}, \tag{2.107}$$

where

$$\left[M^1\right]_{\nu,q} = \left(\mathcal{K}_\nu^- - \mathcal{K}_{q,\nu}^+\right)\mathfrak{I}_{q,\nu}^+, \quad [A]_{q,1} = A_q^g,$$

$$[M_i]_{\nu,1} = b\left(\mathcal{K}_\nu^- - \mathcal{K}_j^+\right)\delta_{\nu,0} - \sum_{q=0}^{\infty} B_q^{g-1}\left(\mathcal{K}_\nu^- - \mathcal{K}_{q,\nu}^-\right)\Upsilon_q^-(0)\mathrm{e}^{-\mathrm{i}k_q^- b\sin\Psi}\mathfrak{I}_{q,\nu}.$$

The R_ν coefficients are then deduced from either (2.104) or (2.105).

The corrected global system of equations at the leading-edge interface is

$$\begin{pmatrix} \mathbf{E_1^1} & \mathbf{F_1^1} \\ \underline{\mathbf{E_2^1}} & \underline{\mathbf{F_2^1}} \end{pmatrix}\begin{pmatrix} \mathbf{A} \\ \mathbf{R} \end{pmatrix} = \begin{pmatrix} \mathbf{H_1^1} \\ \mathbf{H_2^1} \end{pmatrix}, \tag{2.108}$$

where

$$\left[E_1^1\right]_{\nu,q} = \mathfrak{I}_{q,\nu}^+, \quad \left[F_1^1\right]_{\nu,\nu} = -b\delta_{\nu,\nu}, \quad \left[H_1^1\right]_{\nu,1} = b\delta_{\nu,0} - \sum_{q=0}^{\infty} B_q^{g-1}\Upsilon_q^-(0)\mathfrak{I}_{q,\nu}^-\mathrm{e}^{-\mathrm{i}k_q^- b\sin\Psi},$$

$$\left[E_2^1\right]_{\nu,q} = \mathcal{K}_{q,\nu}^+\mathfrak{I}_{q,\nu}^+, \quad \left[F_2^1\right]_{\nu,\nu} = -b\mathcal{K}_\nu^-\delta_{\nu,\nu},$$

$$\left[H_2^1\right]_{\nu,1} = b\mathcal{K}_j^+\delta_{\nu,0} - \sum_{q=0}^{\infty} B_q^{g-1}\Upsilon_q^-(0)\mathcal{K}_{q,\nu}^-\mathfrak{I}_{q,\nu}^-\mathrm{e}^{-\mathrm{i}k_q^- b\sin\Psi},$$

$$[A]_{q,1} = A_q^g, \quad [R]_{\nu,1} = R_\nu^g.$$

Mode-Matching Equations — Summary

The mode-matching equations have been derived for the scattering of an acoustic wave by a cascade of cambered vanes, assuming equivalent straight channels. A subsonic nearly uniform mean flow, continuously deviated through the cascade, has been used. Jump conditions for the staggered leading-edge interface have been detailed with emphasis on the fact that pressure cannot be used, in general, for a staggered interface with flow. Instead, the velocity potential and a combination of axial and transverse velocities is used.

2.4 Comparison with Numerical Results

2.4.1 Methodology

A test case is defined to test the present analytical solution against numerical simulations computed with the commercial software Simcenter 3D Acoustics [1]. A cascade of four vanes ($V = 4$) is considered at a duct radius of $R = 38$ mm, which gives a vane spacing $b = 2\pi R/V \simeq 60$ mm. The camber angle is set at $\Psi = 30°$ and the solidity value at $l/b = 1.04$. No mean flow is considered ($M = 0$) and the mean density and sound speed are assumed constant and set to $D = 1.225$ kg/m^3 and $C = 340$ m/s. Incident acoustic waves of unit amplitude are scattered by the OGV. Computations are performed for two distinct frequencies and modal orders: $j = 1$ at $kb = 2.4289$

[1] Hadrien Bériot, Siemens Industry Software NV (personal communication, January 2019).

($f \simeq 2200$ Hz) and $j = 5$ at $kb = 12.145$ ($f \simeq 11000$ Hz). The angle of incidence of the waves, from the x-axis, is given by $\theta_j = \arcsin(j/kR)$ to ensure the periodicity in the y-direction. This gives $\theta \simeq 40°$ for both cases.

The two-dimensional Helmholtz problem is addressed numerically using a high-order adaptive Finite Element Method (FEM) [9, 7]. Periodic boundary conditions are enforced and spurious reflections at the boundaries are avoided using Perfectly Matched Layers (PML) [6] as shown in Figure 2.15.

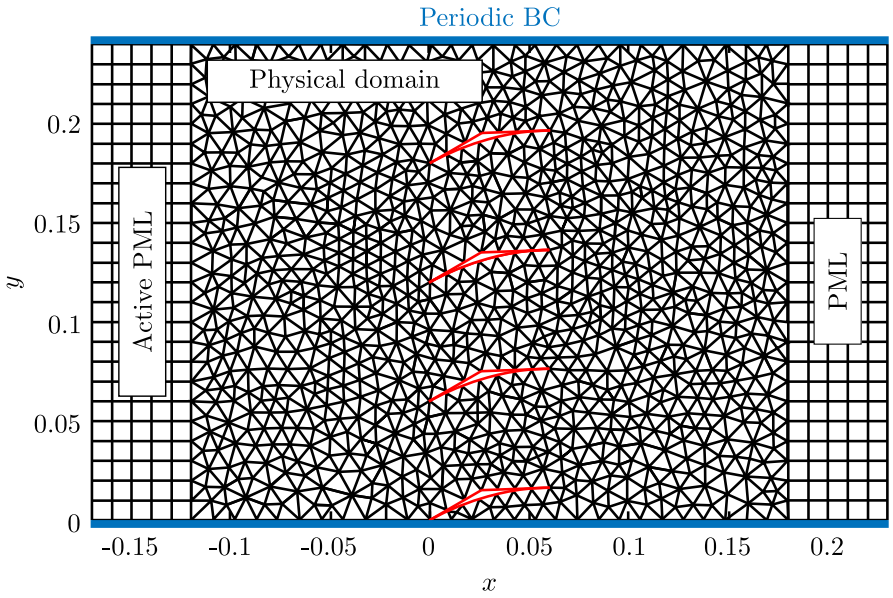

Figure 2.15: Explanatory scheme of the numerical setup displaying the geometry, the mesh and how boundary conditions are treated.

This test case aims at validating the developed method of Mode Matching for Bifurcated Wave-guides (MMBW). The same Helmholtz equation is solved with the same boundary conditions and vanes geometry in both methods (finite element and mode matching). No flow is considered since the numerical method cannot handle a varying mean flow with the Helmholtz equation, and it is better to first assess the validity of the geometrical assumptions of the MMBW in a medium at rest.

Qualitative and quantitative comparisons between FEM and MMBW results in terms of real values of the fluctuating pressure are presented below. Reflected and transmitted acoustic powers are computed for both numerical and analytical results in order to (i) ensure that the power balance is correctly predicted with the MMBW and (ii) attest the accuracy of the technique by comparing the incident power to the sum of the reflected and transmitted powers. Some limitations and possible extensions of this validation process are discussed afterward.

2.4.2 Results

First Scenario: $j = 1$ at $kb = 2.4289$

Figure 2.16 shows the instantaneous pressure maps computed with the FEM and the MMBW for $j = 1$ at $kb = 2.4289$. The pressure patterns are in good agreement upstream and downstream of the cascade, as well as in the inter-vane channels.

Figure 2.17 displays the instantaneous pressure profiles extracted upstream, downstream and through the cascade, at the locations pointed out with dashed black lines in

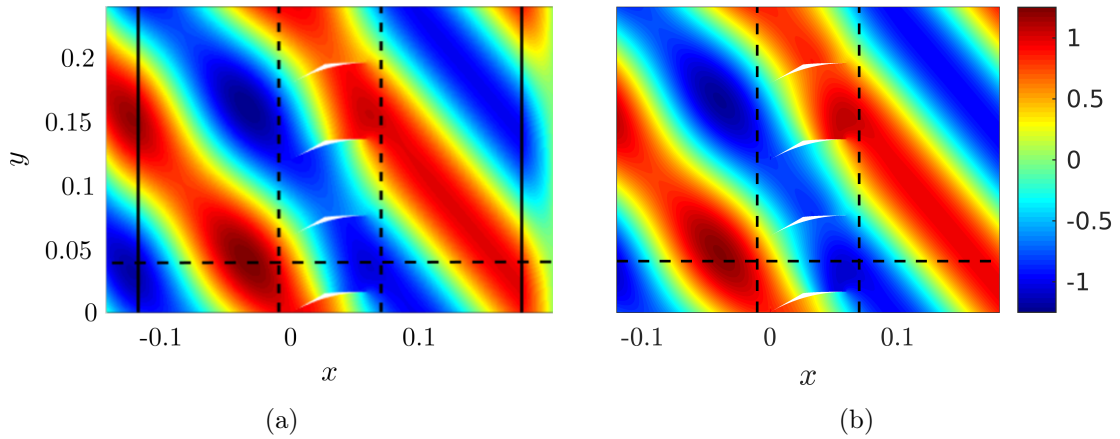

Figure 2.16: Instantaneous pressure maps computed with FEM (a) and MMBW (b) for $j = 1$ at $kb = 2.4289$. Dashed black lines are the locations for quantitative comparisons and solid black lines in (a) show the limit of PML.

Figure 2.16. The pressure field predicted by the analytical model matches the numerical results downstream of the cascade (2.17c), but a difference in amplitude is visible upstream (2.17a).

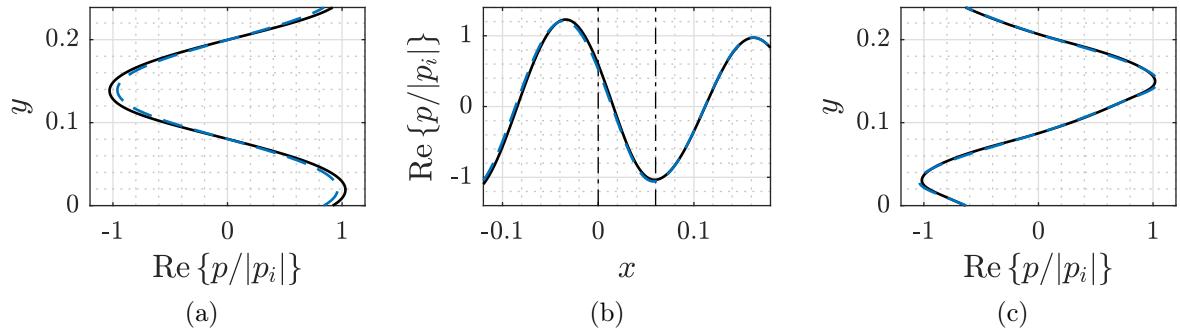

Figure 2.17: Instantaneous pressure profiles using FEM (—) and MMBW (- -) for $j = 1$ at $kb = 2.4289$, at $x = -0.01$ m (a), $y = 0.04$ m (b) and $x = 0.07$ m (c). The vertical dash-dotted lines in (b) represents the LE and TE interfaces.

From the look of the pressure profiles, it is clear that only the mode of order $j + pV = 1$ ($p = 0$) is cut-on in the annular domain. The amplitude of this mode could be under-evaluated by the MMBW in the upstream region. The global acoustic power balance is defined as

$$\mathcal{P}_i + \mathcal{P}_r = \mathcal{P}_t, \tag{2.109}$$

where $\mathcal{P}_i$, $\mathcal{P}_r$ and $\mathcal{P}_t$ are the incident, reflected and transmitted acoustic powers, respectively. They are given by (see [37], p. 41)

$$\mathcal{P}_i = \frac{kZbV}{2\beta_x^2}\mathrm{Re}\left(\sqrt{k^2 - (\beta_x^2 - M_y^2)\alpha_j^2 - 2k\alpha_j M_y}\right), \tag{2.110}$$

$$\mathcal{P}_r = -\frac{kZbV}{2\beta_x^2} \sum_{p=-\infty}^{\infty} \mathrm{Re}\left(\sqrt{k^2 - (\beta_x^2 - M_y^2)\alpha_p^2 - 2k\alpha_p M_y}\right) |R_p|^2, \tag{2.111}$$

and

$$\mathcal{P}_t = \frac{kZbV}{2\beta^2} \sum_{p=-\infty}^{\infty} \mathrm{Re}\left(\sqrt{k^2 - \beta^2\alpha_p^2}\right) |T_p|^2, \tag{2.112}$$

where the mean flow quantities have to be evaluated at either $-\infty$ for $\mathcal{P}_i$ and $\mathcal{P}_r$, or $+\infty$ for $\mathcal{P}_t$. The relative value of the reflected and transmitted powers, in terms of a percentage of the incident power, are given in Table 2.1 with the error $E = 1-(\mathcal{P}_t-\mathcal{P}_r)/\mathcal{P}_i$, for both FEM and MMBW. The relative reflected power $\mathcal{P}_r$ predicted

	$\mathcal{P}_r/\%$	$\mathcal{P}_t/\%$	$E/\%$
FEM	5.270	94.62	0.1100
MMBW	4.926	95.06	0.0140

Table 2.1: Comparison of reflected $\mathcal{P}_r$ and transmitted $\mathcal{P}_t$ relative powers, in terms of the incident power $\mathcal{P}_i$, and the relative error $E = 1 - (\mathcal{P}_t - \mathcal{P}_r)/\mathcal{P}_i$ for $j = 1$ at $kb = 2.4289$.

by the MMBW is lower than what is predicted by the FEM. Since only one mode is cut-on, it is tempting to say that this explains the difference in amplitude seen in Figure 2.17a, but the difference is about 0.344 %, which should not be visible in the pressure profiles. Furthermore, downstream of the cascade, a difference of 0.44 % is observed between the numerical and analytical transmitted powers $\mathcal{P}_t$, and no discrepancies are visible in the pressure profiles (2.17c). Consequently, the difference between the upstream pressure profiles are due to under-predicted cut-off modes in the mode-matching technique. Cut-off modes can play a significant role here since the pressure profiles are extracted at a distance of only $l_x/6$ from the leading-edge interface, which is their defined origin.

Second Scenario: $j = 5$ at $kb = 12.145$

When increasing the frequency to $kb = 12.145$ and changing the incident mode order to $j = 5$, a fairly good agreement is still observed upstream (Figures 2.18 and 2.19a). However, the analytical model displays significant discrepancies compared to the numerical simulation in the axial profile, beyond $x = 2l_x/3$ (Figure 2.19b). These differences are also observable in the pressure map (Figure 2.18b) and the downstream profile (Figure 2.19c).

Table 2.2 shows that the relative error in the acoustic power balance is still very low ($E = -0.001$ %). This indicates that the model is still accurate in this case but does not represent the problem correctly.

In Figure 2.18b, the wavefront in the inter-vane channels is deviated with the inclination of the vanes. This behavior, not observed in the numerical solution (Figure 2.18a), is solely due to the straight-channel approximation in the MMBW. The channel modes are dominated by the plane mode $q = 0$, which is constant along the axis perpendicular to the curvilinear abscissa. In a curved duct, such a mode does not exist, as it will be demonstrated in Chapter 3. Since the discrepancies are due to the propagation model inside the inter-vane channels and that most of the incident wave is transmitted through the cascade, the pressure field downstream of the cascade is the

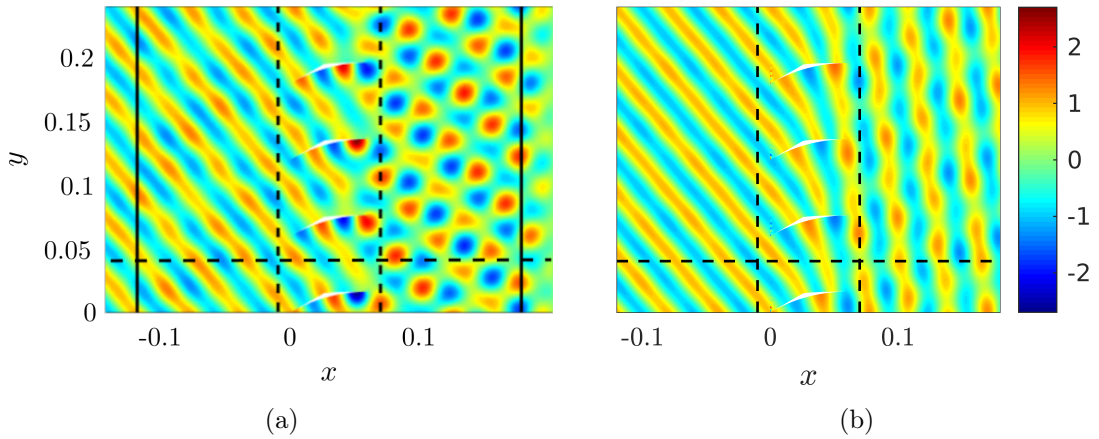

(a) (b)

Figure 2.18: Instantaneous pressure maps computed with FEM (a) and MMBW (b) for $j = 5$ at $kb = 12.145$. Dashed black lines are the locations for quantitative comparisons and solid black lines in (a) show the limit of PML.

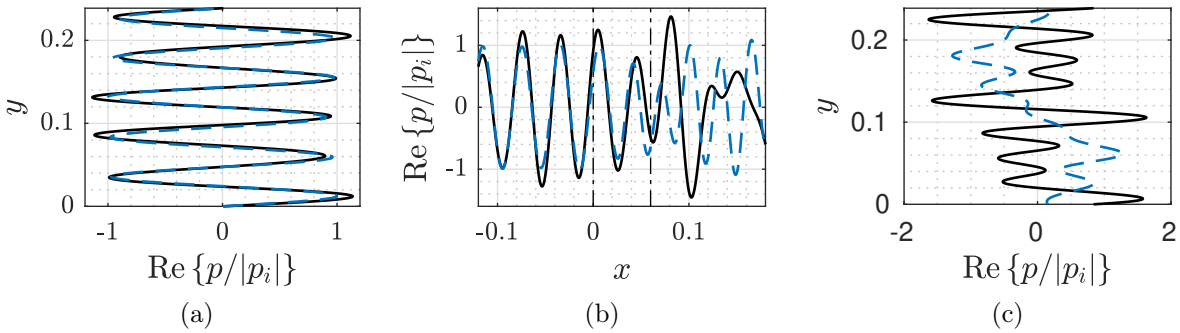

(a) (b) (c)

Figure 2.19: Instantaneous pressure profiles using FEM (—) and MMBW (- -) for $j = 5$ at $kb = 12.145$, at $x = -0.01$ m (a), $y = 0.04$ m (b) and $x = 0.07$ m (c). The vertical dash-dotted lines in (b) represents the LE and TE interfaces.

	$\mathcal{P}_r/\%$	$\mathcal{P}_t/\%$	$E/\%$
FEM	3.950	96.05	<0.11
MMBW	0.3010	99.70	-0.001

Table 2.2: Comparison of reflected $\mathcal{P}_r$ and transmitted $\mathcal{P}_t$ relative powers, in terms of the incident power $\mathcal{P}_i$, and the relative error $E = 1 - (\mathcal{P}_t - \mathcal{P}_r)/\mathcal{P}_i$ for $j = 5$ at $kb = 12.145$.

most affected. The upstream field is mostly dependent on the leading-edge geometry here, not on the back-scattering of the upstream-propagating channel modes generated at the trailing-edge interface.

2.4.3 Discussion

These quantitative results support the assumption that the model based on equivalent straight channels performs well at low frequency, as was indicated by Ref. [25, 51, 119].

However, at higher frequencies, the curvature effects are no longer negligible and the straight-channel approximation induces an artificial deviation of the wavefront through the cascade, ending up to a shifted dominant mode order downstream of the cascade: $j+pV = 1$ ($p = -1$) instead of $j+pV = 5$ ($p = 0$). Curvature effects will be introduced in the next chapter and comparisons will be made between the models to define the frequency limit of the straight-channel approximation.

These results also demonstrate the validity of the slowly-varying approach, and of the channel modal basis approximation in the triangle ABC. Yet, the modal basis approximation seems to generate oscillations similar to the Gibbs phenomenon at the leading-edge interface in the highest frequency case ($kb = 12.145$). This may have an influence on the scattered modal content and, if so, would indicate that the approach based on Green's reciprocity theorem could be more adequate [116].

The impact of the artificial thickness will be assessed in the next chapter with the model accounting for curvature, in order to avoid mixing multiple sources of error.

Comparisons in the presence of a mean flow have not been performed yet. Emphasis has been placed on the other assumptions of the model, such as the neglected curvature, considered of primary importance. However, the study of sound propagation in an axial compressor stage could not be accurate without flow. It is then necessary to evaluate the impact of the mean flow modeling but, unfortunately, this has not been done during the PhD. Quantitative investigations on that matter will be carried out during a post-doctoral fellowship. Yet, qualitative comparisons are made in Chapter 3, Section 3.3.2, and a more realistic mean flow modeling is proposed in the conclusion.

Comparison with Numerical Results — Summary

Results from the present analytical solution have been compared with numerical results obtained from a finite element method. The same Helmholtz equation is solved in both methods, with the same boundary conditions and vane geometry. Computations have been performed at two frequencies and incident mode orders: $j = 1$ at $kb = 2.4289$ (low frequency case) and $j = 5$ at $kb = 12.145$ (high frequency case). Assessments on the validity of the approximations made in the model are given below.

Straight-Channel Approximation:

- Good agreement with numerical results, qualitatively and quantitatively, at low frequency;
- Artificial deviation of the wavefront, starting at two thirds of the channel length, at high frequency due to missing curvature effects.

Slowly-Varying Approximation:

- Adequate approach at low frequency;
- Validation needed at high frequency with curvature effects.

Modal Basis Approximation:

- Adequate approximation at low frequency;

- Oscillations similar to the Gibbs phenomenon at high frequency in the vicinity of the leading edge;
- Green's reciprocity theorem could be used instead to estimate the impact of the oscillations on the modal content.

Geometrical Approximation:

- Will be assessed in the next chapter with curvature effects.

Mean Flow Approximation:

- Qualitative comparisons made in Chapter 3, Section 3.3.2.

2.5 Conclusion

In the first instance, the focus was on the transmission and reflection phenomena of an incident acoustic wave. For the sake of clarity, the mode-matching technique has first been explained in detail in the simpler case of unstaggered flat vanes. Two possible solving procedures have been introduced: an iterative approach made of successive leading-edge and trailing-edge steps, and a direct approach solving a larger global system. Both methods are relevant and usually equivalent, except in some cases that will be discussed when encountered. The possibility to resort to the Wiener-Hopf technique to get a closed-form solution of the modal coefficients has not been presented since it becomes unusable when adding stagger or camber.

Vane camber has a twofold impact on sound propagation through the inter-vane channels:

- curvature of the channel center line;
- expansion of the channel cross-section.

This chapter was dedicated to the modeling of the expansion effect, irrespective of curvature. The latter will be introduced in the next chapter.

Several assumptions have been made on the vane geometry and flow description in order to build an approximate analytical solution of the acoustic potential, based on the multiple-scale analysis of Rienstra [107]. The core assumption of the model is the slow variation of the channel cross-section. The approximate solution of the slowly-varying Helmholtz-like equation is similar to the classical solution of the Helmholtz equation, except that the potential amplitude and wavenumbers can vary with the change in cross-section along the channel.

After incorporating this solution in the mode-matching equations, each assumption has been carefully investigated. The developed model performed well at relatively low frequencies compared to highly accurate numerical results obtained with a finite element method, highlighting the influence of curvature at higher frequencies.

Chapter 3

Acoustic Scattering by a Linear Cascade of Cambered Vanes

Introduction

Camber has been introduced in the previous chapter by only considering the diffuser effect, due to an increasing channel cross-section. The model proved to give accurate results at low frequency but the curvature effects seem to be missing at higher frequencies. In this chapter, the model is extended to account for the curvature on sound propagation. The convected Helmholtz-like equation in the channels is then rewritten in curvilinear coordinates and the solution is integrated into the mode-matching procedure. In the first instance, comparisons are performed with numerical results to assess the validity of the new model. Then, comparisons are performed between both analytical models, accounting or not for curvature, to assess the frequency limit below which the approximate model is valid. This allows one to better understand when curvature effects come into play and how. Finally, parametric studies are performed on the geometrical, disturbance and flow parameters, with emphasis on the resonance phenomenon.

Contents

3.1 Bent Channel of Slowly-Varying Cross-Section

3.1.1 Geometry

Curvature effects on sound propagation inside the inter-vane channels are needed at higher frequencies. In this chapter, curvature is accounted for by use of curvilinear coordinates (s, n), instead of the Cartesian coordinates (x, y) used in the previous chapter. The same geometry is used, as described in Figure 3.1a, but the inter-vane channel is now described without further simplifications, as depicted in Figure 3.1b. The channel height is a function of the slow coordinate $S = \epsilon s$, such that

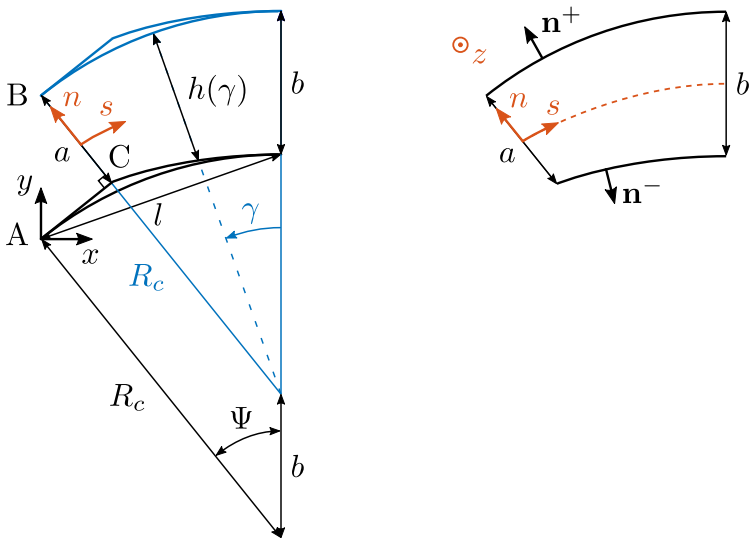

(a) (b)

Figure 3.1: Geometrical approximation of the inter-vane channel (a) and the curved channel of varying cross-section from section BC to the trailing-edge interface (b).

$$h(S) = b\cos\left(\Psi - \frac{S}{b\sin\Psi}\right), \quad 0 \le S \le L_c = b\Psi\sin\Psi. \tag{3.1}$$

Since the center line is almost a circle arc of radius $\bar{R}_c = R_c - b(1+\cos\Psi)/4$ (see 2.2.1), its curvature κ is defined by

$$\kappa b \simeq \frac{-b}{\bar{R}_c} = \frac{\sin\Psi}{\frac{1}{4}(1+\cos\Psi)\sin\Psi - \frac{l}{b}\cos\Psi/2} = \frac{-\epsilon}{\sin\Psi}. \tag{3.2}$$

The evolution of the dimensionless curvature κb is plotted against the camber angle Ψ, for different solidity values l/b, in Figure 3.2. As for the expansion parameter ϵ,

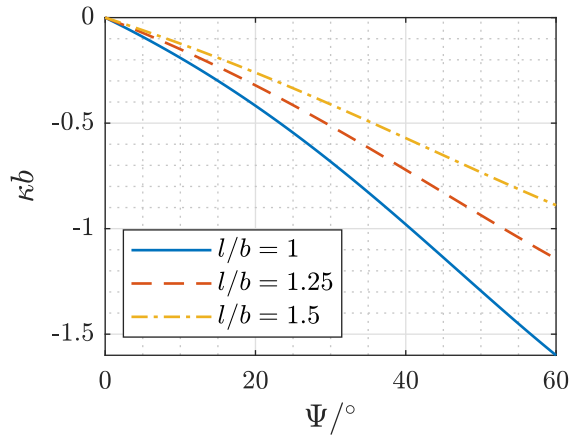

Figure 3.2: Evolution of the dimensionless curvature κb against the camber angle Ψ for different solidity values l/b.

the absolute value of the dimensionless curvature increases with camber, but decreases with solidity.

3.1.2 Mean Flow

The same mean flow description is assumed but expressed in the curvilinear system of coordinates, such that

$$\mathbf{U}(S,n) = U_{0s}(S)\mathbf{e}_s + \epsilon U_{1n}(S,n)\mathbf{e}_n + \mathcal{O}(\epsilon^2), \tag{3.3a}$$

$$C(S,n) = C_0(S) + \mathcal{O}(\epsilon^2), \tag{3.3b}$$

$$D(S,n) = D_0(S) + \mathcal{O}(\epsilon^2), \tag{3.3c}$$

$$P(S,n) = P_0(S) + \mathcal{O}(\epsilon^2). \tag{3.3d}$$

The mean velocity is still given at leading order by

$$U_{0s}(S) = U_{-\infty}\frac{D_{-\infty}a}{D_0(S)h(S)}. \tag{3.4}$$

However, since the channel is now considered as a curved channel, the deviated mean flow is rotational at leading order. Since a constant curvature is assumed along the channel, the curvilinear coordinates used in this work are basically polar coordinates in disguise (see Appendix B.1). Introducing the scale factor $h_s = 1 - \kappa n$ for the coordinate s, the mean vorticity is defined as (see for example [78] Chapter 1.3 – 1.4

or Appendix B.3)

$$\nabla \times \mathbf{U} \sim -\frac{U_{0s}}{h_s}\frac{\mathrm{d}h_s}{\mathrm{d}n}\mathbf{e}_z = \frac{\kappa U_{0s}}{h_s}\mathbf{e}_z. \tag{3.5}$$

This has a consequence on the evolution of the mean density since the mechanical energy is no longer uniform in the flow, as described by Bernoulli's equation (1.8), but now varies from one fluid particle to another. Yet, a scale analysis shows that the rotational term in (1.6b) is negligible compared to the potential term if $\kappa L_c \ll 1$. From (3.2), $\kappa L_c = -\epsilon\Psi = \mathcal{O}(\epsilon)$ for realistic OGV camber angles, which means the rotational term in (1.6b) vanishes at leading order. As a consequence, the mean density value at the location S is still given by the root of the polynomial function

$$D_0(S) \mapsto \frac{1}{\gamma^* - 1}D_0^{\gamma^*+1}(S) - \left(\frac{U_{-\infty}^2}{2} + \frac{D_{-\infty}^{\gamma^*-1}}{\gamma^* - 1}\right)D_0^2(S) + \frac{1}{2}\left(\frac{D_{-\infty}U_{-\infty}a}{h(S)}\right)^2.$$

The validity of this approximation on the mean flow description will be assessed in section 3.3.2.

3.1.3 Slowly-Varying Bent Acoustic Modes

Problem Formulation

The Helmholtz equation (1.11) is written in the curvilinear system of coordinates (see [78] Chapter 1.4 or Appendix B.3 for the differential operators definition). The derivation is then similar to what was done for the straight channel in Appendix A.1.1. With a change of Fourier-transform convention to match Brambley & Peake's result [14], the wave equation now reads

$$\begin{aligned}
&\frac{\beta^2}{h_s^2}\frac{\partial^2\phi}{\partial s^2} + \frac{\partial^2\phi}{\partial n^2} - 2\mathrm{i}\frac{kM}{h_s}\frac{\partial\phi}{\partial s} + \frac{1}{h_s}\frac{\mathrm{d}h_s}{\mathrm{d}n}\frac{\partial\phi}{\partial n} + k^2\phi \\
&+ \epsilon\left\{\left[\frac{1}{D_0 h_s}\frac{\partial D_0}{\partial S} - \frac{U_{0s}}{h_s^2}\frac{\partial}{\partial S}\left(\frac{M}{C_0}\right)\right]\frac{\partial\phi}{\partial s} - \mathrm{i}\omega\frac{U_{0s}}{h_s}\frac{\partial}{\partial S}\left(\frac{1}{C_0^2}\right)\phi - 2\mathrm{i}k\frac{U_{1n}}{C_0}\frac{\partial\phi}{\partial n}\right. \\
&\left. -2M\frac{U_{1n}}{C_0}\frac{\partial^2\phi}{\partial s\partial n}\right\} \\
&+ \mathcal{O}(\epsilon^2) = 0,
\end{aligned} \tag{3.6}$$

where $M = U_{0s}/C_0$, $\beta = \sqrt{1-M^2}$ and $k = \omega/C_0$. The hard wall boundary condition is written as

$$(\nabla\phi \cdot \mathbf{n}) = 0, \quad \text{at} \quad n = \pm h(S)/2, \tag{3.7}$$

where $\mathbf{n}$ is the outer normal unit vector to the respective wall (Figure 3.1b). This time, $\mathbf{n}^+$ is always aligned with $\mathbf{e}_n$, so only $\mathbf{n}^-$ is slightly misaligned. The description of the lower boundary (2.36) does not allow an exact closed-form solution of the misalignment between $\mathbf{n}^-$ and $\mathbf{e}_n$. However, it is still zero at $X = L_c$ and of the same order as ϵ at $X = 0$. This is shown in Figure 3.3, in which the relative alignment difference at $X = 0$, with ϵ as reference, is plotted against the camber angle for different solidity values. For realistic OGV camber angles and solidity values, the misalignment is about 1.5 times ϵ.

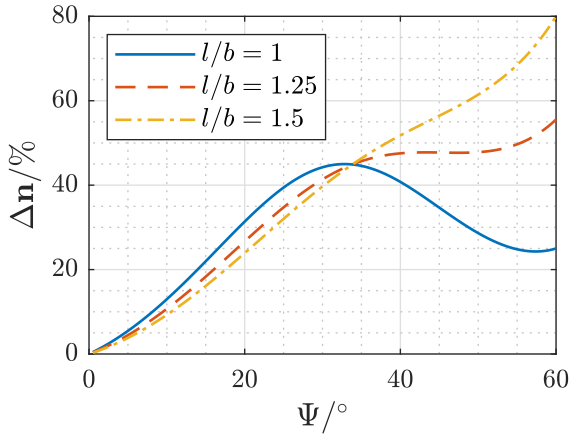

Figure 3.3: Evolution of the relative alignment difference $\Delta\mathbf{n}$, compared to ϵ, against the camber angle Ψ for different solidity values l/b.

WKB Expansion

Introducing the WKB ansatz

$$\phi(S,n) = \exp\left(-\frac{\mathrm{i}}{\epsilon}\int^S \mu(\xi)\,\mathrm{d}\xi\right)\sum_{m=0}^{\infty}\epsilon^m\Phi_m(S,n), \quad 0 \le S \le L_c, \quad -\frac{h(S)}{2} \le n \le \frac{h(S)}{2}, \tag{3.8}$$

where $\mu(S)$ is the axial wavenumber, the leading-order wave equation (3.6) reads

$$\frac{\partial^2\Phi_0}{\partial n^2} + \frac{1}{h_s}\frac{\mathrm{d}h_s}{\mathrm{d}n}\frac{\partial\Phi_0}{\partial n} + \left(\Lambda^2 - \frac{\mu^2}{h_s^2}\right)\Phi_0 = 0, \tag{3.9}$$

where

$$\Lambda = k - \mu M/h_s.$$

Since the misalignment of the normal unit vectors is $\mathcal{O}(\epsilon)$, the upper and lower boundaries can still be assumed parallel at leading order. The boundary condition at $n = \pm h(S)/2$ from (3.7) then reads

$$\left.\frac{\partial\Phi_0}{\partial n}\right|_{n=\pm h(S)/2} = 0. \tag{3.10}$$

Notice that, when $M = 0$, the leading-order equation (3.9) can be restated as a Bessel equation by a change of variable $\bar{n} = -(1-\kappa n)/\kappa$. The solution, in this case, is expressed by a sum of Bessel functions of the first and second kinds: $\mathrm{J}_{\mu/\kappa}\left(-k\left[1-\kappa n\right]/\kappa\right)$ and $\mathrm{Y}_{\mu/\kappa}\left(-k\left[1-\kappa n\right]/\kappa\right)$. The axial wavenumber μ is then defined at each location S by the algebraic equation resulting from the hard wall boundary condition at leading order (3.10). This solution is an extension of Krasnuskin's result [62] to slowly-varying ducts, by noticing that the curvature is negative here $\kappa = -1/\bar{R}_c$. However, this solution requires the use of Bessel functions of complex order that are not built-in functions in the Matlab environment. Thus, it requires some additional work to ensure a stable and accurate implementation that has not been finished during the PhD. Also note that, according to Wolfram Alpha [1], equation (3.9) has a general closed-form solution in presence of a uniform flow, $M \neq 0$, given by a combination of confluent

hypergeometric functions (see for example [85]). The validity of this solution with the boundary conditions in (3.10) has not been assessed though. This solution has not been investigated further during the PhD, but it could lead to a better understanding of the effects of the mean flow.

In this work, the choice was made to develop a numerical solution using the same procedure as in Ingenito [52] and Brambley & Peake [14], who used a pseudo-spectral method based on Chebyshev polynomials of the first kind. This method ensures fast and accurate computations that work with or without flow. Furthermore, the development of such a general solution could be of interest for future extensions in three dimensions, where no closed-form solutions exist even without flow (except for rectangular ducts).

For definiteness, the solution Φ_0 is normalized in the same way as in the previous chapter. It reads

$$\Phi_0(S,n) = N(S)\psi(S,n), \qquad \int_{-h(S)/2}^{h(S)/2} \psi^2(S,n)\,\mathrm{d}n = 1. \tag{3.11}$$

The unknown amplitude $N(S)$ is determined by means of a solvability condition instead of solving for the $\mathcal{O}(\epsilon)$ problem. From Brambley & Peake [14], the solution reads

$$N^2(S) = \frac{Q^2}{F(S)}, \tag{3.12}$$

where Q is a constant to be determined by a known value of $N(S)$ (typically at the inlet) and $F(S)$ is defined by

$$F(S) = \int_{-h(S)/2}^{h(S)/2} D_0\psi^2 \left(kM + \beta^2\frac{\mu}{h_s}\right)\,\mathrm{d}n. \tag{3.13}$$

When $\kappa \to 0$, the numerically solved axial wavenumber μ should tend to the analytical solution $\mu \to -kM/\beta^2 + k\sigma/\beta^2$. Thus, because of the normalization of ψ, $F(S) \to D_0(S)k(S)\sigma(S)$, which is the same result as in the straight channel (2.65). The solution from Brambley & Peake [14] is indeed a generalization of Rienstra's solution [107] to curved ducts.

The remaining unknowns are the eigenfunctions $\psi(S,n)$ (modal shapes) and their associated eigenvalues $\mu(S)$ (axial wavenumbers). They are solved numerically using a Chebyshev collocation method described in the following section.

Chebyshev Collocation Method

In order to formulate a linear eigenvalue problem (according to μ), an intermediate variable is introduced as $\bar{\psi} = \mu\beta^2\psi/h_s$. The system of equations then reads

$$\begin{bmatrix} 0 & h_s/\beta^2 \\ \mathcal{L} & -2kMh_s/\beta^2 \end{bmatrix} \begin{bmatrix} \psi \\ \bar{\psi} \end{bmatrix} = \mu \begin{bmatrix} \psi \\ \bar{\psi} \end{bmatrix}, \tag{3.14}$$

where

$$\mathcal{L} = h_s\frac{\partial^2}{\partial n^2} - \kappa\frac{\partial}{\partial n} + k^2h_s. \tag{3.15}$$

The first line gives the relation between ψ and $\bar{\psi}$ as $h_s\bar{\psi}/\beta^2 = \mu\psi$, whereas the second line is the actual mode shape equation (3.9).

Chebyshev polynomials are widely used to solve non-periodic partial differential equations due to their mathematical properties and exponential convergence (see for example [16] Chapter 2.4 for details). For $-1 \leq x \leq 1$, the Chebyshev polynomials of the first kind are defined by

$$T_m(x) = \cos(m\bar{x}), \quad \bar{x} = \arccos(x), \quad 0 \leq m \leq \infty,$$

which, given the normalization $T_m(1) = 1$, are the eigenfunctions of the singular Sturm-Liouville problem

$$\left(\sqrt{1-x^2}T_m'(x)\right)' + \frac{m^2}{\sqrt{1-x^2}}T_m(x) = 0,$$

where the prime symbol denotes the derivative with respect to x. The Chebyshev expansion of a function f, defined on the interval $[-1, 1]$, is

$$f(x) = \sum_{m=0}^{\infty} \hat{f}_m T_m(x), \quad \hat{f}_m = \frac{2}{\pi c_m}\int_{-1}^{1} f(x)T_m(x)(1-x^2)^{-1/2}\,\mathrm{d}x,$$

where $c_m = 2$, if $m = 0$, or 1, if $m \geq 1$. The discrete form of the Chebyshev polynomials is commonly described on the set of Gauss-Lobatto collocation points n_j, ranging from 1 to -1, given by

$$n_j = \cos\left(\frac{\pi j}{N}\right), \quad 0 \leq j \leq N.$$

Hence, the discrete Chebyshev polynomials of the first kind $T_{m,j}$ and the interpolated function f_j, on the collocation points n_j, are defined as

$$T_{m,j} = \cos\left(\frac{m\pi j}{N}\right), \quad f_j = \sum_{m=0}^{N} \hat{f}_m T_{m,j}.$$

The derivative of the interpolated function at the collocation points can simply be expressed by matrix multiplication, such that

$$f_j' = \sum_{l=0}^{N} (D_N)_{j,l} f_l,$$

where the entries of D_N are deduced from the derivative of the Chebyshev polynomials of the first kind (see [16] Chapter 2.4). This gives

$$(D_N)_{j,l} = \begin{cases} \dfrac{c_j}{c_l}\dfrac{(-1)^{j+l}}{n_j - n_l}, & \text{if} \quad j \neq l, \\ \dfrac{-n_l}{2(1-n_l^2)}, & \text{if} \quad 1 \leq j = l \leq N-1, \\ \dfrac{2N^2+1}{6}, & \text{if} \quad j = l = 0, \\ -\dfrac{2N^2+1}{6}, & \text{if} \quad j = l = N, \end{cases}$$

where

$$c_j = \begin{cases} 2, & \text{if} \quad j = 0,\, N, \\ 1, & \text{if} \quad 1 \leq j \leq N-1. \end{cases}$$

Then, The second derivative can be computed from the square of the matrix D_N. Finally, in order to account for the metric of the physical space, the collocation points n_j and the derivative matrix D_N are scaled by a factor $-h(S)/2$. This gives

$$n_j^* = \frac{-h(S)}{2} n_j, \quad (D_N^*)_{j,l} = \frac{-2}{h(S)} (D_N)_{j,l}, \quad \forall (j,l). \tag{3.16}$$

Each equation in (3.14) is described by a matrix in its discrete form. The boundary conditions are then applied through the first and last lines of each sub-matrix, which correspond to the boundary points. For the first equation, $h_s \bar{\psi}/\beta^2 = \mu\psi$, there is no need for boundary conditions. Hence, the first and last lines are discarded and the vector $\bar{\psi}$ is only evaluated on $N-1$ collocation points, i.e. the inner collocation points $1 \leq i \leq N-1$. For the second equation (the mode shape equation), the first and last lines are replaced by the boundary conditions (3.10) in discrete form, which read

$$\sum_{l=0}^{N} (D_N^*)_{j,l} \psi_l = 0, \quad j = 0,\, N.$$

The eigenvalue problem (3.14) is finally written in discrete form as

$$\begin{bmatrix} \underline{\mathbf{O}} & \underline{\mathbf{M_1}} \\ \underline{\mathcal{L}} & \underline{\mathbf{M_2}} \end{bmatrix} \begin{bmatrix} \psi \\ \bar{\psi} \end{bmatrix} = \underline{\boldsymbol{\mu}} \begin{bmatrix} \psi \\ \bar{\psi} \end{bmatrix}, \tag{3.17}$$

where

$$[O]_{i,l} = 0, \quad [M_1]_{i,i} = (1 - \kappa n_i^*)/\beta^2 \delta_{i,i}, \quad [\mu]_{i+j,l+i} = \mu \delta_{i+j,l+i},$$

$$[\mathcal{L}]_{j,l} = \begin{cases} (1-\kappa n_j^*)(D_N^{*2})_{j,l} - \kappa (D_N^*)_{j,l} + k^2 (1 - \kappa n_j^*), & \text{if} \quad 1 \leq j \leq N-1 \\ (D_N^*)_{j,l}, & \text{if} \quad j = 0,\, N, \end{cases}$$

$$[M_2]_{j,i} = \begin{cases} -2kM(1-\kappa n_j^*)/\beta^2 \delta_{j,i}, & \text{if} \quad 1 \leq j \leq N-1 \\ 0, & \text{if} \quad j = 0,\, N, \end{cases}$$

for $1 \leq i \leq N-1$ and $0 \leq l \leq N$. Notice that $\underline{\mathbf{O}}$ and $\underline{\mathbf{M_2}}$ are not square matrices, but the overall matrix is. The discrete eigenvalue problem (3.17) is solved at each location S by employing a built-in solver in Matlab using a QZ algorithm (*eig* function), which returns the desired eigenfunctions $\psi_l(S, n_j^*)$ and their associated eigenvalues $\mu_l(S)$.

In the following, the validity of the developed routine is assessed by investigating the behavior of the discrete solution in the limit of different parameters, where an analytical solution is known, and also at low frequency to see if the solution in a curved channel tends to the straight-channel solution.

3.1.4 Asymptotic Behavior

In the Limit of Small Curvature without Widening

The numerical solution is first tested in a curved duct of constant height, without flow ($M = 0$). The frequency of study is set at $kb = 4.725$ and the curvature varies from

$\kappa b = 0$ to $\kappa b \simeq -0.381$, which corresponds to values of Ψ ranging from 0° to 60° with a solidity of $l/b = 3$ for an OGV channel. When the curvature tends to 0, the expected eigenfunctions are cosine functions with eigenvalues $k_q = \sqrt{k^2 - (q\pi/b)^2}$, $0 \leq q < \infty$. Figure 3.4 displays the eigenfunctions ψ_0, ψ_1, ψ_2 and ψ_5 computed with the collocation algorithm (solid lines), for the different curvature values, and the corresponding cosine functions for $\kappa b = 0$ (black circles). The collocation algorithm is able to recover the

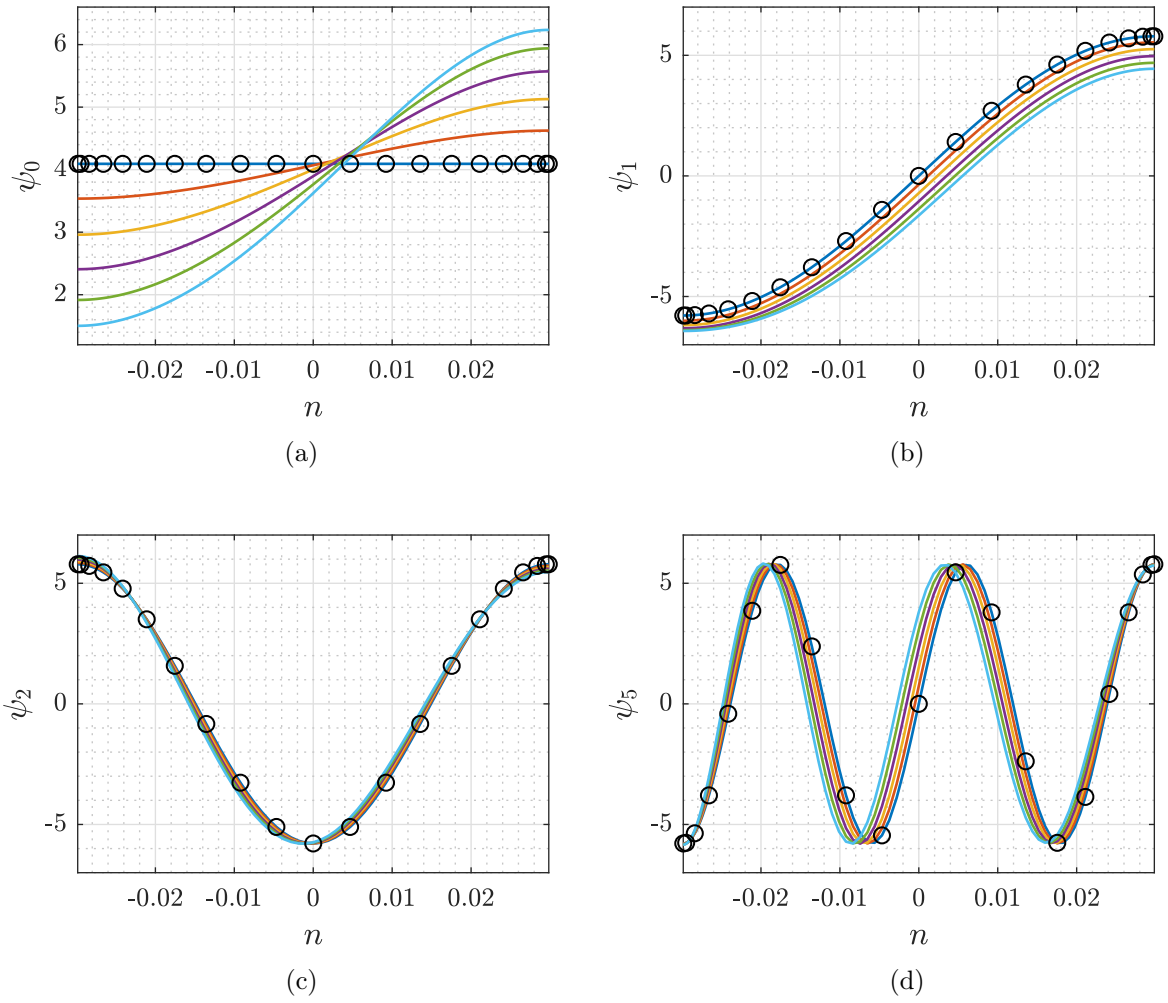

Figure 3.4: Eigenfunctions numerically computed for varying curvature values (solid lines) and the analytical cosine function for $\kappa b = 0$ (○).

analytical solution in the limit of small curvature in all cases. Then, the eigenvalues are compared in Figure 3.5. Here, the frequency has been increased to $kb = 11.219$ to have more cut-on modes. Figure 3.5 shows the evolution of the first four eigenvalues (of the downstream-propagating modes) with the curvature, computed numerically (solid lines). It starts at the cross mark ($\kappa b = 0$) and ends at the square mark ($\kappa b \simeq -0.381$). The analytical values for $\kappa b = 0$ are then added with black circles. Again, the agreement is perfect between the analytical and numerical solutions in the limit $\kappa b \to 0$.

It is also interesting to see the effects of curvature on sound propagation in an infinitely long duct. The plane-wave mode no longer exists (Figure 3.4a) and the energy of this zeroth-order mode tends to concentrate at the top of the curved channel. Some

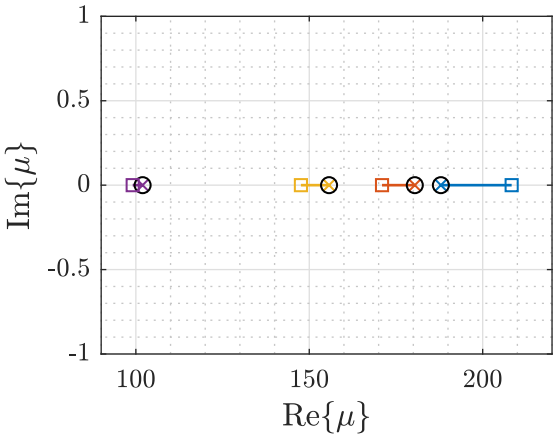

Figure 3.5: Eigenvalues of the first four (from right to left) downstream-propagating cut-on modes computed for varying curvature values. Cross marks at $\kappa b = 0$ and square marks at $\kappa b \simeq -0.381$, with the analytical solution added for $\kappa b = 0$ (○).

sort of contraction happens to the other eigenfunctions. The node[1] of the eigenfunction ψ_1 is shifted to the top, whereas the nodes of all higher-order modes are shifted to the bottom. Thus, the curvature makes the eigenfunctions asymmetric from the center of the duct. Concerning the wavenumbers, an increasing curvature increases the amplitude of μ_0 (in blue in Figure 3.5), but decreases the amplitude of all other cut-on modes $\mu_{l\neq 0}$. Though, changes in curvature alone cannot make a cut-on mode become cut-off. Getting closer to the cut-off frequency of a mode only reduces the impact the curvature has on its wavenumber.

In the Limit of Small Curvature and Small Widening

The collocation algorithm is now tested in a curved duct of slowly-varying height, still without flow ($M = 0$). The frequency of study is set at $kb = 4.725$ and the values of Ψ varies from $\Psi = 0°$ to $\Psi = 60°$, which implies curvature values ranging from $\kappa b = 0$ to $\kappa b \simeq -0.381$ and an expansion parameter ranging from $\epsilon = 0$ to $\epsilon = 0.33$ (for an equivalent OGV channel solidity value of $l/b = 3$). Figure 3.6 displays the eigenfunctions ψ_0, ψ_1, ψ_2 and ψ_5 computed with the collocation algorithm (solid lines), for the different camber angles, and the corresponding cosine functions for $\Psi = 0°$ (black circles). The eigenfunctions and eigenvalues are evaluated at the inlet of the duct. The eigenvalues are compared in Figure 3.7a for a frequency increased to $kb = 11.219$. Figure 3.7a shows the evolution of the first four eigenvalues (of the downstream-propagating modes) with the curvature and shrinkage, with the same notations as in Figure 3.5. Figure 3.7b is a zoom of Figure 3.7a on the first eigenvalue μ_0 to emphasize its particular behavior, starting by increasing up to the point marked by the left triangle, then decreasing for higher values of Ψ. The numerically computed eigenfunctions and eigenvalues perfectly match the analytical solutions in the limit of small curvature and expansion.

The eigenfunctions do not seem to behave differently with changes in cross-section. The differences between Figure 3.4 and Figure 3.6 are only due to the normalization being on the channel height. The eigenfunctions are the same in both cases if plotted

[1] value of n where $\psi(n) = 0$

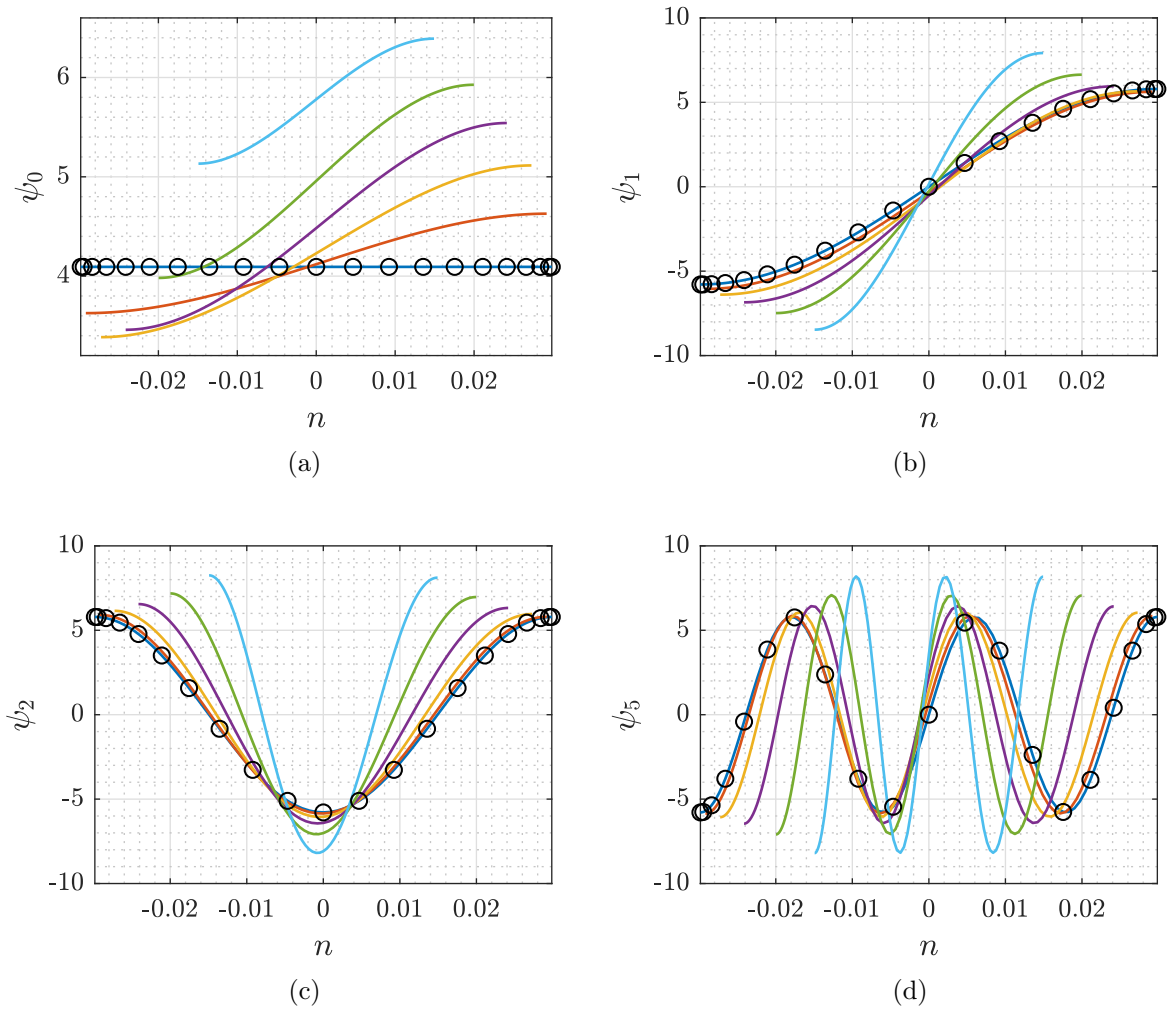

Figure 3.6: Eigenfunctions numerically computed for varying curvature and expansion values (solid lines) and the analytical cosine function for $\Psi = 0°$ (○).

against n/b, so they are only stretched with the cross-section expansion. In Figure 3.7, the eigenvalues $\mu_{l\neq 0}$ are affected similarly by the increasing curvature and the height reduction. This results in a faster decrease in amplitude than in Figure 3.5, where only the curvature was varying. The modes can also become cut-off due to the change of height inducing a change of the cut-off frequencies. The effects of a varying cut-off frequency along the duct are examined in detail in Chapter 4. For the zeroth-order mode wavenumber (μ_0), curvature and shrinkage have opposite effects. The curvature tends to increase its amplitude (as in Figure 3.5) while the shrinkage tends to reduce it. This leads to the presence of a turning point, marked with a left triangle in Figure 3.7b, for the evolution of μ_0 with Ψ.

In the Limit of Low Frequency

The collocation algorithm is tested in a fixed curved duct of slowly-varying height, without flow ($M = 0$), but this time for frequencies varying from $kb = \pi/10 \simeq 0.3142$ to $kb = 4\pi \simeq 12.57$. The parameters are set to $\Psi = 33.7°$ and $l/b = 1.5$, which implies a curvature of $\kappa b \simeq -0.47$ and an expansion parameter of $\epsilon \simeq 0.26$. Figure 3.8

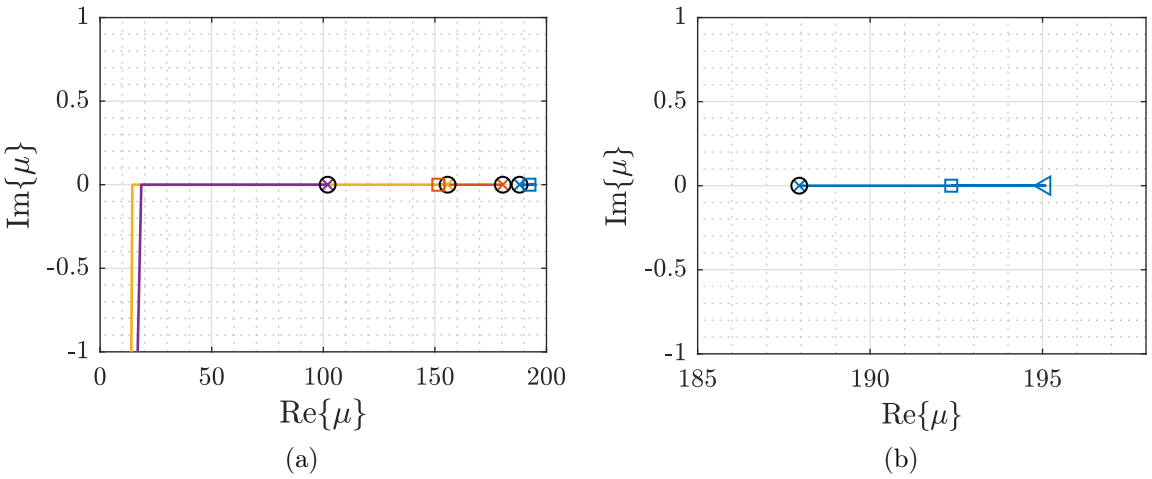

Figure 3.7: Eigenvalues of the first four (from right to left) downstream-propagating cut-on modes computed for varying curvature and expansion values (a) and zoom on the first eigenvalue (b). Cross marks at $\Psi = 0°$ and square marks at $\Psi = 60°$, with the analytical solution added for $\Psi = 0°$ (○).

displays the eigenfunctions ψ_0, ψ_1, ψ_2 and ψ_5 computed with the collocation algorithm (solid lines), for the different frequencies, and the corresponding cosine functions for an equivalent straight duct (black circles). The eigenfunctions and eigenvalues are evaluated at the inlet of the duct. The eigenvalues are plotted in the complex plane in Figure 3.9a, in the same manner as for the previous scenarios. A zoom on the first eigenvalue is also plotted in Figure 3.9b, around the lowest frequencies, to emphasize the difference between the numerically computed value and the analytical straight-channel approximation.

The effects of curvature on the zeroth-order mode eigenfunction are more and more significant as the frequency increases (Figure 3.8a). As could have been expected, this mode tends to a plane-wave mode at low frequency. Yet, none of the other eigenfunctions tends toward the straight-channel solution in the limit. This means that the capacity of the MMBW to accurately predict sound transmission in the low frequency scenario (section 2.4.2) is due to the zeroth-order mode being the only cut-on mode ($kb < \pi$). Discrepancies should be expected above the first channel cut-off frequency then ($kb > \pi$). Also, the eigenvalue μ_0 of the almost plane mode at low frequency is predicted with an error of 25% by the straight-channel value $\mu_0 = k$ (Figure 3.9b). Hence, the straight-channel approximation in the MMBW should be accurate as long as the channel length is small compared to the acoustic wavelength, as was also noticed by Roger & Moreau [119]. This could be estimated by the Helmholtz number $kl > kb$ for typical applications to OGV. If this number is small, an incident wave will propagate through the curved cascade without being significantly affected by it. Finally, it is seen from Figure 3.8 that the higher the mode order, the less sensitive the eigenfunction is to the frequency.

In the Limit of Small Mach Number

To conclude this series of asymptotic comparisons, the collocation algorithm is tested in a fixed curved duct of slowly-varying height, with varying Mach numbers. The

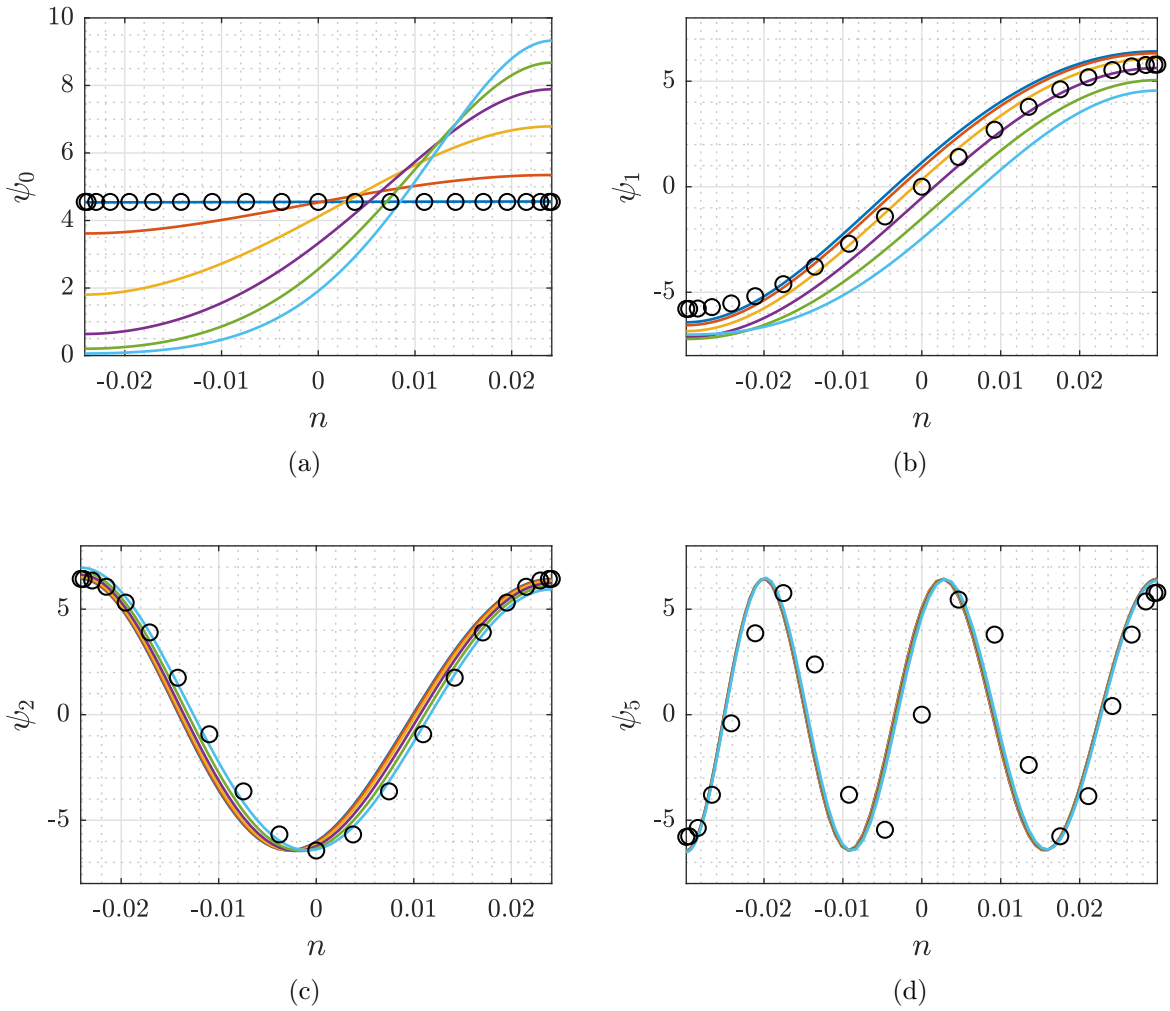

Figure 3.8: Eigenfunctions numerically computed for varying frequencies (solid lines) and the cosine function for an equivalent straight channel (○).

frequency is set at $kb = 4.725$ and the geometrical parameters to $\Psi = 33.7°$ and $l/b = 1.5$, which implies a curvature of $\kappa b \simeq -0.47$ and an expansion parameter of $\epsilon \simeq 0.26$. The incident Mach number ranges from $M = 0$ to $M = 0.5$ and evolves through the duct accounting for compressible effects (see section 3.1.2). Figure 3.10 depicts the eigenfunctions ψ_0, ψ_1, ψ_2 and ψ_5 computed with the collocation algorithm for the different incident Mach numbers. The eigenfunctions and eigenvalues are evaluated at the inlet of the duct.

Surprisingly, the Mach number only affects ψ_0 in this test case, using realistic OGV parameters. In the presence of a mean flow, the solution is described by a combination of confluent hypergeometric functions (from Wolfram Alpha [1]), but it appears that the eigenfunctions behavior remains close to Bessel functions. This argument could be useful if confluent hypergeometric functions are cumbersome to implement and use.

Concerning the eigenvalues (Figure 3.11), increasing the Mach number has the predicted outcome by adding an increasingly negative real part to each eigenvalue, and also reducing the imaginary part of the cut-off mode eigenvalues. However, a strange behavior is seen on the eigenvalue μ_4, which is cut-off for $M = 0$ and undergoes transition with the increase of the Mach number. For Mach numbers at which this mode is

cut-on, increasing the Mach number increases its real part, instead of decreasing it. It is possible that the leading-order equation (3.9) is not adequate to describe the evolution of the eigenvalue in the vicinity of its transition, and artificially causes the amplitude to increase because of missing higher-order mechanisms. In fact, this is known that the modes behavior changes too rapidly in such conditions for the leading-order slowly-varying equation to be accurate. This part is examined in detail in Chapter 4.

The validity of the collocation routine developed in Matlab has been assessed. It performs well for a variety of geometrical and flow parameters, as well as for low and high frequencies. The only limitation observed is due to the leading-order equation solved, which is unable to describe the rapid changes in the modes behavior in the vicinity of cut-on/cut-off transitions. The definition of the curved channel modes will be integrated into the mode-matching procedure in the next section.

Bent Channel of Slowly-Varying Cross-Section ——— Summary

The modeling of sound propagation in cambered inter-vane channels has been extended by taking into account curvature effects, thus relying on curvilinear coordinates instead of Cartesian coordinates to derive the equivalent convected Helmholtz equation. This equation, with hard wall boundary condition, has been rewritten as an eigenvalue problem, which has been solved numerically by means of a pseudo-spectral collocation method based on Chebyshev polynomials of the first kind. This two-dimensional problem has an exact closed-form solution in terms of Bessel functions without flow, and apparently in terms of confluent hypergeometric functions with flow, but the choice was made to rely on a collocation method. The numerical method ensures fast and accurate computations with or without flow. Furthermore, the development of such a general solution could be of interest for future extensions in three dimensions, where no closed-form solutions exist even without flow (except for rectangular ducts). However, the analytical solutions should be investigated to better understand the effects of curvature and mean flow.

The developed collocation routine has been validated by investigating its behavior in the limit of different parameters, where a simple analytical solution is known. The routine proved to be efficient and accurate. It was then used to shed light on the behavior of the eigenfunctions and eigenvalues of the slowly-varying curved duct for varying expansion, curvature, frequency and Mach number.

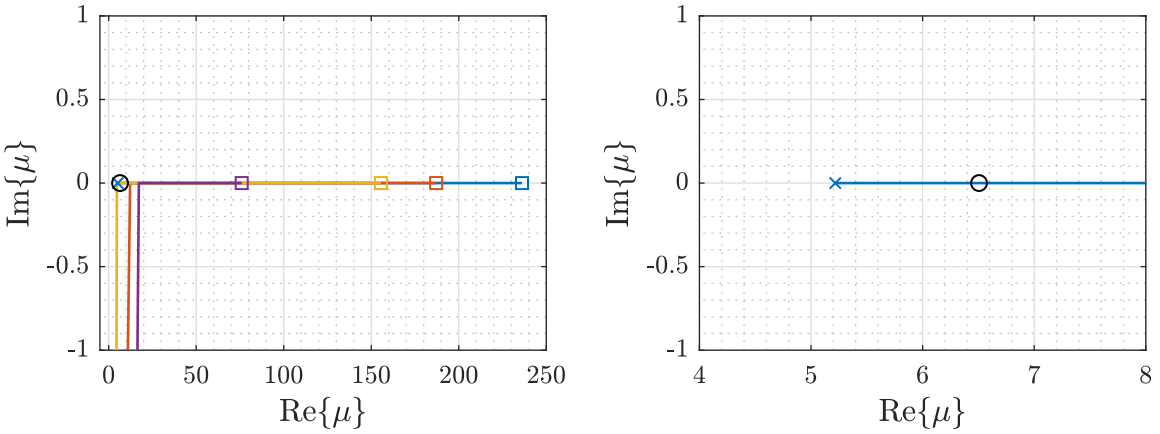

Figure 3.9: Eigenvalues of the first four (from right to left) downstream-propagating cut-on modes computed for varying frequencies (a) and zoom on the first eigenvalue (b). Cross marks at $kb = \pi/10$ and square marks at $kb = 4\pi$, with the approximate straight-channel solution added for $kb = \pi/10$ (○).

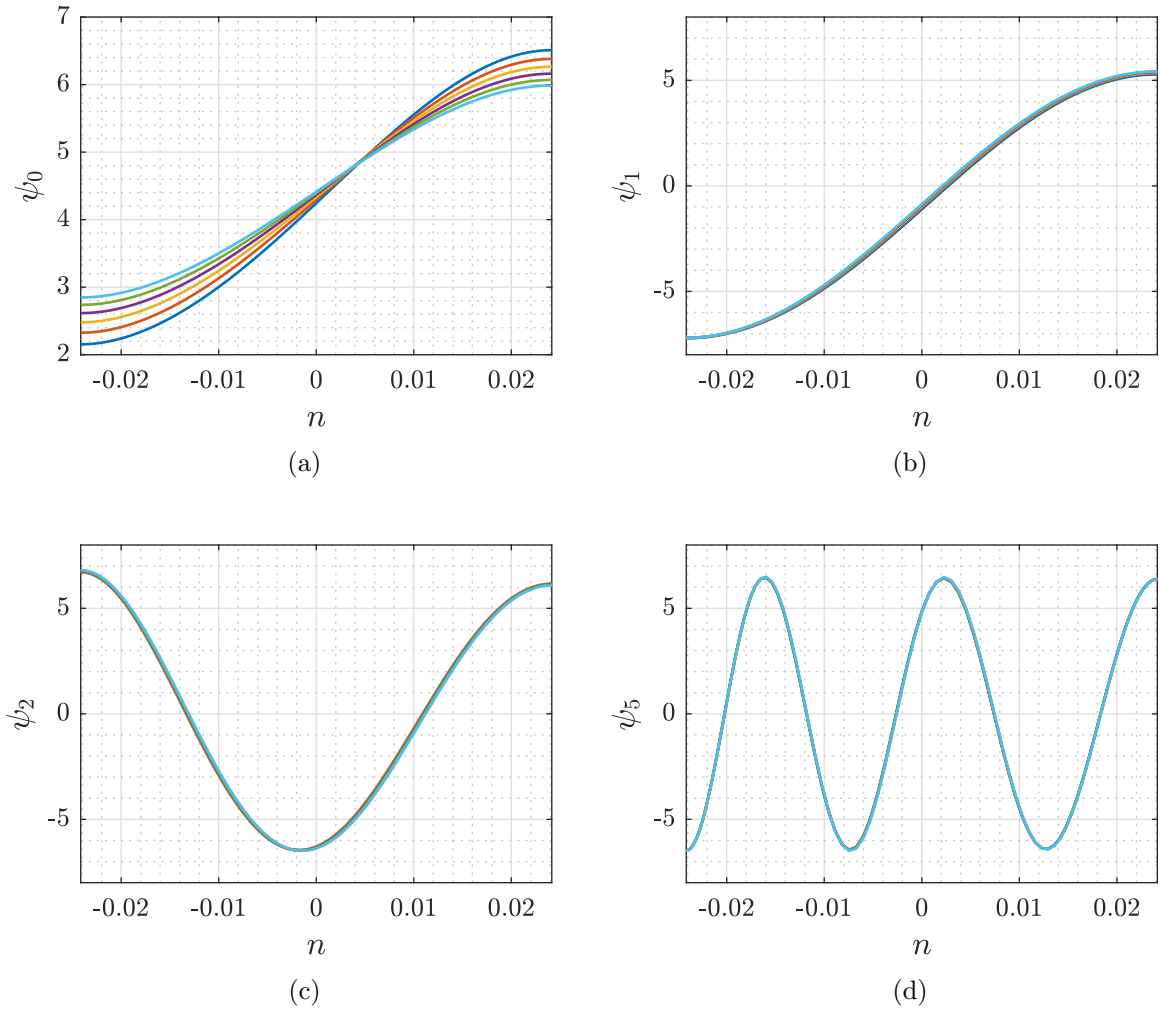

Figure 3.10: Eigenfunctions numerically computed for varying Mach numbers.

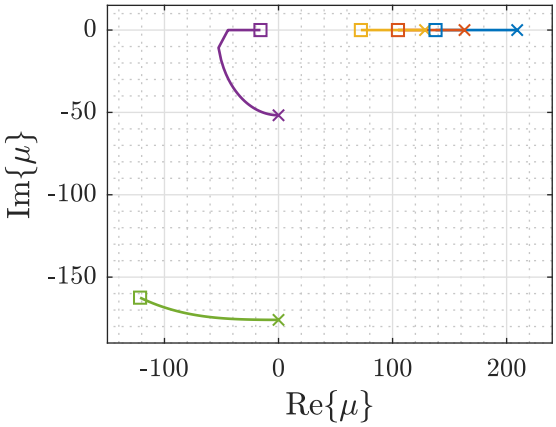

Figure 3.11: Eigenvalues of the first five downstream-propagating modes computed for varying Mach numbers. Cross marks at $M = 0$ and square marks at $M = 0.5$.

3.2 Mode-Matching Equations

3.2.1 Leading-Edge Interface

Only the propagation in the inter-vane channels, from section BC to the trailing-edge interface (Figure 3.12), is changed compared to the low frequency model of Chapter 2. Thus, no change is necessary in the jump conditions.

At the leading-edge interface, only the reflected channel potential ϕ_u, generated at the trailing-edge interface, has to be modified to account for the effects of curvature. To be able to compare the channel modal coefficients with and without accounting

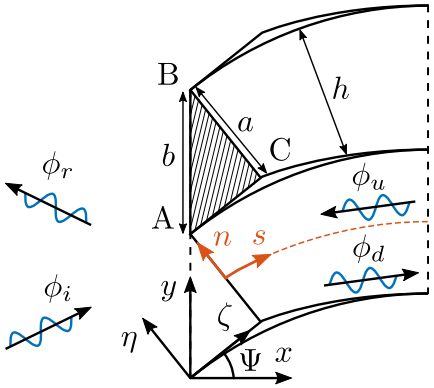

Figure 3.12: Scattering of an incident mode at the staggered leading-edge interface with feedback from the trailing-edge scattering.

for curvature, the modal coefficients will always be those associated to cosine modes. Hence, considering a cosine mode $\phi_{u,q}$ generated at the trailing-edge interface, it is expanded in curved-channel modes ψ_l, such that

$$\phi_{u,q}(L_c, n) = B_q \sum_{l=0}^{\infty} \mathcal{B}_l^q(L_c)\psi_l(L_c, n),$$

where the projection coefficients $\mathcal{B}_l^q(S)$ are defined such that

$$\cos\left(\frac{q\pi}{h(S)}\left[n - \frac{h(S)}{2}\right]\right) = \sum_{l=0}^{\infty} \mathcal{B}_l^q(S)\psi_l(S, n), \quad 0 \leq S \leq L_c, \quad -\frac{h(S)}{2} \leq n \leq \frac{h(S)}{2}. \tag{3.18}$$

The propagation of each of these curved-channel modes, from the trailing-edge interface to the interface BC, is then given by the stream-wise variation function Υ_l^-, defined by

$$\Upsilon_l^-(S) = \sqrt{\frac{F_l^-(L_c)}{F_l^-(S)}} \exp\left(\frac{\mathrm{i}}{\epsilon}\int_{L_c}^{S} \mu_l^-(\xi)\,\mathrm{d}\xi\right), \quad 0 \leq S \leq L_c, \tag{3.19}$$

where F_l^- is identical to the function F defined in (3.13) for the upstream-propagating mode of order l. Finally, each of the curved-channel modes has to be expanded back

to cosine modes at the interface BC, thus

$$\phi_{u,q}(0,n) = B_q \sum_{l=0}^{\infty} \mathcal{B}_l^q(L_c)\Upsilon_l^-(0) \sum_{q^*=0}^{\infty} \mathcal{A}_{q^*}^l(0) \cos\left(\frac{q^*\pi}{a}\left[n - \frac{a}{2}\right]\right),$$

where the projection coefficients $\mathcal{A}_{q^*}^l(S)$ are defined by

$$\psi_l(S,n) = \sum_{q^*=0}^{\infty} \mathcal{A}_{q^*}^l(S) \cos\left(\frac{q\pi}{h(S)}\left[n - \frac{h(S)}{2}\right]\right), \quad 0 \leq S \leq L_c, \quad -\frac{h(S)}{2} \leq n \leq \frac{h(S)}{2}. \tag{3.20}$$

This ensures the continuity of the potential at the interface BC, neglecting any scattering and reflection at this interface. This assumption is based on the relatively low dimensionless curvature and angular length of the inter-vane channels (respectively about 0.5 from Figure 3.2 and 30°) compared to those of the bent ducts studied in, for example, Félix & Pagneux [30], which are respectively about 8 and 150° and give a reflection coefficient lower than 15%. If scattering and reflection at the interface BC become significant, Green's reciprocity theorem could be used instead of the modal approximation in the triangle ABC, as in Roger & François [116]. Finally, the potential ϕ_u is expressed in the triangle ABC as

$$\phi_u(\zeta,\eta) = \sum_{q=0}^{\infty} B_q \sum_{l=0}^{\infty} \mathcal{B}_l^q(L_c)\Upsilon_l^-(0) \sum_{q^*=0}^{\infty} \mathcal{A}_{q^*}^l(0) \cos\left(\frac{q^*\pi}{a}\eta\right) \mathrm{e}^{\mathrm{i}k_{q^*}^-(\xi - a\tan\Psi)}, \tag{3.21}$$

for $\eta\tan\Psi \leq \zeta \leq a\tan\Psi$ and $0 \leq \eta \leq a$. The other potentials are reminded hereafter for the sake of clarity.

$$\phi_i(x,y) = \mathrm{e}^{\mathrm{i}\alpha_j y}\mathrm{e}^{\mathrm{i}k_j^+ x}, \quad -\infty < x \leq 0, \quad 0 \leq y < 2\pi R,$$

$$\phi_r(x,y) = \sum_{p=-\infty}^{\infty} R_p \mathrm{e}^{\mathrm{i}\alpha_p y}\mathrm{e}^{\mathrm{i}k_p^- x}, \quad -\infty < x \leq 0, \quad 0 \leq y < 2\pi R,$$

$$\phi_d(\zeta,\eta) = \sum_{q=0}^{\infty} A_q \cos\left(\frac{q\pi}{a}\eta\right) \mathrm{e}^{\mathrm{i}k_q^+\zeta}, \quad \eta\tan\Psi \leq \zeta \leq a\tan\Psi, \quad 0 \leq \eta \leq a.$$

Using the same projection on the annular modal basis (2.13), as previously, leads to the potential continuity

$$\boxed{\sum_{q=0}^{\infty}\left[A_q\mathfrak{I}_{q,\nu}^+ + B_q\sum_{l=0}^{\infty}\mathcal{B}_l^q(L_c)\Upsilon_l^-(0)\sum_{q^*=0}^{\infty}\mathcal{A}_{q^*}^l(0)\mathrm{e}^{-\mathrm{i}k_{q^*}^- b\sin\Psi}\mathfrak{I}_{q^*,\nu}^-\right] = b\left(R_\nu + \delta_{\nu,0}\right)}, \tag{3.22}$$

and the modified acoustic velocity $(\beta_x^2 u_x - M_x M_y u_y)$ continuity

$$\boxed{\begin{aligned}\sum_{q=0}^{\infty}\Bigg[A_q\mathcal{K}_{q,\nu}^+\mathfrak{I}_{q,\nu}^+ + B_q\sum_{l=0}^{\infty}\mathcal{B}_l^q(L_c)\Upsilon_l^-(0)\sum_{q^*=0}^{\infty}\mathcal{A}_{q^*}^l(0)\mathrm{e}^{-\mathrm{i}k_{q^*}^- b\sin\Psi}\ \mathcal{K}_{q^*,\nu}^-\mathfrak{I}_{q^*,\nu}^-\Bigg] \\ = b\left(\mathcal{K}_\nu^- R_\nu + \mathcal{K}_j^+\delta_{\nu,0}\right)\end{aligned}}. \tag{3.23}$$

Combining equations (3.22) and (3.23) to cancel out the unknown R_ν coefficients yields

$$\begin{aligned}\sum_{q=0}^{\infty} A_q \left(\mathcal{K}_\nu^- - \mathcal{K}_{q,\nu}^+\right) \mathfrak{I}_{q,\nu}^+ &= b\left(\mathcal{K}_\nu^- - \mathcal{K}_j^+\right)\delta_{\nu,0} \\ &- \sum_{q=0}^{\infty} B_q \sum_{l=0}^{\infty} \mathcal{B}_l^q(L_c)\Upsilon_l^-(0) \sum_{q^*=0}^{\infty} \mathcal{A}_{q^*}^l(0)\left(\mathcal{K}_\nu^- - \mathcal{K}_{q^*,\nu}^-\right) \mathrm{e}^{-\mathrm{i}k_{q^*}^- b\sin\Psi}\mathfrak{I}_{q^*,\nu}^-.\end{aligned} \tag{3.24}$$

After a modal truncation ($\nu \in [-(N_\nu-1)/2, (N_\nu-1)/2]$ and $q \in [0, N_q-1]$), the system of equations at the leading-edge interface reads

$$\underline{\mathbf{M^1}}\mathbf{A} = \mathbf{M_i}, \tag{3.25}$$

where

$$\left[M^1\right]_{\nu,q} = \left(\mathcal{K}_\nu^- - \mathcal{K}_{q,\nu}^+\right)\mathfrak{I}_{q,\nu}^+, \quad [A]_{q,1} = A_q,$$

$$\begin{aligned}[M_i]_{\nu,1} = b\left(\mathcal{K}_\nu^- - \mathcal{K}_j^+\right)\delta_{\nu,0} &- \sum_{q=0}^{\infty} B_q \sum_{l=0}^{\infty} \mathcal{B}_l^q(L_c)\Upsilon_l^-(0) \\ &\times \sum_{q^*=0}^{\infty} \mathcal{A}_{q^*}^l(0)\left(\mathcal{K}_\nu^- - \mathcal{K}_{q^*,\nu}^-\right)\mathrm{e}^{-\mathrm{i}k_{q^*}^- b\sin\Psi}\mathfrak{I}_{q^*,\nu}^-.\end{aligned}$$

This is solved with the knowledge of the B_q coefficients from the previous iteration of trailing-edge matching. Then, the R_ν coefficients are deduced from either (3.22) or (3.23).

The global system of equations at the leading-edge interface is

$$\begin{pmatrix} \mathbf{E_1^1} & \mathbf{F_1^1} \\ \underline{\mathbf{E_2^1}} & \underline{\mathbf{F_2^1}} \end{pmatrix} \begin{pmatrix} \mathbf{A} \\ \mathbf{R} \end{pmatrix} = \begin{pmatrix} \mathbf{H_1^1} \\ \mathbf{H_2^1} \end{pmatrix}, \tag{3.26}$$

where

$$\left[E_1^1\right]_{\nu,q} = \mathfrak{I}_{q,\nu}^+, \quad \left[F_1^1\right]_{\nu,\nu} = -b\delta_{\nu,\nu},$$

$$\left[H_1^1\right]_{\nu,1} = b\delta_{\nu,0} - \sum_{q=0}^{\infty} B_q \sum_{l=0}^{\infty} \mathcal{B}_l^q(L_c)\Upsilon_l^-(0) \sum_{q^*=0}^{\infty} \mathcal{A}_{q^*}^l(0)\mathrm{e}^{-\mathrm{i}k_{q^*}^- b\sin\Psi}\mathfrak{I}_{q^*,\nu}^-,$$

$$\left[E_2^1\right]_{\nu,q} = \mathcal{K}_{q,\nu}^+\mathfrak{I}_{q,\nu}^+, \quad \left[F_2^1\right]_{\nu,\nu} = -b\mathcal{K}_\nu^-\delta_{\nu,\nu},$$

$$\left[H_2^1\right]_{\nu,1} = b\mathcal{K}_j^+\delta_{\nu,0} - \sum_{q=0}^{\infty} B_q \sum_{l=0}^{\infty} \mathcal{B}_l^q(L_c)\Upsilon_l^-(0) \sum_{q^*=0}^{\infty} \mathcal{A}_{q^*}^l(0)\mathrm{e}^{-\mathrm{i}k_{q^*}^- b\sin\Psi}\mathcal{K}_{q^*,\nu}^-\mathfrak{I}_{q^*,\nu}^-,$$

$$[A]_{q,1} = A_q, \quad [R]_{\nu,1} = R_\nu.$$

3.2.2 Trailing-Edge Interface

The trailing-edge matching now involves the curved channel potentials ϕ_d and ϕ_u, which need to be matched with the transmitted potential ϕ_t as represented in Figure 3.13. The coefficients B_q of the upstream-propagating modes $\phi_{u,q}$ have been associated to cosine modes generated at the trailing-edge interface. Hence, the related potential is

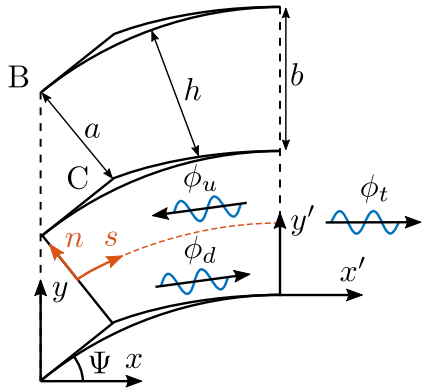

Figure 3.13: Scattering of a downstream-propagating channel mode at the trailing-edge interface.

given by

$$\phi_u(S,n) = \sum_{q=0}^{\infty} B_q \sum_{l=0}^{\infty} \mathcal{B}_l^q(L_c)\Upsilon_l^-(S) \sum_{q^*=0}^{\infty} \mathcal{A}_{q^*}^l(S) \cos\left(\frac{q^*\pi}{h(S)}\left[n - \frac{h(S)}{2}\right]\right), \tag{3.27}$$

for $0 \leq S \leq L_c$ and $-h(S)/2 \leq n \leq h(S)/2$. From (3.18), (3.19) and (3.20), this expression of the potential ϕ_u at the trailing-edge interface reduces to

$$\phi_u(L_c, y') = \sum_{q=0}^{\infty} B_q \cos\left(\frac{q\pi}{b} y'\right).$$

Following the same procedure for the downstream-propagating modes $\phi_{d,q}$, their coefficients A_q are associated to cosine modes generated at the leading-edge interface. After an expansion on the curved-channel modes at the interface BC, and introducing the stream-wise variation function Υ_l^+ as

$$\Upsilon_l^+(S) = \sqrt{\frac{F_l^+(0)}{F_l^+(S)}} \exp\left(\frac{\mathrm{i}}{\epsilon}\int_0^S \mu_l^+(\xi)\,\mathrm{d}\xi\right), \quad 0 \leq S \leq L_c, \tag{3.28}$$

the related potential reads

$$\phi_d(S,n) = \sum_{q=0}^{\infty} A_q \mathrm{e}^{\mathrm{i}k_q^+ a\tan\Psi} \sum_{l=0}^{\infty} \mathcal{B}_l^q(0)\Upsilon_l^+(S) \sum_{q^*=0}^{\infty} \mathcal{A}_{q^*}^l(S) \cos\left(\frac{q^*\pi}{h(S)}\left[n - \frac{h(S)}{2}\right]\right), \tag{3.29}$$

for $0 \leq S \leq L_c$, $-h(S)/2 \leq n \leq h(S)/2$. Thus, it is given at the trailing-edge interface by

$$\phi_d(L_c, y') = \sum_{q=0}^{\infty} A_q \mathrm{e}^{\mathrm{i}k_q^+ a\tan\Psi} \sum_{l=0}^{\infty} \mathcal{B}_l^q(0)\Upsilon_l^+(L_c) \sum_{q^*=0}^{\infty} \mathcal{A}_{q^*}^l(L_c) \cos\left(\frac{q^*\pi}{b} y'\right).$$

As a reminder, the transmitted potential ϕ_t is expressed as

$$\phi_t(x', y') = \sum_{p=-\infty}^{\infty} T_p \mathrm{e}^{\mathrm{i}\alpha_p y'} \mathrm{e}^{\mathrm{i}k_p^+ x'}, \quad 0 \leq x' < \infty, \quad 0 \leq y' < 2\pi R.$$

Projecting on the annular modal basis, as in (2.13), leads to the potential continuity

$$\boxed{\sum_{q=0}^{\infty}\left[B_q\mathfrak{I}^0_{q,\nu}+A_q\mathrm{e}^{\mathrm{i}k_q^+ a\tan\Psi}\sum_{l=0}^{\infty}\mathcal{B}_l^q(0)\Upsilon_l^+(L_c)\sum_{q^*=0}^{\infty}\mathcal{A}_{q^*}^l(L_c)\mathfrak{I}^0_{q^*,\nu}\right]=bT_\nu}. \tag{3.30}$$

As for the slowly-varying straight channel, the leading-order variations of the potentials along the channel are given by the exponential term in $\Upsilon^{\pm}$ (see 2.3.3). The axial velocity of the curved channel modes is then defined as

$$\frac{\partial\phi_u}{\partial s}(S,n)=\mathrm{i}\sum_{q=0}^{\infty}B_q\sum_{l=0}^{\infty}\mathcal{B}_l^q(L_c)\frac{\mu_l^-(S)}{h_s(n)}\Upsilon_l^-(S)\psi_l(S,n)+\mathcal{O}(\epsilon),$$

and

$$\frac{\partial\phi_d}{\partial s}(S,n)=\mathrm{i}\sum_{q=0}^{\infty}A_q\mathrm{e}^{\mathrm{i}k_q^+ a\tan\Psi}\sum_{l=0}^{\infty}\mathcal{B}_l^q(0)\frac{\mu_l^+(S)}{h_s(n)}\Upsilon_l^+(S)\psi_l(S,n)+\mathcal{O}(\epsilon).$$

Thus, a new projection is needed to expand the eigenfunctions $\psi_l(S,n)/h_s(n)$ into cosine functions. This is defined by

$$\frac{\psi_l(S,n)}{h_s(n)}=\sum_{q^*=0}^{\infty}\tilde{\mathcal{A}}_{q^*}^l(S)\cos\left(\frac{q\pi}{h(S)}\left[n-\frac{h(S)}{2}\right]\right),\quad 0\le S\le L_c,\quad -\frac{h(S)}{2}\le n\le\frac{h(S)}{2}. \tag{3.31}$$

Finally, the axial velocity continuity at the trailing-edge interface reads

$$\boxed{\sum_{q=0}^{\infty}\sum_{l=0}^{\infty}\sum_{q^*=0}^{\infty}\left[B_q\mathcal{B}_l^q(L_c)\mu_l^-(L_c)+A_q\mathrm{e}^{\mathrm{i}k_q^+ a\tan\Psi}\mathcal{B}_l^q(0)\mu_l^+(L_c)\Upsilon_l^+(L_c)\right]\tilde{\mathcal{A}}_{q^*}^l(L_c)\mathfrak{I}^0_{q^*,\nu}=bk_\nu^+T_\nu}. \tag{3.32}$$

Combining equations (3.30) and (3.32) to cancel out the unknown T_ν coefficients yields

$$\begin{aligned}\sum_{q=0}^{\infty}\sum_{l=0}^{\infty}\sum_{q^*=0}^{\infty}B_q\mathcal{B}_l^q(L_c)\left[k_\nu^+\mathcal{A}_{q^*}^l(L_c)-\mu_l^-(L_c)\tilde{\mathcal{A}}_{q^*}^l(L_c)\right]\mathfrak{I}^0_{q^*,\nu}=\\ -\sum_{q=0}^{\infty}\sum_{l=0}^{\infty}\sum_{q^*=0}^{\infty}A_q\mathrm{e}^{\mathrm{i}k_q^+ a\tan\Psi}\mathcal{B}_l^q(0)\Upsilon_l^+(L_c)\left[k_\nu^+\mathcal{A}_{q^*}^l(L_c)-\mu_l^+(L_c)\tilde{\mathcal{A}}_{q^*}^l(L_c)\right]\mathfrak{I}^0_{q^*,\nu}.\end{aligned} \tag{3.33}$$

The modal truncation ($\nu\in[-(N_\nu-1)/2,(N_\nu-1)/2]$ and $q\in[0,N_q-1]$) allows one to numerically compute the B_q coefficients from the linear system of equations

$$\underline{\mathbf{M}}^{\mathbf{2}}\mathbf{B}=\mathbf{M_d}, \tag{3.34}$$

where

$$\left[M^2\right]_{\nu,q}=\sum_{l=0}^{\infty}\sum_{q^*=0}^{\infty}\mathcal{B}_l^q(L_c)\left[k_\nu^+\mathcal{A}_{q^*}^l(L_c)-\mu_l^-(L_c)\tilde{\mathcal{A}}_{q^*}^l(L_c)\right]\mathfrak{I}^0_{q^*,\nu},$$

$$[M_d]_{\nu,1} = \sum_{q=0}^{\infty}\sum_{l=0}^{\infty}\sum_{q^*=0}^{\infty} A_q \mathrm{e}^{\mathrm{i}k_q^+ a\tan\Psi}\mathcal{B}_l^q(0)\Upsilon_l^+(L_c)\left[\mu_l^+(L_c)\tilde{\mathcal{A}}_{q^*}^l(L_c) - k_\nu^+\mathcal{A}_{q^*}^l(L_c)\right]\mathfrak{I}_{q^*,\nu}^0,$$

$$[B]_{q,1} = B_q.$$

The continuity equation (3.30) or (3.32) can then be used to deduce the T_ν coefficients.

Finally, the general matrix equation for this interface is

$$\begin{pmatrix} \mathbf{E_1^2} & \mathbf{F_1^2} \\ \underline{\mathbf{E_2^2}} & \underline{\mathbf{F_2^2}} \end{pmatrix}\begin{pmatrix} \mathbf{B} \\ \mathbf{T} \end{pmatrix} = \begin{pmatrix} \mathbf{H_1^2} \\ \mathbf{H_2^2} \end{pmatrix}, \tag{3.35}$$

where

$$\left[E_1^2\right]_{\nu,q} = \mathfrak{I}_{q,\nu}^0, \quad \left[F_1^2\right]_{\nu,\nu} = -b\delta_{\nu,\nu},$$

$$\left[H_1^2\right]_{\nu,1} = -\sum_{q=0}^{\infty} A_q \mathrm{e}^{\mathrm{i}k_q^+ a\tan\Psi}\sum_{l=0}^{\infty}\mathcal{B}_l^q(0)\Upsilon_l^+(L_c)\sum_{q^*=0}^{\infty}\mathcal{A}_{q^*}^l(L_c)\mathfrak{I}_{q^*,\nu}^0,$$

$$\left[E_2^2\right]_{\nu,q} = \sum_{l=0}^{\infty}\mathcal{B}_l^q(L_c)\mu_l^-(L_c)\sum_{q^*=0}^{\infty}\tilde{\mathcal{A}}_{q^*}^l(L_c)\mathfrak{I}_{q^*,\nu}^0, \quad \left[F_2^2\right]_{\nu,\nu} = -bk_\nu^+\delta_{\nu,\nu},$$

$$\left[H_2^2\right]_{\nu,1} = -\sum_{q=0}^{\infty} A_q \mathrm{e}^{\mathrm{i}k_q^+ a\tan\Psi}\sum_{l=0}^{\infty}\mathcal{B}_l^q(0)\mu_l^+(L_c)\Upsilon_l^+(L_c)\sum_{q^*=0}^{\infty}\tilde{\mathcal{A}}_{q^*}^l(L_c)\mathfrak{I}_{q^*,\nu}^0,$$

$$[B]_{q,1} = A_q, \quad [T]_{\nu,1} = R_\nu.$$

3.2.3 Implementation of a Kutta Condition

In the presence of an inviscid mean flow, a Kutta condition is needed on the fluctuating variables. This condition enforces a finite velocity at the trailing edges, allowing to indirectly account for some viscous effects within an inviscid flow. The Kutta condition has a significant influence on the acoustic field, as was pointed out by many authors (e.g. Jones [57], Rienstra [104], Howe [49] and Job [56]). According to Rienstra [104], this condition is equivalently expressed by enforcing a zero pressure jump at the trailing edge of the vanes. This has for consequence the generation of a vortex shedding from the edges, which is modeled by infinitely thin vortical sheets convected at the speed of the mean flow (Howe [49]). This adds a vortical velocity field $\mathbf{u}_K^R$ downstream of the vanes, that has to be accounted for in the matching equations. The new problem to solve at the trailing-edge interface is depicted in Figure 3.14.

The zero pressure jump at the trailing edge, between a reference channel (p^0) and

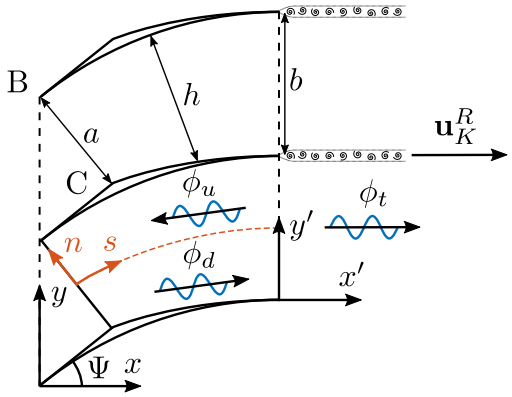

Figure 3.14: Scattering of a downstream-propagating channel mode at the trailing-edge interface with infinitely thin vorticity sheets induced by the Kutta condition.

the channel below (p^{-1}), is derived as

$$
\begin{aligned}
&p^{-1}(S=L_c, n=b/2) = p^{0}(S=L_c, n=-b/2),\\
\Leftrightarrow &\sum_{q=0}^{\infty}\sum_{l=0}^{\infty}\sum_{q^*=0}^{\infty}\Big[A_q \mathrm{e}^{\mathrm{i}k_q^+ a\tan\Psi}\mathcal{B}_l^q(0)\Upsilon_l^+\left(k\mathcal{A}_{q^*}^l(L_c) - M\mu_l^+\tilde{\mathcal{A}}_{q^*}^l(L_c)\right)\\
&\qquad + B_q\mathcal{B}_l^q(L_c)\left(k\mathcal{A}_{q^*}^l(L_c) - M\mu_l^-\tilde{\mathcal{A}}_{q^*}^l(L_c)\right)\Big]\cos(q^*\pi)\mathrm{e}^{-\mathrm{i}\alpha_j b}\\
= &\sum_{q=0}^{\infty}\sum_{l=0}^{\infty}\sum_{q^*=0}^{\infty}\Big[A_q \mathrm{e}^{\mathrm{i}k_q^+ a\tan\Psi}\mathcal{B}_l^q(0)\Upsilon_l^+\left(k\mathcal{A}_{q^*}^l(L_c) - M\mu_l^+\tilde{\mathcal{A}}_{q^*}^l(L_c)\right)\\
&\qquad + B_q\mathcal{B}_l^q(L_c)\left(k\mathcal{A}_{q^*}^l(L_c) - M\mu_l^-\tilde{\mathcal{A}}_{q^*}^l(L_c)\right)\Big],
\end{aligned}
$$

which can be rewritten as

$$
\boxed{
\begin{aligned}
&\sum_{q=0}^{\infty}\sum_{l=0}^{\infty}\sum_{q^*=0}^{\infty} A_q \mathrm{e}^{\mathrm{i}k_q^+ a\tan\Psi}\mathcal{B}_l^q(0)\Upsilon_l^+\left(k\mathcal{A}_{q^*}^l(L_c) - M\mu_l^+\tilde{\mathcal{A}}_{q^*}^l(L_c)\right)\left(1-(-1)^{q^*}\mathrm{e}^{-\mathrm{i}\alpha_j b}\right)\\
&= -\sum_{q=0}^{\infty}\sum_{l=0}^{\infty}\sum_{q^*=0}^{\infty} B_q\mathcal{B}_l^q(L_c)\left(k\mathcal{A}_{q^*}^l(L_c) - M\mu_l^-\tilde{\mathcal{A}}_{q^*}^l(L_c)\right)\left(1-(-1)^{q^*}\mathrm{e}^{-\mathrm{i}\alpha_j b}\right)
\end{aligned}
}
\tag{3.36}
$$

The vortical sheets are defined by a velocity field $\mathbf{u}_K^R$. Since the vanes are locally aligned with the turbomachinery axis at the trailing edge, the vortical sheets are the same as for unstaggered flat vanes. Hence, the velocity field $\mathbf{u}_K^R$ is described from Bouley et al. [12] as

$$
\mathbf{u}_K^R(x',y') = \sum_{p=-\infty}^{\infty}\mathbf{U}_p^R \mathrm{e}^{\mathrm{i}\alpha_p y'}\mathrm{e}^{\mathrm{i}(k/M)x'}, \quad 0\le x'<\infty, \quad 0\le y'<2\pi R, \tag{3.37}
$$

$$
\mathbf{U}_p^R = \frac{\mathrm{i}\Omega_K}{b}\frac{[\alpha_p\mathbf{e}_x - (k/M)\mathbf{e}_y]}{\alpha_p^2 + (k/M)^2}, \tag{3.38}
$$

where Ω_K is the unknown amplitude of the associated vortical field. Due to the presence of the vortical field, the total velocity field is not potential anymore downstream of the OGV. Thus, the continuity of the fluctuating velocity potential ϕ no longer enforces

the continuity of the total enthalpy (1.17). The trailing-edge matching equations with a Kutta condition are then expressed on the set of variables (p, u_x). The velocity field $\mathbf{u}_K^R$ being pressure-free, the continuity of the fluctuating pressure p is given by

$$\boxed{\sum_{q=0}^{\infty}\sum_{l=0}^{\infty}\sum_{q^*=0}^{\infty}\Big[A_q\mathrm{e}^{\mathrm{i}k_q^+ a\tan\Psi}\mathcal{B}_l^q(0)\Upsilon_l^+\left(k\mathcal{A}_{q^*}^l(L_c)-M\mu_l^+\tilde{\mathcal{A}}_{q^*}^l(L_c)\right) +B_q\mathcal{B}_l^q(L_c)\left(k\mathcal{A}_{q^*}^l(L_c)-M\mu_l^-\tilde{\mathcal{A}}_{q^*}^l(L_c)\right)\Big]\mathfrak{I}_{q^*,\nu}^0 = b(k-Mk_\nu^+)T_\nu} \quad (3.39)$$

On the other hand, the continuity of the fluctuating axial velocity u_x with the Kutta condition yields

$$\boxed{\sum_{q=0}^{\infty}\sum_{l=0}^{\infty}\sum_{q^*=0}^{\infty}\left[A_q\mathrm{e}^{\mathrm{i}k_q^+ a\tan\Psi}\mathcal{B}_l^q(0)\mu_l^+\Upsilon_l^+ + B_q\mathcal{B}_l^q(L_c)\mu_l^-\right]\tilde{\mathcal{A}}_{q^*}^l(L_c)\mathfrak{I}_{q^*,\nu}^0 = bk_\nu^+T_\nu + \frac{\alpha_\nu}{\alpha_\nu^2+(k/M)^2}\Omega_K} \quad (3.40)$$

Finally, the matrix equation for the trailing-edge interface with a Kutta condition reads

$$\begin{pmatrix}\mathbf{E_1^2} & \mathbf{F_1^2} & \mathbf{0}\\ \mathbf{E_2^2} & \mathbf{F_2^2} & \mathbf{G_K^2}\\ \mathbf{E_K^2} & \mathbf{0} & 0\end{pmatrix}\begin{pmatrix}\mathbf{B}\\ \mathbf{T}\\ \Omega_K\end{pmatrix} = \begin{pmatrix}\mathbf{H_1^2}\\ \mathbf{H_2^2}\\ H_K^2\end{pmatrix}, \quad (3.41)$$

where

$$\left[E_1^2\right]_{\nu,q} = \sum_{l=0}^{\infty}\sum_{q^*=0}^{\infty}\mathcal{B}_l^q(L_c)\left(k\mathcal{A}_{q^*}^l(L_c)-M\mu_l^-\tilde{\mathcal{A}}_{q^*}^l(L_c)\right)\mathfrak{I}_{q^*,\nu}^0, \quad \left[F_1^2\right]_{\nu,\nu} = -b(k-Mk_\nu^+)\delta_{\nu,\nu},$$

$$\left[H_1^2\right]_{\nu,1} = -\sum_{q=0}^{\infty}\sum_{l=0}^{\infty}\sum_{q^*=0}^{\infty}A_q\mathrm{e}^{\mathrm{i}k_q^+ a\tan\Psi}\mathcal{B}_l^q(0)\Upsilon_l^+\left(k\mathcal{A}_{q^*}^l(L_c)-M\mu_l^+\tilde{\mathcal{A}}_{q^*}^l(L_c)\right)\mathfrak{I}_{q^*,\nu}^0,$$

$$\left[E_2^2\right]_{\nu,q} = \sum_{l=0}^{\infty}\sum_{q^*=0}^{\infty}\mathcal{B}_l^q(L_c)\mu_l^-\tilde{\mathcal{A}}_{q^*}^l(L_c)\mathfrak{I}_{q^*,\nu}^0, \quad \left[F_2^2\right]_{\nu,\nu} = -bk_\nu^+\delta_{\nu,\nu},$$

$$\left[G_K^2\right]_{\nu,1} = -\frac{\alpha_\nu}{\alpha_\nu^2+(k/M)^2}, \quad \left[H_2^2\right]_{\nu,1} = -\sum_{q=0}^{\infty}\sum_{l=0}^{\infty}\sum_{q^*=0}^{\infty}A_q\mathrm{e}^{\mathrm{i}k_q^+ a\tan\Psi}\mathcal{B}_l^q(0)\mu_l^+\Upsilon_l^+\tilde{\mathcal{A}}_{q^*}^l(L_c)\mathfrak{I}_{q^*,\nu}^0,$$

$$\left[E_K^2\right]_{1,q} = \sum_{l=0}^{\infty}\sum_{q^*=0}^{\infty}\mathcal{B}_l^q(L_c)\left(k\mathcal{A}_{q^*}^l(L_c)-M\mu_l^-\tilde{\mathcal{A}}_{q^*}^l(L_c)\right)\left(1-(-1)^{q^*}\mathrm{e}^{-\mathrm{i}\alpha_j b}\right),$$

$$H_K^2 = -\sum_{q=0}^{\infty}\sum_{l=0}^{\infty}\sum_{q^*=0}^{\infty}A_q\mathrm{e}^{\mathrm{i}k_q^+ a\tan\Psi}\mathcal{B}_l^q(0)\Upsilon_l^+\left(k\mathcal{A}_{q^*}^l(L_c)-M\mu_l^+\tilde{\mathcal{A}}_{q^*}^l(L_c)\right)\left(1-(-1)^{q^*}\mathrm{e}^{-\mathrm{i}\alpha_j b}\right),$$

$$[B]_{q,1} = B_q, \quad [T]_{\nu,1} = T_\nu.$$

Mode-Matching Equations — Summary

The mode-matching equations have been derived for the scattering of an acoustic wave by a cascade of cambered vanes. A subsonic nearly uniform mean flow, continuously deviated through the cascade, has been used. Jump conditions for the staggered leading-edge interface have been detailed with emphasis on the fact that pressure cannot be used, in general, for a staggered interface with flow. Instead, the velocity potential and a combination of axial and transverse velocities is used. Finally, a Kutta condition has been derived at the trailing-edge interface and incorporated into the associated system of matching equations.

3.3 Comparison with Numerical Results

3.3.1 Methodology

Without Flow

A couple of test cases are defined to assess the validity of the newly developed model of Mode Matching for Bifurcated Curved Wave-guides (MMBCW), and the remaining untested assumptions of the previous chapter.

In the first instance, the same test case as in the previous chapter is used, for which the numerical simulations are done with the exact same geometry as in the mode-matching model. Computations are performed with the FEM, MMBW and MMBCW at two different frequencies and mode orders: $j = 1$ at $kb = 2.4289$ and $j = 5$ at $kb = 12.145$. This aims at i) validating the implementation of the curvature and ii) verifying if a better description of the pressure field at high frequency is achieved. As a reminder, the parameters of the test case are gathered into Table 3.1.

	V	$\Psi/^\circ$	l/b	$M_{-\infty}$	$D_{-\infty}/D_{ref}$	$C_{-\infty}/C_{ref}$
Setup	4	30	1.04	0	1	1

Table 3.1: Input parameters of the academic test case without flow, $D_{ref} = 1.2258$ kg/m^3 and $C_{ref} = 340$ m/s.

As a second case, the performance of the MMBCW is assessed by comparisons with simulations on a realistic vane geometry. In an industrial context, the vane geometry has thickness and camber varying along the chord. It is therefore important to quantify the effects of the approximate vane geometry on the acoustic predictions. For that matter, the geometry of the NASA Source Diagnostic Test (SDT) baseline configuration at mid-span has been chosen [98] for the numerical simulations. Computations are performed with the MMBCW using two different approximate vane geometries: the stagger-angle geometry and the camber-angle geometry (Figure 3.15). The camber-angle geometry has the same leading-edge camber angle $\Psi = 33.7^\circ$ than the SDT, in order to fit the inclination of the vane (and of the equivalent dipoles) at the leading edge. It has therefore a larger stagger angle (16.8°) than the real stagger angle of 11°, and a slightly higher solidity value $l/b \simeq 1.58$. The stagger-angle model has instead the same stagger angle of 11°, but a substantially lower camber angle ($\Psi = 22^\circ$). The parameters of the different configurations are reminded in Table 3.2. Computations

are performed for two different incident acoustic waves: mode order $j = 6$ at $kb \simeq 2.75$ ($f = 5726$ Hz) and mode order $j = -18$ at $kb \simeq 5.50$ ($f = 11452$ Hz).

	V	$\Psi/^\circ$	l/b	$M_{-\infty}$	$D_{-\infty}/D_{ref}$	$C_{-\infty}/C_{ref}$
SDT	54	33.7	1.54	0	1	1
Stagger	54	22.0	1.54	0	1	1
Camber	54	33.7	1.58	0	1	1

Table 3.2: Input parameters of the realistic test case without flow, $D_{ref} = 1.2258$ kg/m^3 and $C_{ref} = 340$ m/s.

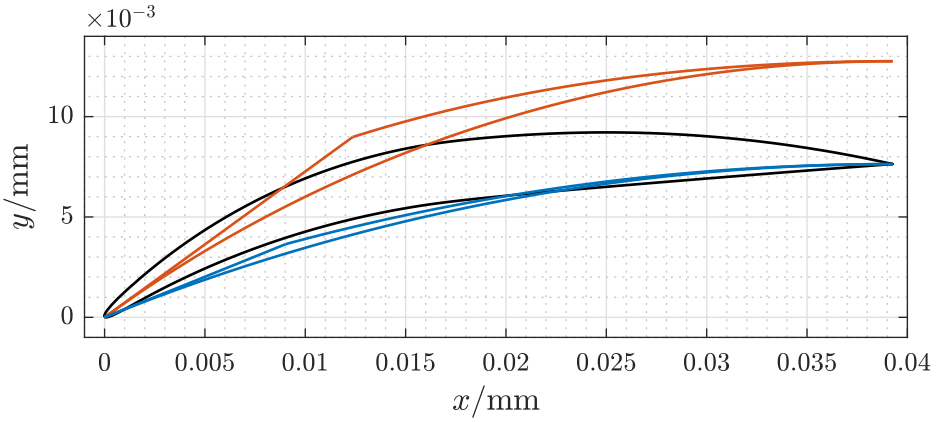

Figure 3.15: SDT baseline geometry (—) used in the FEM compared to the approximate vane geometries used in the MMBCW: stagger-angle geometry (—) and camber-angle geometry (—).

All the numerical simulations for these test cases are performed with the commercial software Simcenter 3D Acoustics, thanks to Hadrien Bériot from Siemens Industry Software NV. As a reminder, the two-dimensional Helmholtz problem is addressed numerically using a high-order adaptive finite element method [9, 7]. Periodic boundary conditions are enforced and the far-field reflections are avoided using perfectly matched layers [6]. The mesh used in the FEM is displayed in Figure 3.16 with the PML highlighted in blue.

With Flow

In the first instance, the validity of the overall change in the mean flow, which is assumed to stay nearly uniform and vary slowly across the channels due to cross-section variations only[2], is assessed. For that matter, the results presented by Edmane Envia for the 4$^{\text{th}}$ NASA CAA workshop, category 3, problem 2 [24], are used as reference results. The test-case parameters are those of the SDT baseline configuration at mid-span and are detailed in Table 3.3 as SDT. Since the geometry is approximated in the analytical model, two configurations are tested in order to give guidance on how to tune the parameters: the geometrical configuration (Geom) and the flow configuration (Flow). The latter ensures the same incident flow angle as in the numerical simulation,

[2]The same mean flow description is used in both MMBW and MMBCW since the effects of curvature on the mean flow have been neglected (section 3.1.2).

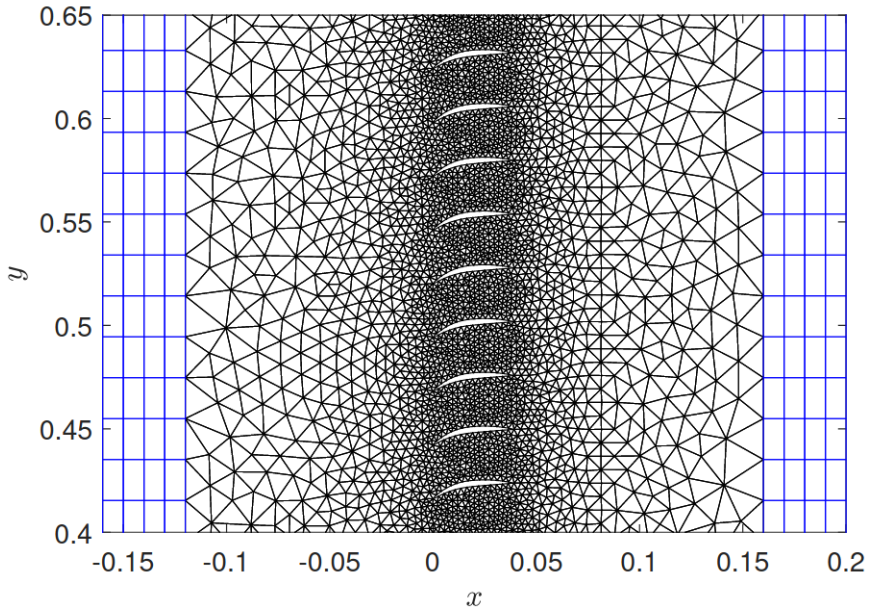

Figure 3.16: FEM mesh of the SDT test case without flow.

whereas the former ensures the same leading-edge camber angle. Both configurations are detailed in Table 3.3 as well.

	V	$\Psi/^\circ$	l/b	$M_{-\infty}$	$D_{-\infty}/D_{ref}$	$C_{-\infty}/C_{ref}$	Flow angle/°
SDT	54	33.7	1.54	0.44958	0.90567	0.98038	36.0
Geom	54	33.7	1.58	0.44958	0.90569	0.98088	33.7
Flow	54	36.0	1.59	0.44958	0.90569	0.98088	36.0

Table 3.3: Input parameters of the mean-flow test case, $D_{ref} = 1.2258$ kg/m^3 and $C_{ref} = 340$ m/s.

At the same time, results of acoustic scattering obtained with the MMBCW are compared with those from Hixon [46] to assess the performance of the model in presence of a mean flow. Hixon's results [46] have been computed with the NASA Glenn Research Center Broadband Aeroacoustic Stator Simulation (BASS) code. The BASS code solves the two-dimensional nonlinear Euler equations in the time domain using an explicit fourth-order time marching scheme combined with high-order spatial differencing schemes. It seems the mean flow has no angle of attack in Hixon's simulations [46], thus the choice of the camber angle in the MMBCW is straightforward. The parameters for this test case are collected in Table 3.4. Computations are performed at a fixed frequency $kb = 2.75$ ($f = 5726$ Hz), for two mode orders: $j = 6$ and $j = -12$. Note that, due to some uncertainties on the simulation parameters of Hixon [46] and the lack of extracted pressure profiles, these comparisons will be only qualitative.

	V	$\Psi/^\circ$	l/b	$M_{-\infty}$	$D_{-\infty}/D_{ref}$	$C_{-\infty}/C_{ref}$	Flow angle/°
SDT	54	33.7	1.54	0.4	1	1	33.7
MMBCW	54	33.7	1.58	0.4	1	1	33.7

Table 3.4: Input parameters of the realistic test case with flow, $D_{ref} = 1.2258$ kg/m^3 and $C_{ref} = 340$ m/s.

3.3.2 Results

Curvature Effects

The instantaneous pressure maps computed with the FEM and MMBCW on the academic test case, for $j = 1$ at $kc_x = 2.44$, are presented in Figure 3.17. In Figure 3.18, the pressure profiles extracted upstream, downstream and through the OGV cascade are shown with the addition of the results obtained with the MMBW in the previous chapter.

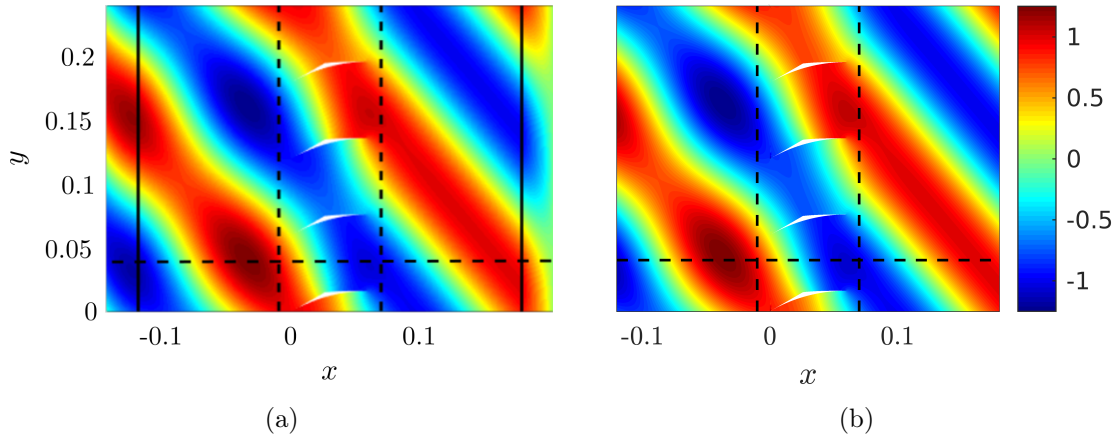

Figure 3.17: Instantaneous pressure maps computed with FEM (a) and MMBCW (b) for $j = 1$ at $kb = 2.4289$. Dashed black lines are the locations for quantitative comparisons and solid black lines in (a) show the limit of PML.

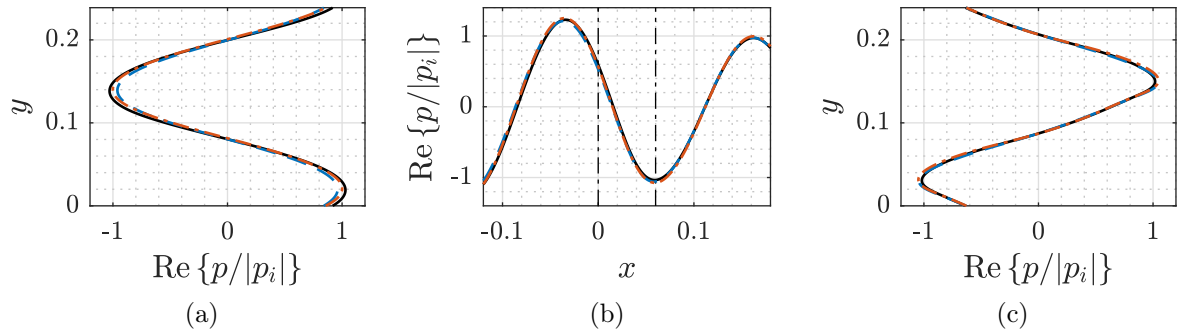

Figure 3.18: Instantaneous pressure profiles computed with FEM (—), MMBW (- -) and MMBCW (-·-) for $j = 1$ at $kb = 2.4289$, extracted at $x = -0.01$ m (a), $y = 0.04$ m (b) and $x = 0.07$ m (c). The vertical dash-dotted lines in (b) represents the LE and TE interfaces.

The MMBCW is in good agreement compared to the FEM results, with a slightly better estimation of the reflected field amplitude compared to the MMBW. The frequency of study being below the first channel cut-off frequency, the straight-channel approximation is relevant here (see section 3.1.4). In other words, this confirms that curvature effects on sound propagation are negligible at low frequency, at least below the first channel cut-off frequency ($kb < \pi$). Parametric studies are carried out in Sec-

tion 3.4 to define a dimensionless number that evaluates the impact of the curvature effects on sound transmission, hence delimiting the validity range of the MMBW.

The radiated acoustic powers are also computed for the MMBCW and compared to those of the MMBW and FEM in Table 3.5. It confirms that the reflected power

	$\mathcal{P}_r/\%$	$\mathcal{P}_t/\%$	$E/\%$
FEM	5.270	94.62	0.1100
MMBW	4.926	95.06	0.0140
MMBCW	5.200	96.32	-1.520

Table 3.5: Comparison of reflected $\mathcal{P}_r$ and transmitted $\mathcal{P}_t$ relative powers, in terms of the incident power $\mathcal{P}_i$, and the relative error $E = 1 - (\mathcal{P}_t - \mathcal{P}_r)/\mathcal{P}_i$ for $j = 1$ at $kb = 2.4289$.

is slightly better estimated with the MMBCW, compared to the MMBW, but also indicates that the MMBCW is less accurate with a greater absolute error of 1.5%. The MMBCW results are not significantly improved by increasing the number of modes in the modal truncation. It seems that either the numerical computations of the channel modes and projection coefficients ($\mathcal{B}_l^q$, $\mathcal{A}_{q^*}^l$, $\tilde{\mathcal{A}}_{q^*}^l$) or the physical assumptions keep the MMBCW results from converging in terms of accuracy in this case. Further analyses are done in section 3.5.

When increasing the frequency to $kb = 12.145$ and changing the incident mode order to $j = 5$, the MMBCW is still able to recover the pressure patterns of the FEM (Figure 3.19).

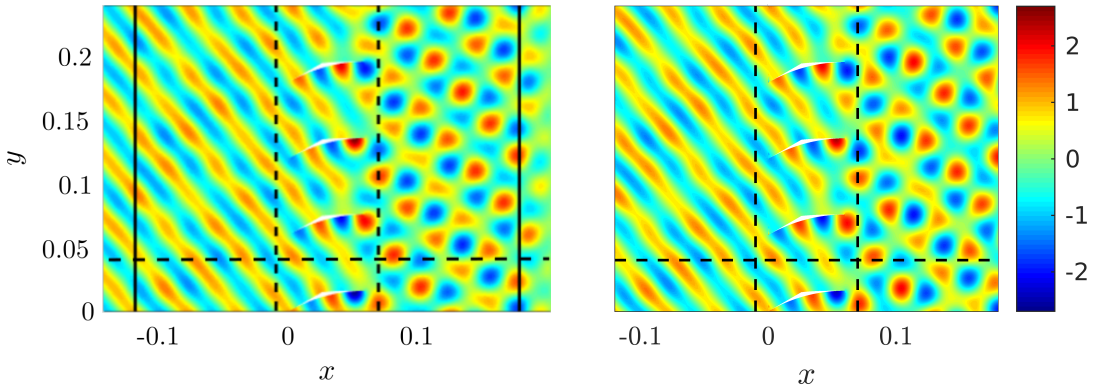

Figure 3.19: Instantaneous pressure maps computed with FEM (a) and MMBCW (b) for $j = 5$ at $kb = 12.145$. Dashed black lines are the locations for quantitative comparisons and solid black lines in (a) show the limit of PML.

The pressure profiles extracted upstream, downstream and through the OGV cascade are presented in Figure 3.20 for the FEM, MMBW and MMBCW. The MMBCW results show a good agreement with the FEM results, where the MMBW was unable to accurately predict the scattered field downstream of the cascade. The difference is undoubtedly due to the propagation inside the inter-vane channels, as shown by the discrepancies in the MMBW starting at about two thirds of the channel length (Figure 3.20b). Though there are still some discrepancies in amplitude with the MMBCW,

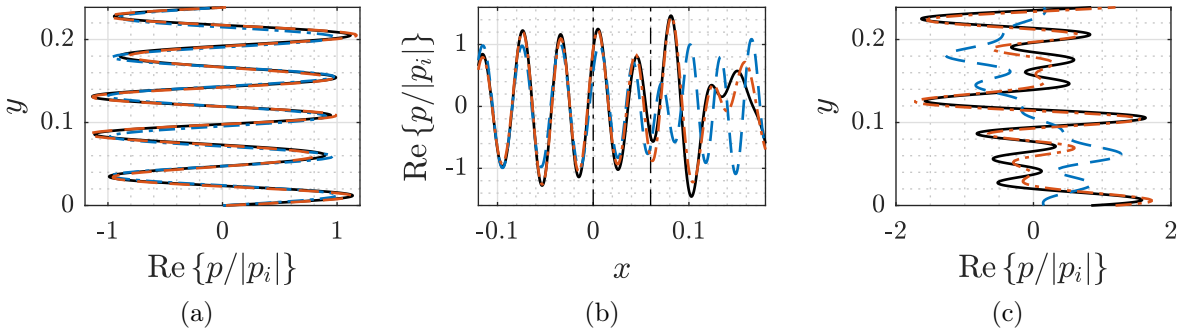

Figure 3.20: Instantaneous pressure profiles computed with FEM (—), MMBW (- - -) and MMBCW (-·-·-) for $j = 5$ at $kb = 12.145$, extracted at $x = -0.01$ m (a), $y = 0.04$ m (b) and $x = 0.07$ m (c). The vertical dash-dotted lines in (b) represents the LE and TE interfaces.

the phase is well predicted downstream (Figure 3.20c), which suggests that the modal distribution should also be.

Concerning the acoustic power balance, this time it reaches the 1% validity target (Table 3.6). The MMBCW is also able to recover the reflected power that was totally missing with the MMBW.

	$\mathcal{P}_r/\%$	$\mathcal{P}_t/\%$	$E/\%$
FEM	3.950	96.05	<0.11
MMBW	0.3010	99.70	-0.001
MMBCW	2.5600	96.61	0.8300

Table 3.6: Comparison of reflected $\mathcal{P}_r$ and transmitted $\mathcal{P}_t$ relative powers, in terms of the incident power $\mathcal{P}_i$, and the relative error $E = 1 - (\mathcal{P}_t - \mathcal{P}_r)/\mathcal{P}_i$ for $j = 5$ at $kb = 12.145$.

These results on the academic test case without flow demonstrate the validity of the developed routine and the relative importance of the curvature effects on sound propagation, depending on the frequency. This new model shows promising capabilities at the cost of a reasonably higher computation time.

Geometrical Approximation Effects

In the previous analysis, numerical simulations were performed using the same geometry as in the mode-matching model. Here, the geometrical approximations in the model are tested on the SDT test case defined in Table 3.2. Figure 3.21 shows the instantaneous pressure fields obtained at $kb = 2.75$, with the incident mode order $j = 6$, for the FEM on the SDT geometry and the MMBCW on the approximate geometries, using the same camber angle or the same stagger angle. The extracted pressure profiles are then presented in Figure 3.22.

The scattered sound field is well reproduced by the modified circle arc geometry used in the mode-matching procedure in this case, using either the stagger-angle or the camber-angle geometry. Yet, the approximate vane geometry with the real stagger angle gives a slightly better amplitude inside the inter-vane channels and, surprisingly, upstream of the OGV, than the geometry using the real leading-edge camber

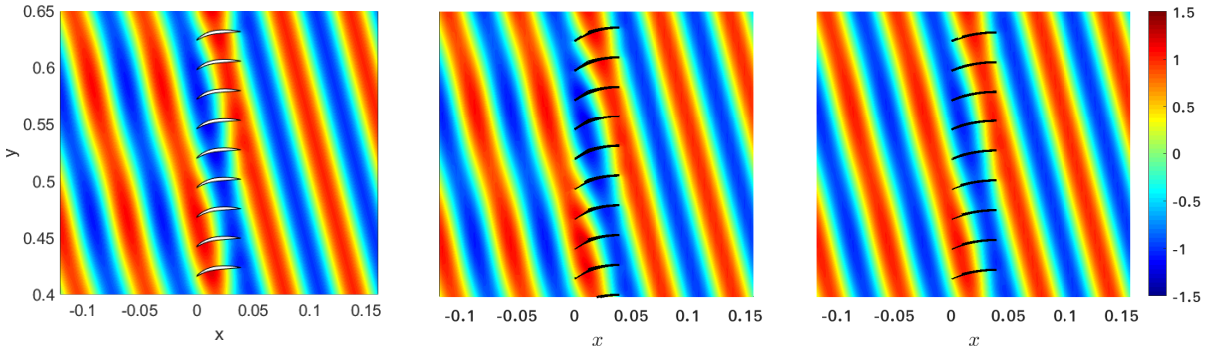

(a) (b) (c)

Figure 3.21: Instantaneous pressure maps computed with FEM (a), MMBCW/Camber (b) and MMBCW/Stagger (c) for $j = 6$ and $kb = 2.75$.

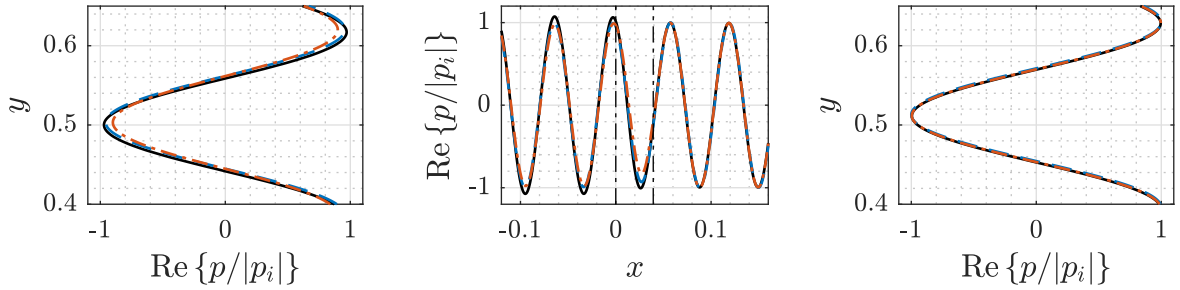

(a) (b) (c)

Figure 3.22: Instantaneous pressure profiles computed with FEM (—), MMBCW/Stagger (– –) and MMBCW/Camber (-·-) for $j = 6$ at $kb = 2.75$, extracted at $x = -0.04$ m (a), $y = 0.013$ m (b) and $x = 0.08$ m (c). The vertical dash-dotted lines in (b) represents the LE and TE interfaces.

angle. Since the camber-angle geometry is more representative of the real geometry at the leading edge, the reflected field was expected to be more accurate. However, downstream of the cascade, using the stagger-angle or camber-angle model makes no difference at this frequency.

Table 3.7 shows the reflected and transmitted acoustic powers, as well as the balance error, for both models. It confirms that the difference between them resides in the reflected field and demonstrates that the MMBCW can reach a good accuracy in a real test case.

	$\mathcal{P}_r/\%$	$\mathcal{P}_t/\%$	$E/\%$
MMBCW/Stagger	0.190	99.67	0.140
MMBCW/Camber	1.080	99.37	-0.450

Table 3.7: Comparison of reflected $\mathcal{P}_r$ and transmitted $\mathcal{P}_t$ relative powers, in terms of the incident power $\mathcal{P}_i$, and the relative error $E = 1 - (\mathcal{P}_t - \mathcal{P}_r)/\mathcal{P}_i$ for $j = 6$ at $kb = 2.75$.

Figures 3.23 and 3.24 display results at twice the previous frequency ($kb = 5.5$), and with an incident mode order of $j = -18$.

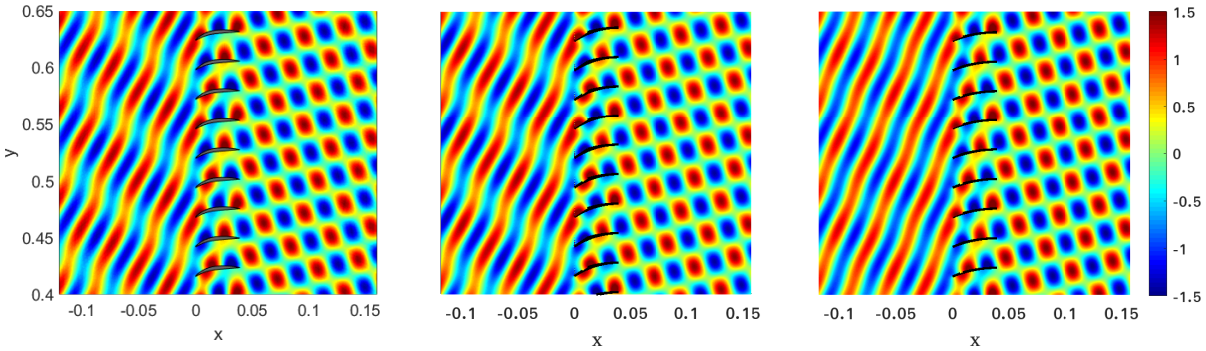

(a) (b) (c)

Figure 3.23: Instantaneous pressure maps computed with FEM (a), MMBCW/Camber (b) and MMBCW/Stagger (c) for $j = -18$ and $kb = 5.5$.

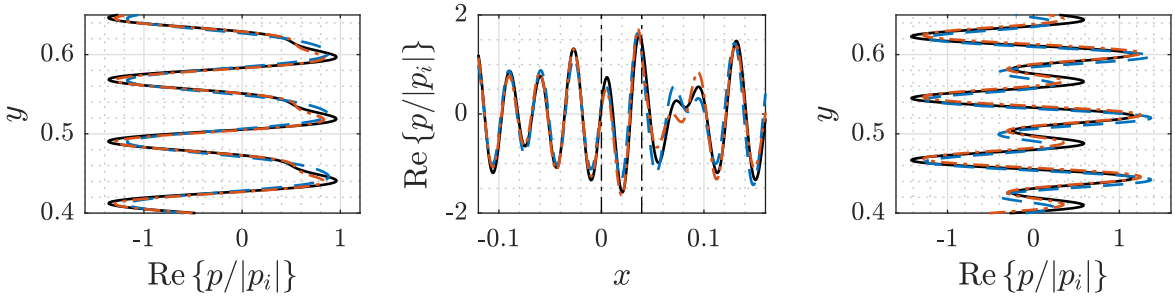

(a) (b) (c)

Figure 3.24: Instantaneous pressure profiles computed with FEM (—), MMBCW/Stagger (– –) and MMBCW/Camber (-·-·-) for $j = -18$ and $kb = 5.5$, extracted at $x = -0.04$ m (a), $y = 0.013$ m (b) and $x = 0.08$ m (c). The vertical dash-dotted lines in (b) represents the LE and TE interfaces.

Discrepancies between the analytical solutions and the numerical solution are more significant at this frequency. This is expected since high frequency waves are more sensitive to small details of the vane geometry. Though, the predicted pressure field from the MMBCW is still in good agreement with the FEM results. This time, the camber-angle model gives better results, especially upstream of the OGV where the stagger-angle model seems to miss a cut-on reflected mode. It is visible in Figure 3.24a that the stagger-angle model predicts a sinuous pattern reflected field, thus composed of a single mode, whereas the camber-angle model correctly reproduces the disturbed sinusoid, representative of a stronger reflection. Table 3.8 confirms this result, indicating a reflected power two times stronger with the camber-angle model.

	$\mathcal{P}_r/\%$	$\mathcal{P}_t/\%$	$E/\%$
MMBCW/Stagger	4.420	95.37	0.210
MMBCW/Camber	9.620	90.58	-0.200

Table 3.8: Comparison of reflected $\mathcal{P}_r$ and transmitted $\mathcal{P}_t$ relative powers, in terms of the incident power $\mathcal{P}_i$, and the relative error $E = 1 - (\mathcal{P}_t - \mathcal{P}_r)/\mathcal{P}_i$ for $j = -18$ at $kb = 5.50$.

Up to the frequency $kb = 5.5$, the modified circle arc geometry used in the model is able to generate a pressure field in fairly good agreement with the FEM results on a realistic geometry. This is encouraging for reliable and fast sound predictions in an industrial context. The model using the same leading-edge camber angle should be preferred as it reproduces more precisely the reflected scattered waves in the highest-frequency case, and is relatively similar in the lowest-frequency case. Furthermore, the accuracy of the model is always within the 1% error range, giving confidence in the model if used for parametric studies.

Mean Flow Approximation Effects

In the first instance, the inviscid mean flow description used in the mode-matching model is compared to the inviscid mean flow computed with TURBO [55], from the 4^{th} NASA CAA workshop, category 3, problem 2 [24]. Figure 3.25 shows the qualitative numerical and analytical (flow configuration) mean flow evolution through the cascade, while Table 3.9 presents the quantitative results downstream of the cascade, as well as the difference between the analytical results and the numerical results indicated by the Δ symbol (in percentage of the numerical value).

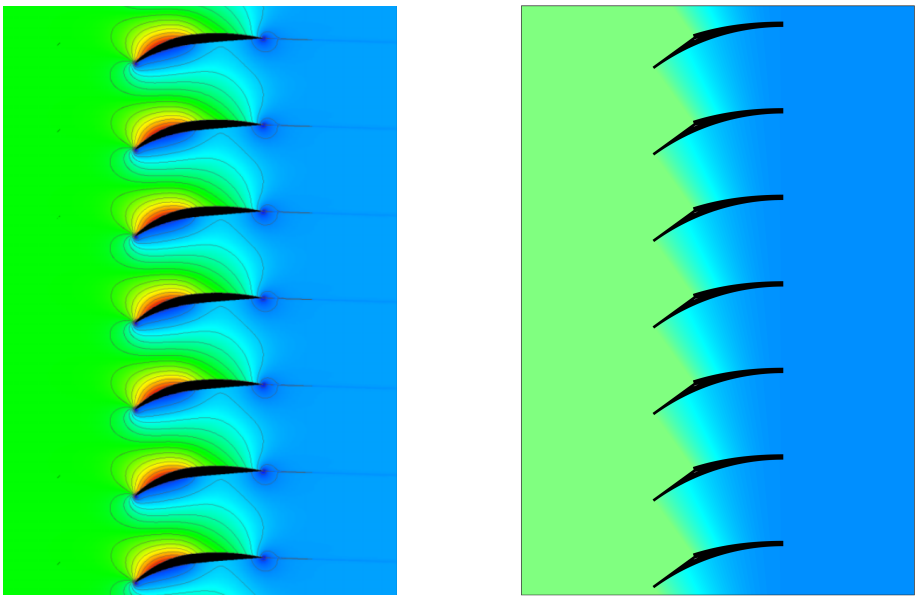

(a) (b)

Figure 3.25: Qualitative comparisons of total Mach number obtained with TURBO (a) and the analytical description used in the mode-matching models (b) for input parameters defined in Table 3.3. Color scales are not equal.

The mean flow quantities downstream of the cascade are well recovered by the analytical model using the geometry optimized for the flow description (Flow), whereas the true vane geometry (Geom) suffers from a relative error of more than 3% on the Mach number. Though, both geometries give an accurate change of the mean density and sound speed. These results demonstrate that the overall change in the inviscid mean flow through a realistic OGV cascade is mainly due to the cross-section variations of the inter-vane channels in this case, and so is well recovered by a nearly uniform

	$M_{+\infty}$	$D_{+\infty}/D_{ref}$	$C_{+\infty}/C_{ref}$	$\Delta M/\%$	$\Delta\left(D/D_{ref}\right)/\%$	$\Delta\left(C/C_{ref}\right)/\%$
SDT	0.34704	0.94216	0.98817	0.0000	0.0000	0.0000
Geom	0.35836	0.93859	0.98791	3.2619	0.3789	0.0263
Flow	0.34682	0.94232	0.98869	0.0634	0.0170	0.0526

Table 3.9: Mean flow quantities downstream of the cascade computed with TURBO on the SDT geometry, and analytical mean flow quantities predicted with a uniform flow using the geometrical and flow configurations. Input parameters defined in Table 3.3.

mean flow description neglecting curvature and mean loading effects. However, when looking at local variations of the mean flow inside the inter-vane channels, the nearly uniform mean flow description is clearly inadequate. Some perspectives of improvement concerning that part are discussed in conclusion of this chapter. In the meantime, qualitative comparisons of scattered pressure fields in presence of such numerical and analytical mean flows are analyzed in the following.

Figures 3.26 and 3.27 display the pressure fields computed with BASS (from Hixon [46]) and with the MMBCW (with a Kutta condition) at $kb = 2.75$ and with $M_{-\infty} = 0.4$, for two different incident mode orders: $j = 6$ and $j = -12$ respectively. The parameters are given in detail in Table 3.4. TURBO solves the steady part of the same nonlinear Euler equations than BASS, except TURBO is a 3-D solver whereas BASS is 2-D. Although the mean flow description computed with BASS is not given in Hixon [46], it should be fairly the same as in Figure 3.25a.

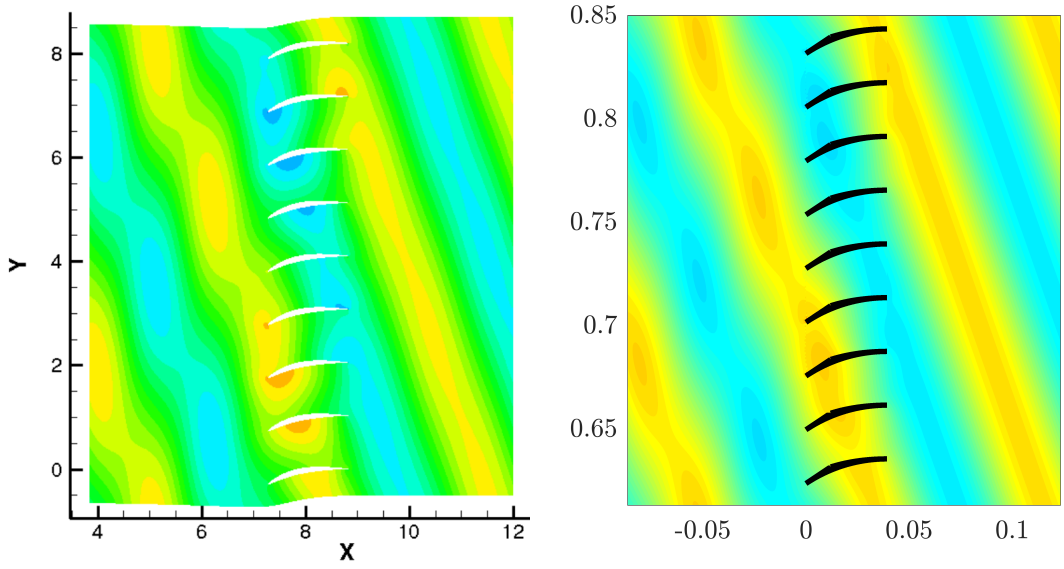

(a) (b)

Figure 3.26: Instantaneous pressure maps computed with BASS (a) and MMBCW with a Kutta condition (b) for $j = 6$ at $kb = 2.75$, $M_{-\infty} = 0.4$. Color scales are not equal.

In both cases, the pressure field from the MMBCW is in a good agreement with the numerical result. The inclination and relative phase of the scattered waves are well reproduced upstream and downstream of the cascade. The amplitude of the reflections also seems correctly predicted when looking at the "wiggling" pattern of the wave.

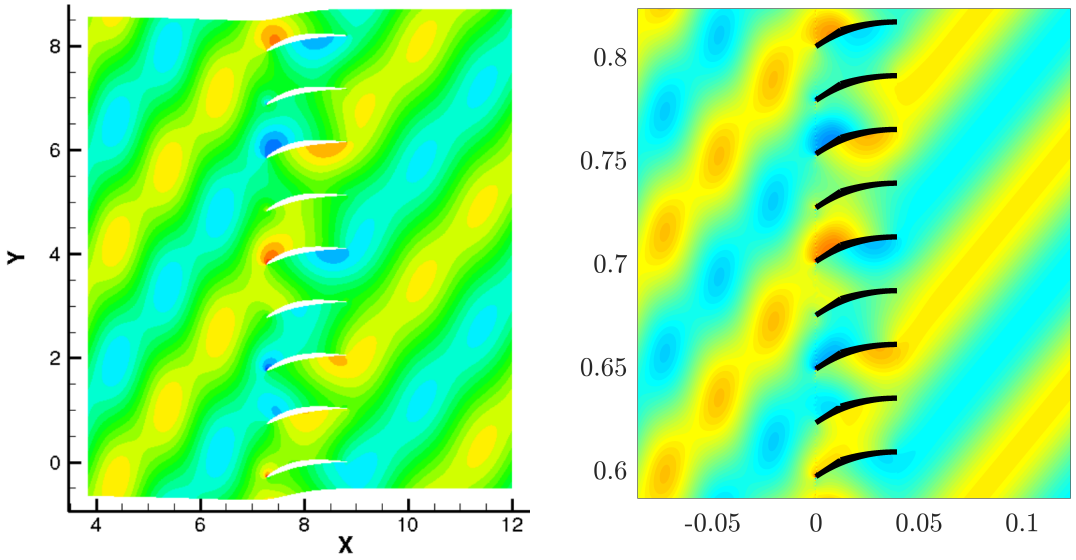

(a) (b)

Figure 3.27: Instantaneous pressure maps computed with BASS (a) and MMBCW with a Kutta condition (b) for $j = -12$ at $kb = 2.75$, $M_{-\infty} = 0.4$. Color scales are not equal.

In Figure 3.27a, downstream of the cascade, the pressure field is polluted by spurious numerical reflections at the boundary (see Hixon [46]). Only a single cut-on mode should propagate as predicted by the mode-matching model in Figure 3.27b.

Though only qualitative, these results are very satisfactory and encouraging. They show that the model of sound reflection and transmission performs well even in the presence of a mean flow, and that a uniform mean flow can give reasonable acoustic results in this case. However, these results are only at a relatively low frequency $kb = 2.75 < \pi$. Further comparisons with reference results at higher frequencies would be needed to assess the validity of the model, especially for the uniform mean flow assumption that neglects the mean loading of the cambered vanes and can have an influence at higher frequencies [92, 93].

3.3.3 Discussion

The assumptions that remained to be assessed at high frequency have shown to be adequate for the problem of sound propagation in an OGV row. The slowly-varying assumption is still valid at such frequencies, as well as the modal approximation in the triangle ABC. The neglected reflections at the interface BC, due to the abrupt change of curvature between the straight part and the curved part, do not play a significant role in the case studied. Furthermore, the geometrical approximation of the vane profile (circle arc with artificial thickness and approximate center line curvature) has demonstrated to give reasonable results when used on the SDT test case at mid-span. This is indeed only relevant for this geometry but is nevertheless promising. However, comparisons have been performed at relatively low and moderate frequencies ($kb = 2.75$ and $kb = 5.5$), which would barely cover the first four BPF in the NASA SDT baseline configuration (7808 RPM). Geometrical discrepancies between the model

and the real profile will have more and more impact as the frequency increases. Further investigations are then needed to assess the validity of the model at higher frequencies.

The mean flow modeling has been shown to accurately reproduce the overall change in the mean flow quantities. However, the local description in the inter-vane channels and near the OGV is completely different from what is seen in the numerical inviscid computations. This local difference is mainly due to the mean loading of the vanes, which generates a non-uniform mean flow. Suggestions for improvement in that direction are made in conclusion of this chapter. Regarding the acoustic field, the results of the model are in good qualitative agreement with numerical results. However, no quantitative comparisons have been made and the available numerical results are at low frequency ($kb = 2.75$). Further investigations are also needed for that part. Numerical samples could be obtained with the SU2 open-source solver[3] for example.

Comparison with Numerical Results — Summary

Results from the present analytical solution accounting for curvature effects (MMBCW) have been compared in different test cases with numerical results obtained by

1. without flow: using Simcenter 3D Acoustics FEM code;
2. with flow: relying on results from the literature using inviscid non-linear solvers such as TURBO [55] for the steady mean flow [24], and BASS for the acoustic results [46].

Computations have been performed without flow on the same test case as in the previous chapter, and with and without flow on the realistic vane geometry of the NASA SDT baseline configuration at mid-span [98]. Assessments on the validity of the approximations made in the model are given below.

Modal Basis Approximation:

- Adequate approximation at all frequencies;
- Oscillations similar to the Gibbs phenomenon at high frequency in the vicinity of the leading edge;
- Green's reciprocity theorem could be used instead to estimate the impact of the oscillations on the modal content.

Neglected Modal Scattering at the Interface BC:

- Adequate approximation at all frequencies;
- Green's reciprocity theorem could be used instead to take the scattering into account (or an additional matching interface).

Slowly-Varying Approximation:

- Adequate approach at all frequencies.

Geometrical Approximation:

[3] SU2 code. [Online]. Available: https://su2foundation.org/

- Two-parts definition of the channel with artificial thickness and approximate center line curvature;
- Reasonable approximation for realistic vane cascades (such as the NASA SDT) at low and moderate frequency.

Mean Flow Approximation:

- Accurate approximation for the change in mean flow quantities but missing local non-uniformity due to the vanes mean loading;
- Adequate approximation for the scattered sound field at low frequency.

3.4 Validity Range of the Low-Frequency Model

In this section, the validity range of the low-frequency model is assessed. For this purpose, a reference test case similar to the SDT is used, as described in Table 3.10. Figures 3.28 and 3.29 then display results of reflected acoustic power for both models,

	V	$\Psi/^\circ$	l/b	$M_{-\infty}$	$D_{-\infty}/D_{ref}$	$C_{-\infty}/C_{ref}$
Setup	54	36	1.5	0	1	1

Table 3.10: Input parameters of the test case used for the low-frequency model validity assessment, $D_{ref} = 1.2258$ kg/m^3 and $C_{ref} = 340$ m/s.

with different camber angles and incident mode orders. The vertical dash-dotted lines are the limits of the transition ranges, in which a mode undergoes transition from cut-off to cut-on or vice versa. This phenomenon was already mentioned when investigating the asymptotic behavior of the model in section 3.1.4 and will be examined in detail in the next chapter. For now, the rapid variations that the mode undergoes in the vicinity of the transition location are not accounted for, thus the model cannot be trusted in these frequency ranges. On top of these plots is also drawn the value of the following criterion:

$$\kappa_{ac} = \underbrace{kl}_{compactness} \times \underbrace{b/\bar{R}_c}_{curvature} , \tag{3.42}$$

which is a proposed criterion for estimating the influence of the camber effects on sound propagation through the OGV. Curvature effects should be negligible when $\kappa_{ac} \ll 1$, thus both MMBW and MMBCW results should be similar in this case. Note that the compactness term can also be interpreted as the product of the dimensionless frequency kb (transverse compactness) with the solidity l/b. Thus, even at frequencies of order $\mathcal{O}(1)$ or higher, the effects of camber should be negligible if the solidity is low. This criterion is built upon the investigation made in section 3.1.4, on the asymptotic behavior of the eigenfunctions and eigenvalues of the slowly-varying curved channel.

From this investigation, it appears that below the first cut-off frequency of the channel, sound propagation could be approximated with a straight-channel assumption in the absence of flow. This is confirmed by the results of the MMBCW in each case of Figures 3.28 and 3.29. Above the first cut-off frequency of the channel, discrepancies

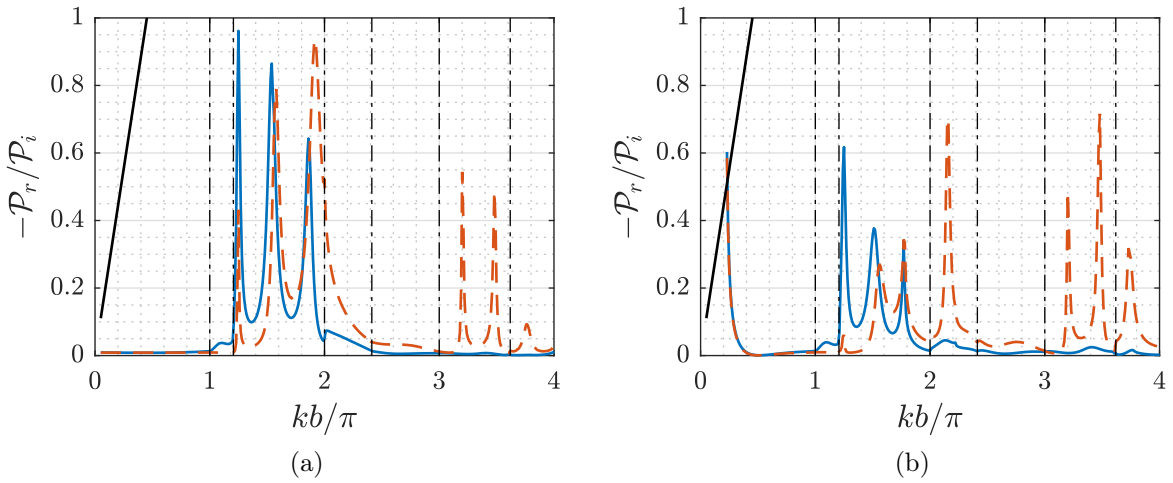

Figure 3.28: Reflected acoustic power against the frequency without flow calculated with MMBCW (—) and MMBW (- -), for an incident mode order $j = 0$ (a) and $j = 6$ (b), and the proposed criterion for estimating the influence of camber effects (—)

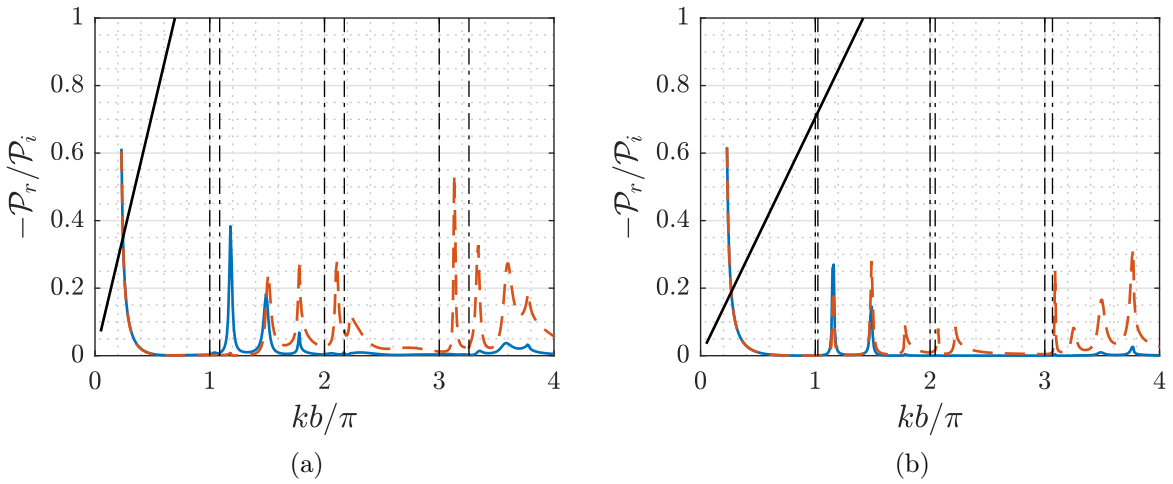

Figure 3.29: Reflected acoustic power against the frequency without flow calculated with MMBCW (—) and MMBW (- -), for a camber angle $\Psi = 23°$ (a) and $\Psi = 12°$ (b), and the proposed criterion for estimating the influence of camber effects (—)

start to be visible between both models. With $\Psi = 36°$, the MMBW model is generally off, except for particular isolated frequencies. Then, when lowering the camber angle, the camber effects become less and less dominant on sound propagation, and the MMBW is able to recover the results of the MMBCW up to $kb/\pi \simeq 1.7$ for $\Psi = 12°$ (Figure 3.29b). This seems in agreement with the proposed criterion, which is then greater than one.

The reflected power spectra also show the presence of peaks, which are due to acoustic resonances. This phenomenon is examined in detail in section 3.6. What can be observed now is that the resonant frequencies are reasonably well estimated by the MMBW, but the latter seems to over predict resonance phenomena, especially for $kb/\pi \geq 2$. The resonances involved here are longitudinal resonances between the

leading-edge and trailing-edge interfaces. Thus, it appears that the straight-channel assumption in the MMBW tends to strengthen such resonance by artificially considering the inlet and outlet of the channel as parallel. Note that the resonances still appear with the MMBCW but with a drastically lower strength, seemingly due to the non-parallelism of the inlet and outlet.

Figures 3.30 and 3.31 represent the pressure maps calculated with both MMBW and MMBCW, with an incident Mach number $M_{-\infty} = 0.4$ at two different frequencies above the first cut-off of the channel. At $kb/\pi = 1.6$, the MMBW is able to

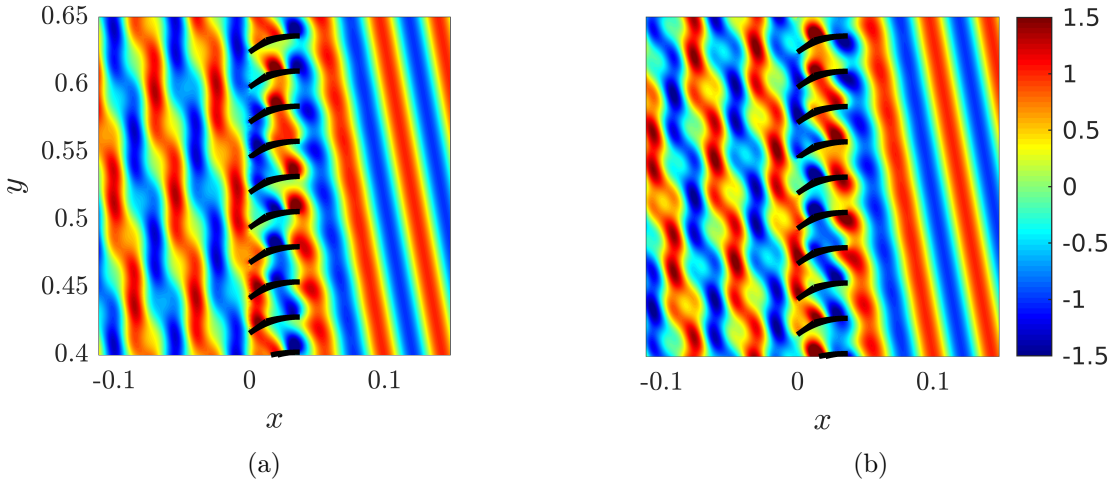

Figure 3.30: Pressure maps at $kb/\pi = 1.6$, with $\Psi = 23°$ and $M_{-\infty} = 0.4$, calculated with MMBW (a) and MMBCW (b).

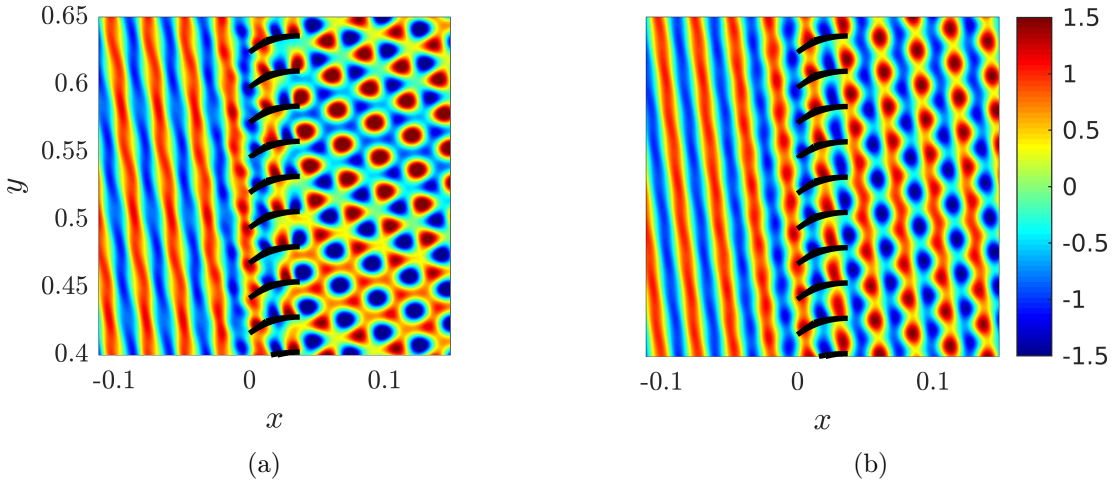

Figure 3.31: Pressure maps at $kb/\pi = 2.6$, with $\Psi = 23°$ and $M_{-\infty} = 0.4$, calculated with MMBW (a) and MMBCW (b).

qualitatively and quantitatively reproduce the scattered sound field downstream of the cascade predicted by the MMBCW. This is due to the fact that only one mode is cut-on downstream of the OGV, and also to the fact that the mean flow makes the channel mode D_0 dominant in this case, which is the only mode that the MMBW is capable of estimating. However, upstream of the cascade, two modes are cut-on and then

the modal distribution is no longer well estimated by the MMBW. This is a general conclusion that also appears at $kb/\pi = 2.6$, where, this time, the downstream modal content is composed of several cut-on modes, and thus the MMBW shows significant discrepancies with the MMBCW.

Validity Range of the Low-Frequency Model — Summary

The MMBW (called low-frequency model) is capable of correctly predicting the scattered fields below the first cut-off frequency of the channels. Above this frequency, the MMBCW needs to be used instead. Yet, the MMBW can still be accurate if the camber effects are not dominant, which can be estimated by the proposed criterion in (3.42). In the presence of a mean flow, the MMBW appears to be accurate up to the first cut-off frequency of the annular domain, which is different upstream and downstream of the cascade due to the swirl recovery.

3.5 Parametric Studies

3.5.1 Influence of Stagger and Camber

Unless mentioned, all following results are obtained with the MMBCW model, thus accounting for curvature effects. The influence of camber on the reflected $\mathcal{P}_r$ and transmitted $\mathcal{P}_t$ acoustic powers, and on the modal content, is assessed in this first part. Attention is paid to the evolution of the acoustic power balance $(\mathcal{P}_t - \mathcal{P}_r)/\mathcal{P}_i$ with the frequency and camber angle, since this is the main criterion to estimate the accuracy of the method. Figure 3.32 displays this balance for $\Psi = 23°$ and $\Psi = 34°$, without flow ($M_{-\infty} = 0$), with a solidity value of $l/b = 1.5$ and an incident mode order $j = 6$. The horizontal dashed lines represent the limits of the 1% confidence range in which the results can be trusted. The vertical dash-dotted lines are the limits of the transition ranges, in which a mode undergoes transition from cut-off to cut-on or vice versa. As mentioned earlier, this phenomenon will be examined in detail in the next chapter and the current model cannot be trusted in these frequency ranges.

Comparing the results at $\Psi = 23°$ (Figure 3.32a) and $\Psi = 34°$ (Figure 3.32b) clearly indicates that the accuracy is better for lower camber angles. The balance at $\Psi = 23°$ is closer to 1, and the fluctuations are much weaker. In Figure 3.32b, the balance is just at the limit for $2.41 \lesssim kb/\pi < 3$ and $3.62 \lesssim kb/\pi \leq 4$, but could be improved by taking more modes in the modal truncation. Between $1.2 \lesssim kb/\pi < 2$, three significant drops can be seen. Similar drops, but much weaker, are also seen in Figure 3.32a for $1.09 \lesssim kb < 2$. When looking at Figure 3.33, which represents the reflected and transmitted acoustic powers evolution with the frequency and camber angle, the drops in the acoustic power balance seem to be due to resonance phenomena. The occurrence of a resonance in $1 < kb/\pi < 2$ induces a high reflection, up to 80% of relative power, whereas the acoustic power is almost entirely transmitted otherwise. The favored reflected power in these cases indicates that the resonances create some sort of a blockage for the acoustic energy. In such conditions, the number of modes accounted for in the modal truncation should also be optimized. This will be further investigated in section 3.6. In conclusion, fluctuations of the acoustic power balance seem to appear for two reasons: when a transition or a resonance occurs. To improve

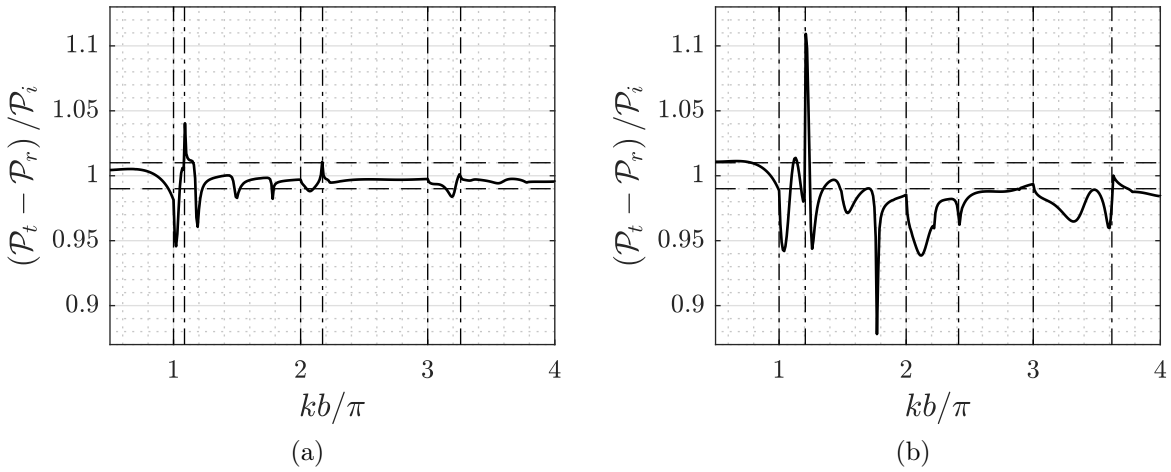

Figure 3.32: Acoustic power balance against the frequency with a camber angle $\Psi = 23°$ (a) and $\Psi = 34°$ (b).

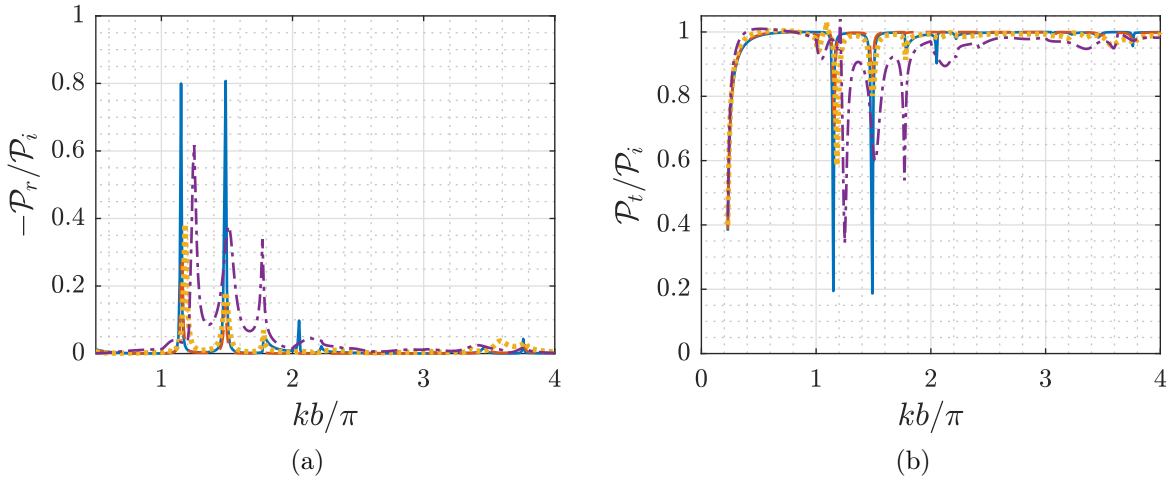

Figure 3.33: Reflected (a) and transmitted (b) acoustic power against the frequency for varying camber angles: $\Psi = 1°$ (—), $\Psi = 12°$ (– –), $\Psi = 23°$ (····) and $\Psi = 34°$ (–·–·).

the accuracy in the latter, an optimized number of modes needs to be used in the modal truncation, whereas in the former, the model needs to be adjusted as in Chapter 4.

On the other hand, Figure 3.33 shows that outside the resonant frequencies, the acoustic power is almost fully transmitted, without significant effects of the camber angle. However, camber plays a role in the modal content produced downstream of the cascade. Figure 3.34 displays the pressure maps and associated modal contents for two different camber angles ($\Psi = 1°$ and $\Psi = 34°$) at $kb/\pi = 2.7$. Upstream of the cascade, a higher vane inclination at the leading edge increases the relative angle between the vanes and the incident wave. As a consequence, it significantly changes the balance of the reflected modes. Even if their amplitude is small at this frequency, a shift from a dominant mode R_{42} to R_{-66} is seen. In the channels, the dominant modes D_0 and D_1 are replaced by D_1 and D_2, but the reflection at the trailing-edge remains close

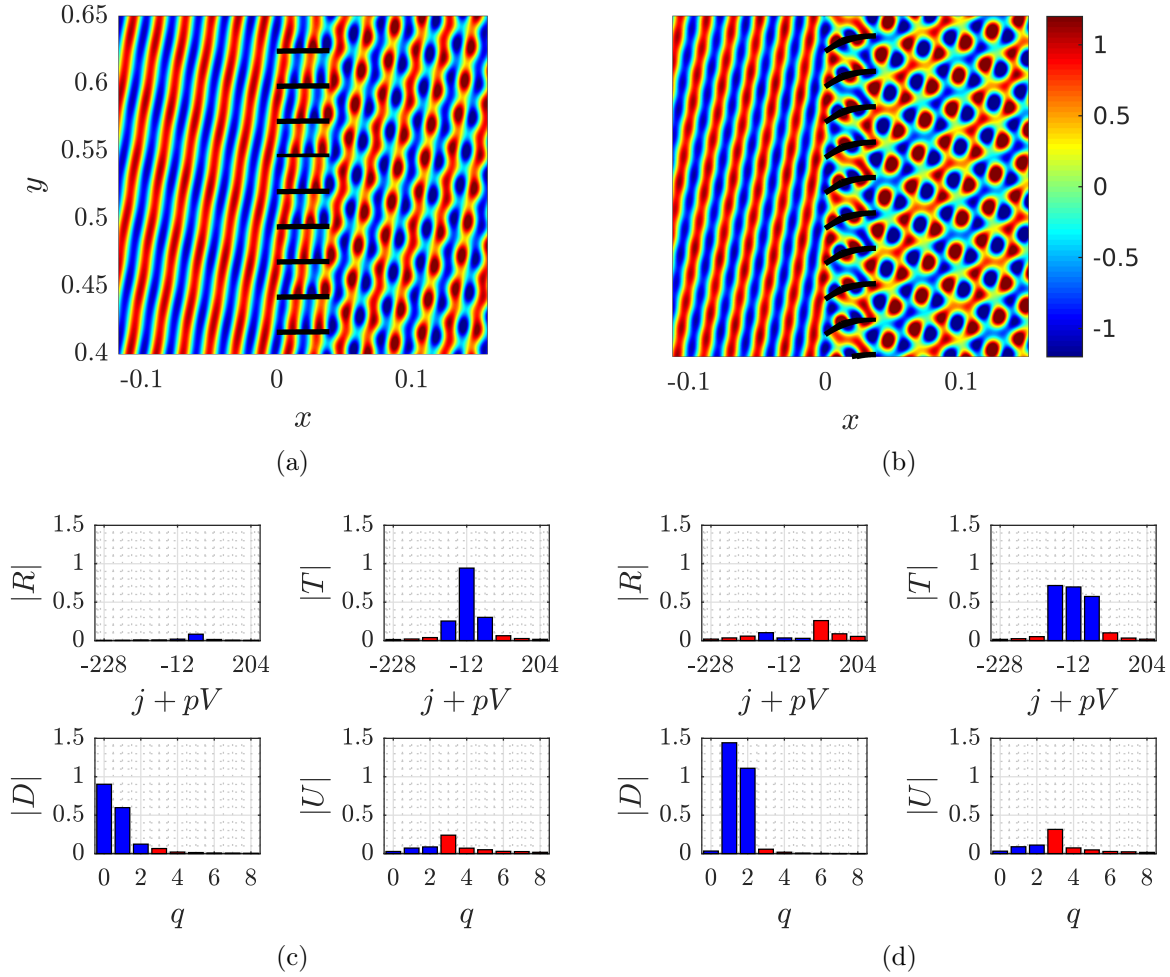

Figure 3.34: Pressure maps and corresponding modal contents without flow ($M_{-\infty} = 0$), for an incident mode order $j = -12$ at $kb/\pi = 2.7$, a solidity value $l/b = 1.5$ and a camber angle $\Psi = 1°$ (a,c) or $\Psi = 34°$ (b,d).

to zero. Downstream of the cascade, because of the difference in the channel modal content being scattered at the trailing edges, a more evenly distributed modal content is produced. The transmitted field dominated by the mode T_{-12} for $\Psi = 1°$, same mode as the incident one, is more complex for $\Psi = 34°$ due to interference patterns between all three modes T_{-66}, T_{-12} and T_{42}. Even if the transmitted power is roughly the same in both cases, this difference in modal content could have a significant impact on the scattering at the engine exhaust, thus on the directivity of the noise propagating outside. Noise pollution measurements on the ground could be affected by it.

3.5.2 Influence of Solidity

According to the previous results, the MMBCW is inaccurate within the transition ranges of the channel modes. At $\Psi = 34°$, these transitions occur on a significant portion of the frequency range in $0.5 \leq kb/\pi \leq 4$. For that reason, the following results are calculated with a camber angle of 23°. Figure 3.35 displays the acoustic power balance for varying solidity values, without flow $M_{-\infty} = 0$, and with parameters $\Psi = 23°$, $l/b = 1.5$ and $j = 6$. Again, the horizontal dashed lines represent the limits

of the 1% confidence range and the vertical dash-dotted lines are the limits of the transition ranges. Figure 3.36 then shows the detail of the balance between reflected $\mathcal{P}_r$ and transmitted $\mathcal{P}_t$ acoustic powers.

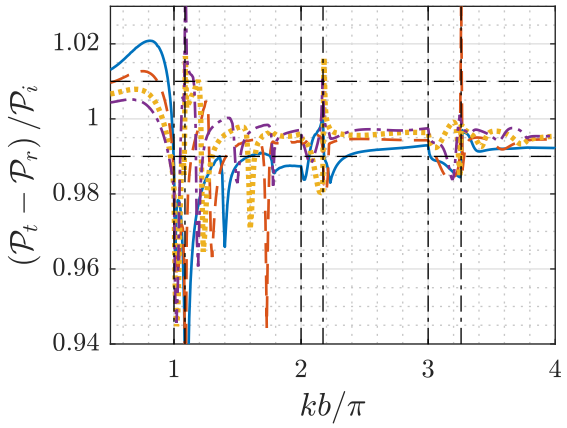

Figure 3.35: Acoustic power balance against the frequency for varying solidity values: $l/b = 0.75$ (—), $l/b = 1$ (– –), $l/b = 1.25$ (····) and $l/b = 1.5$ (–·–·).

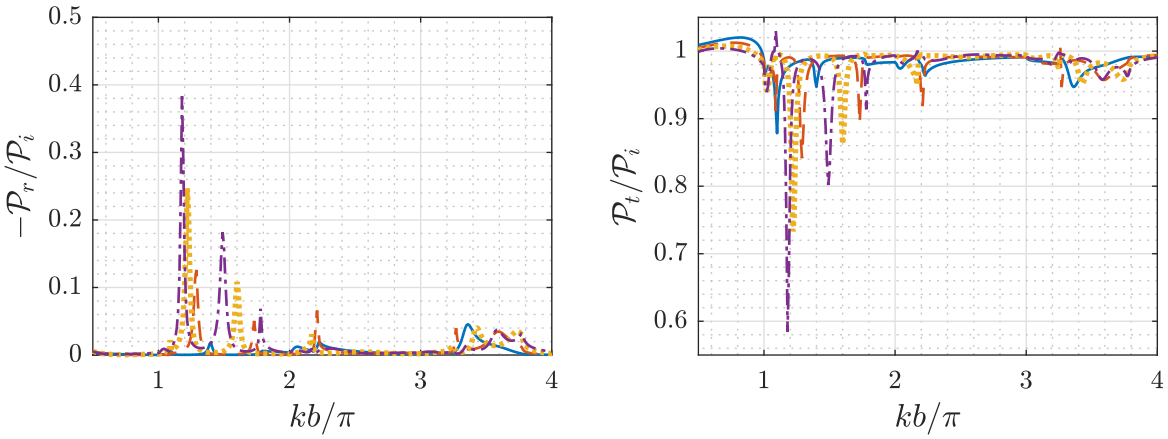

Figure 3.36: Reflected (a) and transmitted (b) acoustic power against the frequency for varying solidity values: $l/b = 0.75$ (—), $l/b = 1$ (– –), $l/b = 1.25$ (····) and $l/b = 1.5$ (–·–·).

The acoustic power balance lies within the confidence range for all frequencies greater than $kb/\pi = 1$, except within the transition ranges and at the resonant frequencies. Below $kb/\pi = 1$, Figures 3.35 and 3.36b indicate an overestimation of transmitted power. For all frequencies though, the balance becomes more and more accurate with increasing solidity value. This is in agreement with i) the mode-matching technique being better suited when sound propagation is governed by in-duct acoustics and ii) results from Figure 2.10, showing the error ϵ of the approximate channel potential decreasing with the solidity value l/b.

Concerning the resonances, it appears without surprise that they get stronger with increasing solidity. However, the predicted amplitudes of the reflected and transmitted

powers at the resonant frequencies need to be taken with a pinch of salt since this phenomenon displays a highly non-linear behavior in real applications. However, linear analysis is able to give insights on this phenomenon. The resonant frequencies are correctly estimated with linear acoustics for example, but the amplitude of the pressure field inside the channels, and thus the radiated acoustic powers, are subject to a large uncertainty.

Finally, Figure 3.37 represents the pressure maps and associated modal contents for two different solidity values ($l/b = 0.75$ and $l/b = 1.5$) at $kb/\pi = 2.7$. Reducing the

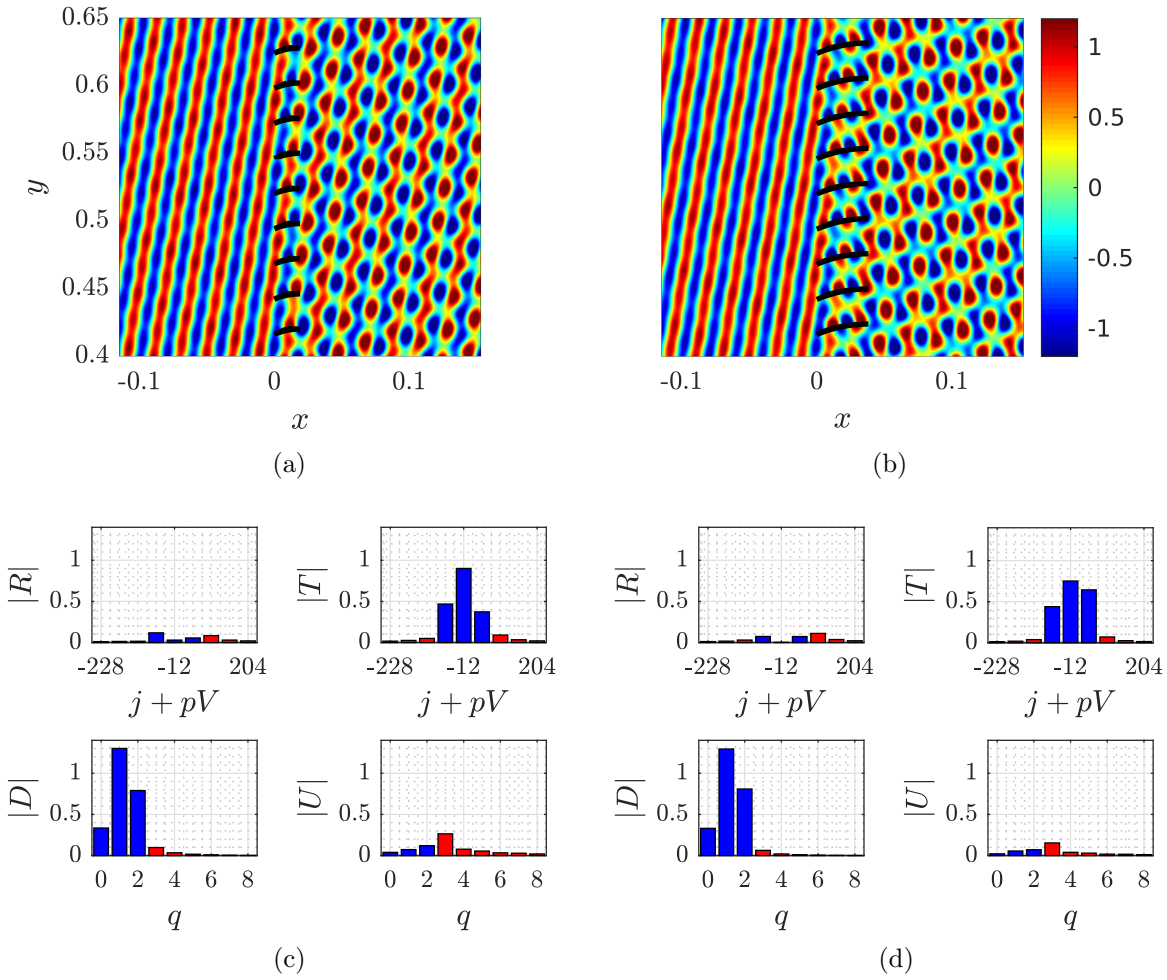

Figure 3.37: Pressure maps and corresponding modal contents without flow ($M_{-\infty} = 0$), for an incident mode order $j = -12$ at $kb/\pi = 2.7$, a camber angle $\Psi = 23°$ and a solidity value $l/b = 0.75$ (a,c) or $l/b = 1.5$ (b,d).

solidity by half has no significant impact on the modal distribution except downstream of the cascade. Interestingly enough, a low solidity has the same effect as a low camber angle here. Both result in a lower impact of the cascade scattering edges, hence in a transmitted field similar to the incident one. Note that this conclusion is dependent on the incident mode order though, since for a given solidity or camber/stagger angle, more reflections inside the channels would occur with a greater relative angle between the incident wave and the vanes. The influence of the incident mode order is then naturally investigated in the following.

3.5.3 Influence of Incident Mode Order

The influence of the mode order is studied with the same configuration as previously: $\Psi = 23°$, $l/b = 1.5$ and $M_{-\infty} = 0$, but with varying incident mode orders j. Figure 3.38 shows the acoustic power balance as a function of frequency in this case. Again, the horizontal dashed lines represent the limits of the 1% confidence range and the vertical dash-dotted lines are the limits of the transition ranges. Figure 3.39 gives the detail of the balance between reflected $\mathcal{P}_r$ and transmitted $\mathcal{P}_t$ acoustic powers. Bear in mind that the different curves, corresponding to different incident mode orders, do not each correspond to a unique angle of incidence since the latter vary with frequency.

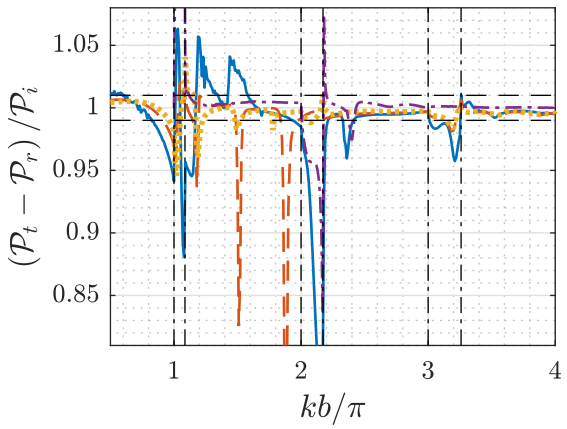

Figure 3.38: Acoustic power balance against the frequency for varying incident mode orders: $j = -12$ (—), $j = 0$ (– –), $j = 6$ (····) and $j = 27$ (–·–).

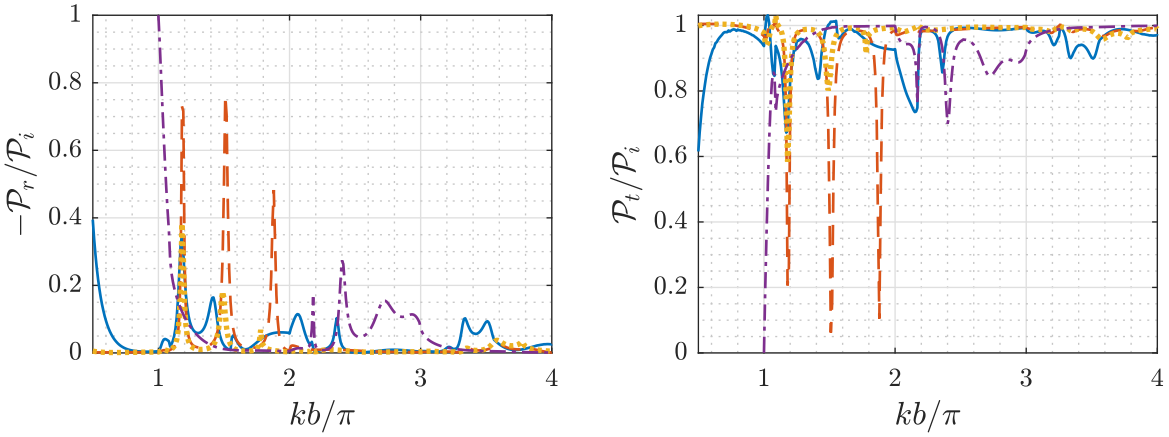

Figure 3.39: Reflected (a) and transmitted (b) acoustic power against the frequency for varying incident mode orders: $j = -12$ (—), $j = 0$ (– –), $j = 6$ (····) and $j = 27$ (–·–).

Again, the acoustic power balance is well within the confidence range except in the transition ranges and at the resonant frequencies. When looking at the reflected and transmitted powers, the resonant frequencies are functions of the incident mode

order j. Indeed such a result is well known, since the incident mode order controls the inter-vane phase shift. However, a deeper look at the effect of the inter-vane phase shift, usually not mentioned, will be given in Section 3.6. The inter-vane phase shift is given by $\alpha_j b = 2\pi j/V$. The expected behavior is seen for $j = 0$ and $j = 27$, which respectively trigger the resonances in $1 \leq kb/\pi < 2$ (adjacent channels of equal phases) and $2 \leq kb/\pi < 3$ (adjacent channels of opposite phases). On the other hand, $j = -12$ and $j = 6$ also seem to trigger some resonances though, with a weaker strength.

Another important aspect of the incident mode order is the so-called "Venetian blind" configuration [44], when the incident wavefront is perpendicular to the vanes. In such a case, the acoustic wave is fully transmitted for flat vanes, without any influence of the cascade. The following results prove that such a configuration no longer exists when the vanes are curved. Figure 3.40 shows the pressure maps and associated modal contents for two different scenarios: $\Psi = 23.5°$ at $kb/\pi = 2.7$ and $\Psi = 27°$ at $kb/\pi = 2.45$. Both cases are calculated without flow and for a solidity value $l/b = 1.5$ and an incident mode order $j = 27$. In the right scenario (Figure 3.40b), nothing special

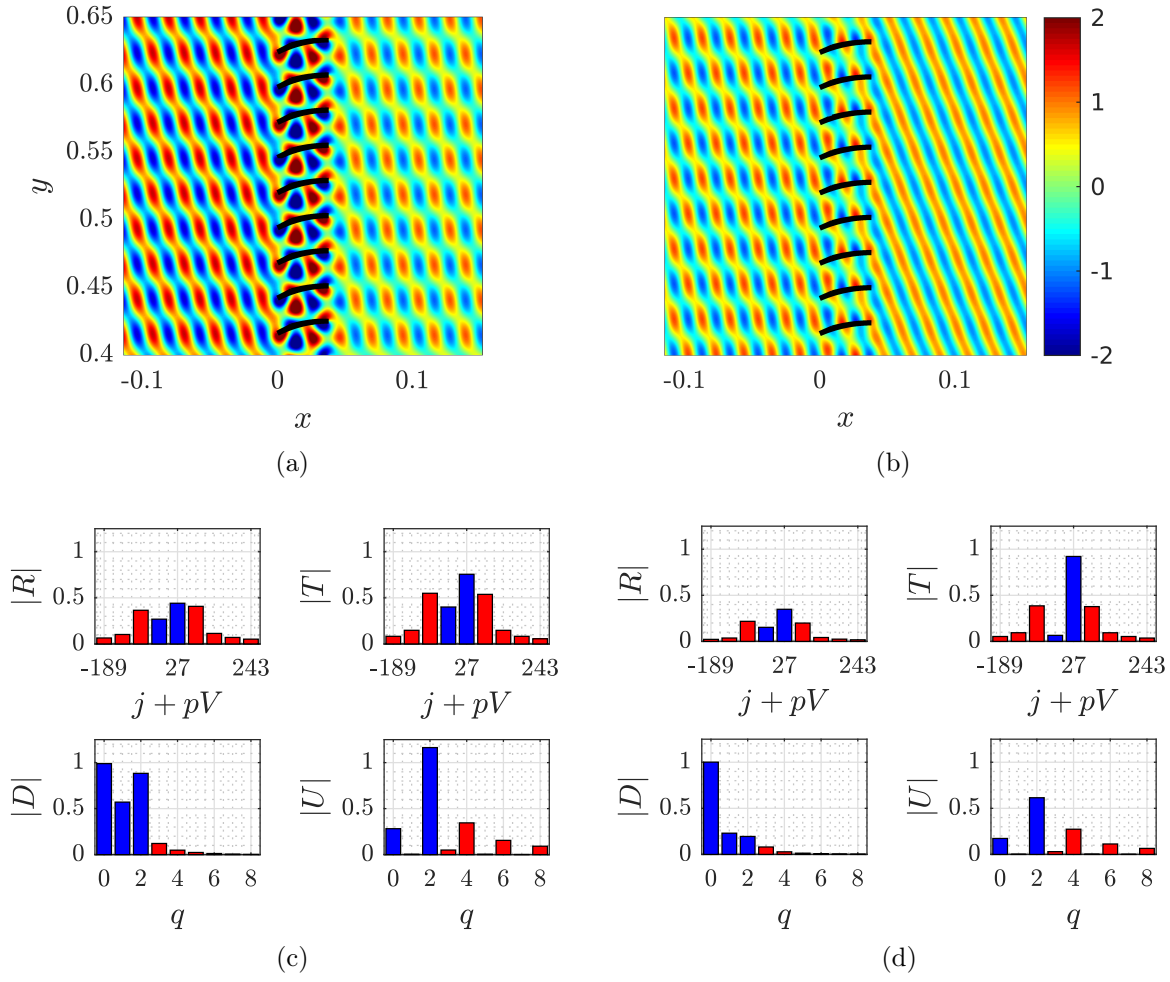

Figure 3.40: Pressure maps and corresponding modal contents without flow ($M_{-\infty} = 0$), for an incident wavefront perpendicular to the vane leading edges: with a resonance (a,c) and without (b,d).

happens, but the simple fact that the vanes are no longer parallel allows reflections to occur. The acoustic power balance in this case gives a reflected power of 14.49%

and a transmitted power of 85.36%. In the left scenario (Figure 3.40a), a resonance is even able to take place, which cannot happen with flat vanes in the "Venetian blind" configuration. The acoustic power balance in this case gives a reflected power of 26.73% and a transmitted power of 73.18%.

3.5.4 Influence of Mach Number

In the presence of a mean flow and a Kutta condition, the acoustic power balance can no longer be calculated in the same manner due to energy transfer between the acoustic and vortical motions. This energy transfer usually takes the form of a loss, in the point of view of the acoustic, which concedes energy to the wake downstream of the cascade. This acoustic energy loss has been investigated for a single plate in a ducted flow by, for example, Howe [49] with an analytical model for low-subsonic Mach numbers, and Job [56] with an efficient numerical finite element method. Recent works from Maierhofer & Peake [68] give an interesting insight into the distribution of radiated powers, between acoustic and hydrodynamic, for an infinite cascade of flat plates with a mean flow. Such a work could be used to better understand energy conversions in the current model and help to build an accurate estimation of the global power balance, so as to have a criterion to measure the accuracy of MMBCW even in the presence of a mean flow. Such a work has not been done during the PhD. The accuracy of the method cannot be estimated then, but the influence of the mean flow on the acoustic resonances, which is known [60], can at least be visualized. Figure 3.41 displays the balance and acoustic reflected power for $\Psi = 23°$, a solidity value of $l/b = 1.5$ and an incident mode order $j = 0$. The Mach number is either $M_{-\infty} = 0$ or $M_{-\infty} = 0.4$. The horizontal dashed lines representing the limits of the 1% confidence range in which the results can be trusted are also added, along the vertical dash-dotted lines showing the limits of the transition ranges.

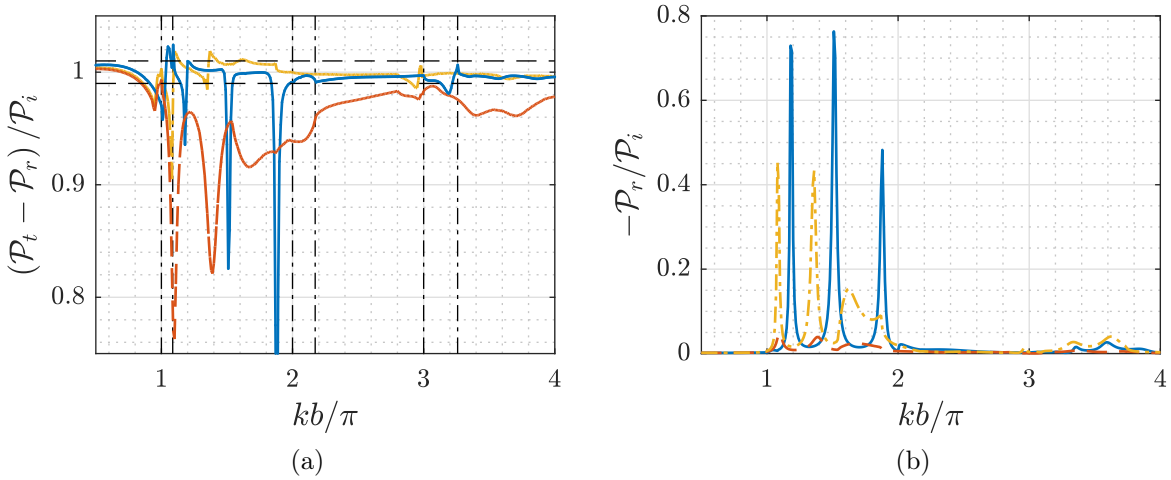

Figure 3.41: Acoustic power balance (a) and reflected acoustic power (b) against the frequency for $M_{-\infty} = 0$ (—), $M_{-\infty} = 0.4$ (– –) and $M_{-\infty} = 0.4$ without Kutta condition (-·-·).

Figure 3.41a shows that the presence of a mean flow induces a loss in the acoustic power in the whole range of frequencies studied. Note that, even if not reported here,

some scenarios of a transmitted acoustic power exceeding 100% happened. Whether this means that the acoustic field harvested energy from the mean flow, as reported by Maierhofer & Peake [68], or that the model was inaccurate remains an open question without a correct estimation of the hydrodynamic power. On the other hand, Figure 3.41b highlights the well known effect of the mean flow on the acoustic resonance, which consists in i) reducing the resonant frequencies and ii) adding a damping that lowers the resonance amplitude. In this case, an incident Mach number of 0.4 is sufficient to drastically attenuate the resonances.

Results are then provided for the transmission of the oblique incident wave of order $j = -12$ at $kb/\pi = 2.7$ in Figure 3.42 (pressure field), Figure 3.43 (axial velocity field) and Figure 3.44 (transverse velocity field). The mean flow increases the wavelength of

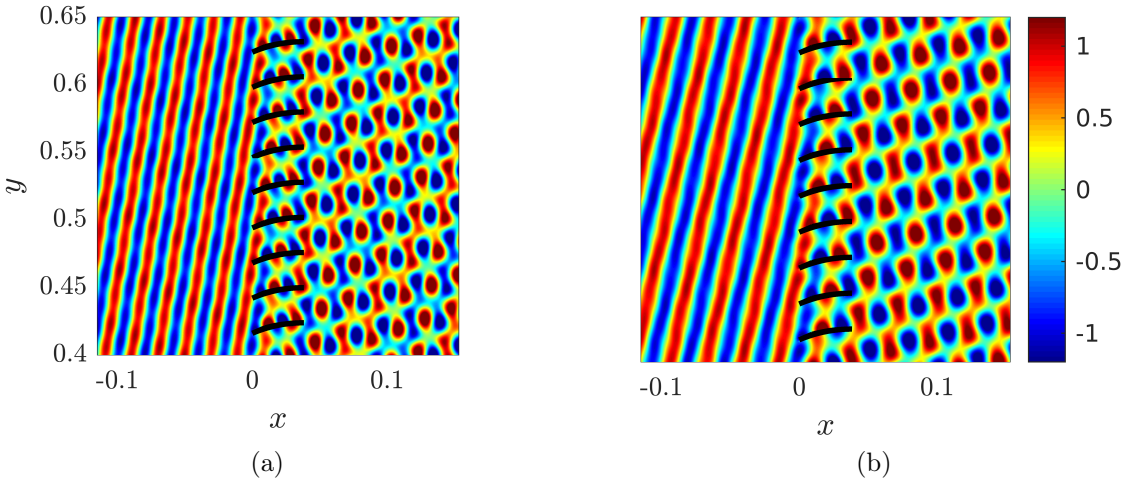

Figure 3.42: Pressure maps for an incident mode order $j = -12$ at $kb/\pi = 2.7$, a camber angle $\Psi = 23°$, a solidity value $l/b = 1.5$ and a Mach number $M_{-\infty} = 0$ (a) or $M_{-\infty} = 0.4$ (b).

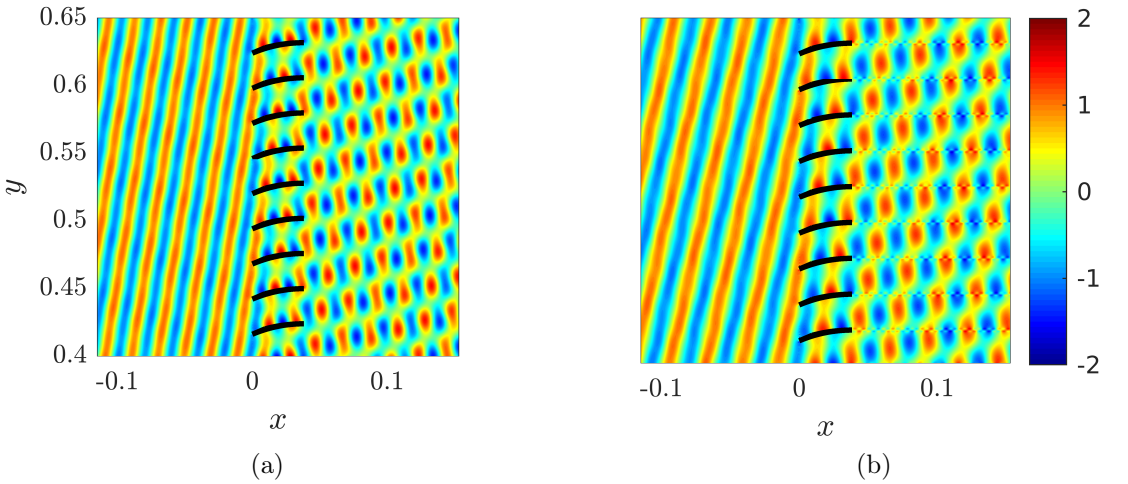

Figure 3.43: Axial velocity maps for an incident mode order $j = -12$ at $kb/\pi = 2.7$, a camber angle $\Psi = 23°$, a solidity value $l/b = 1.5$ and a Mach number $M_{-\infty} = 0$ (a) or $M_{-\infty} = 0.4$ (b).

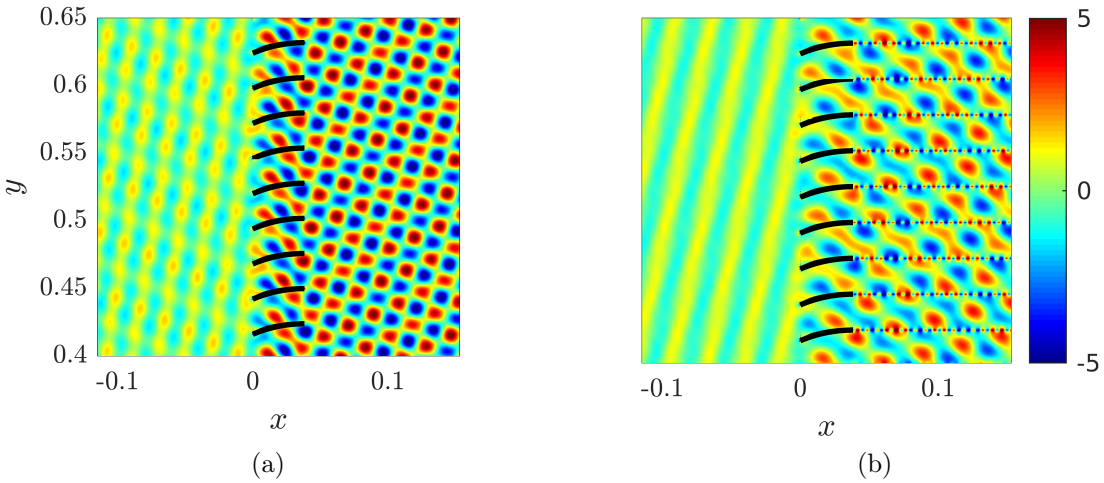

Figure 3.44: Transverse velocity maps for an incident mode order $j = -12$ at $kb/\pi = 2.7$, a camber angle $\Psi = 23°$, a solidity value $l/b = 1.5$ and a Mach number $M_{-\infty} = 0$ (a) or $M_{-\infty} = 0.4$ (b).

the incident and transmitted waves by convection effect, which is clearly visible since the reflection coefficient is low. The mean flow also seems to favor the transmitted mode that propagates in the closest direction to it, thus the lowest order $j = -12$ in this case. Finally, Figures 3.43 and 3.44 shows the presence of the vortex sheet induced by the Kutta condition. The transverse velocity field seems to be the most affected by the presence of the mean flow, with a noticeably reduced amplitude.

Parametric Studies — Summary

Acoustic power balance and accuracy of the method:

Increasing stagger/camber or decreasing solidity deteriorates the accuracy of the model. Around resonant frequencies, the accuracy depends on camber, solidity and incident mode order, and the 1% confidence range cannot be reached in some cases. In the presence of a mean flow, energy conversions between acoustic and vortical motions happens. The power contained in the vortical sheet induced by the Kutta condition has not been estimated in this work, hence the power balance can no longer serve as a measure of the accuracy in this case.

Influence of input parameters on sound:

Apart from the vicinity of the resonant frequencies, neither stagger/camber, solidity or incident mode order has a significant impact on the acoustic power balance between reflection and transmission. Although, stagger/camber and solidity do change the distribution of modal energy in the scattered fields for a given incident wave. Camber induces reflections in the inter-vane channels even when the incident wavefront is perfectly perpendicular to the vane leading edges. For flat vanes, such a configuration is sometimes called "Venetian blind" and leads to a fully transmitted field. With curved vanes, reflected scattered waves appear upstream of the cascade, and a resonance can even take place in the cascade.

3.6 Resonance of a Cascade of Cambered Vanes

The field of acoustic resonances relates to high-intensity fluctuations of the air volume comprised within the inter-vane channels, without involving the mechanical vibration of the plates. It has experienced a revival of interest when Parker [89] showed experimental proofs that such resonances can be triggered by vortex shedding in wind tunnels, and all other engineering systems involving air flowing over a cascade of flat parallel plates. Experimental evidences of such resonances have then been discovered for staggered flat plates in a compressor stage by Parker [90], and for cambered vanes in a bend by Honjo & Tominaga [48]. A number of attempts to predict the resonant frequencies by means of linear analysis have seen the day. For example, Koch [60] tackled the problem of a cascade of staggered flat plates with the Wiener-Hopf technique, and more recently relied on a numerical solution to address the acoustic resonances in three-dimensional annular plate cascades [61]. The latter provides a good overview of the historical evolution of knowledge about resonances in a compressor stage.

Nayfeh & Huddleston [79] developed a method based on mode matching to calculate the resonant frequencies. A similar procedure could then be used to study the resonances with the current model of cambered vanes. Unfortunately, time was missing to carry out such a study during the PhD. Consequently, two concessions were made:

1. resonant frequencies are found by looking for local maxima of the reflected acoustic power over a given frequency range, hence trapped modes cannot be identified;

2. results are calculated using the MMBW model, neglecting the effects of curvature. It is expected that the missing curvature effects induce uncertainty in the predicted resonant frequencies (see section 3.4), which could be plotted as error bars, but the overall shape and trend should be well captured in the restricted frequency range $1 \leq kb/\pi < 2$. All pressure maps are, however, computed with the MMBCW model.

The resonant frequencies are generally regrouped into "families", each family lying in a frequency range of unit length (in terms of kb/π) and involving a given channel mode. The channel mode $q = 0$ is responsible for the resonances happening in $0 \leq kb/\pi < 1$, the channel mode $q = 1$ then takes over for $1 \leq kb/\pi < 2$, and so on. This is usually pictured via the so-called "Parker mode diagram", representing the evolution of the resonant frequencies with the solidity value of the cascade. Thus, results are presented in this convenient form in the following.

3.6.1 Influence of Stagger and Camber

In the first instance, the influence of camber is studied. Figure 3.45 shows an example of resonance for a weakly cambered/staggered cascade ($\Psi = 5°$) and a more cambered/staggered cascade ($\Psi = 36°$).

As expected from a resonance, a relatively high pressure amplitude is seen in the inter-vane channels, with a particular pattern. The resonance pattern shows one horizontal nodal line and one vertical nodal line, thus four lobes alternatively vibrating within the inter-vane channels. The resonances can be named from those numbers. The resonance displayed in Figure 3.45 is called resonance (1,1), referring to its number of vertical and horizontal nodal lines respectively. The second number also happens to indicate the channel mode responsible for the resonance, which is the mode $q = 1$ in this

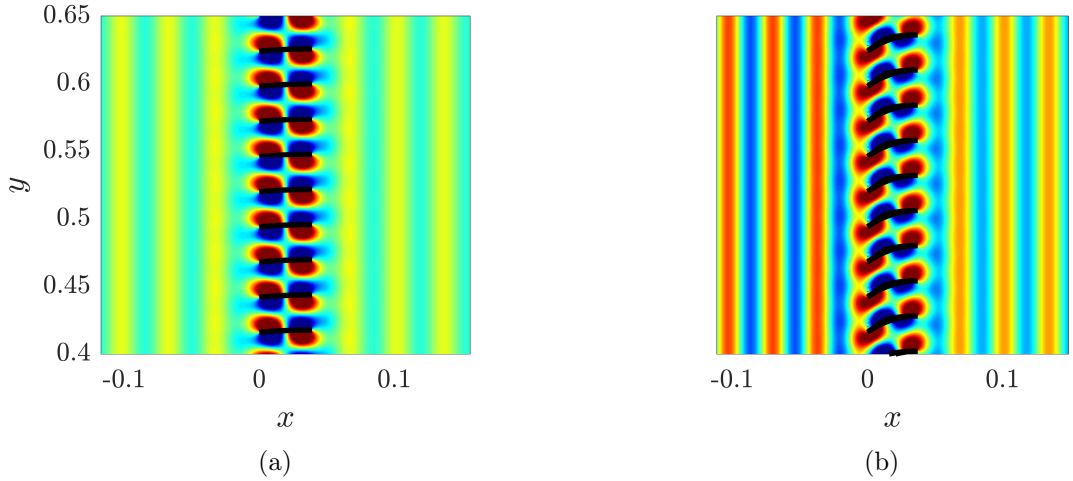

Figure 3.45: Resonance (1,1) seen in a cascade of $\Psi = 5°$ (a) and $\Psi = 36°$ (b), with $l/b = 1.5$ and $M_{-\infty} = 0$.

case. Figure 3.46 represents the "Parker mode diagram" for the family of resonances induced by the channel mode $q = 1$, at two different camber angles. As expected, the

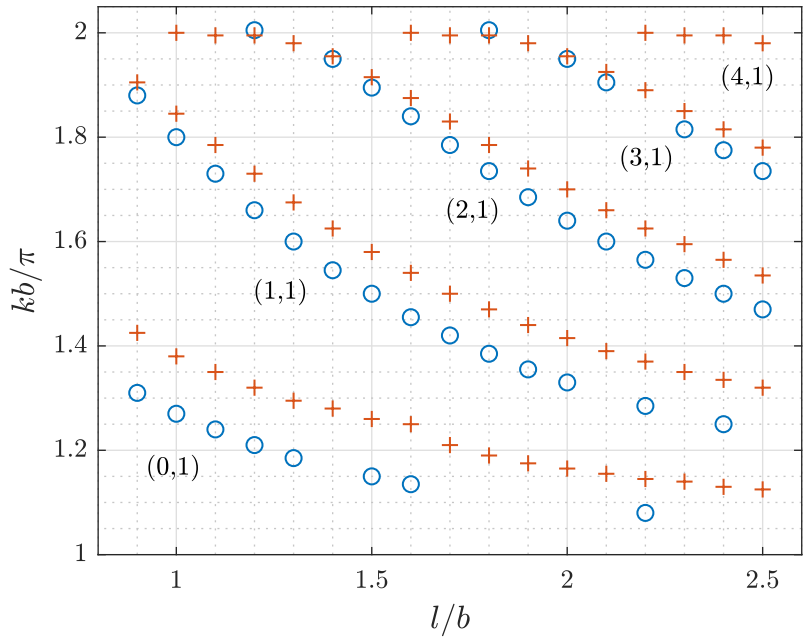

Figure 3.46: Parker-like mode diagram for resonances in $1 \leq kb/\pi = 2$, with $\Psi = 5°$ (○) and $\Psi = 36°$ (+).

resonant frequencies decrease with the solidity value and reach a limit at $kb/\pi = 2$ when the solidity value decreases. It is known that each resonance has a limiting solidity value below which it cannot exist, thus the curves can never cross. Notice that this limit is not necessarily reached in Figure 3.46 since some resonant frequencies have been missed by the searching algorithm.

The trend observed for stagger angle by Koch [60] is recovered: the resonant frequencies increase with Ψ. Camber seems to only exacerbate this effect.

3.6.2 Influence of Mach Number

Figure 3.47 and 3.48 display examples of the resonance (0,1) and the effect of the mean flow on the "Parker mode diagram", respectively.

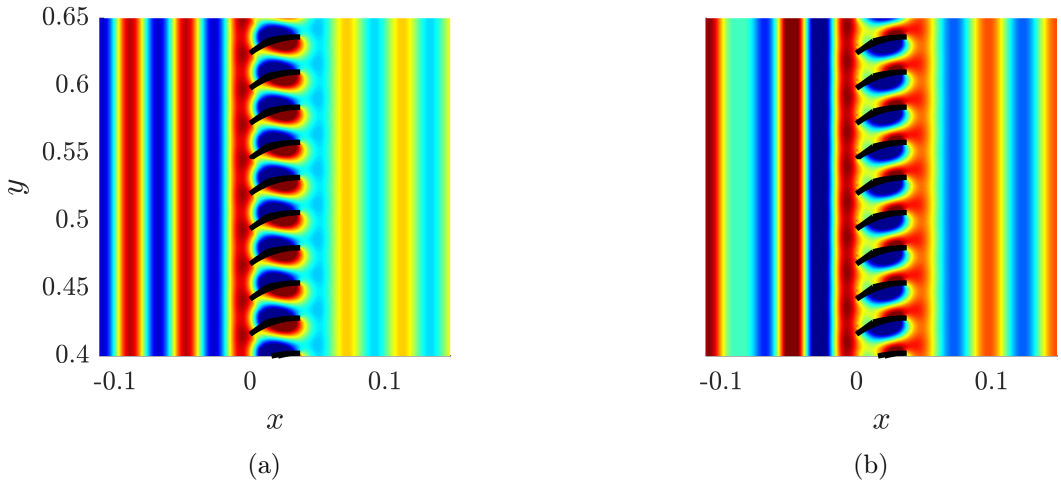

Figure 3.47: Resonance (0,1) with $M_{-\infty} = 0$ (a) and $M_{-\infty} = 0.4$ (b), with $\Psi = 36°$ and $l/b = 1.5$.

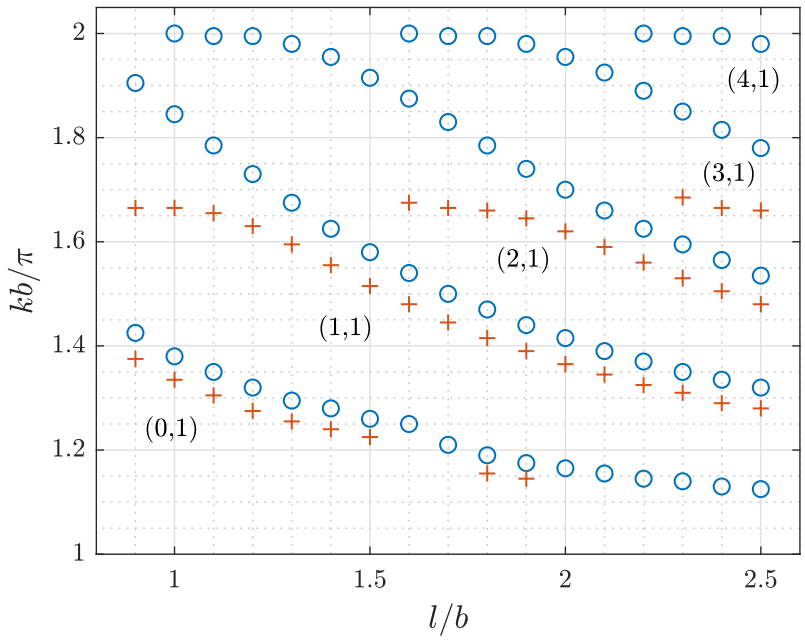

Figure 3.48: Real part of Parker-like mode diagram for resonances in $1 \leq kb/\pi = 2$, with $M_{-\infty} = 0$ (○) and $M_{-\infty} = 0.25$ (+).

It is clear from Figure 3.47b that the strength of the resonance has been drastically reduced with an incident Mach number $M_{-\infty} = 0.4$, compared to the no-flow case in Figure 3.47a. Moreover, when looking at the "Parker mode diagram", the resonant frequencies are reduced as expected but also seem to depend on solidity. The mean flow drastically reduces the frequencies at the lowest solidity values of existence for a given

resonance, but does not have a significant effect otherwise. Notice that some resonances related to the channel mode $q = 2$ can occur below $kb/\pi = 2$ with $M_{-\infty} = 0.25$ but have been discarded from Figure 3.48.

3.6.3 Influence of Incident Mode Order

Finally, the influence of the incident mode order on the resonance phenomenon is investigated to shed light on properties usually not mentioned in research papers. The resonances shown previously are what could be called "ideal" resonances. Those are triggered by an adequate inter-vane phase shift, which is controlled by the incident mode order in this case. When the resonance is related to an even channel mode order, $q = 0$, 2, ..., adjacent inter-vane channels need to be of opposite phases. On the contrary, when the resonance is related to an odd channel mode order, $q = 1$, 3, ..., adjacent inter-vane channels need to be in phase. Each resonance can only exist in a frequency range given by the corresponding channel mode order as $q \leq kb/\pi < q + 1$. The inter-vane phase shift is given by $\alpha_j b = 2\pi j/V$. Hence, to trigger the resonances related to $q = 1$, which occur in $1 \leq kb/\pi < 2$, the incident mode order needs to be an even multiple of the number of vanes V, in other words $j = 0\,[V]$. A resonance in this case exhibits pressure fluctuations that have a uniform and steady maximal amplitude over the cascade. On the contrary, when the phase shift is not ideal, a "resonance" can still occur but does not take place steadily throughout the whole cascade. Instead, the resonance appears in "patches" of noticeably high pressure, which move along the cascade with time. This can be seen in Figure 3.49 for the "non-ideal" resonance (2,1) with $j = 5$.

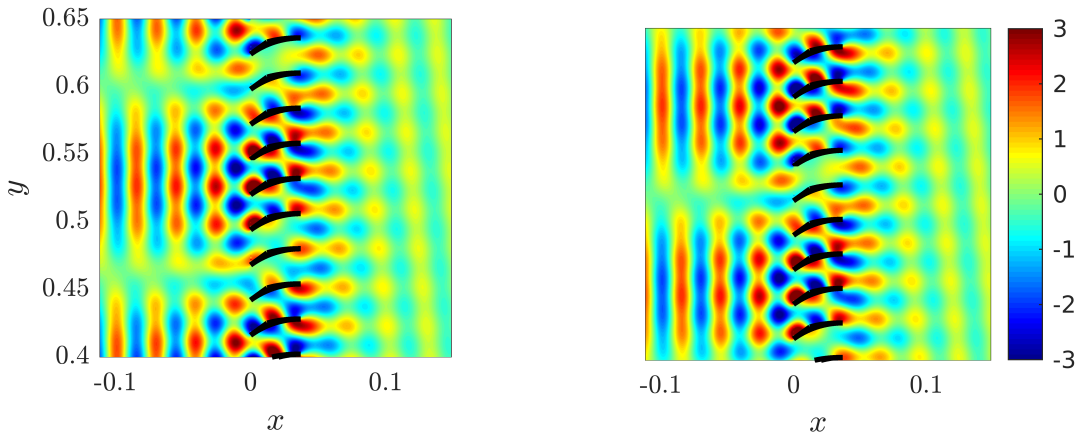

Figure 3.49: Resonance (2,1) seen in a cascade of $\Psi = 36°$ with $l/b = 1.5$, $M_{-\infty} = 0$ and $j = 5$, at $t = 0$ (a) and $t = 3\alpha_j b/\omega$ (b).

In fact, the "non-ideal" resonance represents the general case of resonance since the "ideal" scenario happens only for the particular phase shifts 0 and π in the continuous range $[0, 2\pi[$. For these two particular cases, the relation between the incident wavelength and the cascade periodicity creates a steady pattern. Otherwise, the resonance pattern is seen as modulated by the incoming wave. This modulation also generates an interesting pattern upstream of the cascade, as seen in Figure 3.50. Adjacent "patches" of resonance oscillate in phase opposition, generating destructive interference with the

incident field between each patch (seen as shadow zones upstream) and constructive interference in front of each patch (seen as high-amplitude plane waves concentrated in a layer of the patch height). The number of patches is two times the difference between the "ideal" incident mode order $j = 0$ and the current incident mode order j. Thus being equal to 0, 2, 8 and 10, respectively, in Figure 3.50. This indicates a modulation by the number of lobes of this difference: each positive lobe generates a patch of resonance oscillating in opposite phase with its neighbor, the latter being modulated by a negative lobe. This modulation is still seen around $j = 27$, for the resonances related to $q = 2$, where it might be less obvious that the modulation is given by the difference between the incident mode order j and the ideal mode order $j = 27$.

Finally, the Parker-like mode diagram is plotted for $j = 0$ and $j = 5$ in Figure 3.51. On the contrary to the effect of mean flow, the non-ideal phase shift does not just lower the resonant frequencies, it reduces their range of existence. In this case, no resonance can occur between $kb/\pi \simeq 1.8$ and $kb/\pi = 2$ for $j = 5$. Going to the limit $j = 27$ would totally cancel any resonance related to the channel mode $q = 1$, due to a phase shift in perfect opposite phase from the ideal phase shift of those resonances.

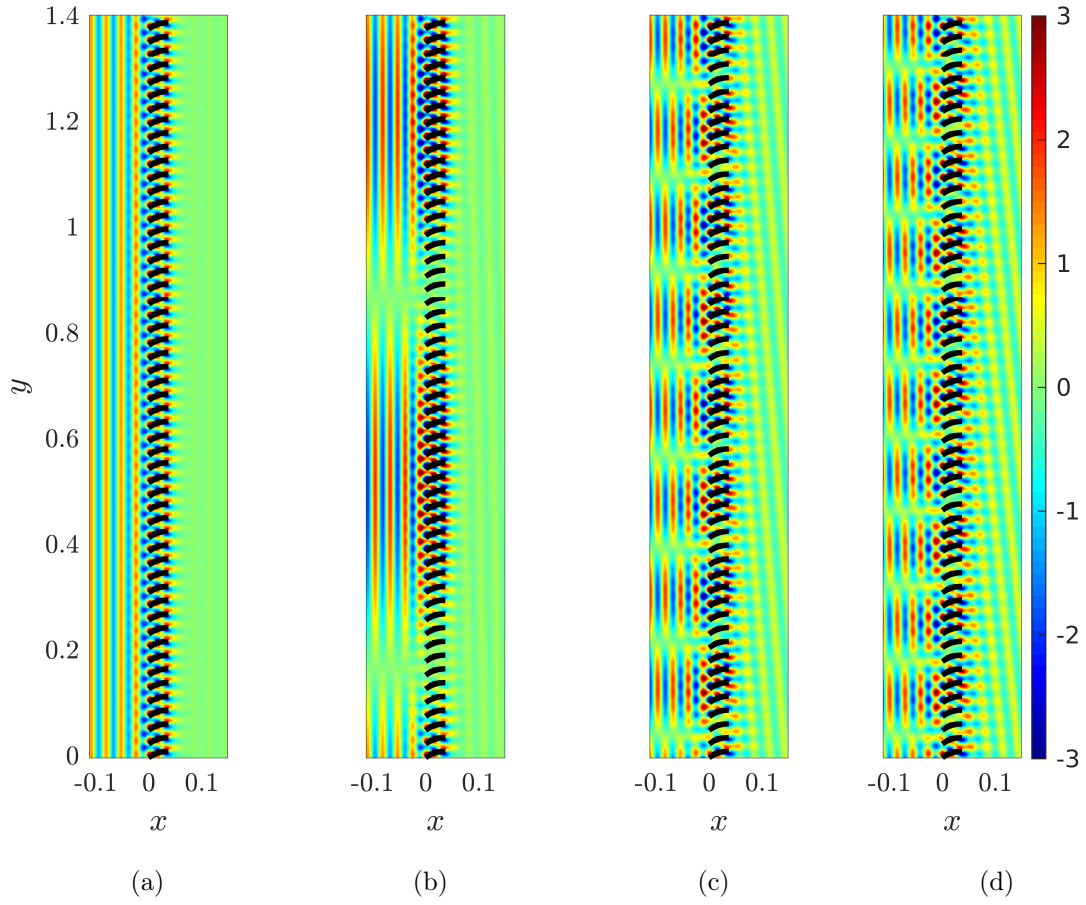

Figure 3.50: Resonance (2,1) seen in a cascade of $\Psi = 36°$, with $l/b = 1.5$ and $M_{-\infty} = 0$, for $j = 0$ (a), $j = 1$ (b), $j = 4$ (c) and $j = 5$ (d).

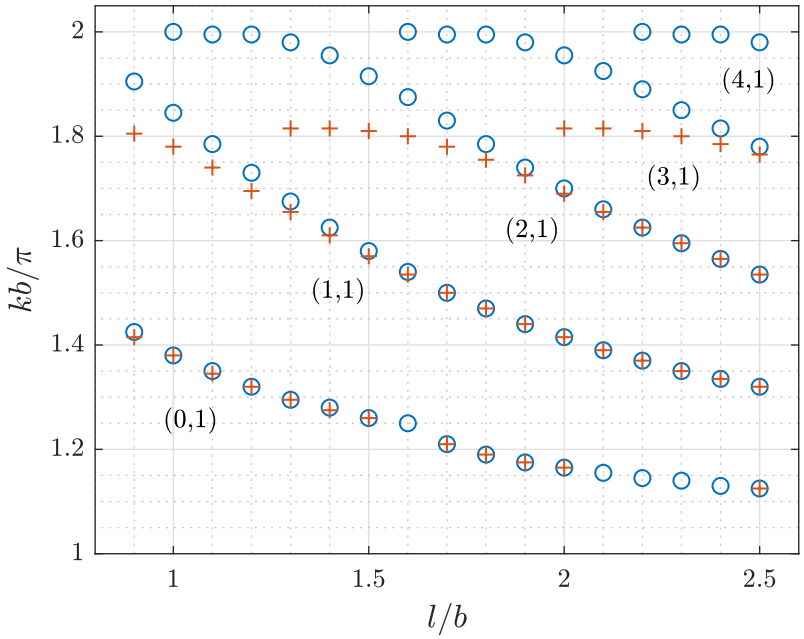

Figure 3.51: Parker-like mode diagram in $1 \leq kb/\pi = 2$, with $\Psi = 36°$, for "ideal" resonances $j = 0$ (○) and "non-ideal" resonances $j = 5$ (+).

Resonance of a Cascade of Cambered Vanes — Summary

The high amplitudes and non-linear mechanisms involved at resonant frequencies make the prediction too sensitive to numerical errors, thus the value of reflected and transmitted powers at such frequencies should be taken with care. Yet, the frequencies at which resonances occur should be reasonably well predicted within the scope of linear acoustics. "Parker mode diagrams" have been plotted for varying stagger/camber angles, Mach numbers and incident mode orders. The derivation of the system of equations providing the resonant frequencies is beyond the scope of the PhD, instead their estimation relies on a search for local maxima of the reflected power in a given frequency range. Computations have been performed with the MMBW model, neglecting curvature effects, which induces error bars in the frequencies (of the order of a few percents) but should give the correct trends. In that regard, the effect of camber seems similar to that of stagger. The mean flow, as already known, reduces the resonant frequencies and damps their amplitude. The incident mode order also significantly decreases the resonant frequencies, but only below a given solidity value, which depends on the resonance considered. A peculiar phenomenon, generally not mentioned in research papers, has also been brought to light when the incident mode order does not induce an "ideal" inter-vane phase shift for the resonance. In this case, the resonance pattern is seen as modulated by the incoming wave, instead of being uniform and seemingly attached to the cascade. The upstream reflected field is also drastically changed by this patchwork resonance. Shadow zones appear between the resonant patches and, in front of them, constructive interference with the incident wave generates a strong standing-wave pattern concentrated in a layer of the patch height.

3.7 Conclusion

The modeling of sound propagation in cambered inter-vane channels has been extended by taking into account curvature effects, thus relying on curvilinear coordinates instead of Cartesian coordinates to derive the equivalent convected Helmholtz-like equation. This equation, with hard wall boundary condition, has been rewritten as an eigenvalue problem, which has been solved numerically by means of a pseudo-spectral collocation method based on Chebyshev polynomials of the first kind. Though this two-dimensional problem has an exact closed-form solution in terms of Bessel functions without flow, and apparently in terms of confluent hypergeometric functions with flow [1], the choice was made to resort to a collocation method. This pseudo-spectral method ensures fast and accurate computations, with or without flow, and could be extended to three dimensions, where no closed-form solutions exist (except for rectangular ducts). Yet, the analytical solutions should be investigated to better understand the effects of curvature and mean flow.

The validity of each assumption in the model of Mode Matching for Bifurcated Curved Wave-guides (MMBCW) has been carefully investigated up to relatively high frequencies. The model remained accurate in terms of acoustic power balance but, in the presence of a mean flow with a Kutta conditions, energy conversions between acoustic and vortical motions can happen. Hence the acoustic power balance alone can no longer serve as a measure of the accuracy in this case. A more general power balance needs to be derived.

Comparisons with results of the previous model, referred to as MMBW, have shown that curvature effects are needed above the first channel cut-off frequency, except if camber and/or frequency remain small and the almost plane-wave mode is dominant in the channels.

Parametric studies have been carried out on the different physical parameters of the MMBCW model. Apart from the vicinity of the cascade resonant frequencies, neither stagger/camber, solidity or incident mode order has a significant impact on the acoustic power balance between reflection and transmission. Although, stagger/camber and solidity do change the distribution of modal energy in the scattered fields for a given incident wave. Furthermore, camber induces reflections in the inter-vane channels even when the incident wavefront is perfectly perpendicular to the vane leading edges. For flat vanes, such a configuration is sometimes called "Venetian blind" and leads to a fully transmitted field, without any reflection or scattering. With curved vanes, reflected scattered waves appear upstream of the cascade, and a resonance can even take place in it.

Acoustic resonances occurring above the cut-off frequency of the annular domain, thus putting aside trapped modes, have also been investigated, but with the MMBW model. Within the limitations of this model, it appeared that camber has a similar effect as stagger on resonant frequencies, which consists in an increase of the frequency when solidity is large enough, depending on the resonance considered. The influence of incident mode order has also been investigated since usually left aside in the literature. A peculiar phenomenon of resonance by layers was brought to light, due to a modulation induced by the incident wave when its wavelength no longer matches the cascade periodicity.

On the note of possible improvement, the MMBCW model could be extended to

account for a non-uniform mean flow inside the inter-vane channels, thus to account for some sort of mean loading effects. Enforcing the mean flow to be irrotational and divergence-free leads to the following description in two dimensions:

$$M_0(S,n) = \frac{M_{-\infty}\kappa a}{h_s(n)\ln\left(\frac{2+\kappa h(S)}{2-\kappa h(S)}\right)}.$$

In the assumption of small curvature $\kappa h(S) \ll 1, \forall S \in [0, L_c]$, this relation even reduces to

$$M_0(S,n) = \frac{M_{-\infty}a}{h_s(n)h(S)} + \mathcal{O}(\kappa h),$$

which is almost the same relation as for the uniform flow (3.4), except for a coefficient $h_s(n)$ driving the non-uniformity. Notice that, if the compressibility effects are to be accounted for, $M_0(S,n)$ no longer has an exact closed-form solution and a numerical integration of the mass-flow continuity equation is needed.

The new eigenvalue problem, already derived by Rienstra [110] in a more general case, could be solved by collocation. However, a new geometrical description of the vanes would be needed. The non-uniformity of the mean flow, in this case, directly depends on the curvature κ. With a constant camber distribution along the chord, i.e. vanes modeled as circle arcs, a discontinuity of the curvature is seen at the interface BC and the trailing-edge interface. Outside of the inter-vane channels, the curvature is $\kappa = 0$, and inside it, $\kappa = 1/\bar{R}_c$. In order to have a continuous description of the mean flow through the cascade, a new description of the vane camber distribution is needed. A Gaussian distribution could be used, or any combination of functions that ensures a curvature distribution going to 0 at both limits. This would remove the two-parts definition of the channels and the induced artificial thickness, thus describing the mean camber line only. This is currently an ongoing work.

On the other hand, frequency limitations have been observed due to modes undergoing transition from cut-off to cut-on or vice versa. This phenomenon is possible due to the varying channel height, inducing a varying cut-off frequency along the channel. The rapid variations that a mode undergoes in the vicinity of such transition were not accounted for in this chapter. An extension of the model of sound propagation is derived in the next chapter to include the transition mechanism in the mode-matching procedure.

Chapter 4

Cut-on/Cut-off Transition of Sound Inside Cambered Inter-Vane Channels

Introduction

A leading-order multiple-scale solution of the acoustic potential has been developed inside the inter-vane channels, assuming slow variations of the cross-section. With the variation of the cross-section also vary the acoustic modes cut-off frequencies. Hence, a given mode at a given frequency can be cut-on in one part of the channel and cut-off in the other part. The location at which the transition happens is called a turning point, or transition point. In its vicinity, the mode behavior changes too rapidly for the leading-order multiple-scale solution to remain valid. In this chapter, the approximate solution of the potential is regularized near the transition point and the impact of the cut-on/cut-off transition on the modal energy distribution is investigated. The extension is only made for the solution of Chapter 2, considering a straight duct, following the work of Rienstra [109] and Ovenden [86]. Transition in a bent duct, which Brambley & Peake [14] studied, has neither been derived nor implemented in the mode-matching procedure yet.

Contents

4.1 Transition Point Analysis

4.1.1 Boundary Layer

In chapter 2, the approximate solution for the acoustic potential inside the inter-vane channels was derived as (2.67)

$$\phi(X,y) \sim \frac{N(X)}{\sqrt{\sigma(X)}}\psi(X,y)\exp\left(\frac{\mathrm{i}}{\epsilon}\int^X \frac{k(\xi)M(\xi)}{\beta^2(\xi)}\,\mathrm{d}\xi\right) \times\left[I\exp\left(-\frac{\mathrm{i}}{\epsilon}\int^X \frac{k(\xi)\sigma(\xi)}{\beta^2(\xi)}\,\mathrm{d}\xi\right)+R\exp\left(\frac{\mathrm{i}}{\epsilon}\int^X \frac{k(\xi)\sigma(\xi)}{\beta^2(\xi)}\,\mathrm{d}\xi\right)\right].$$

The above expression fails when the medium and the channel height vary in such a way that, at some point $X = X_t$, the reduced axial wavenumber $\sigma(X_t) = 0$. In a small interval around X_t the mode does not vary slowly and a different approximation is needed. In the terminology of matched asymptotic expansions [47], this is a boundary layer in X. The following analysis is strongly based on Holmes' book [47] and so it is advised to look into it if any doubts remain.

In the outer region of this layer, the solutions on either side are named

$$\phi \sim \begin{cases}\phi_L(X,y;X_t) & \text{if} \quad X < X_t,\\ \phi_R(X,y;X_t) & \text{if} \quad X_t < X,\end{cases}$$

where

$$\phi_L(X,y;X_t) = \frac{N(X)}{\sqrt{\sigma(X)}}\psi(X,y)\exp\left(-\frac{\mathrm{i}}{\epsilon}\int_X^{X_t} \frac{k(\xi)M(\xi)}{\beta^2(\xi)}\,\mathrm{d}\xi\right) \times\left[A_L^+\exp\left(\frac{1}{\epsilon}\int_X^{X_t} \frac{k(\xi)|\sigma(\xi)|}{\beta^2(\xi)}\,\mathrm{d}\xi\right)+A_L^-\exp\left(-\frac{1}{\epsilon}\int_X^{X_t} \frac{k(\xi)|\sigma(\xi)|}{\beta^2(\xi)}\,\mathrm{d}\xi\right)\right], \tag{4.1}$$

$$\phi_R(X,y;X_t) = \frac{N(X)}{\sqrt{\sigma(X)}}\psi(X,y)\exp\left(\frac{\mathrm{i}}{\epsilon}\int_{X_t}^X \frac{k(\xi)M(\xi)}{\beta^2(\xi)}\,\mathrm{d}\xi\right) \times\left[A_R^+\exp\left(-\frac{\mathrm{i}}{\epsilon}\int_{X_t}^X \frac{k(\xi)\sigma(\xi)}{\beta^2(\xi)}\,\mathrm{d}\xi\right)+A_R^-\exp\left(\frac{\mathrm{i}}{\epsilon}\int_{X_t}^X \frac{k(\xi)\sigma(\xi)}{\beta^2(\xi)}\,\mathrm{d}\xi\right)\right], \tag{4.2}$$

and $(A_L^+, A_L^-, A_R^+, A_R^-) \in \mathbb{C}^4$ are arbitrary constants. They are represented in Figure 4.1 with a schematic view of the problem. Note that for the cut-off modes in ϕ_L, the chosen roots are $\sigma = -\mathrm{i}|\sigma|$ and $\sqrt{\sigma} = \mathrm{e}^{-\mathrm{i}\pi/4}\sqrt{|\sigma|}$.

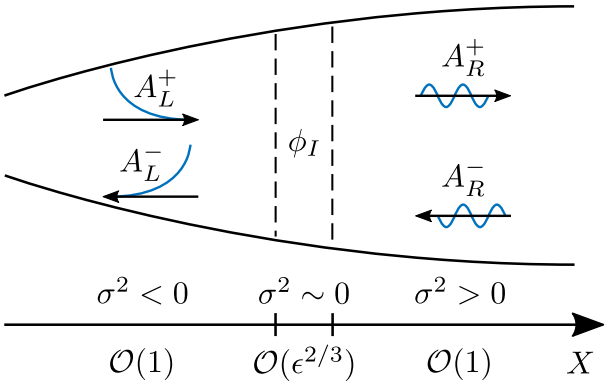

Figure 4.1: Sketch of a diverging duct with a boundary layer in X dividing the domain into two regions : a cut-off region on the left side and a cut-on region on the right side.

To understand the nature of the singularity, the analysis starts back from the convected wave equation at leading order (2.53):

$$\beta^2 \frac{\partial^2 \phi}{\partial x^2} + \frac{\partial^2 \phi}{\partial y^2} - 2\mathrm{i}kM\frac{\partial \phi}{\partial x} + k^2\phi = \mathcal{O}(\epsilon).$$

Using the Reissner transformation [101] adapted for a slowly-varying duct gives

$$\frac{\partial^2 \tilde{\phi}}{\partial \tilde{x}^2} + \frac{\partial^2 \tilde{\phi}}{\partial \tilde{y}^2} + \tilde{k}^2\tilde{\phi} = \mathcal{O}(\epsilon), \tag{4.3}$$

where $\tilde{x} = x/\beta$, $\tilde{k} = k/\beta$, $\tilde{\phi} = \phi \exp(-\mathrm{i}\int^{\tilde{x}} \tilde{k}M \,\mathrm{d}\tilde{\xi})$ and $\beta = \sqrt{1-M^2}$, all other variables being unchanged unless mentioned. Now, assuming that even when a transition occurs, the acoustic mode is still a solution of the eigenvalue problem (2.59) at leading order, the $\tilde{y}$-derivative $\partial^2/\partial\tilde{y}^2$ in (4.3) can be replaced by $-\tilde{\theta}^2$. Hence, using the relationship $\tilde{k}^2 - \tilde{\theta}^2 = \tilde{k}^2\tilde{\sigma}^2$ and replacing the variable $\tilde{x}$ by the slow variable $\tilde{X} = \epsilon\tilde{x}$, the Helmholtz equation becomes

$$\epsilon^2 \frac{\partial^2 \tilde{\phi}}{\partial \tilde{X}^2} + \tilde{k}^2\tilde{\sigma}^2(\tilde{X})\tilde{\phi} = \mathcal{O}(\epsilon). \tag{4.4}$$

This equation is known to have a turning point when $\tilde{\sigma}^2(\tilde{X}) = 0$ (see Ref. [47] Chapter 4.3). In the inter-vane channels, the increasing height governs the variation of $\tilde{\sigma}^2$. Since it is a monotonously increasing function, if a point $\tilde{X}_t$ exists, it is always a single transition point for the mode considered (see Figure 4.2).

As depicted in Figure 4.1 the transition point is not actually a point but a layer in which the potential behaves differently. The solution in this layer, called the inner solution ϕ_I, is described in the following.

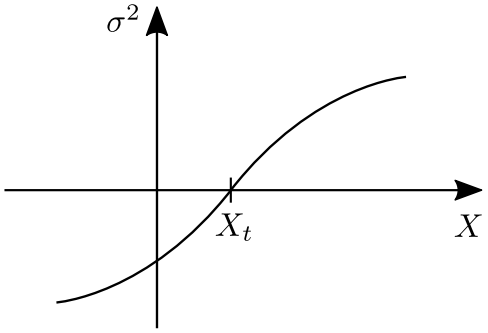

Figure 4.2: Sketch of the evolution of $\sigma^2(X)$ in the inter-vane channels.

4.1.2 Inner Solution

The first step in deriving the inner solution ϕ_I of (4.4) is to determine the boundary-layer thickness. Introducing a boundary-layer variable

$$X_\delta = \frac{\tilde{X} - \tilde{X}_t}{\epsilon^\delta},$$

Taylor's theorem states that

$$\tilde{\sigma}^2(\tilde{X}) = \tilde{\sigma}^2(\tilde{X}_t + \epsilon^\delta X_\delta) = \epsilon^\delta X_\delta (\tilde{\sigma}^2)'_t + \mathcal{O}(\epsilon^{2\delta}),$$

where the prime symbol denotes the derivative of $\tilde{\sigma}^2$ and the subscript t the evaluation of the function at the transition location $\tilde{X} = \tilde{X}_t$. Applying the stretching to (4.4) and letting $\phi_I(X_\delta, y)$ be the solution in this layer, gives

$$\epsilon^{2-2\delta} \frac{\partial^2 \phi_I}{\partial X_\delta^2} + \epsilon^\delta \tilde{k}_t^2 X_\delta (\tilde{\sigma}^2)'_t \phi_I = \mathcal{O}(\epsilon) + \mathcal{O}(\epsilon^{2\delta}). \tag{4.5}$$

For balancing it is required that $2 - 2\delta = \delta$, and so $\delta = 2/3$. It also agrees with the order of magnitude of the neglected term $\mathcal{O}(\epsilon^{2\delta}) = \mathcal{O}(\epsilon^{4/3})$ which is then lower than $\mathcal{O}(\epsilon)$. This demonstrates the order of magnitude of the boundary-layer thickness shown in Figure 4.1.

In order to derive the inner solution $\phi_I(X_\delta, y)$, its transverse structure is assumed unaffected in the relatively short transition region, which is consistent with the approximation of the $\tilde{y}$-derivative $\partial^2/\partial\tilde{y}^2$ in (4.3). It reads

$$\phi_I(X_\delta, y) = \chi(X_\delta)\psi(X, y), \tag{4.6}$$

where $X = X_t + \beta\epsilon^{2/3} X_\delta$ and so $\psi(X, y)$ is the same transverse function, or modal shape, as defined in (2.62) for the outer solutions.

The appropriate expansion of the unknown inner function $\chi(X_\delta)$ is

$$\chi = \epsilon^\gamma \chi_0 + \mathcal{O}(\epsilon^{2\gamma}). \tag{4.7}$$

Introducing this into (4.5) yields the equation

$$\epsilon^{\gamma+2/3} \chi_0'' + \epsilon^{\gamma+2/3} \tilde{k}_t^2 X_\delta (\tilde{\sigma}^2)'_t \chi_0 = \mathcal{O}(\epsilon), \tag{4.8}$$

which requires $\gamma < 1/3$. Letting $r = X_\delta \left(\tilde{k}_t^2 (\tilde{\sigma}^2)'_t\right)^{1/3}$ be a dimensionless inner coordinate, it appears that the inner function is the solution of Airy's equation at leading order, which is

$$\chi_0'' + r\chi_0 = 0, \quad \text{for } -\infty < r < \infty. \tag{4.9}$$

The general solution can be written as

$$\chi_0 = a\mathrm{A_i}(-r) + b\mathrm{B_i}(-r), \tag{4.10}$$

where $\mathrm{A_i}$ and $\mathrm{B_i}$ are Airy functions of the first and second kinds, respectively, and a and b are arbitrary constants. Note that r is of the same sign as X_δ, since $(\tilde{\sigma}^2)'_t > 0$ (Figure 4.2), and so the argument of the Airy functions is positive on the left side of the transition and negative on the right side. This is understandable since the mode goes from cut-off to cut-on in the case studied, hence the Airy functions need to be traveled in the negative direction (see Figure 4.3).

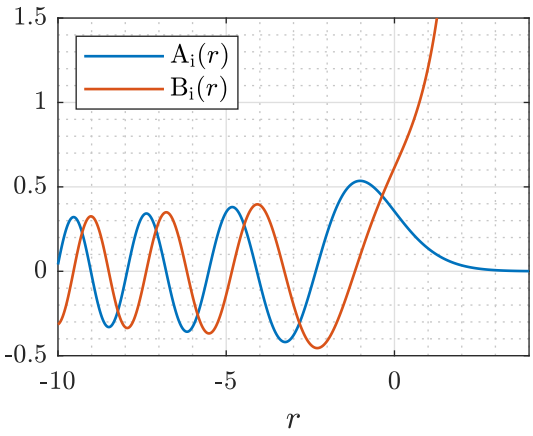

Figure 4.3: Airy functions.

Finally the inner solution is written at leading order as

$$\phi_I(X,y) = \left[a\mathrm{A_i}\left(-\lambda\frac{X-X_t}{\epsilon^{2/3}}\right) + b\mathrm{B_i}\left(-\lambda\frac{X-X_t}{\epsilon^{2/3}}\right)\right]\psi(X,y)\exp\left(\frac{\mathrm{i}}{\epsilon}\int_{X_t}^{X}\frac{kM}{\beta^2}\,\mathrm{d}\xi\right), \tag{4.11}$$

for $|X - X_t| = \mathcal{O}(\epsilon^{2/3})$ and where λ is defined by

$$\lambda^3 = \frac{k_t^2(\sigma^2)'_t}{\beta_t^4} > 0.$$

Note that the coefficient λ here is not equivalent to the coefficient λ in Refs. [109, 86]. It has to be multiplied by $-k_t^2/\beta_t^2\theta_t^2$ to recover the value of the aforementioned authors.

4.1.3 Matching

To determine the waves coefficients in the outer region, a matching between the outer solutions (4.1 - 4.2) and the inner solution (4.11) is necessary. To do so an intermediate variable is introduced, which corresponds to the intermediate region at each side of the

boundary layer where the inner solution overlaps the outer solutions. Let

$$X_\eta = \frac{X - X_t}{\epsilon^\eta},$$

where $0 < \eta < 2/3$. Both outer solutions and the inner solution are expressed in terms of the intermediate variable X_η to be matched.

Matching for $X < X_t$

In the cut-off region $X < X_t$, the inner variable $r = \lambda\epsilon^{\eta-2/3}X_\eta$ is negative. Thus the asymptotic expansion of Airy functions given in Appendix C.1 yields

$$\chi(-r) \sim a\epsilon^\gamma \frac{\exp\left(-\frac{2}{3}(-r)^{3/2}\right)}{2\sqrt{\pi}(-r)^{1/4}} + b\epsilon^\gamma \frac{\exp\left(\frac{2}{3}(-r)^{3/2}\right)}{\sqrt{\pi}(-r)^{1/4}}.$$

The evanescent integral to be evaluated in the outer solution (4.1) is

$$\begin{aligned}\frac{1}{\epsilon}\int_{X_\eta}^0 \frac{k|\sigma|}{\beta^2}\,\mathrm{d}\xi_\eta &\sim -\frac{1}{\epsilon}\lambda^{3/2}\int_{X_\eta}^0 \sqrt{\epsilon^\eta(-\xi_\eta)}\,\mathrm{d}\xi_\eta \\ &= \lambda^{3/2}\frac{2}{3}\epsilon^{3/2\eta-1}(-X_\eta)^{3/2} \\ &= \frac{2}{3}(-r)^{3/2}.\end{aligned}$$

The amplitude of (4.1) in the intermediate region is

$$\begin{aligned}\frac{N}{\sqrt{\sigma}} &\sim N_t\frac{\sqrt{k_t}}{\beta_t}\left[-\epsilon^\eta(-X_\eta)\lambda^3\right]^{-1/4} \\ &= \frac{\bar{N}_t \mathrm{e}^{\mathrm{i}\pi/4}}{\epsilon^{1/6}\lambda^{1/2}(-r)^{1/4}},\end{aligned}$$

where $\bar{N}_t = N_t k_t^{1/2}/\beta_t$. Then the matching gives

$$\begin{aligned}a\epsilon^\gamma \frac{\exp\left(-\frac{2}{3}(-r)^{3/2}\right)}{2\sqrt{\pi}(-r)^{1/4}} + b\epsilon^\gamma \frac{\exp\left(\frac{2}{3}(-r)^{3/2}\right)}{\sqrt{\pi}(-r)^{1/4}} = \frac{\bar{N}_t \mathrm{e}^{\mathrm{i}\pi/4}}{\epsilon^{1/6}\lambda^{1/2}(-r)^{1/4}}&\left[A_L^+ \exp\left(\frac{2}{3}(-r)^{3/2}\right)\right. \\ &\left. + A_L^- \exp\left(-\frac{2}{3}(-r)^{3/2}\right)\right],\end{aligned}$$

which implies $\gamma = -1/6$ and

$$\begin{cases} A_L^+ = \dfrac{\mathrm{e}^{-\mathrm{i}\pi/4}\lambda^{1/2}}{\bar{N}_t\sqrt{\pi}}b, \\ A_L^- = \dfrac{\mathrm{e}^{-\mathrm{i}\pi/4}\lambda^{1/2}}{2\bar{N}_t\sqrt{\pi}}a. \end{cases} \tag{4.12}$$

Matching for $X > X_t$

When $X > X_t$, in the cut-on region, the inner variable $r = \lambda\epsilon^{\eta-2/3}X_\eta$ is positive. The asymptotic expansion of Airy functions given in Appendix C.1 gives

$$\chi(-r) \sim a\epsilon^\gamma \frac{\cos\left(\frac{2}{3}r^{3/2} - \frac{\pi}{4}\right)}{\sqrt{\pi}r^{1/4}} - b\epsilon^\gamma \frac{\sin\left(\frac{2}{3}r^{3/2} - \frac{\pi}{4}\right)}{\sqrt{\pi}r^{1/4}}.$$

The propagating integral in (4.2) is

$$\begin{aligned}\frac{1}{\epsilon}\int_0^{X_\eta} \frac{k\sigma}{\beta^2}\,\mathrm{d}\xi_\eta &\sim \frac{1}{\epsilon}\lambda^{3/2}\int_0^{X_\eta}\sqrt{\epsilon^\eta \xi_\eta}\,\mathrm{d}\xi_\eta \\ &= \lambda^{3/2}\frac{2}{3}\epsilon^{3/2\eta-1}X_\eta^{3/2} \\ &= \frac{2}{3}r^{3/2},\end{aligned}$$

and the amplitude is

$$\begin{aligned}\frac{N}{\sqrt{\sigma}} &\sim N_t\frac{\sqrt{k_t}}{\beta_t}\left(\epsilon^\eta X_\eta\lambda^3\right)^{-1/4} \\ &= \frac{\bar{N}_t}{\epsilon^{1/6}\lambda^{1/2}r^{1/4}},\end{aligned}$$

where $\bar{N}_t = N_t k_t^{1/2}/\beta_t$. The matching gives

$$\begin{aligned}a\epsilon^\gamma \frac{\cos\left(\frac{2}{3}r^{3/2} - \frac{\pi}{4}\right)}{\sqrt{\pi}r^{1/4}} - b\epsilon^\gamma \frac{\sin\left(\frac{2}{3}r^{3/2} - \frac{\pi}{4}\right)}{\sqrt{\pi}r^{1/4}} = \frac{\bar{N}_t}{\epsilon^{1/6}\lambda^{1/2}r^{1/4}}&\left[A_R^+\exp\left(-\mathrm{i}\frac{2}{3}r^{3/2}\right)\right. \\ &\left.+A_R^-\exp\left(\mathrm{i}\frac{2}{3}r^{3/2}\right)\right].\end{aligned}$$

The value $\gamma = -1/6$ is retrieved and the outer-right coefficients are related to the inner coefficients by

$$\begin{cases} A_R^+ = \dfrac{\mathrm{e}^{-\mathrm{i}\pi/4}\lambda^{1/2}}{2\bar{N}_t\sqrt{\pi}}(\mathrm{i}a + b), \\ A_R^- = \dfrac{\mathrm{e}^{-\mathrm{i}\pi/4}\lambda^{1/2}}{2\bar{N}_t\sqrt{\pi}}(a + \mathrm{i}b). \end{cases} \tag{4.13}$$

4.1.4 Connection Formulas

The systems of equations (4.12) and (4.13) form what is known as the connection formulas between both sides of the boundary layer and are summed up by

$$\begin{pmatrix} A_L^- \\ A_R^+ \end{pmatrix} = \begin{bmatrix} -\mathrm{i}/2 & 1 \\ 1 & \mathrm{i} \end{bmatrix} \begin{pmatrix} A_L^+ \\ A_R^- \end{pmatrix}. \tag{4.14}$$

They are expressed in a way that is useful for the implementation in the mode-matching procedure since the coefficients A_L^+ and A_R^- are the known inputs. For example, Rienstra [108, 109] and Ovenden [87, 88] investigated the case of a transition for an incident cut-on mode in a infinite duct, which corresponds to $A_L^+ = 0$ and $A_R^- = 1$, and they found the same result: reflection coefficient $A_R^+ = \mathrm{i}$ and transmission coefficient $A_L^- = 1$.

Furthermore, Ovenden [88] also treated the case of an incident cut-off mode undergoing transition, transposing to $A_L^+ = 1$ and $A_R^- = 0$, but didn't explicitly derived the reflection and transmission coefficients. Though it will appear that the same result is obtained by looking at the composite solution later on: reflection coefficient $A_L^- = -\mathrm{i}/2$ and transmission coefficient $A_R^+ = 1$.

In both cases the transmission coefficient is the same but the reflection coefficient has a phase shift of either $+\pi/2$ or $-\pi/2$ and in the case of an incident cut-off mode the amplitude is also halved. This reduces noticeably the impact of the reflected cut-off mode at the leading-edge interface. The significant outcome should then be the transmitted cut-on mode which, if the transition appears sufficiently close to the leading edge compared to the decaying rate of the cut-off mode, could carry energy to the trailing-edge interface by acoustic tunnel effect. On the other hand, for an incident cut-on mode, the reflection at the transition generates a standing wave in the cut-on region. Indeed it could have a significant impact if the mode undergoing transition starts to prevail over the other modes in the inter-vane channels.

In order to attest the impact of such phenomena, the mode-matching procedure needs to be modified to account for the reflected part of the modes undergoing transition. This could be implemented with the actual piece-wise solution (ϕ_L, ϕ_I, ϕ_R) but the choice of the solution to use depending on the transition location is problematic and could end up to a wrong evaluation of the potential. To solve this issue, a composite solution valid throughout the whole channel, inside and outside the transition region, is now derived.

4.1.5 Uniformly Valid Solution

Langer [63] seems to be the first to give a uniform solution to such a mathematical problem. In the field of slowly-varying duct acoustics, Nayfeh & Telionis [83] derived a solution for converging hard-walled rectangular and circular ducts without flow. Then Ovenden [86] expressed the solution for slowly-varying ducts with irrotational flow and arbitrary cross-section. The final result was always given for an incident cut-on mode in an infinitely long duct and, as a consequence, the exponentially growing term beyond the turning point was discarded. In the inter-vane channels, this discarded term corresponds to an incident cut-off mode generated at the leading-edge interface and cannot be neglected. In order to account for this cut-off mode, the mathematical procedure used by Ovenden [86] is followed and adapted for a more general case where no solution of the Helmholtz equation is discarded in the outer solutions.

Mimicking the form of the outer solutions (4.1 – 4.2) and inner solution (4.11), the desired composite solution $\tilde{\phi}$ of (4.4) is expressed as

$$\tilde{\phi}(\tilde{X}, y) = \tilde{f}(\tilde{X}, y)\chi(r). \tag{4.15}$$

The function $\tilde{f}(\tilde{X}, y)$ represents the slowly varying part in terms of the slow variable $\tilde{X}$ while $\chi(r)$ is a transitional part around the turning point. Knowing the boundary-layer thickness from the balancing in (4.5) leads to choose

$$r = \frac{g(\tilde{X})}{\epsilon^{2/3}},$$

where the function g remains unknown at the moment. Substituting these expressions

into (4.4) gives

$$\epsilon^{2/3}(g')^2\chi'' + \tilde{k}^2\tilde{\sigma}^2\chi = \mathcal{O}(\epsilon). \tag{4.16}$$

Letting

$$r = \frac{g}{\epsilon^{2/3}} = \frac{\tilde{k}^2\tilde{\sigma}^2}{\epsilon^{2/3}(g')^2}, \tag{4.17}$$

and introducing it into (4.16) concludes that the transitional function χ is solution of Airy's equation at leading order

$$\chi''(r) + r\chi(r) = \mathcal{O}(\epsilon), \tag{4.18}$$

whose general solution is

$$\chi(r) = a\mathrm{A_i}(-r) + b\mathrm{B_i}(-r). \tag{4.19}$$

The variable r can be expressed after solving the ordinary differential equation on $g(\tilde{X})$ in (4.17) as

$$r = \begin{cases} -\left(\dfrac{3}{2\epsilon}\displaystyle\int_{\tilde{X}}^{\tilde{X}_t} \tilde{k}|\tilde{\sigma}|\,\mathrm{d}\tilde{\xi}\right)^{2/3} & < 0 \quad \text{if} \quad \tilde{X} < \tilde{X}_t, \\ \left(\dfrac{3}{2\epsilon}\displaystyle\int_{\tilde{X}_t}^{\tilde{X}} \tilde{k}|\tilde{\sigma}|\,\mathrm{d}\tilde{\xi}\right)^{2/3} & \geq 0 \quad \text{if} \quad \tilde{X}_t \leq \tilde{X}, \end{cases}$$

so that r is negative real for $\tilde{X} < \tilde{X}_t$ (cut-off region) and positive real for $\tilde{X} \geq \tilde{X}_t$ (cut-on region). The uniform solution (4.15) is now written as

$$\tilde{\phi}(\tilde{X}, y) = \tilde{f}_1(\tilde{X}, y)\mathrm{A_i}(-r) + \tilde{f}_2(\tilde{X}, y)\mathrm{B_i}(-r). \tag{4.20}$$

An expression for $\tilde{f}_1$ and $\tilde{f}_2$ is found by knowing that, far beyond the transition location, the composite solution (4.20) must match the outer solutions (4.1 – 4.2). These outer solutions are recast into

$$\tilde{\phi}_L(\tilde{X}, y) = \frac{\tilde{N}(\tilde{X})}{\sqrt{\tilde{\sigma}(\tilde{X})}}\tilde{\psi}(\tilde{X}, y)\left[A_L^+ \exp\left(\frac{2}{3}(-r)^{3/2}\right) + A_L^- \exp\left(-\frac{2}{3}(-r)^{3/2}\right)\right],$$

for $\tilde{X} < \tilde{X}_t$ and

$$\tilde{\phi}_R(\tilde{X}, y) = \frac{\tilde{N}(\tilde{X})}{\sqrt{\tilde{\sigma}(\tilde{X})}}\tilde{\psi}(\tilde{X}, y)\left[A_R^+ \exp\left(-\mathrm{i}\frac{2}{3}r^{3/2}\right) + A_R^- \exp\left(\mathrm{i}\frac{2}{3}r^{3/2}\right)\right],$$

for $\tilde{X} > \tilde{X}_t$. Hence using the asymptotic expansion of Airy functions in Appendix C.1, the matching at $r \to \pm\infty$ yields at leading order

$$\tilde{f}_1(\tilde{X}, y) = 2\sqrt{\pi}\exp\left(\frac{\mathrm{i}\pi}{4}\right)\tilde{N}(\tilde{X})\tilde{\psi}(\tilde{X}, y)\left(\frac{3}{2\epsilon}\frac{1}{|\tilde{\sigma}|^3}\int_{\tilde{X}_t}^{\tilde{X}} \tilde{k}|\tilde{\sigma}|\,\mathrm{d}\tilde{\xi}\right)^{1/6} A_L^-,$$

$$\tilde{f}_2(\tilde{X}, y) = \sqrt{\pi}\exp\left(\frac{\mathrm{i}\pi}{4}\right)\tilde{N}(\tilde{X})\tilde{\psi}(\tilde{X}, y)\left(\frac{3}{2\epsilon}\frac{1}{|\tilde{\sigma}|^3}\int_{\tilde{X}_t}^{\tilde{X}} \tilde{k}|\tilde{\sigma}|\,\mathrm{d}\tilde{\xi}\right)^{1/6} A_L^+,$$

for $r \to -\infty$ and

$$\tilde{f}_1(\tilde{X}, y) = \sqrt{\pi}\exp\left(\frac{\mathrm{i}\pi}{4}\right)\tilde{N}(\tilde{X})\tilde{\psi}(\tilde{X}, y)\left(\frac{3}{2\epsilon}\frac{1}{|\tilde{\sigma}|^3}\int_{\tilde{X}_t}^{\tilde{X}}\tilde{k}|\tilde{\sigma}|\,\mathrm{d}\tilde{\xi}\right)^{1/6}(A_R^- - \mathrm{i}A_R^+),$$

$$\tilde{f}_2(\tilde{X}, y) = \sqrt{\pi}\exp\left(\frac{\mathrm{i}\pi}{4}\right)\tilde{N}(\tilde{X})\tilde{\psi}(\tilde{X}, y)\left(\frac{3}{2\epsilon}\frac{1}{|\tilde{\sigma}|^3}\int_{\tilde{X}_t}^{\tilde{X}}\tilde{k}|\tilde{\sigma}|\,\mathrm{d}\tilde{\xi}\right)^{1/6}(A_R^+ - \mathrm{i}A_R^-),$$

for $r \to +\infty$. Each matching gives a solution for $\tilde{f}_1$ and $\tilde{f}_2$ that should end up to the same uniform solution. Thus

$$\begin{pmatrix} A_L^- \\ A_R^+ \end{pmatrix} = \begin{bmatrix} -\mathrm{i}/2 & 1 \\ 1 & \mathrm{i} \end{bmatrix}\begin{pmatrix} A_L^+ \\ A_R^- \end{pmatrix},$$

which demonstrates that the connection formulas (4.14) are recovered. The uniformly valid solution can finally be expressed as, for example,

$$\boxed{\phi(X, y) = \frac{\bar{Q}}{\sqrt{Dk}}\psi(X, y)\left|\frac{r}{\sigma^2}\right|^{1/4}\exp\left(\frac{\mathrm{i}}{\epsilon}\int_{X_t}^{X}\frac{kM}{\beta^2}\,\mathrm{d}\xi\right)\left[(A_R^- - \frac{\mathrm{i}}{2}A_L^+)\mathrm{A_i}(-r) + \frac{1}{2}A_L^+\mathrm{B_i}(-r)\right]}, \tag{4.21}$$

where $\bar{Q} = 2\sqrt{\pi}\mathrm{e}^{\mathrm{i}\pi/4}Q$ and

$$r = \begin{cases} -\left(\dfrac{3}{2\epsilon}\displaystyle\int_X^{X_t}\frac{k|\sigma|}{\beta^2}\,\mathrm{d}\xi\right)^{2/3} & < 0 \quad \text{if} \quad X < X_t, \\ \left(\dfrac{3}{2\epsilon}\displaystyle\int_{X_t}^{X}\frac{k|\sigma|}{\beta^2}\,\mathrm{d}\xi\right)^{2/3} & \geq 0 \quad \text{if} \quad X_t \leq X. \end{cases}$$

It should be noted that the term $|r/\sigma^2|^{1/4}$ in (4.21) is always real positive and is not singular when $\sigma^2(X_t) = 0$. In the boundary layer, let $X = X_t + \epsilon^{2/3}X_\delta$, so

$$|\sigma|^2(X) = |\sigma|^2(X_t + \epsilon^{2/3}X_\delta) \sim \epsilon^{2/3}\frac{\beta_t^4}{k_t^2}\lambda^3|X_\delta|,$$

and

$$|r| \sim \lambda|X_\delta|,$$

where

$$\lambda^3 = \frac{k_t^2(\sigma^2)_t'}{\beta_t^4} > 0.$$

These inner-region expansions at leading order demonstrate that

$$\left|\frac{r}{\sigma^2}\right|^{1/4} \sim \epsilon^{-1/6}\sqrt{\frac{k_t}{\lambda\beta_t^2}} > 0 \quad \text{for} \quad |X - X_t| = \mathcal{O}(\epsilon^{2/3}). \tag{4.22}$$

In the following, the validity and usefulness of the derived composite solution is highlighted through both examples of an incident cut-on mode and an incident cut-off mode.

Transition Point Analysis — Summary

A singularity in the leading-order approximate slowly-varying acoustic potential has been highlighted and investigated. The singularity is due to the transition of a mode from cut-on to cut-off, or vice-versa, and thus is called a transition point. In the terminology of matched asymptotic expansions [47] this is a boundary layer and its thickness has been evaluated to $\mathcal{O}(\epsilon^{2/3})$. An inner solution has been derived along with the connection formulas between the outer solutions coefficients. Hence the reflected and transmitted coefficients for the case of an incident cut-on mode and the case of an incident cut-off mode has been deduced and the results agree with the literature. Finally, a uniformly valid solution for a mode undergoing transition has been developed which covers both cases of an incident right-running cut-off mode and an incident left-running cut-on mode that will be used in the mode-matching procedure.

4.2 Examples of Acoustic Modes Undergoing Transition

4.2.1 Cut-on to Cut-off Transition

In the inter-vane channels, an upstream-propagating mode generated at the trailing-edge interface could undergo cut-on to cut-off transition along its way. In this case the input parameters for the composite solution (4.21) are $A_L^+ = 0$ and $A_R^- = 1$ (see Figure 4.1), which yields

$$\phi(X,y) = \frac{\bar{Q}}{\sqrt{Dk}}\psi(X,y)\left|\frac{r}{\sigma^2}\right|^{1/4}\exp\left(\mathrm{i}\int_{X_t}^{X}\frac{kM}{\beta^2}\,\mathrm{d}\xi\right)\mathrm{A_i}(-r). \tag{4.23}$$

Figure 4.4 shows the result of the uniform solution compared to the outer solutions for $\epsilon \simeq 0.14$ at two different frequencies. For both frequencies the uniform solution fits well with the outer solutions outside the vicinity of the boundary layer and the asymptotic expansion (4.22) is used at the transition location to smooth out the numerical results.

The crucial feature is the superposition of the incident mode and its reflection which generates a standing wave between the turning point and the trailing-edge interface. Depending on the transition location, the amplitude of the standing wave at the trailing edge ranges from zero to its maximal value. Hence if the mode considered carries a significant amount of energy, the transition location could have a noticeable impact on the energy distribution between trailing-edge scattered modes. On the other hand, an evanescent mode is transmitted beyond the transition point. In the first scenario at $ka = 9.3$ shown in Figure 4.4a, the transition occurs sufficiently close to the inlet so that the outer solution fails. Thus both uniform and outer solution exhibit different values at this location. This emphasizes the importance and practical interest of a uniform solution. Though in the second scenario in Figure 4.4b, at $ka = 8.5$, the transmitted cut-off mode has completely vanished at the leading-edge interface and so the outer solution is valid in this case.

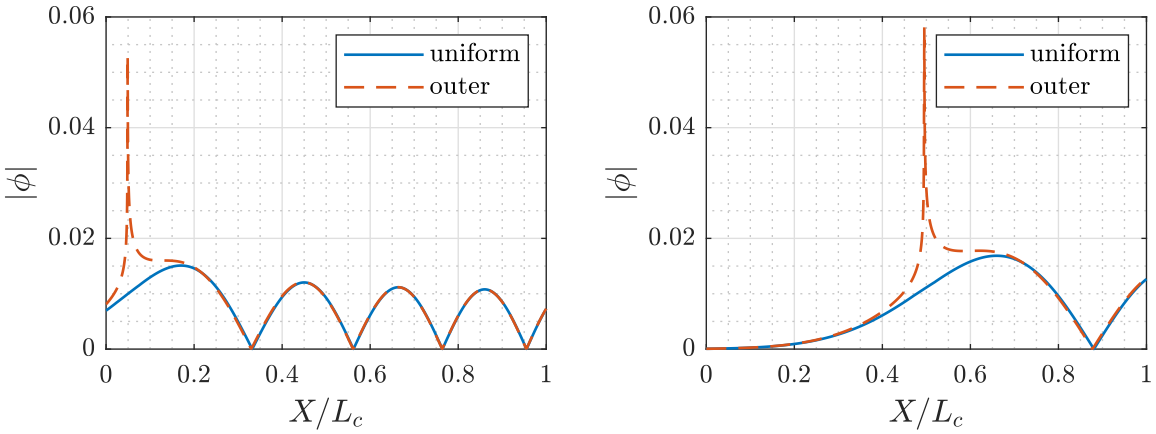

Figure 4.4: Left-running cut-on mode undergoing transition in a duct of $\epsilon \simeq 0.14$. The left scenario is at $ka = 9.3$ while the right scenario is at $ka = 8.5$. The amplitude of the uniform solution is shown in blue line and the outer solutions in red dashed lines.

4.2.2 Cut-off to Cut-on Transition

For an incident cut-off mode generated at the leading-edge interface and undergoing transition, the input parameters are $A_L^+ = 1$ and $A_R^- = 0$ (see Figure 4.1). This yields a uniformly valid solution as

$$\phi(X,y) = \frac{\bar{Q}}{\sqrt{Dk}}\psi(X,y)\left|\frac{r}{\sigma^2}\right|^{1/4}\exp\left(\mathrm{i}\int_{X_t}^{X}\frac{kM}{\beta^2}\,\mathrm{d}\xi\right)\bar{\mathrm{F}}_{\mathrm{BA}}(-r), \tag{4.24}$$

where $\bar{\mathrm{F}}_{\mathrm{BA}} \equiv \frac{1}{2}(\mathrm{B_i} - \mathrm{iA_i})$. Figure 4.5 shows the amplitude of the uniform solution and outer solutions for $\epsilon \simeq 0.14$ at two different frequencies. Again the asymptotic expansion (4.22) is used at the transition location to smooth out the numerical results.

In the first scenario, at $ka = 9.0$, the transition occurs sufficiently close to the leading edge compared to the decaying rate of the cut-off mode and thus it transmits some energy to the propagating mode beyond. There is also a reflected cut-off mode but it should hardly be noticeable here since the reflection coefficient amplitude is half the incident one which has already been reduced by almost two thirds from the inlet to the transition location. The discrepancy seen between the outer and uniform solutions on the left side of the transition in Figure 4.5a is solely due to the asymptotic approximation of the Airy function of second kind $\mathrm{B_i}$ (see Appendix C.1) and shows that the potential is not out of the boundary layer yet. This is clear when looking at the second scenario in Figure 4.5b, at $ka = 8.5$, where the transition occurs farther away from the leading edge. In this case both outer and uniform solutions match well outside the vicinity of the transition location.

In the next section, the uniform solutions for an incident cut-off or cut-on mode are used to adapt the mode-matching equations to the presence of a transition. The example of an incident cut-on mode is used for the trailing-edge interface matching and the incident cut-off mode for the leading-edge interface matching.

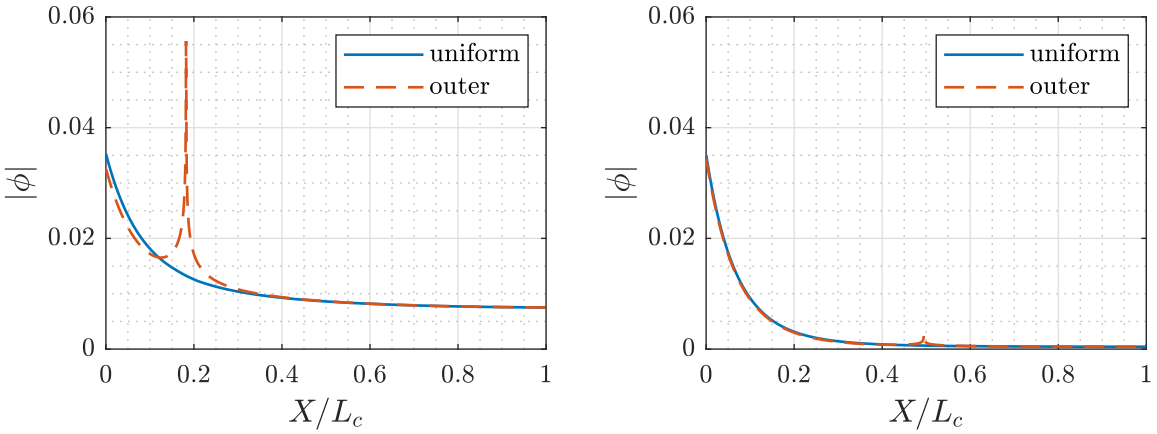

Figure 4.5: Right-running cut-off mode undergoing transition in a duct of $\epsilon \simeq 0.14$. The left scenario is at $ka = 9.0$ while the right scenario is at $ka = 8.5$. The amplitude of the uniform solution is shown as a blue line and the outer solutions as a red dashed lines.

Examples of Modes Undergoing Transition — Summary

The uniform solution has been validated against the outer solutions and proves to be an adequate regularization of the leading-order slowly-varying acoustic potential usable for both cases of an incident cut-on mode and an incident cut-off mode. For numerical computation it can be necessary to smooth out the value of the regularized solution at the transition location using (4.22) in order to avoid discrepancies in the modal amplitudes when the transition occurs close to an interface.

4.3 Mode-Matching Equations

4.3.1 Initial Leading-Edge Interface

Acoustic Potentials

Here the potentials formulations need to be adjusted to account for the reflected part of a cut-off mode undergoing transition in the slowly-varying part of the channel. In the annular domain (Figure 4.6) the incident ϕ_i and reflected ϕ_r acoustic potentials remain unchanged, so

$$\phi_i(x,y) = \mathrm{e}^{\mathrm{i}\alpha_j y}\mathrm{e}^{\mathrm{i}k_j^+ x}, \quad \phi_r(x,y) = \sum_{p=-\infty}^{\infty} R_p \mathrm{e}^{\mathrm{i}\alpha_p y}\mathrm{e}^{\mathrm{i}k_p^- x}, \tag{4.25}$$

where

$$\alpha_j = \frac{j}{R}, \quad k_j^+ = \frac{-(k-\alpha_j M_y)M_x + \sqrt{k^2 - (\beta_x^2 - M_y^2)\alpha_j^2 - 2k\alpha_j M_y}}{\beta_x^2},$$

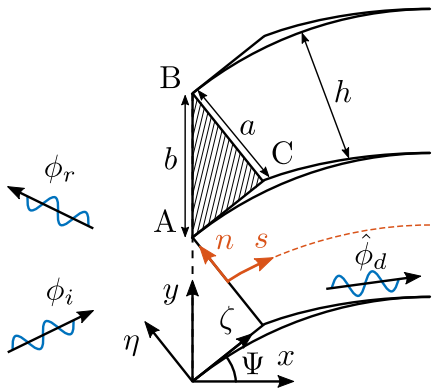

Figure 4.6: Scattering of an incident mode at the staggered leading-edge interface.

$$\alpha_p = \alpha_j + p\frac{2\pi}{b}, \quad k_p^- = \frac{-(k-\alpha_p M_y)M_x - \sqrt{k^2-(\beta_x^2-M_y^2)\alpha_p^2 - 2k\alpha_p M_y}}{\beta_x^2}.$$

The validity domain is

$$\begin{cases} y \in [0, 2\pi R], \\ x \in]-\infty, 0]. \end{cases}$$

In the constant part of the channel (triangle ABC in Figure 4.6) the downstream- and upstream-propagating modes ϕ_d and ϕ_u are

$$\phi_d(\zeta,\eta) = \sum_{q=0}^{\infty} A_q \cos(\alpha_q \eta)\, \mathrm{e}^{\mathrm{i}k_q^+ \zeta}, \tag{4.26}$$

$$\phi_u(\zeta,\eta) = \sum_{q=0}^{\infty} B_q \cos(\alpha_q \eta)\, \mathrm{e}^{\mathrm{i}k_q^- (\zeta - a\tan\Psi)}, \tag{4.27}$$

where

$$\alpha_q = \frac{q\pi}{a}, \quad k_q^{\pm} = \frac{-kM \pm \sqrt{k^2-\beta^2\alpha_q^2}}{\beta^2},$$

and

$$\begin{cases} \eta \in [0, a], \\ \zeta \in [\eta\tan\Psi, a\tan\Psi]. \end{cases} \tag{4.28}$$

Assuming a mode q undergoes transition from cut-off to cut-on in the slowly-varying part of the channel (beyond the interface BC in Figure 4.6), its acoustic potential is given by (4.24). Because of the opposite Fourier-transform convention used here, the complex conjugate of the solution is taken. It reads

$$\phi_q(S,n) = Q_{dq}\sqrt{\frac{2}{Dkh}}\cos\left(\theta_q\left[n+\frac{h}{2}\right]\right)\left|\frac{r_q}{\sigma_q^2}\right|^{1/4}\exp\left(-\mathrm{i}\int_{S_t}^{S}\frac{kM}{\beta^2}\,\mathrm{d}\xi\right)\mathrm{F_{BA}}(r_q), \tag{4.29}$$

where

$$\theta_q(S) = \frac{q\pi}{h}, \quad \sigma_q(S) = \sqrt{1-\left(\frac{\beta\theta_q}{k}\right)^2},$$

$$r_q(S) = \begin{cases} \left(\dfrac{3}{2}\displaystyle\int_S^{S_t} \frac{k|\sigma_q|}{\beta^2}\,\mathrm{d}\xi\right)^{2/3} & > 0 \quad \text{if} \quad S < S_t, \\ -\left(\dfrac{3}{2}\displaystyle\int_{S_t}^{S} \frac{k|\sigma_q|}{\beta^2}\,\mathrm{d}\xi\right)^{2/3} & \leq 0 \quad \text{if} \quad S_t \leq S, \end{cases}$$

and $\mathrm{F_{BA}} \equiv \frac{1}{2}(\mathrm{B_i} + \mathrm{iA_i})$, which is a composition of Airy functions of second and first kinds, respectively. The validity domain for this expression is

$$\begin{cases} n \in [-h(S)/2, h(S)/2], \\ S \in [0, L_c]. \end{cases}$$

Upstream of the transition, in the cut-off region where $r_q > 0$, the incident and reflected parts of the solution are easily distinguishable in (4.29). The incident part, with exponentially decaying amplitude, is associated to the function $\mathrm{B_i}$ whereas the reflected part, with exponentially growing amplitude, is associated to $\mathrm{A_i}$. In order to determine the constant coefficient Q_{dq} in terms of A_q, both formulations from (4.26) and (4.29) are matched at the interface between the constant and slowly varying parts of the channel (segment BC from Figure 4.6). On this interface $h(S = 0) = a$, thus

$$\begin{cases} \eta \in [0, a], \\ \zeta = a\tan\Psi, \end{cases} \quad \text{and} \quad \begin{cases} n = \eta - a/2, \\ S = 0. \end{cases}$$

In that respect, the equality of (4.26) and the incident part of (4.29) results in

$$Q_{dq} = A_q \frac{\sqrt{2}\mathrm{e}^{\mathrm{i}k_q^+ a\tan\Psi}}{G_q(0)\mathrm{B_i}(r_q(0))}, \tag{4.30}$$

where

$$G_q(S) = \left|\frac{r_q(S)}{D^2(S)k^2(S)h^2(S)\sigma_q^2(S)}\right|^{1/4} \exp\left(-\mathrm{i}\int_{S_t}^{S} \frac{k(\xi)M(\xi)}{\beta^2(\xi)}\,\mathrm{d}\xi\right). \tag{4.31}$$

Note that $k = \omega/C$ can be a function of the curvilinear abscissa s if compressible effects are accounted for. Now equating the reflected part of (4.29) with its counterpart (4.27) yields

$$Q_{dq} = B_q \frac{\sqrt{2}\mathrm{e}^{-\mathrm{i}\pi/2}}{G_q(0)\mathrm{A_i}(r_q(0))}. \tag{4.32}$$

From equations (4.30) and (4.32) the reflected coefficients B_q can be expressed in terms of A_q as

$$B_q = A_q \frac{\mathrm{A_i}(r_q(0))}{\mathrm{B_i}(r_q(0))}\mathrm{e}^{\mathrm{i}(k_q^+ a\tan\Psi + \pi/2)}. \tag{4.33}$$

Consequently the channel mode and its reflection at the transition point can be gathered together and, introducing the coefficient

$$\mathcal{F}_q = \begin{cases} \dfrac{\mathrm{A_i}(r_q(0))}{\mathrm{B_i}(r_q(0))}\mathrm{e}^{-2b\sin\Psi\sqrt{\beta^2\alpha_q^2 - k^2}/\beta^2 + \mathrm{i}\frac{\pi}{2}} & \text{if} \quad \exists S_t \in [0, L_c],\ \sigma_q^2(S_t) = 0, \\ 0 & \text{otherwise}, \end{cases} \tag{4.34}$$

the general acoustic potential $\hat{\phi}_d$ is expressed as

$$\boxed{\hat{\phi}_d(\zeta,\eta) = \sum_{q=0}^{\infty} A_q \cos(\alpha_q \eta)\left[\mathrm{e}^{\mathrm{i}k_q^+\zeta} + \mathcal{F}_q \mathrm{e}^{\mathrm{i}k_q^-\zeta}\right]}. \tag{4.35}$$

The reflected part for modes undergoing transition is simply added along with the coefficient $\mathcal{F}_q$ being zero for modes not undergoing transition. Furthermore, the coefficient $\mathcal{F}_q$ represents the back and forth propagation between the leading-edge interface and the transition location with a ratio of Airy functions for the slowly varying part of the channel and, for the constant part, an exponential decay corresponding to the distance traveled. It also has the phase shift of $\pi/2$ which occurs at the transition and the amplitude reduction by a half which is given by the ratio of Airy functions at their origin. It is interesting to see that the ratio of $\mathrm{A_i}(r_q(0))$ over $\mathrm{B_i}(r_q(0))$ is maximum if $S_t = 0$ (the closest transition location to the leading-edge interface) and decreases as s_t increases (transition location moving away from the leading edge). As expected, it shows that the greater the distance the reflected mode has to travel before going back to the leading edge, the weaker its influence. Hence its impact should be noticeable only in cases where the distance it travels times its decaying rate is small: $(b\sin\Psi + s_t)\sqrt{\beta^2\alpha_q^2 - k^2}/\beta^2 \ll 1$.

Continuity of the Acoustic Potential

To derive the continuity equations, a change of variables is performed to express all potentials in terms of (x, y). It yields

$$\begin{aligned}\hat{\phi}_d(x,y) = \frac{1}{2}\sum_{q=0}^{\infty} A_q \Big[&\mathrm{e}^{\mathrm{i}\left(-\frac{q\pi}{a}\sin\Psi + k_q^+\cos\Psi\right)x}\mathrm{e}^{\mathrm{i}\left(\frac{q\pi}{a}\cos\Psi + k_q^+\sin\Psi\right)y}\\ &+ \mathrm{e}^{\mathrm{i}\left(\frac{q\pi}{a}\sin\Psi + k_q^+\cos\Psi\right)x}\mathrm{e}^{\mathrm{i}\left(-\frac{q\pi}{a}\cos\Psi + k_q^+\sin\Psi\right)y}\\ &+ \mathcal{F}_q\Big(\mathrm{e}^{\mathrm{i}\left(-\frac{q\pi}{a}\sin\Psi + k_q^-\cos\Psi\right)x}\mathrm{e}^{\mathrm{i}\left(\frac{q\pi}{a}\cos\Psi + k_q^-\sin\Psi\right)y}\\ &+\mathrm{e}^{\mathrm{i}\left(\frac{q\pi}{a}\sin\Psi + k_q^-\cos\Psi\right)x}\mathrm{e}^{\mathrm{i}\left(-\frac{q\pi}{a}\cos\Psi + k_q^-\sin\Psi\right)y}\Big)\Big].\end{aligned} \tag{4.36}$$

Then the acoustic potential continuity at the leading-edge interface reads

$$\begin{aligned}\mathrm{e}^{\mathrm{i}\alpha_j y} + \sum_{p=-\infty}^{\infty} R_p \mathrm{e}^{\mathrm{i}\alpha_p y} = \frac{1}{2}\sum_{q=0}^{\infty} A_q \Big[&\mathrm{e}^{\mathrm{i}\left(\frac{q\pi}{b} + k_q^+\sin\Psi\right)y} + \mathrm{e}^{\mathrm{i}\left(-\frac{q\pi}{b} + k_q^+\sin\Psi\right)y}\\ &+\mathcal{F}_q\left(\mathrm{e}^{\mathrm{i}\left(\frac{q\pi}{b} + k_q^-\sin\Psi\right)y} + \mathrm{e}^{\mathrm{i}\left(-\frac{q\pi}{b} + k_q^-\sin\Psi\right)y}\right)\Big].\end{aligned} \tag{4.37}$$

Since all coefficients R_p and A_q are unknowns, a projection is performed on the modal basis of the reflected waves to decouple them in (4.37), ending up with one equation on each reflected wave. The corresponding operator is

$$\int_0^b (\bullet)\mathrm{e}^{-\mathrm{i}\alpha_\nu y}\,\mathrm{d}y, \quad \text{with} \quad \alpha_\nu = \alpha_j + \nu\frac{2\pi}{b},\ \nu \in \mathbb{Z}.$$

This leads to three kinds of integrals in (4.37), namely $\mathfrak{I}_{i,\nu}$, $\mathfrak{I}_{p,\nu}$ and $\mathfrak{I}^{\pm\pm}_{q,\nu}$, as

$$\mathfrak{I}_{i,\nu} + \sum_{p=-\infty}^{\infty} R_p \mathfrak{I}_{p,\nu} = \sum_{q=0}^{\infty} A_q \left[\mathfrak{I}^{++}_{q,\nu} + \mathfrak{I}^{-+}_{q,\nu} + \mathcal{F}_q \left(\mathfrak{I}^{+-}_{q,\nu} + \mathfrak{I}^{--}_{q,\nu}\right)\right]. \tag{4.38}$$

The integral based on the incident wave is

$$\mathfrak{I}_{i,\nu} = \int_0^b \mathrm{e}^{\mathrm{i}(\alpha_j - \alpha_\nu)y}\,\mathrm{d}y = \int_0^b \mathrm{e}^{-\mathrm{i}2\pi\nu y/b}\,\mathrm{d}y = \begin{cases} b & \text{if} \quad \nu = 0, \\ 0 & \text{if} \quad \nu \neq 0. \end{cases}$$

Hence, $\mathfrak{I}_{i,\nu} = b\delta_{\nu,0}$ where δ represents the Kronecker symbol. The integral associated with the reflected waves is

$$\mathfrak{I}_{p,\nu} = \int_0^b \mathrm{e}^{\mathrm{i}(\alpha_p - \alpha_\nu)y}\,\mathrm{d}y = \int_0^b \mathrm{e}^{\mathrm{i}2\pi(p-\nu)y/b}\,\mathrm{d}y = \begin{cases} b & \text{if} \quad \nu = p, \\ 0 & \text{if} \quad \nu \neq p. \end{cases}$$

Hence, $\sum_{p=-\infty}^{\infty} R_p \mathfrak{I}_{p,\nu} = bR_\nu$. Finally, the transmitted waves in the inter-vane channel yield different integrals denoted by the $\pm$ symbols as

$$\mathfrak{I}^{\pm\pm}_{q,\nu} = \frac{1}{2}\int_0^b \mathrm{e}^{\mathrm{i}(\pm\frac{q\pi}{b} + k_q^{\pm}\sin\Psi - \alpha_\nu)y}\,\mathrm{d}y = \frac{b}{2}\frac{\sin\left(\varphi^{\pm\pm}_{q,\nu}\right)}{\varphi^{\pm\pm}_{q,\nu}}\mathrm{e}^{\mathrm{i}\varphi^{\pm\pm}_{q,\nu}},$$

where

$$\varphi^{\pm\pm}_{q,\nu} = \frac{b}{2}\left(\pm\frac{q\pi}{b} + \varphi^{\pm}_{q,\nu}(\Psi)\right) \quad \text{and} \quad \varphi^{\pm}_{q,\nu}(\Psi) = k_q^{\pm}\sin\Psi - \alpha_\nu.$$

This last integrals can also be recast together in the potential continuity equation to give

$$\boxed{b\left(R_\nu + \delta_{\nu,0}\right) = \sum_{q=0}^{\infty} A_q \left(\mathfrak{I}^{+}_{q,\nu} + \mathcal{F}_q \mathfrak{I}^{-}_{q,\nu}\right)}, \tag{4.39}$$

where

$$\mathfrak{I}^{\pm}_{q,\nu}(\Psi) = \mathfrak{I}^{+\pm}_{q,\nu} + \mathfrak{I}^{-\pm}_{q,\nu} = \begin{cases} \dfrac{-\mathrm{i}\varphi^{\pm}_{q,\nu}(\Psi)}{(q\pi/b)^2 - \varphi^{\pm\,2}_{q,\nu}(\Psi)}\left(1 - (-1)^q \mathrm{e}^{\mathrm{i}b\varphi^{\pm}_{q,\nu}(\Psi)}\right), \\ \dfrac{b}{2}\left(1 + \delta_{q,0}\right) \quad \text{if} \quad \left|\varphi^{\pm}_{q,\nu}(\Psi)\right| = \dfrac{q\pi}{b}. \end{cases} \tag{4.40}$$

Continuity of the Modified Acoustic Velocity

To write the continuity equation on the modified acoustic velocity $\beta_x^2 u_x - M_x M_y u_y$, the derivative of the potential (4.36) with respect to each coordinate is needed. It yields

$$\begin{aligned} \frac{\partial\hat{\phi}_d}{\partial x} = \frac{\mathrm{i}}{2}\sum_{q=0}^{\infty} A_q \Bigg[& \left(-\frac{q\pi}{a}\sin\Psi + k_q^{+}\cos\Psi\right)\mathrm{e}^{\mathrm{i}\left(-\frac{q\pi}{a}\sin\Psi + k_q^{+}\cos\Psi\right)x}\mathrm{e}^{\mathrm{i}\left(\frac{q\pi}{a}\cos\Psi + k_q^{+}\sin\Psi\right)y} \\ & + \left(\frac{q\pi}{a}\sin\Psi + k_q^{+}\cos\Psi\right)\mathrm{e}^{\mathrm{i}\left(\frac{q\pi}{a}\sin\Psi + k_q^{+}\cos\Psi\right)x}\mathrm{e}^{\mathrm{i}\left(-\frac{q\pi}{a}\cos\Psi + k_q^{+}\sin\Psi\right)y} \\ & + \mathcal{F}_q\Bigg\{\left(-\frac{q\pi}{a}\sin\Psi + k_q^{-}\cos\Psi\right)\mathrm{e}^{\mathrm{i}\left(-\frac{q\pi}{a}\sin\Psi + k_q^{-}\cos\Psi\right)x}\mathrm{e}^{\mathrm{i}\left(\frac{q\pi}{a}\cos\Psi + k_q^{-}\sin\Psi\right)y} \\ & + \left(\frac{q\pi}{a}\sin\Psi + k_q^{-}\cos\Psi\right)\mathrm{e}^{\mathrm{i}\left(\frac{q\pi}{a}\sin\Psi + k_q^{-}\cos\Psi\right)x}\mathrm{e}^{\mathrm{i}\left(-\frac{q\pi}{a}\cos\Psi + k_q^{-}\sin\Psi\right)y}\Bigg\}\Bigg], \end{aligned} \tag{4.41}$$

and

$$\begin{aligned}\frac{\partial\hat{\phi}_d}{\partial y} = \frac{\mathrm{i}}{2}\sum_{q=0}^{\infty} A_q \Big[&\Big(\frac{q\pi}{a}\cos\Psi + k_q^+\sin\Psi\Big)\,\mathrm{e}^{\mathrm{i}\left(-\frac{q\pi}{a}\sin\Psi + k_q^+\cos\Psi\right)x}\mathrm{e}^{\mathrm{i}\left(\frac{q\pi}{a}\cos\Psi + k_q^+\sin\Psi\right)y} \\ &+ \Big(-\frac{q\pi}{a}\cos\Psi + k_q^+\sin\Psi\Big)\,\mathrm{e}^{\mathrm{i}\left(\frac{q\pi}{a}\sin\Psi + k_q^+\cos\Psi\right)x}\mathrm{e}^{\mathrm{i}\left(-\frac{q\pi}{a}\cos\Psi + k_q^+\sin\Psi\right)y} \\ &+ \mathcal{F}_q\Big\{\Big(\frac{q\pi}{a}\cos\Psi + k_q^-\sin\Psi\Big)\,\mathrm{e}^{\mathrm{i}\left(-\frac{q\pi}{a}\sin\Psi + k_q^-\cos\Psi\right)x}\mathrm{e}^{\mathrm{i}\left(\frac{q\pi}{a}\cos\Psi + k_q^-\sin\Psi\right)y} \\ &+ \Big(-\frac{q\pi}{a}\cos\Psi + k_q^-\sin\Psi\Big)\,\mathrm{e}^{\mathrm{i}\left(\frac{q\pi}{a}\sin\Psi + k_q^-\cos\Psi\right)x}\mathrm{e}^{\mathrm{i}\left(-\frac{q\pi}{a}\cos\Psi + k_q^-\sin\Psi\right)y}\Big\}\Big]. \end{aligned} \tag{4.42}$$

Thus the modified velocity continuity at the leading-edge interface reads

$$\begin{aligned}&(\beta_x^2 k_j^+ - M_x M_y\alpha_j)\mathrm{e}^{\mathrm{i}\alpha_j y} + \sum_{p=-\infty}^{\infty} R_p\left(\beta_x^2 k_p^- - M_x M_y\alpha_p\right)\mathrm{e}^{\mathrm{i}\alpha_p y} \\ &\quad= \frac{1}{2}\sum_{q=0}^{\infty} A_q\Big[\left(\beta_x^2 K_q^{+-} - M_x M_y A_q^{++}\right)\mathrm{e}^{\mathrm{i}A_q^{++}y} + \left(\beta_x^2 K_q^{++} - M_x M_y A_q^{-+}\right)\mathrm{e}^{\mathrm{i}A_q^{-+}y} \\ &\quad+\mathcal{F}_q\Big\{\left(\beta_x^2 K_q^{--} - M_x M_y A_q^{+-}\right)\mathrm{e}^{\mathrm{i}A_q^{+-}y} + \left(\beta_x^2 K_q^{-+} - M_x M_y A_q^{--}\right)\mathrm{e}^{\mathrm{i}A_q^{--}y}\Big\}\Big], \end{aligned} \tag{4.43}$$

where

$$K_q^{\pm\pm} = k_q^{\pm}\cos\Psi \pm \frac{q\pi}{a}\sin\Psi, \quad A_q^{\pm\pm} = \pm\frac{q\pi}{a}\cos\Psi + k_q^{\pm}\sin\Psi.$$

Using the same projection method as previously gives

$$\begin{aligned}&(\beta_x^2 k_j^+ - M_x M_y\alpha_j)\mathfrak{I}_{i,\nu} + \sum_{p=-\infty}^{\infty} R_p\left(\beta_x^2 k_p^- - M_x M_y\alpha_p\right)\mathfrak{I}_{p,\nu} \\ &\quad= \frac{1}{2}\sum_{q=0}^{\infty} A_q\left[\left(\beta_x^2 K_q^{+-} - M_x M_y A_q^{++}\right)\mathfrak{I}_{q,\nu}^{++} + \left(\beta_x^2 K_q^{++} - M_x M_y A_q^{-+}\right)\mathfrak{I}_{q,\nu}^{-+}\right. \\ &\quad\left.+\mathcal{F}_q\left\{\left(\beta_x^2 K_q^{--} - M_x M_y A_q^{+-}\right)\mathfrak{I}_{q,\nu}^{+-} + \left(\beta_x^2 K_q^{-+} - M_x M_y A_q^{--}\right)\mathfrak{I}_{q,\nu}^{--}\right\}\right]. \end{aligned} \tag{4.44}$$

After some algebra, the modified velocity continuity reads

$$\boxed{b\left(\mathcal{K}_j^+\delta_{\nu,0} + \mathcal{K}_\nu^- R_\nu\right) = \sum_{q=0}^{\infty} A_q\left(\mathcal{K}_{q,\nu}^+\mathfrak{I}_{q,\nu}^+ + \mathcal{F}_q\mathcal{K}_{q,\nu}^-\mathfrak{I}_{q,\nu}^-\right)}, \tag{4.45}$$

where

$$\begin{aligned}\mathcal{K}_j^+ &= \beta_x^2 k_j^+ - M_x M_y\alpha_j, \\ \mathcal{K}_\nu^- &= \beta_x^2 k_\nu^- - M_x M_y\alpha_\nu, \\ \mathcal{K}_{q,\nu}^{\pm} &= \left(\beta_x^2\cos\Psi - M_x M_y\sin\Psi\right)k_q^{\pm} + \frac{\tan\Psi}{\varphi_{q,\nu}^{\pm}(\Psi)}\left(\frac{q\pi}{b}\right)^2.\end{aligned}$$

Linear System of the Mode-Matching Condition

To solve the problem on the A_q coefficients, the R_ν terms are canceled out by subtracting (4.45) to $\mathcal{K}_\nu^-$ times (4.39). This yields

$$\sum_{q=0}^{\infty} A_q \left[\mathfrak{I}_{q,\nu}^+ \left(\mathcal{K}_\nu^- - \mathcal{K}_{q,\nu}^+\right) + \mathcal{F}_q \mathfrak{I}_{q,\nu}^- \left(\mathcal{K}_\nu^- - \mathcal{K}_{q,\nu}^-\right)\right] = b\left(\mathcal{K}_\nu^- - \mathcal{K}_j^+\right)\delta_{\nu,0}. \tag{4.46}$$

After a modal truncation ($\nu \in [-(N_\nu-1)/2, (N_\nu-1)/2]$ and $q \in [0, N_q-1]$), the matrix form of the equations to solve is

$$\underline{\mathbf{\Phi_q^1}}\mathbf{A} = \mathbf{\Phi_i}, \tag{4.47}$$

where

$$\Phi_q^1(\nu,q) = \mathfrak{I}_{q,\nu}^+ \left(\mathcal{K}_\nu^- - \mathcal{K}_{q,\nu}^+\right) + \mathcal{F}_q \mathfrak{I}_{q,\nu}^- \left(\mathcal{K}_\nu^- - \mathcal{K}_{q,\nu}^-\right) \quad \text{and} \quad \Phi_i(\nu,1) = b\left(\mathcal{K}_\nu^- - \mathcal{K}_j^+\right)\delta_{\nu,0}.$$

This has to be solved numerically using, for example, an algorithm based on the LU decomposition. Then the R_ν coefficients can be deduced from either the potential continuity (4.39) or the modified velocity continuity (4.45).

Another possibility is to solve the A_q and R_ν coefficients simultaneously with a global matrix equation of the form

$$\begin{pmatrix} \underline{\mathbf{E_1^1}} & \underline{\mathbf{F_1^1}} \\ \underline{\mathbf{E_2^1}} & \underline{\mathbf{F_2^1}} \end{pmatrix} \begin{pmatrix} \mathbf{A} \\ \mathbf{R} \end{pmatrix} = \begin{pmatrix} \mathbf{H_1^1} \\ \mathbf{H_2^1} \end{pmatrix}, \tag{4.48}$$

where

$$E_1^1(\nu,q) = \mathfrak{I}_{q,\nu}^+ + \mathcal{F}_q \mathfrak{I}_{q,\nu}^-, \quad F_1^1(\nu,\nu) = -b\delta_{\nu,\nu}, \quad H_1^1(\nu,1) = b\delta_{\nu,0},$$
$$E_2^1(\nu,q) = \mathcal{K}_{q,\nu}^+ \mathfrak{I}_{q,\nu}^+ + \mathcal{F}_q \mathcal{K}_{q,\nu}^- \mathfrak{I}_{q,\nu}^-, \quad F_2^1(\nu,\nu) = -b\mathcal{K}_\nu^- \delta_{\nu,\nu}, \quad H_2^1(\nu,1) = b\mathcal{K}_j^+ \delta_{\nu,0}.$$

4.3.2 Trailing-Edge Interface

Acoustic Potentials

At the trailing-edge interface, the acoustic potentials involved are represented in Figure 4.7. The expression of the transmitted ϕ_t acoustic potential is

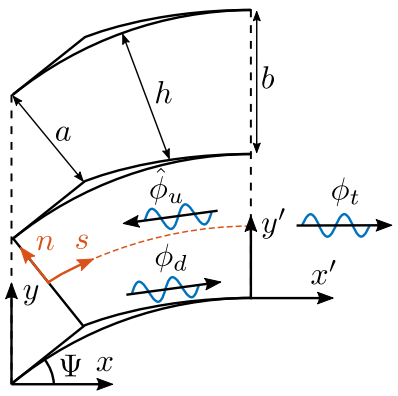

Figure 4.7: Scattering of a downstream-propagating channel mode at the trailing-edge interface.

$$\phi_t(x',y') = \sum_{p=-\infty}^{\infty} T_p \mathrm{e}^{\mathrm{i}\alpha_p y'} \mathrm{e}^{\mathrm{i}k_p^+ x'}, \tag{4.49}$$

where

$$x' = x - c_x, \quad y' = y - R_c(1-\cos\Psi), \quad \alpha_p = \alpha_j + p\frac{2\pi}{b}, \quad k_p^+ = \frac{-kM + \sqrt{k^2 - \beta^2\alpha_p^2}}{\beta^2},$$

c_x is the projection of the chord length on the $x-$axis and R_c is the vanes curvature radius. The validity domain is

$$\begin{cases} y' \in [0, 2\pi R], \\ x' \in [0, \infty[. \end{cases}$$

In the inter-vane channels, an incident mode propagating downstream from the leading edge and undergoing transition along its way is expressed from (4.29) and (4.30) as

$$\phi_{dq}(S,n) = A_q \frac{G_q(S)}{G_q(0)} \frac{\mathrm{B_i}(r_q(S)) + i\mathrm{A_i}(r_q(S))}{\mathrm{B_i}(r_q(0))} \cos\left(\theta_q\left[n+\frac{h}{2}\right]\right) \mathrm{e}^{\mathrm{i}k_q^+ a\tan\Psi}. \tag{4.50}$$

In order to have a general expression of the acoustic potential ϕ_d, let Υ_q^+ be the amplitude and phase stream-wise variation of a mode not undergoing transition. It reads from (2.92 – 2.95):

$$\Upsilon_q^{\pm}(S) = \sqrt{\frac{D_0(S_0)k(S_0)\sigma_q(S_0)h(S_0)}{D_0(S)k(S)\sigma_q(S)h(S)}} \exp\left(\mathrm{i}\int_{S_0}^{s} \mu_q^{\pm}(\xi)\,\mathrm{d}\xi\right), \quad S_0 = \begin{cases} 0 & \text{for } \Upsilon_q^+, \\ L_c & \text{for } \Upsilon_q^-. \end{cases}$$

and

$$\mu_q^{\pm}(S) = \frac{-kM \pm k\sigma_q}{\beta^2}, \quad \sigma_q(S) = \sqrt{1-\left(\frac{\beta\theta_q}{k}\right)^2}, \quad \theta_q(S) = \frac{q\pi}{h(S)}.$$

Introducing the general function Ξ_q^+ as

$$\Xi_q^+(S) = \begin{cases} \dfrac{G_q(S)}{G_q(0)} \dfrac{\mathrm{B_i}(r_q(S)) + i\mathrm{A_i}(r_q(S))}{\mathrm{B_i}(r_q(0))} \mathrm{e}^{\mathrm{i}k_q^+ a\tan\Psi} & \text{if} \quad \exists s_t \in [0, L_c],\ \sigma_q^2(S_t) = 0, \\ \Upsilon_q^+(S)\mathrm{e}^{\mathrm{i}k_q^+ a\tan\Psi} & \text{otherwise,} \end{cases} \tag{4.51}$$

allows one to write the acoustic potential as

$$\boxed{\phi_d(S,n) = \sum_{q=0}^{\infty} A_q \Xi_q^+(S) \cos\left(\theta_q\left[n+\frac{h}{2}\right]\right).} \tag{4.52}$$

Reflected modes ϕ_{uq} are generated from the scattering of the acoustic modes ϕ_{dq} by the trailing edges. Indeed these modes can also undergo transition in the channel. The sum of an upstream-propagating mode and its reflection at the transition point is

$$\hat{\phi}_{uq}(S,n) = Q_{uq}\sqrt{\frac{2}{Dkh}} \cos\left(\theta_q\left[n+\frac{h}{2}\right]\right) \left|\frac{r_q}{\sigma_q^2}\right|^{1/4} \exp\left(-\mathrm{i}\int_{S_t}^{s} \frac{kM}{\beta^2}\,\mathrm{d}\xi\right) \mathrm{A_i}(r_q(S)). \tag{4.53}$$

The normalization is chosen such that the amplitude at the trailing-edge interface locally equates to

$$Q_{uq}\sqrt{\frac{2}{Dkh}}\left|\frac{r_q}{\sigma_q^2}\right|^{1/4}\exp\left(-\mathrm{i}\int_{S_t}^{L_c}\frac{kM}{\beta^2}\,\mathrm{d}\xi\right)\mathrm{A_i}(r_q(L_c))=B_q. \tag{4.54}$$

Hence

$$Q_{uq}=\frac{B_q}{\sqrt{2}G_q(L_c)\mathrm{A_i}(r_q(L_c))}, \tag{4.55}$$

and the upstream-propagating modes undergoing transition are written as

$$\hat{\phi}_{uq}(S,n)=B_q\frac{G_q(S)}{G_q(L_c)}\frac{\mathrm{A_i}(r_q(S))}{\mathrm{A_i}(r_q(L_c))}\cos\left(\theta_q\left[n+\frac{h}{2}\right]\right). \tag{4.56}$$

In order to write a general expression for the acoustic potential whether or not a mode undergoes transition, another general function Ξ_q^- is introduced as

$$\Xi_q^-(S)=\begin{cases}\dfrac{G_q(S)}{G_q(L_c)}\dfrac{\mathrm{A_i}(r_q(S))}{\mathrm{A_i}(r_q(L_c))} & \text{if}\quad \exists s_t\in[0,L_c],\ \sigma_q^2(S_t)=0,\\ \Upsilon_q^-(S) & \text{otherwise.}\end{cases} \tag{4.57}$$

The acoustic potential corresponding to the upstream-propagating modes is expressed as

$$\boxed{\hat{\phi}_u(S,n)=\sum_{q=0}^{\infty}B_q\Xi_q^-(S)\cos\left(\theta_q\left[n+\frac{h}{2}\right]\right).} \tag{4.58}$$

For both ϕ_d (4.52) and $\hat{\phi}_u$ (4.58) the validity range is

$$\begin{cases} n\in[-h(S)/2,h(S)/2],\\ s\in[0,L_c].\end{cases}$$

Continuity of the Acoustic Potential

At the trailing-edge interface, the continuity of the potential reads

$$\sum_{q=0}^{\infty}\left[A_q\Xi_q^+(L_c)+B_q\right]\cos\left(\theta_q(L_c)y'\right)=\sum_{p=-\infty}^{\infty}T_p\mathrm{e}^{\mathrm{i}\alpha_p y'}. \tag{4.59}$$

After a projection on the modal basis of the transmitted modes

$$\int_0^b(\bullet)\mathrm{e}^{-\mathrm{i}\alpha_\nu y'}\,\mathrm{d}y',\quad\text{with}\quad\alpha_\nu=\alpha_j+\nu\frac{2\pi}{b},\ \nu\in\mathbb{Z},$$

the integrals yields

$$\int_0^b\mathrm{e}^{\mathrm{i}(\alpha_p-\alpha_\nu)y'}\,\mathrm{d}y'=b\delta_{\nu,p},$$

and

$$\mathfrak{I}^0_{q,\nu} = \int_0^b \cos\left(\theta_q(L_c)y'\right) \mathrm{e}^{-\mathrm{i}\alpha_\nu y'}\, \mathrm{d}y' = \begin{cases} \dfrac{\mathrm{i}\alpha_\nu}{(\alpha_q)^2 - \alpha_\nu^2}\left[1-(-1)^q \mathrm{e}^{-\mathrm{i}\alpha_j b}\right], \\ \dfrac{b}{2}(1+\delta_{q,0}) \quad \text{if} \quad \alpha_\nu = \dfrac{q\pi}{b}. \end{cases}$$

Notice that $\mathfrak{I}^0_{q,\nu}$ is a particular case of the previously defined inner product $\mathfrak{I}^{\pm}_{q,\nu}(\Psi = 0)$ in (4.40) for a null stagger angle. Compiling these results together yields

$$\boxed{\sum_{q=0}^{\infty} \left[A_q \Xi^+_q(L_c) + B_q\right] \mathfrak{I}^0_{q,\nu} = bT_\nu}. \tag{4.60}$$

Continuity of the Acoustic Axial Velocity

The derivation of the axial velocities in the slowly varying part of the channel are given in Appendix C.2. It yields at leading order

$$\frac{\partial \phi_d}{\partial s}(S,n) \sim \sum_{q=0}^{\infty} i\left(-\frac{kM}{\beta^2} + \frac{k\varsigma^+_q}{\beta^2}\right) A_q \Xi^+_q(S) \cos\left(\theta_q\left[n+\frac{h}{2}\right]\right), \tag{4.61}$$

where the general reduced axial wavenumber ς^+_q is

$$\varsigma^+_q = \sigma_q \quad \text{if} \quad \nexists s_t \in [0, L_c],\, \sigma_q^2(S_t) = 0,$$

and otherwise

$$\varsigma^+_q = \mathrm{i}|\sigma_q| \times \begin{cases} \dfrac{1}{|r_q|^{1/2}} \dfrac{\mathrm{B_i}'(r_q) + \mathrm{iA_i}'(r_q)}{\mathrm{B_i}(r_q) + i\mathrm{A_i}(r_q)} + \dfrac{1}{4|r_q|^{3/2}} & \text{if} \quad S < S_t, \\ \dfrac{1}{|r_q|^{1/2}} \dfrac{\mathrm{B_i}'(r_q) + \mathrm{iA_i}'(r_q)}{\mathrm{B_i}(r_q) + i\mathrm{A_i}(r_q)} - \dfrac{1}{4|r_q|^{3/2}} & \text{if} \quad S_t \le S. \end{cases}$$

Also, the acoustic velocity corresponding to the upstream-propagating modes is given by

$$\frac{\partial \phi_u}{\partial s}(S,n) \sim \sum_{q=0}^{\infty} i\left(-\frac{kM}{\beta^2} - \frac{k\varsigma^-_q}{\beta^2}\right) B_q \Xi^-_q(S) \cos\left(\theta_q\left[n+\frac{h}{2}\right]\right), \tag{4.62}$$

where the general reduced axial wavenumber ς^-_q is

$$\varsigma^-_q = \sigma_q \quad \text{if} \quad \nexists s_t \in [0, L_c],\, \sigma_q^2(S_t) = 0,$$

and otherwise

$$\varsigma^-_q = -\mathrm{i}|\sigma_q| \times \begin{cases} \dfrac{1}{|r_q|^{1/2}} \dfrac{\mathrm{A_i}'(r_q)}{\mathrm{A_i}(r_q)} + \dfrac{1}{4|r_q|^{3/2}} & \text{if} \quad S < S_t, \\ \dfrac{1}{|r_q|^{1/2}} \dfrac{\mathrm{A_i}'(r_q)}{\mathrm{A_i}(r_q)} - \dfrac{1}{4|r_q|^{3/2}} & \text{if} \quad S_t \le S. \end{cases}$$

Introducing the general axial wavenumber as

$$\tau_q^{\pm} = -\frac{kM}{\beta^2} \pm \frac{k\varsigma_q^{\pm}}{\beta^2},$$

and projecting on the annular modal basis, the axial velocity continuity at the trailing-edge interface reads

$$\boxed{\sum_{q=0}^{\infty} \left[\tau_q^+(L_c) A_q \Xi_q^+(L_c) + \tau_q^-(L_c) B_q\right] \mathfrak{I}_{q,\nu}^0 = k_\nu^+ b T_\nu}. \tag{4.63}$$

Linear System of the Mode-Matching Condition

The matrix equation for this interface reads

$$\begin{pmatrix} \mathbf{E_1^2} & \mathbf{F_1^2} & \mathbf{0} \\ \mathbf{E_2^2} & \mathbf{F_2^2} & \mathbf{G_K^2} \\ \mathbf{E_K^2} & \mathbf{0} & 0 \end{pmatrix} \begin{pmatrix} \mathbf{B} \\ \mathbf{T} \\ \Omega_K \end{pmatrix} = \begin{pmatrix} \mathbf{H_1^2} \\ \mathbf{H_2^2} \\ H_K^2 \end{pmatrix}, \tag{4.64}$$

$$\begin{pmatrix} \mathbf{E_p^2} & \mathbf{F_p^2} \\ \mathbf{E_v^2} & \mathbf{F_v^2} \end{pmatrix} \begin{pmatrix} \mathbf{U} \\ \mathbf{T} \end{pmatrix} = \begin{pmatrix} \mathbf{H_p^2} \\ \mathbf{H_v^2} \end{pmatrix}, \tag{4.65}$$

where

$$E_p^2(\nu,q) = \mathfrak{I}_{q,\nu}^0, \quad F_p^2(\nu,\nu) = -b\delta_{\nu,\nu}, \quad H_p^2(\nu,1) = -\sum_{q=0}^{\infty} A_q \Xi_q^+(L_c) \mathfrak{I}_{q,\nu}^0,$$

$$E_v^2(\nu,q) = \tau_q^-(L_c)\mathfrak{I}_{q,\nu}^0, \quad F_v^2(\nu,\nu) = -bk_\nu^+\delta_{\nu,\nu}, \quad H_v^2(\nu,1) = -\sum_{q=0}^{\infty} \tau_q^+(L_c) A_q \Xi_q^+(L_c) \mathfrak{I}_{q,\nu}^0,$$

4.3.3 Correction to the Leading-Edge Interface

For the next steps in the iterative procedure, the leading-edge matching (4.48) needs to be modified to account for the upstream scattered modes ϕ_{uq} traveling from the trailing-edge interface to the leading-edge interface, see Figure 4.8. The potential continuity

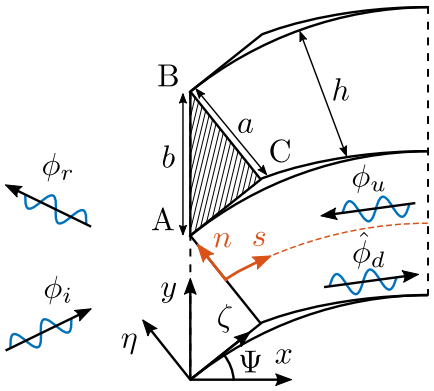

Figure 4.8: Scattering of an incident mode at the staggered leading-edge interface.

and modified velocity continuity read, at the g^{th} iteration,

$$\boxed{\sum_{q=0}^{\infty} A_q^g \left(\mathfrak{I}_{q,\nu}^+ + \mathcal{F}_q \mathfrak{I}_{q,\nu}^-\right) + B_q^{g-1} \Xi_q^-(0) \mathrm{e}^{-\mathrm{i}k_q^- b \sin\Psi} \mathfrak{I}_{q,\nu}^- = b\left(R_\nu^g + \delta_{\nu,0}\right)}, \tag{4.66}$$

and

$$\boxed{\sum_{q=0}^{\infty} A_q^g \left(\mathcal{K}_{q,\nu}^+ \mathfrak{I}_{q,\nu}^+ + \mathcal{F}_q \mathcal{K}_{q,\nu}^- \mathfrak{I}_{q,\nu}^-\right) + B_q^{g-1} \Xi_q^-(0) \mathrm{e}^{-\mathrm{i}k_q^- b \sin\Psi} \mathcal{K}_{q,\nu}^- \mathfrak{I}_{q,\nu}^- = b\left(\mathcal{K}_\nu^- R_\nu^g + \mathcal{K}_j^+ \delta_{\nu,0}\right)}. \tag{4.67}$$

Combining them to cancel out the unknown R_ν^g coefficients yields

$$\begin{aligned}\sum_{q=0}^{\infty} A_q^g \left[\mathfrak{I}_{q,\nu}^+ \left(\mathcal{K}_\nu^- - \mathcal{K}_{q,\nu}^+\right) + \mathcal{F}_q \mathfrak{I}_{q,\nu}^- \left(\mathcal{K}_\nu^- - \mathcal{K}_{q,\nu}^-\right)\right] &= b\left(\mathcal{K}_\nu^- - \mathcal{K}_j^+\right)\delta_{\nu,0} \\ &- \sum_{q=0}^{\infty} B_q^{g-1} \Xi_q^-(0) \mathfrak{I}_{q,\nu}^- \left(\mathcal{K}_\nu^- - \mathcal{K}_{q,\nu}^-\right) \mathrm{e}^{-\mathrm{i}k_q^- b \sin\Psi}.\end{aligned} \tag{4.68}$$

After a modal truncation ($\nu \in [-(N_\nu - 1)/2, (N_\nu - 1)/2]$ and $q \in [0, N_q - 1]$), the corrected system of equations at the leading-edge interface is

$$\underline{\mathbf{\Phi_q^1}} \mathbf{A} = \mathbf{\Phi_i}, \tag{4.69}$$

where

$$\Phi_q^1(\nu, q) = \mathfrak{I}_{q,\nu}^+ \left(\mathcal{K}_\nu^- - \mathcal{K}_{q,\nu}^+\right) + \mathcal{F}_q \mathfrak{I}_{q,\nu}^- \left(\mathcal{K}_\nu^- - \mathcal{K}_{q,\nu}^-\right),$$

$$\Phi_i(\nu, 1) = b\left(\mathcal{K}_\nu^- - \mathcal{K}_j^+\right)\delta_{\nu,0} - \sum_{q=0}^{\infty} B_q^{g-1} \Xi_q^-(0) \mathfrak{I}_{q,\nu}^- \left(\mathcal{K}_\nu^- - \mathcal{K}_{q,\nu}^-\right) \mathrm{e}^{-\mathrm{i}k_q^- b \sin\Psi}.$$

The R_ν coefficients are then deduced from either (4.66) or (4.67).

The corrected global system of equations at the leading-edge interface is

$$\begin{pmatrix} \underline{\mathbf{E_1^1}} & \underline{\mathbf{F_1^1}} \\ \underline{\mathbf{E_2^1}} & \underline{\mathbf{F_2^1}} \end{pmatrix} \begin{pmatrix} \mathbf{A} \\ \mathbf{R} \end{pmatrix} = \begin{pmatrix} \mathbf{H_1^1} \\ \mathbf{H_2^1} \end{pmatrix}, \tag{4.70}$$

where

$$E_1^1(\nu, q) = \mathfrak{I}_{q,\nu}^+ + \mathcal{F}_q \mathfrak{I}_{q,\nu}^-, \quad F_1^1(\nu, \nu) = -b\delta_{\nu,\nu},$$

$$H_1^1(\nu, 1) = b\delta_{\nu,0} - \sum_{q=0}^{\infty} B_q^{g-1} \Xi_q^-(0) \mathfrak{I}_{q,\nu}^- \mathrm{e}^{-\mathrm{i}k_q^- b \sin\Psi},$$

$$E_2^1(\nu, q) = \mathcal{K}_{q,\nu}^+ \mathfrak{I}_{q,\nu}^+ + \mathcal{F}_q \mathcal{K}_{q,\nu}^- \mathfrak{I}_{q,\nu}^-, \quad F_2^1(\nu, \nu) = -b\mathcal{K}_\nu^- \delta_{\nu,\nu},$$

$$H_2^1(\nu, 1) = b\mathcal{K}_j^+ \delta_{\nu,0} - \sum_{q=0}^{\infty} B_q^{g-1} \Xi_q^-(0) \mathcal{K}_{q,\nu}^- \mathfrak{I}_{q,\nu}^- \mathrm{e}^{-\mathrm{i}k_q^- b \sin\Psi},$$

4.3.4 Global Matching

In order to avoid convergence issues when a transition occurs near the leading-edge interface (see section 4.4.2), the iterative procedure going back and forth between the leading edge (4.70) and trailing edge (4.65) can be replaced by a direct approach. This method solves the matching equations on the whole cascade directly, as represented in Figure 4.9. Thus all four unknown potentials are computed simultaneously as the solution of the four matching equations: two at the leading edge and two at the trailing edge. The weakness of the direct approach is that the size of the matrix is multiplied

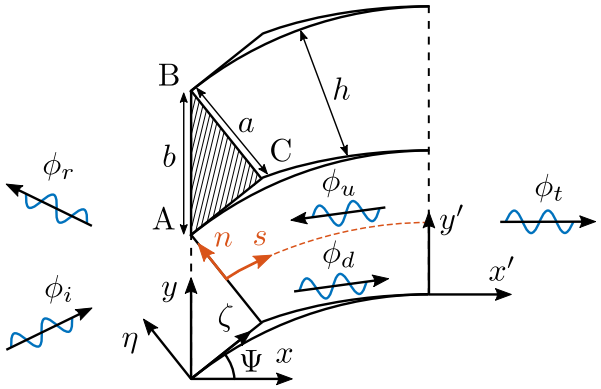

Figure 4.9: Scattering of an incident mode by the cascade of cambered vanes.

by four by comparison to the matrices in the iterative approach. Since the matrix to invert is larger it has a worse conditioning and so caution is required. Comparisons in terms of acoustic power balance are shown in section 4.4.2.

Combining the continuity equations (4.66), (4.67), (4.60) and (4.63) leads to the global system of equations

$$\begin{pmatrix} \mathbf{R_p^1} & \mathbf{D_p^1} & \mathbf{U_p^1} & \underline{\mathbf{0}} \\ \underline{\mathbf{R_v^1}} & \underline{\mathbf{D_v^1}} & \underline{\mathbf{U_v^1}} & \underline{\mathbf{0}} \\ \underline{\mathbf{0}} & \underline{\mathbf{D_p^2}} & \underline{\mathbf{U_p^2}} & \underline{\mathbf{T_p^2}} \\ \underline{\mathbf{0}} & \underline{\mathbf{D_v^2}} & \underline{\mathbf{U_v^2}} & \underline{\mathbf{T_v^2}} \end{pmatrix} \begin{pmatrix} \mathbf{R} \\ \mathbf{D} \\ \mathbf{U} \\ \mathbf{T} \end{pmatrix} = \begin{pmatrix} \mathbf{H_p^1} \\ \mathbf{H_v^1} \\ \mathbf{0} \\ \mathbf{0} \end{pmatrix}, \tag{4.71}$$

where

$$R_p^1(\nu,\nu) = -b\delta_{\nu,\nu}, \quad D_p^1(\nu,q) = \mathfrak{I}_{q,\nu}^+ + \mathcal{F}_q\mathfrak{I}_{q,\nu}^-, \quad U_p^1(\nu,q) = \Xi_q^-(0)\mathfrak{I}_{q,\nu}^- \mathrm{e}^{-\mathrm{i}k_q^- b\sin\Psi},$$

$$R_v^1(\nu,\nu) = -b\mathcal{K}_\nu^-\delta_{\nu,\nu}, \quad D_v^1(\nu,q) = \mathcal{K}_{q,\nu}^+\mathfrak{I}_{q,\nu}^+ + \mathcal{F}_q\mathcal{K}_{q,\nu}^-\mathfrak{I}_{q,\nu}^-,$$

$$U_v^1(\nu,q) = \Xi_q^-(0)\mathcal{K}_{q,\nu}^-\mathfrak{I}_{q,\nu}^- \mathrm{e}^{-\mathrm{i}k_q^- b\sin\Psi},$$

$$D_p^2(\nu,q) = \Xi_q^+(L_c)\mathfrak{I}_{q,\nu}^0, \quad U_p^2(\nu,q) = \mathfrak{I}_{q,\nu}^0, \quad T_p^2(\nu,\nu) = -b\delta_{\nu,\nu},$$

$$D_v^2(\nu,q) = \tau_q^+(L_c)\Xi_q^+(L_c)\mathfrak{I}_{q,\nu}^0, \quad U_v^2(\nu,q) = \tau_q^-(L_c)\mathfrak{I}_{q,\nu}^0, \quad T_v^2(\nu,\nu) = -bk_\nu^+\delta_{\nu,\nu},$$

and

$$H_p^1(\nu,1) = b\delta_{\nu,0}, \quad H_v^1(\nu,1) = b\mathcal{K}_j^+\delta_{\nu,0}.$$

Mode-Matching Equations — Summary

A general formulation of the continuity equations has been derived which covers both cases of acoustic modes undergoing transition and not. The continuity equations have the same structure whereas a transition occurs or not due to a general expression of axial wavenumbers $\tau_q^{\pm}$ and axial modal-evolution functions $\Xi_q^{\pm}$. Finally, a global linear system of equations encompassing both leading-edge and trailing-edge matching equations has been developed. It enables a direct computation of all modal coefficients R, D, U, T. The choice of a direct approach instead of an iterative approach was motivated by non-converging cases with the iterative approach when a transition takes place close to the leading-edge interface. The pros and cons of both methods are detailed in the next section.

4.4 Validation

4.4.1 Modal Truncation

The following analyses are focused on the transition of the first two channel modes $q = 1$ and $q = 2$, respectively named q_1- and q_2-transitions, for the geometry of the fourth NASA CAA workshop, category 3, problem 2 [24]. The validation is performed without flow $M = 0$ and with a camber angle of $\Psi = 36°$. Thus the maximal dimensionless frequency of interest is $kb = q\pi/\cos\Psi \simeq 2.5\pi$. Curvature effects are expected to play a role at such frequencies in the acoustic propagation. Nonetheless, some aspects of the transition effects should still be reliable due to the reflection and transmission coefficients at the transition location being independent to the curvature [14]. A special attention is paid to that matter when investigating resonant phenomena in Section 4.5.2.

Preliminary computations are done to assess the optimal number of modes N to account for in the modal truncation and are shown in Figure 4.10. The error E at a

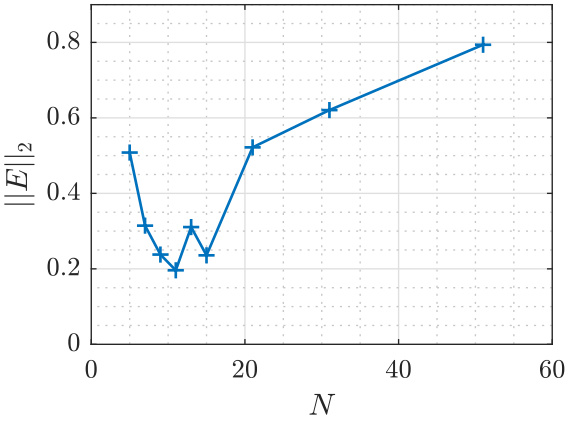

Figure 4.10: Norm of the acoustic power balance error, for $j = 2$, integrated from $kb = 0.9\pi$ to 2.6π.

given dimensionless frequency kb is given by the acoustic power balance as

$$E(kb) = 1 - \frac{\mathcal{P}_t - \mathcal{P}_r}{\mathcal{P}_i}, \tag{4.72}$$

where $\mathcal{P}_i$, $\mathcal{P}_r$ and $\mathcal{P}_t$ are the incident, reflected and transmitted acoustic powers, respectively, as defined in (2.110 - 2.112). Then the 2-norm is defined as

$$||E||_2 = \left[\sum_i |E(kb_i)|^2\right]^{1/2}, \tag{4.73}$$

where the $(kb)_i$ values are the set of discrete dimensionless frequencies at which the error E has been evaluated. To compute the result of Figure 4.10, 341 points have been used linearly ranging from $kb = 0.9\pi$ to 2.6π, which covers both transition ranges of the modes $q = 1$ and $q = 2$. It is found that the optimal number of modes is $N = 11$ for $j = 2$ and then the error increases for higher N due to ill-conditioning at the staggered interface.

4.4.2 Iterative Procedure vs. Global Matching

A direct global approach has been developed in 4.3.4 to overcome convergence issues with the iterative procedure when a transition occurs near the leading-edge interface. These issues are highlighted in Figure 4.11 which shows the evolution of the acoustic power balance with the frequency using both methods. The horizontal dashed lines represent the limits of the 1% confidence range in which the results can be trusted. The vertical dash-dotted lines are the limits of the transition ranges: $1 \leq kb/\pi \lesssim 1.235$ for the q_1-transition and $2 \leq kb/\pi \lesssim 2.47$ for the q_2-transition. With an incident mode of order $j = 0$ (Figure 4.11a), the iterative procedure does not converge at the right-end side of the first transition range, corresponding to the closest transition locations to the leading-edge interface. This behavior seems to be due to numerical difficulties to handle the exponentially growing reflected mode, the amplitude of which becomes larger and larger as the transition approaches the leading edge. Since it happens in the q_1-transition range, only the mode $q = 0$ is cut-on at the leading-edge interface. It is believed the channel mode D_0 and the reflected annular modes R_ν are not sufficient to locally ensure enough dissipation while enforcing continuity. Using the global approach allows one to account for the channel mode D_1, which is cut-on in the other part of the channel and can dissipate energy from the cut-off region. This method solves the convergence problem smoothly for $j = 0$ but the balance suffers a drop of up to 1.8% for $j = 2$ and 4.6% for $j = 5$ (Figures 4.11b - 4.11c). Caution should then be taken when analyzing results at these frequencies. As observed in Chapter 2, the method does not give sufficiently accurate results for some incident modes due to the ill-conditioned problem at the staggered interface. This appears to be also true with the direct approach and inside the transition ranges as shown in Figure 4.11d for the incident modal order $j = -7$. The acoustic balance is off of the 1% confidence range for almost all frequencies in this case.

When lowering the camber angle to $\Psi = 25°$ there is no convergence issue anymore, see Figure 4.12. The global approach gives smoother results but sometimes shows instabilities resulting in an error of 18% for an incident modal order of $j = 0$ at $kb/\pi = 2$, as shown in Figure 4.12a. Furthermore, using the iterative procedure with

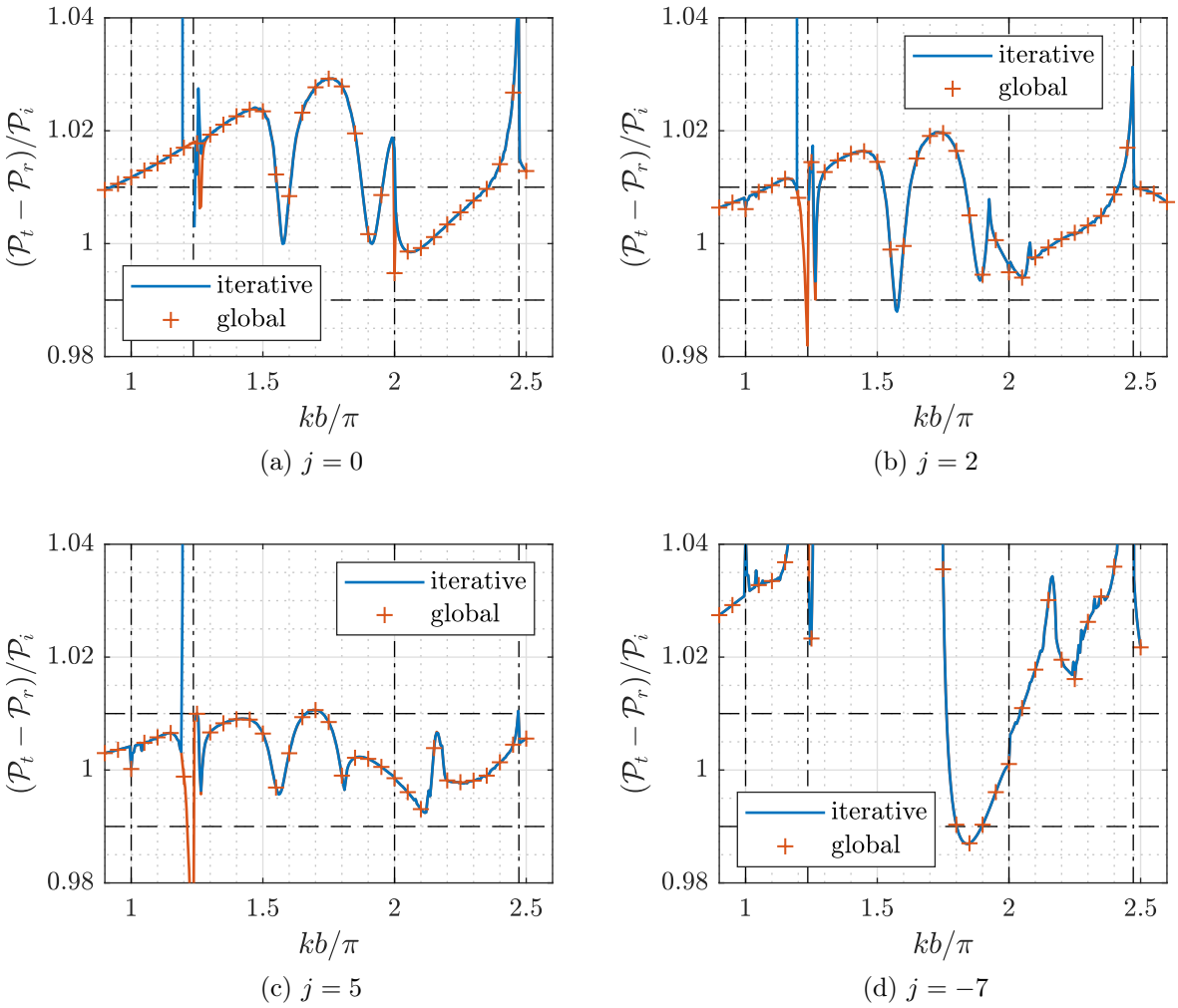

(a) $j = 0$ (b) $j = 2$

(c) $j = 5$ (d) $j = -7$

Figure 4.11: Evolution of the acoustic power balance with the frequency using both iterative and direct methods for different incident modal orders, $\Psi = 36°$.

$N = 31$ modes ensures accurate results for the scattering of the incident mode $j = -7$ which was badly resolved using $N = 11$ modes (see Figure 4.13). Although a similar improvement is not possible when $\Psi = 36°$, it appears that the iterative procedure should be used by default and the direct method only when convergence issues occur. This is how all further results are obtained.

Validation — **Summary**

The direct approach always converges and so it solves the issues encountered with the iterative method in some cases where a transition occurs near the leading-edge interface. However, even if it most often gives similar or identical results to the iterative approach, sometimes the direct method is off by many percents while the iterative method performs well. This behavior is seen at $kb = 2\pi$ and for some incident perturbations when increasing the number of modes in the modal truncation. For that reason, the global approach should be used only for frequencies at which the iterative approach has convergence issues.

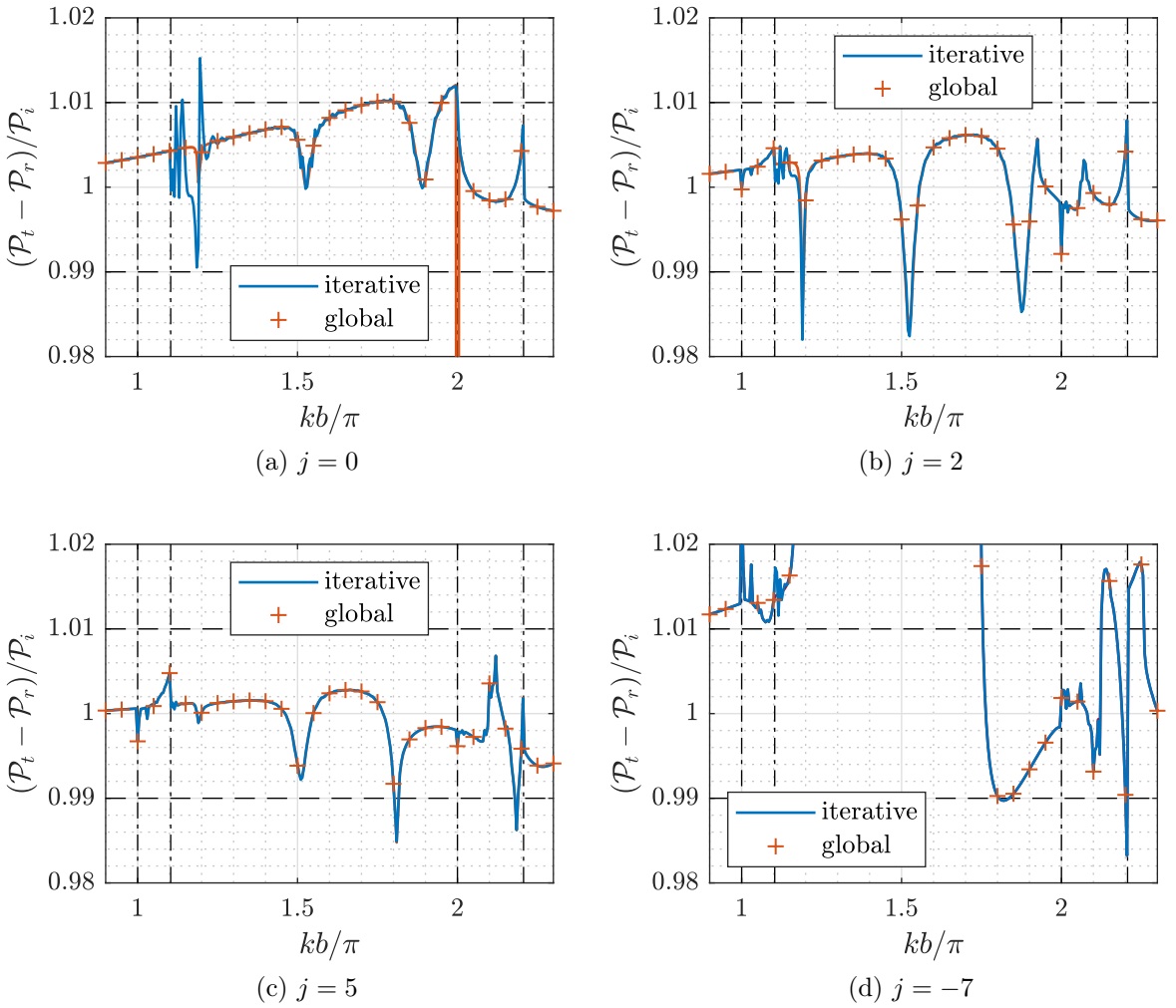

(a) $j = 0$ (b) $j = 2$

(c) $j = 5$ (d) $j = -7$

Figure 4.12: Evolution of the acoustic power balance with the frequency using both iterative and direct methods for different incident modal orders, $\Psi = 25°$.

4.5 Results

4.5.1 Influence of the Transition on the Acoustic Power Balance

The necessity to account for the transition mechanism in the acoustic propagation is highlighted in Figure 4.14. It shows the evolution of the acoustic power balance with the frequency when accounting or not for the reflected modes at the transition. This is basically a comparison of what is predicted with the model described in Chapter 2 and the extended model of the current chapter. When the transition appears exactly at the trailing-edge interface, $kb/\pi = 1, 2, ...$, the computation does not converge without the reflection at the transition location. Then the discrepancy remains large especially for the q_2-transition, and decreases with the transition moving toward the leading edge.

The drop in the q_2-transition range indicates a lack of energy in the scattered modes when the transition occurs near the trailing-edge interface. In this case, the reflection of the right-running cut-off mode is negligible in view of the distance traveled. The left-running mode propagating from the trailing-edge interface undergoes a cut-on to cut-off transition and so its energy vanishes with the transmitted evanescent mode beyond the

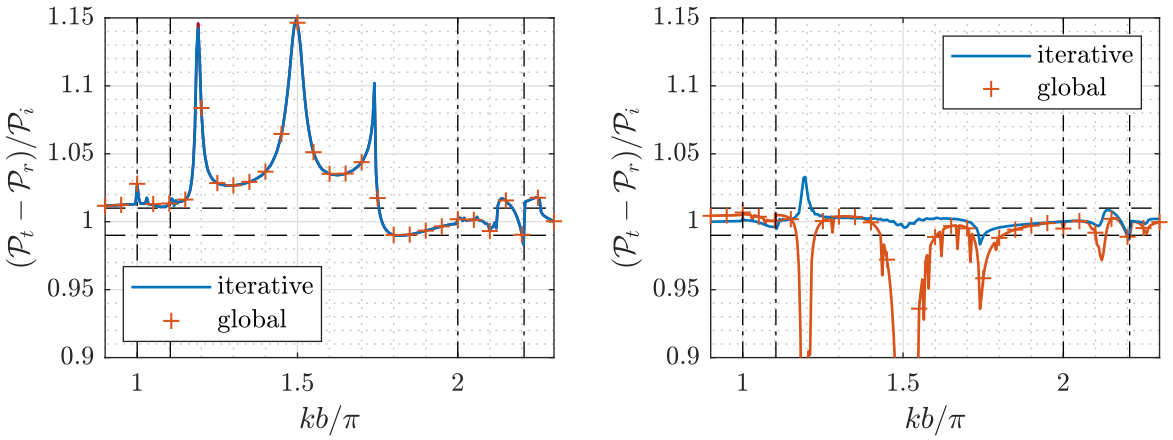

(a) $N = 11$ (b) $N = 31$

Figure 4.13: Acoustic power balance for $j = -7$ and different modal truncations, $\Psi = 25°$.

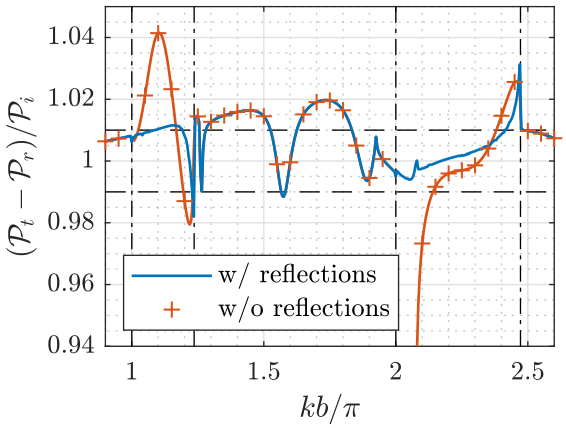

Figure 4.14: Influence of the transition modeling on the acoustic power balance for $j = 2$ and $\Psi = 36°$.

transition location. Adding the reflected propagating mode allows one to recover this missing energy. This demonstrates that a single mode can have a significant impact on the acoustic power balance and so in the modal distribution. In the q_1-transition range, the energy is sometimes higher than it should be and sometimes lower, indicating a more complex role of the mode undergoing transition on the power balance. These results show the importance to properly model the transition mechanism in order to accurately predict the scattering of an acoustic wave by a cascade of cambered vanes.

Figure 4.15a shows the detail of the power distribution when computed with the transition properly modeled. It appears that the larger discrepancy of Figure 4.14 between $kb/\pi = 2$ and $kb/\pi \simeq 2.1$ is due to a resonance phenomenon. Since the mode responsible for the resonance undergoes transition at these frequencies, both mechanisms could be coupled in this case. In the following, acoustic power distributions, modal distributions and pressure maps are analyzed to further understand the role of the transition at resonant frequencies.

4.5.2 Resonant Phenomena in the Transition Range

The acoustic power distribution, between reflected and transmitted powers, for the incident mode $j = 2$ is plotted in Figure 4.15 against the dimensionless frequency kb/π with and without modeling the reflected modes at the transition.

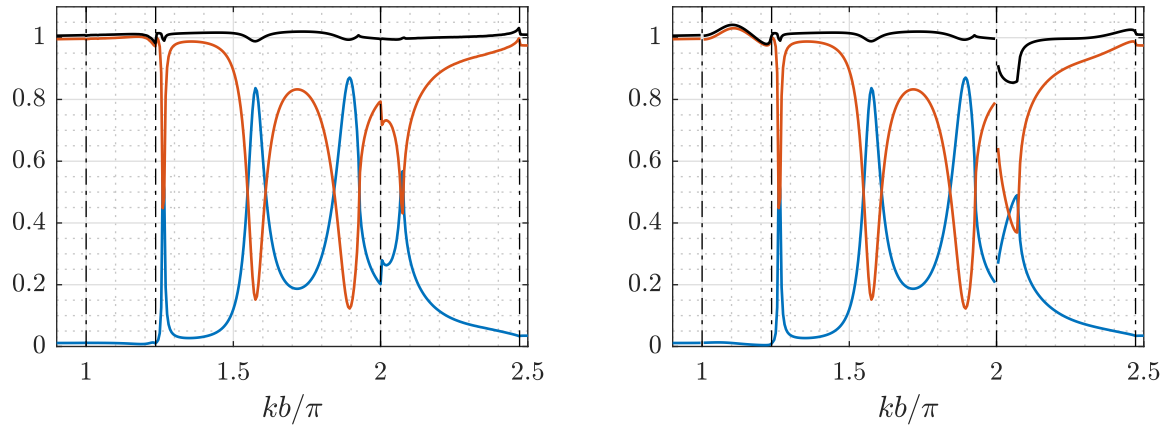

(a) with reflections at the transition

(b) without reflections at the transition

Figure 4.15: Reflected $-\mathcal{P}_r/\mathcal{P}_i$ (—), transmitted $\mathcal{P}_t/\mathcal{P}_i$ (—) and total $(\mathcal{P}_t - \mathcal{P}_r)/\mathcal{P}_i$ (—) powers evolution for $j = 2$ and $\Psi = 36°$.

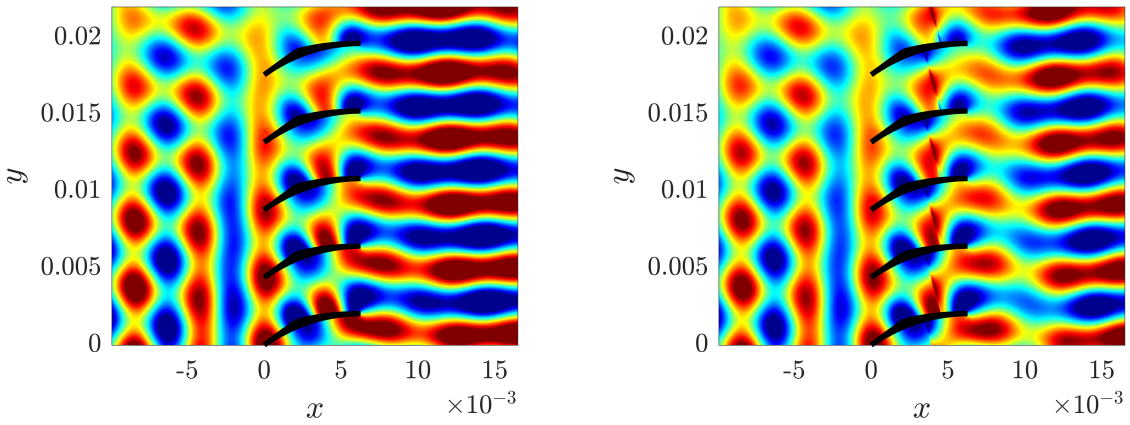

(a) with reflections at the transition

(b) without reflections at the transition

Figure 4.16: Instantaneous pressure maps at the (0,2) resonance for $j = 2$ and $\Psi = 36°$.

In this case, not modeling the reflected modes at the transition does not seem to change drastically the quasi-resonance spotted in the q_2-transition range. The relative reflected power still reaches a peak of 42%, without reflections, instead of 57% with reflections. The difference could be due to the missing energy in the total balance. Figure 4.16 shows the corresponding pressure maps for five of the fifty four vanes at the frequency of the quasi-resonance. Though the amplitudes look the same qualitatively, Figure 4.17 shows the left-running cut-on channel mode U of order $q = 2$ is two times higher when its reflection at the transition is modeled, while the right-running cut-off channel mode D_2 is almost the same. However the quasi-resonance is too weak to

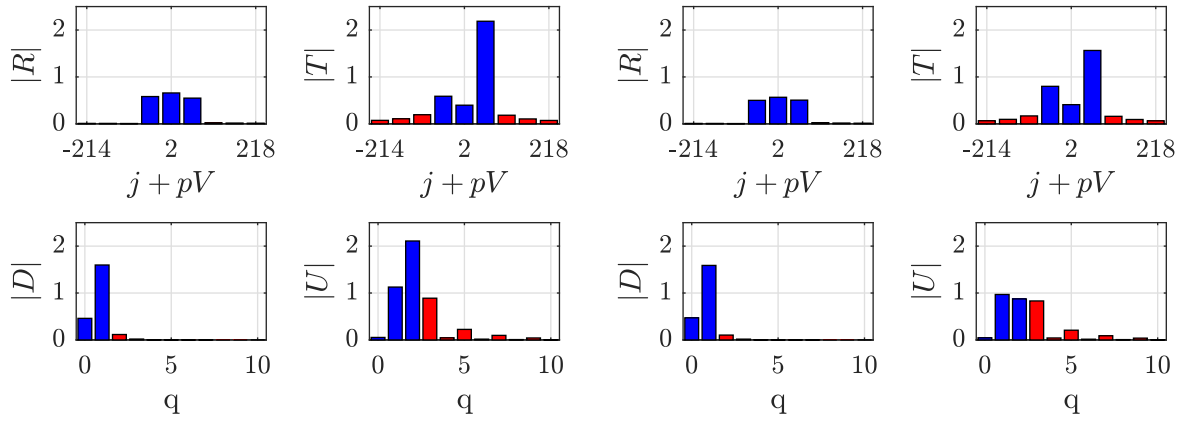

(a) with reflections at the transition (b) without reflections at the transition

Figure 4.17: Reflected R, transmitted T, downstream D and upstream U modal distributions at the (0,2) resonance for $j = 2$ and $\Psi = 36°$.

conclude on any influence of the transition modeling and the reflected modes in this case.

The incident modal order is now changed to $j = 22$ to observe the same quasi-resonances but with a different inter-vane phase shift. The acoustic power distribution is shown in Figure 4.18. This time, the first quasi-resonance in $1 \leq kb/\pi < 2$ occurs in the q_1-transition range but is also too weak to give further conclusions. On the other hand, the quasi-resonance in the q_2-transition range is now stronger and totally disappears when neglecting the reflected modes at the transition. This could indicate a particular role of the transition mechanism.

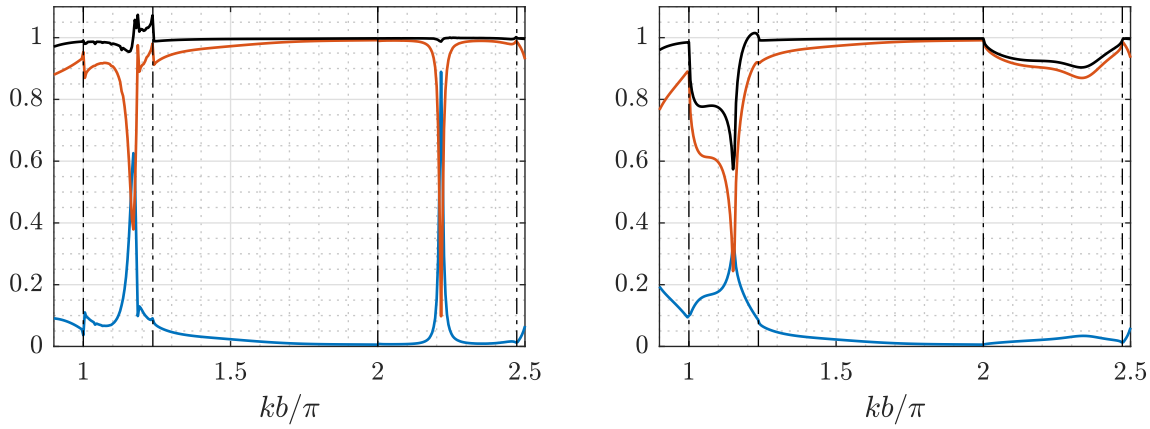

(a) with reflections at the transition (b) without reflections at the transition

Figure 4.18: Reflected $-\mathcal{P}_r/\mathcal{P}_i$ (—), transmitted $\mathcal{P}_t/\mathcal{P}_i$ (—) and total $(\mathcal{P}_t - \mathcal{P}_r)/\mathcal{P}_i$ (—) powers evolution for $j = 22$ and $\Psi = 36°$.

Changing the incident modal order to $j = 22$ triggers the quasi-resonance noticeably stronger than with $j = 2$ as displayed in Figures 4.19 and 4.20. Again, the major difference between the modal distributions, with and without properly modeling the transition, is the left-running cut-on channel mode U_2. It is almost five times higher in 4.20a than in 4.20b. For a resonance, or quasi-resonance, to happen, both right-

and left-running modes of the same order need to have a relatively high amplitude to form a standing-wave pattern along the channel. In this case, the transition occurs at 30% of the slowly-varying part of the channel. At the transition location, the cut-off channel mode D_2 has vanished and so the resonance pattern is solely due to the left-propagating mode U_2 and its reflection at the transition. This explains why the quasi-resonance is missing when neglecting this reflected mode.

Notice that, at such frequency, the curvature effects could change the behavior of the resonance, as shown in section 3.4. Though the resonance amplitude could be overestimated by the straight-channel assumption, its existence should not be compromised but only shifted in frequency. Furthermore, this observation on the role of the upstream-propagating mode U_2 is independent of the curvature since Brambley and Peake [14] demonstrated that the reflection and transmission coefficients at the transition location are the same for bent and straight ducts. Hence, the standing-wave pattern should appear in both cases. To summarize, only the transition location and the shape of the pressure field would be different if accounting for curvature effects, not compromising the occurrence of the resonance due to the reflection of the upstream-propagating mode.

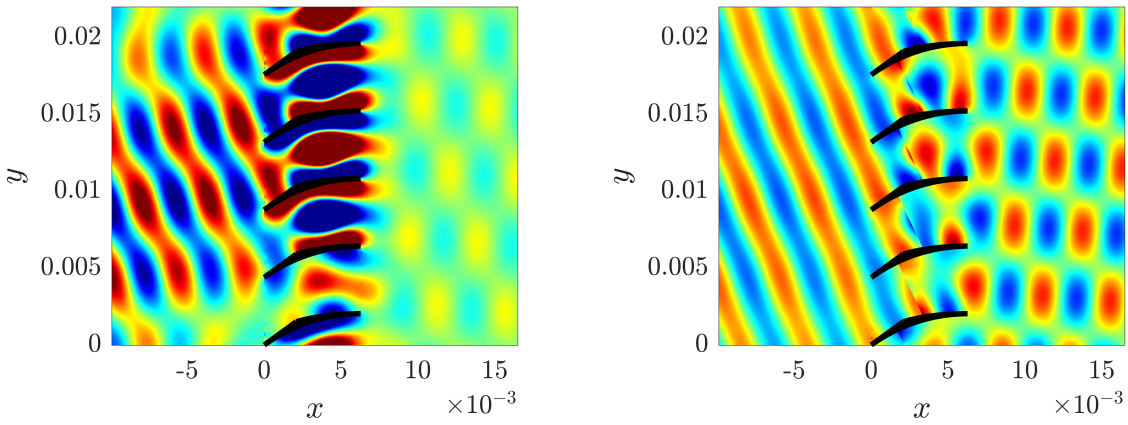

(a) with reflections at the transition

(b) without reflections at the transition

Figure 4.19: Instantaneous pressure maps at the (0,2) resonance for $j = 22$ and $\Psi = 36°$.

The remaining question is whether or not this type of resonance is a new phenomenon triggered by the transition mechanism and coexisting alongside the classical resonances of the cascade. The so-called Parker mode diagram, which displays the evolution of the resonant frequencies with the solidity value, is plotted in Figure 4.21. The horizontal dash-dotted lines represent the limits of the transition ranges. The resonant frequencies are not directly computed from the mode-matching equations but found by looking for local maxima of the relative reflected acoustic power at different solidity values.

The resonant modes (0,1) and (1,2) have frequencies both inside and outside their respective transition ranges in Figure 4.21, and the curve slope does not seem to be altered by the occurrence of the transition. If a new resonance mechanism were triggered by the transition, two different curves for the modes (0,1) and (1,2), or a bifurcation at the limits $kb/\pi = 1/\cos(\Psi) \simeq 1.23$ and $kb/\pi = 2/\cos(\Psi) \simeq 2.47$, would be expected. It seems that there is no new resonances for a cascade of cambered vanes compared to

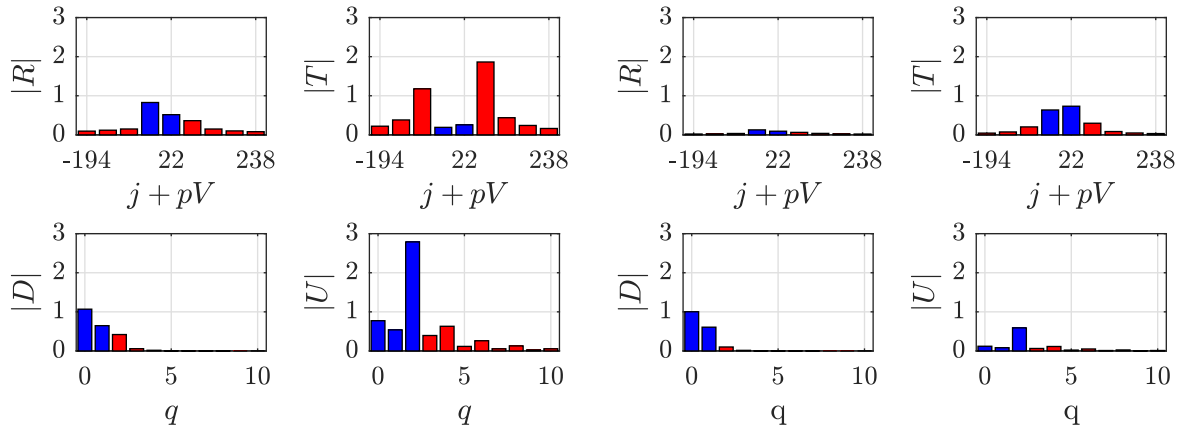

(a) with reflections at the transition (b) without reflections at the transition

Figure 4.20: Reflected R, transmitted T, downstream D and upstream U modal distributions at the (0,2) resonance for $j = 22$ and $\Psi = 36°$.

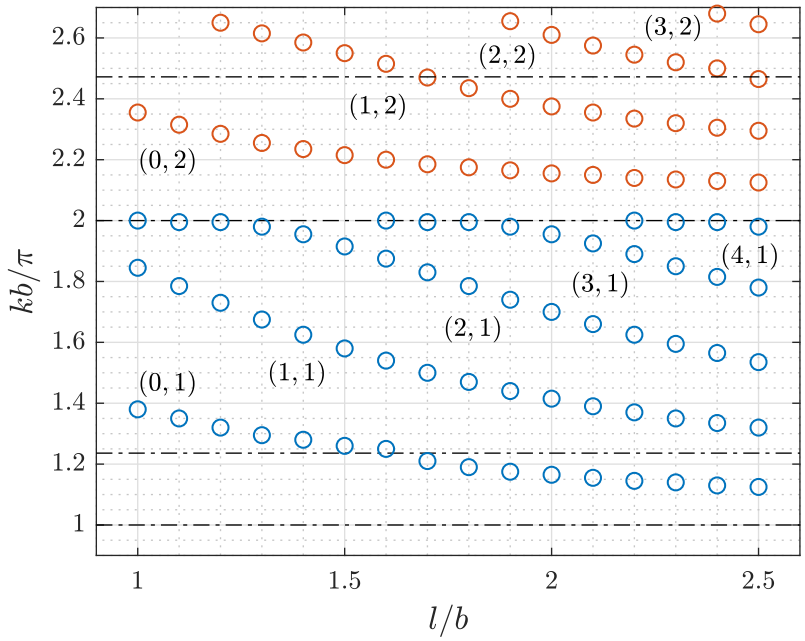

Figure 4.21: "Parker mode diagram" for ideal resonances with $j = 0$ (○) and $j = V/2$ (○).

flat vanes. The origin of the phenomenon is only more subtle due to the occurrence of transitions. The transition mechanism is needed to ensure the continuity of the resonances in Figure 4.21 when the right-running mode D vanishes and the reflection of the left-running mode U takes his role.

4.5.3 Influence of a Uniform Mean Flow on the Transition Range

The addition of a mean flow, assumed uniform in any cross-section, shifts and reduces the frequency ranges over which transitions occur. It is useful to know how much of the frequency range is covered by occurrences of transitions. It allows one to estimate the

influence the transitions could have on the noise prediction, especially for broadband noise. The distribution of the transition areas and the influence of the Mach number are explained in the following.

Figure 4.22 shows the dimensionless frequency ranges over which the modes undergo transition by hatched areas for increasing values of the camber angle. When $\Psi =$

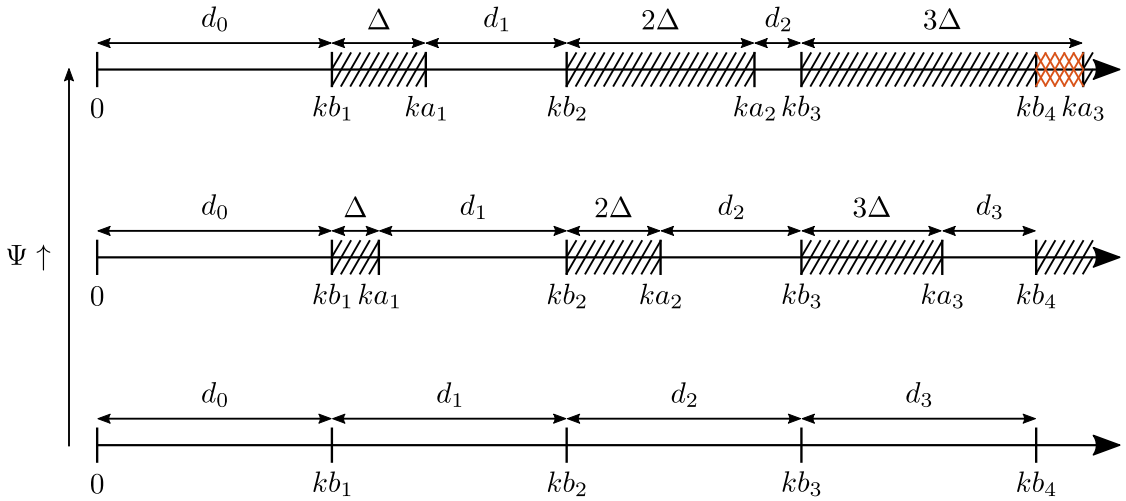

Figure 4.22: Sketch of the evolution of the modes transition ranges with the frequency and the camber angle. The transition location moves from the trailing edge at the cut-off frequency kb to the leading edge at the cut-off frequency ka.

0 no transition occurs and so the dimensionless cut-off frequencies are separated by a constant distance $d_q = \pi\beta$ for each modal order q, where $\beta = \sqrt{1-M^2}$. With increasing camber angle, transition ranges of growing length are observed. The length of a transition range, for a given mode q, is given by the difference between the cut-off frequencies at the inlet and the outlet $ka_q - kb_q = q\Delta$. Its value is defined by

$$\Delta = \pi\left(\frac{b\beta_a - a\beta_b}{a}\right) = \pi\left(\frac{\beta_a - \beta_b\cos\Psi}{\cos\Psi}\right), \tag{4.74}$$

where $\beta_a = \sqrt{1-M_a^2}$, $\beta_b = \sqrt{1-(D_aC_aM_a\cos\Psi)^2/(D_bC_b)^2}$ and the subscripts a and b indicate that the variable is evaluated at the inlet or outlet of the slowly-varying part of the channel. Without flow $\beta_a = \beta_b = 1$ and so $\Delta \geq 0$ for any value of the camber angle. In the presence of a mean flow, an increasing Mach number reduces the cut-off frequencies so they are shifted to the left in Figure 4.22. Because the Mach number is higher at the inlet than the outlet, the inlet cut-off frequencies ka_q are shifted faster than the outlet cut-off frequencies kb_q. The lengths of the transition areas are reduced and the cut-off frequencies of a mode can even be inverted, when $\Delta < 0$. For a given camber angle $\Psi \neq 0$, if the inlet Mach number M_a takes the exact value that cancels out Δ, it will result in a similar case to when $\Psi = 0$ and no transition can occur. For higher Mach numbers, the modes are no longer cut-off then cut-on, but cut-on then cut-off along the inter-vane channels. However, this case is not examined here since it appears for relatively high subsonic Mach numbers $M_a \gtrsim 0.7$ that are out of the scope of this study. An example of which has been given by Ingenito & Roger [52] in the inlet-duct of a centrifugal compressor with a Mach number artificially increased to 0.72. Consequently, the distance d_q separating the transition ranges of the modes q

and $q+1$ is

$$d_q = \pi\beta_b - q\Delta. \tag{4.75}$$

When $d_q \leq 0$ the modes q and $q+1$ both undergo transition on the overlapping frequency area. It is illustrated by double red hatches in Figure 4.22 for the highest camber angle case. An estimation of the occurrence of transitions can be given by the probability of having at least one mode undergoing transition over a given frequency range. This implies to not account for the overlapping transition frequencies more than once. Thus, letting Tr denote the number of modes undergoing transition, the probability for frequencies ranging from 0 to $kb_{N_q} = N_q\pi\beta_b$ is given by

$$P_{N_q}(Tr \geq 1) = 1 - \frac{\sum_{q=0}^{N_q-1} d_q}{N_q\pi\beta_b}, \quad \text{if} \quad d_q > 0. \tag{4.76}$$

The probabilities $P_3(Tr \geq 1)$ and $P_5(Tr \geq 1)$ are plotted against the camber angle in Figure 4.23 for $M = 0$ and $M = 0.45$, neglecting any compressible effect. For the NASA SDT baseline configuration (7808 RPM), these frequency ranges would cover the first six BPF ($N_q = 3$) and the first ten BPF ($N_q = 5$).

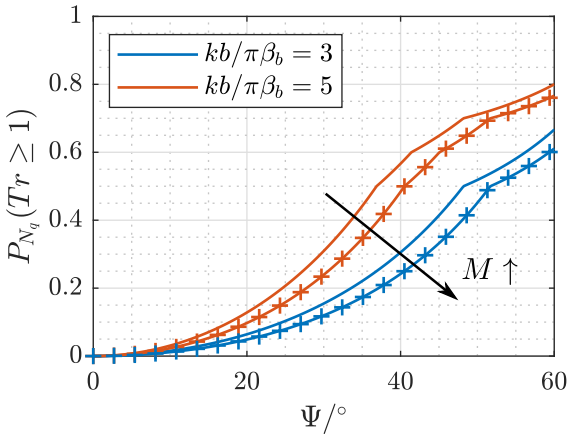

Figure 4.23: Evolution of the probability of having at least one mode undergoing transition with increasing values of the camber angle. The frequency ranges are chosen from 0 to $kb/\pi\beta_b = 3$ and 5. The solid lines represent the cases where $M = 0$ whereas the cross marks are for $M = 0.45$ without compressible effects.

Depending on the bandwidth considered, Figure 4.23 shows that 23% to 47% of the frequencies contain at least one transition for $\Psi = 36°$ at $M_a = 0$, and 18% to 37% at $M_a = 0.45$. The wider the integration range, the higher the probability. Hence, for broadband noise predictions it might be necessary to account for the transition mechanism when dealing with cambered vanes. However, for tonal noise predictions, the first BPFs can be outside of any transition ranges. As a consequence, depending on the architecture and the number of BPFs of interest, there could be no transition to account for.

Results — Summary

Relatively large discrepancies of the acoustic power balance, compared to the 1% confidence range, have been observed in the transition frequency areas when the transition mechanism is not properly modeled. The extension of the sound propagation model proposed in this chapter for the inter-vane channels has reduced the relative error to less than 1%, proving that the cause of the discrepancies was the neglected reflection of the modes undergoing transition. This mechanism also proved to be at the root of the resonance phenomenon for a cascade of cambered vanes at certain frequencies. Without it, the resonance could not take place when the corresponding right-running mode is cut-off in the left part of the channel and vanishes too quickly. In this case, the reflection at the transition location of the left-running mode replaces it to form a standing wave pattern of relatively high amplitude in the channels.
The presence of a uniform mean flow reduces the length of the transition areas. The higher the Mach number, the smaller the transition range. Nevertheless, transitions are present in a significant range of frequencies even at a Mach number of 0.45. They cannot be neglected for broadband noise predictions when using such approximate analytical solutions. It has also been proved that at sufficiently high Mach numbers, typically above 0.7, the cut-off frequencies of the channel modes are switched. Hence the modes are no longer cut-off then cut-on but rather cut-on then cut-off, which could change the tendencies observed in the acoustic power balance for this range of nearly sonic Mach numbers.

4.6 Conclusion

This chapter highlighted the singularity in the leading-order multiple-scale solution derived for the acoustic potential inside the cambered inter-vane channels in Chapter 2. The singularity was shown to arise when an acoustic mode undergoes transition from cut-on to cut-off, or vice-versa, due to the change of cross-section along the channel. In the vicinity of the transition, the mode no longer varies slowly and another solution is required. The so-called inner solution has been derived and used to compute the connection formulas between the outer modal coefficients. These general formulas can be applied in the particular case of an incident cut-on or cut-off mode to obtain the reflection and transmission coefficients through the transition. A uniformly valid solution has then been derived based on Langer's result [63] and following the work of Ovenden [86]. This composite solution has been introduced into the mode-matching equations to form a more general set of equations that works for modes undergoing transition or not. The method performed well in the transition areas but some non-converging cases were observed, when resorting to the iterative approach, for transitions occurring near the leading-edge interface. It seems the problem comes from the mode $q = 1$ and its reflection at the turning point, whose amplitude becomes larger and larger as the transition gets closer to the leading edge. In these cases, its growing amplitude cannot be compensated while enforcing the continuity equations, due to the lack of cut-on modes at these frequencies. Using a direct approach that computes all modal coefficients simultaneously, from a global matrix covering the leading-edge and trailing-edge continuity equations, fixed the convergence issues. At other frequencies,

the direct and iterative methods give similar results except in some rare cases. In conclusion, the direct approach could be used in place of the iterative approach to avoid convergence issues.

Comparing the acoustic power balances obtained with this model and the model of Chapter 2 when a transition occurs has shown the necessity to account for transitions when dealing with cambered vanes. If they are neglected, as in Chapter 2, the acoustic power balance is wrong by many percents while the error is negligible with the model of the current chapter. The difference is mainly due to the reflected part of the mode undergoing transition while the regularization at the transition location is only needed when the transition happens close to an interface. On top of that, this reflected part has been shown to play a role in resonant phenomena of the cascade. To not account for it means to miss some resonances that drastically change the way sound propagates through the cascade. Finally, the distribution of transitions in the frequency domain and how the mean flow influences it has been explained. The higher the order of a mode, the higher and numerous its transition frequencies. Also, the transition frequencies range expands with the camber angle but shrinks with the Mach number. For the realistic test-case of the fourth NASA CAA workshop, category 3, problem 2 [24], around 37% of the frequencies between 0 and the ninth BPF contain at least a transition. In terms of broadband noise prediction, it is indeed necessary to account for transitions. However, it might not be needed for tonal noise prediction depending on the architecture and the number of BPF of interest.

About limitations of the current model, the most crucial would be the frequency. As shown in the previous chapter, the straight-channel approximation only works at low frequencies or for weakly cambered vanes. For a realistic OGV geometry it would be needed to derive a new composite solution for a mode undergoing transition inside a slowly-varying bent channel. Brambley & Peake [14] paved the way for such a work and their results could serve as a starting point. Another limit of the current model is that no energy transfer between neighboring modes at the transition point is considered whereas it is known to occur at high frequencies, especially for large modal orders [88, 126, 127]. Some works from Smith [126, 127] highlighted higher-order scattering mechanisms becoming significant and introducing a coupling between neighboring modes in the inner region. A new purely geometrical mechanism due to the slowly-varying cross-section was brought to light with another mechanism induced by the presence of a mean flow.

Chapter 5

Sound Generation by Periodic Wake Impingement on a Linear Cascade of Cambered Vanes

Introduction

This chapter addresses the problem of sound generation by periodic wake impingement by modeling the wakes as incident vortical gusts. The linearity of the problem for perturbations of small amplitude allows one to describe the vortical gusts independently of the acoustic waves generated. Thus, the potentials defined in the previous chapters can be reused, and only the description of the gust is needed. This is done in the first section of this Chapter, after a brief presentation of the problem, in the assumption of an equivalent straight channel due to yet unresolved complexities for modeling the vortical gust evolution in a curved channel. The matching equations are then derived and comparisons with numerical and analytical results are made to assess the validity of the model. Finally, a parametric study on the effect of camber and acoustic resonance is performed.

Contents

5.1 General Considerations

In this chapter, noise generated by periodic interactions of the fan wakes with the OGV is investigated. The difference with the transmission of a sound wave is that the incident disturbance is now a vortical gust, corresponding to an azimuthal Fourier component of the wake mean velocity deficit. Different options for obtaining the wake characteristics at the OGV leading edge have been presented in Chapter 1, Section 1.2.3. Whether the wake mean velocity deficit is modeled or extracted from a RANS simulation is not a concern here. The only assumption is that azimuthal Fourier components are available at the OGV leading edge.

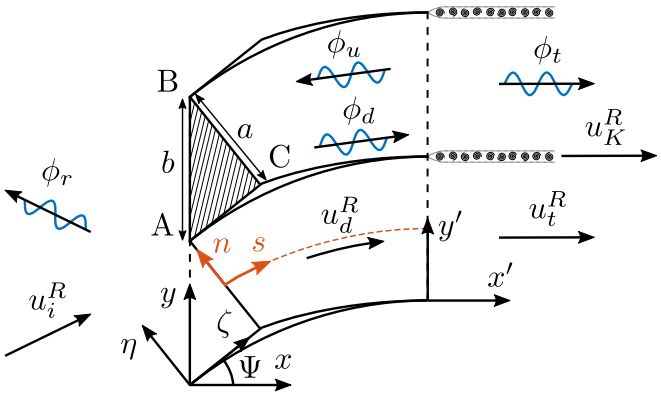

Figure 5.1: Impingement of a vorticity gust on the cascade of cambered vanes.

Figure 5.1 depicts the problem of sound generation tackled in this Chapter. The fluctuating velocity field is now composed of acoustic (potential) and vortical motions: $u = \nabla\phi + u^R$. From the linearized analysis of Chu and Kovásznay [20] for small perturbations, both motions are independent away from the cascade. Hence, they can be expressed separately and added up together at the end. The validity of this approach inside the inter-vane channels will also be assessed in this Chapter.

In the following, only the tonal noise is investigated but the model could be extended to broadband noise predictions as explained by François et al.[34]. The first section defines the vortical velocity field in each sub-domain. Then, the matching equations are derived with the knowledge of the acoustic potentials already derived in the previous Chapters. The matching equations are the cement that links both motions together, whereas it is usually done in a mathematically equivalent way at the vane surface.

5.2 Wake Model

5.2.1 Vorticity Field Upstream of the Cascade

The fan, composed of B blades, is assumed to generate B identical and regularly spaced wakes, which are convected at the speed of the mean flow $\mathbf{U}$ and rotate at the rate of the fan Ω_R. This means a given OGV is periodically interacting with a wake at the characteristic period $T = 2\pi/B\Omega_R$. Hence, an azimuthal Fourier component of the wake of order j, referred to as vortical gust, has a characteristic frequency equals to a multiple of the Blade Passing Frequency (BPF): $\omega_j = jB\Omega_R$.

The axial component of the wake vortical velocity is written as a sum of gusts:

$$\mathbf{u}_i^R(x,y)\cdot\mathbf{e}_x = u_{ix}^R(x,y) = \sum_{j=-\infty}^{\infty} w_j \mathrm{e}^{\mathrm{i}\alpha_j y}\mathrm{e}^{\mathrm{i}k_{jx}^R x}, \quad j\neq 0, \quad -\infty < x \leq 0, \quad 0 \leq y < 2\pi R, \tag{5.1}$$

where the order $j = 0$ is discarded because it corresponds to the mean part of the wakes, not a fluctuation, and contributes to the mean loading only. The periodicity condition in the transverse direction is now reduced to the distance separating two adjacent wakes. It reads $u_{ix}^R(x,0) = u_{ix}^R(x,2\pi R/B)$, which gives

$$\alpha_j = \frac{jB}{R}, \quad j\in\mathbb{Z}^*.$$

The axial wavenumber k_{jx}^R is defined from (1.10), which states that in a uniform and irrotational mean flow the velocity gusts are purely convected. This reads

$$\left(-\mathrm{i}\omega_j + \mathbf{U}\cdot\nabla\right)\mathbf{u}_i^R(x,y) = 0, \quad -\infty < x \leq 0, \quad 0 \leq y < 2\pi R. \tag{5.2}$$

The above equation is solved in the flow-attached frame of reference (ζ,η) of Figure 5.1, which is the same as the vane-attached frame of reference since no angle of attack is considered. In this frame of reference, the incident vortical velocity reads

$$u_{i\zeta}^R(\zeta,\eta) = \sum_{j=-\infty}^{\infty} w_{j\zeta}\mathrm{e}^{\mathrm{i}(\alpha_j\cos\Psi + k_{jx}^R\sin\Psi)\eta}\mathrm{e}^{\mathrm{i}(k_{jx}^R\cos\Psi - \alpha_j\sin\Psi)\zeta}.$$

Introducing the above expression into equation (5.2) gives

$$-\omega_j + U_{-\infty}(k_{jx}^R\cos\Psi - \alpha_j\sin\Psi) = 0,$$

which defines the axial wavenumber as

$$k_{jx}^R = \frac{\omega_j/U_{-\infty} + \alpha_j\sin\Psi}{\cos\Psi} = \frac{k_j + \alpha_j M_{-\infty y}}{M_{-\infty x}}, \tag{5.3}$$

where $k_j = \omega_j/C$, $M_{-\infty x} = U_{-\infty x}/C$ and $M_{-\infty y} = U_{-\infty y}/C$.

Finally, since $\mathbf{u}_i^R$ is divergence-free ($\nabla\cdot\mathbf{u}_i^R = 0$), its transverse component is defined by

$$u_{iy}^R(x,y) = -\sum_{j=-\infty}^{\infty} w_j\frac{k_{jx}^R}{\alpha_j}\mathrm{e}^{\mathrm{i}\alpha_j y}\mathrm{e}^{\mathrm{i}k_{jx}^R x}, \quad j\neq 0, \quad -\infty < x \leq 0, \quad 0 \leq y < 2\pi R. \tag{5.4}$$

Hence, the incident vortical velocity field is written as

$$\mathbf{u}_i^R \cdot \left\{ \begin{array}{l} \mathbf{e}_x \\ \mathbf{e}_y \end{array} \right. = \sum_{j=-\infty}^{\infty} \begin{pmatrix} 1 \\ -k_{jx}^R/\alpha_j \end{pmatrix} w_j \mathrm{e}^{\mathrm{i}\alpha_j y} \mathrm{e}^{\mathrm{i}k_{jx}^R x}, \quad j \neq 0, \tag{5.5}$$

and the associated vorticity field $\left(\nabla \times \mathbf{u}_i^R\right) \cdot \mathbf{e}_z$ as

$$\left(\nabla \times \mathbf{u}_i^R\right) \cdot \mathbf{e}_z = -\sum_{j=-\infty}^{\infty} \mathrm{i} \left(\frac{\alpha_j^2 + (k_{jx}^R)^2}{\alpha_j} \right) w_j \mathrm{e}^{\mathrm{i}\alpha_j y} \mathrm{e}^{\mathrm{i}k_{jx}^R x}, \quad j \neq 0, \tag{5.6}$$

for $-\infty < x \leq 0$ and $0 \leq y < 2\pi R$.

5.2.2 Vorticity Field Inside the Inter-Vane Channels

Triangle ABC

The definition of the velocity gusts in the triangle ABC needs to satisfy the following conditions: convection by the mean flow, hard-walled channel and inter-vane phase shift enforced by the trace-velocity matching principle [97]. For a given incident gust of order j, the longitudinal component of the vortical velocity disturbance in the channel reference frame reads

$$\mathbf{u}_d^R \cdot \mathbf{e}_\zeta = \sum_{q=1}^{\infty} A_q^R \cos(\alpha_q \eta) \mathrm{e}^{\mathrm{i}k_j^R \zeta}, \quad \eta \tan\Psi \leq \zeta \leq a \tan\Psi, \quad 0 \leq \eta \leq a, \tag{5.7}$$

where

$$\alpha_q = \frac{q\pi}{a}, \quad k_j^R = k_{jx}^R \cos\Psi - \alpha_j \sin\Psi = \frac{k_j}{M_{-\infty}}.$$

Applying the divergence-free condition leads to the definition of the vortical velocity field in the transverse direction, such that

$$\mathbf{u}_d^R \cdot \left\{ \begin{array}{l} \mathbf{e}_\zeta \\ \mathbf{e}_\eta \end{array} \right. = \sum_{q=1}^{\infty} \begin{pmatrix} 1 \\ -\mathrm{i}k_j^R/\alpha_q \end{pmatrix} A_q^R \begin{pmatrix} \cos(\alpha_q \eta) \\ \sin(\alpha_q \eta) \end{pmatrix} \mathrm{e}^{\mathrm{i}k_j^R \zeta}, \quad \eta \tan\Psi \leq \zeta \leq a \tan\Psi, \quad 0 \leq \eta \leq a. \tag{5.8}$$

The associated vorticity field $\left(\nabla \times \mathbf{u}_d^R\right) \cdot \mathbf{e}_z$ reads

$$\left(\nabla \times \mathbf{u}_d^R\right) \cdot \mathbf{e}_z = \sum_{q=1}^{\infty} \left(\frac{\alpha_q^2 + (k_j^R)^2}{\alpha_q} \right) A_q^R \sin(\alpha_q \eta) \mathrm{e}^{\mathrm{i}k_j^R \zeta}, \quad \eta \tan\Psi \leq \zeta \leq a \tan\Psi, \quad 0 \leq \eta \leq a, \tag{5.9}$$

The vortical fields in the other channels are then recovered by a phase shift of $\alpha_j b$, in the same manner as for the acoustic fields.

In order to identify the modal coefficients A_q^R, a new matching condition is required. From the linear analysis of Chu and Kovásznay [20], the vorticity can be used as a conservative variable through the interface. Since the acoustic velocity field is irrotational, the vorticity continuity at the leading-edge interface states that

$$\nabla \times \mathbf{u}_i^R = \nabla \times \mathbf{u}_d^R, \quad x = 0, \quad 0 \leq y < 2\pi R. \tag{5.10}$$

Extracting a closed-form solution for the coefficients A_q^R requires to integrate the above equation. This is done by projecting onto some sort of a weighted sine basis, the operator of which is defined as

$$\int_0^b (\bullet) \mathrm{e}^{-\mathrm{i}k_j^R y \sin\Psi} \sin\left(\alpha_\nu y \cos\Psi\right) \mathrm{d}y, \quad \text{with} \quad \alpha_\nu = \frac{\nu\pi}{a},\ \nu \in \mathbb{N}^*. \tag{5.11}$$

This allows one to compensate for the remaining exponential term in the channel vorticity field (5.9) at $x = 0$ when $\Psi \neq 0$, thus taking advantage of the orthogonality of the sine functions. Applying this operator to (5.10) gives

$$-\mathrm{i}\left(\frac{\alpha_j^2 + (k_{jx}^R)^2}{\alpha_j}\right) w_j \mathfrak{J}_{j,\nu}^R = \left(\frac{\alpha_\nu^2 + (k_j^R)^2}{\alpha_\nu}\right) A_\nu^R \frac{b}{2}\left(1 - \delta_{\nu,0}\right)$$

where

$$\mathfrak{J}_{j,\nu}^R(\Psi) = \int_0^b \mathrm{e}^{\mathrm{i}\alpha_j y} \mathrm{e}^{-\mathrm{i}k_j^R y \sin\Psi} \sin\left(\alpha_\nu y \cos\Psi\right) \mathrm{d}y = \begin{cases} \dfrac{\nu\pi/b}{(\nu\pi/b)^2 - (\varphi_j^R)^2}\left(1 - (-1)^\nu \mathrm{e}^{-\mathrm{i}b\varphi_j^R}\right), \\ \dfrac{\mathrm{i}b}{2}\left(1 - \delta_{\nu,0}\right) \quad \text{if} \quad \left|\varphi_j^R\right| = \nu\pi/b, \end{cases} \tag{5.12}$$

and

$$\varphi_j^R(\Psi) = k_j^R \sin\Psi - \alpha_j.$$

Consequently, the modal coefficients of the vortical velocity field inside the triangle ABC are defined by

$$A_{q\neq 0}^R = \frac{-\mathrm{i}\left(\dfrac{\alpha_j^2 + (k_{jx}^R)^2}{\alpha_j}\right) w_j \mathfrak{J}_{j,q}^R}{\left(\dfrac{\alpha_q^2 + (k_j^R)^2}{\alpha_q}\right)\dfrac{b}{2}}. \tag{5.13}$$

Slowly-Varying Curved Part

Between the interface BC and the trailing-edge interface, in the slowly-varying curved part of the channel, the evolution of the vortical disturbance becomes more complex due to the mean flow no longer being uniform and irrotational. Equation (1.10) states that

$$(-\mathrm{i}\omega_j + \mathbf{U}\cdot\nabla)\mathbf{u}_d^R + \left(\mathbf{u}_d^R \cdot \nabla\right)\mathbf{U} = -\left(\nabla \times \mathbf{U}\right)\times\nabla\phi, \quad 0 \leq S \leq L_c, \quad -\frac{h(S)}{2} \leq n \leq \frac{h(S)}{2}. \tag{5.14}$$

Using the notation $\mathbf{u}_d^R = u_{ds}^R \cdot \mathbf{e_s} + u_{dn}^R \cdot \mathbf{e_n}$, the different terms of the above equation are expressed under the slowly-varying approach in curvilinear coordinates as (see [78]

Chapter 1.4 for the differential operators definition)

$$(\mathbf{U}\cdot\nabla)\mathbf{u}_d^R = \epsilon\frac{U_{0s}}{h_s}\frac{\partial \mathbf{u}_d^R}{\partial S} + \epsilon U_{1n}\frac{\partial \mathbf{u}_d^R}{\partial n} + \frac{U_{0s}}{h_s}\frac{\mathrm{d}h_s}{\mathrm{d}n}\left(u_{dn}^R\cdot\mathbf{e_s} - u_{ds}^R\cdot\mathbf{e_n}\right) + O(\epsilon^2),$$

$$\left(\mathbf{u}_d^R\cdot\nabla\right)\mathbf{U} = \epsilon\frac{u_{ds}^R}{h_s}\frac{\partial U_{0s}}{\partial S}\cdot\mathbf{e_s} + \epsilon u_{dn}^R\frac{\partial U_{1n}}{\partial n}\cdot\mathbf{e_n} + \epsilon\frac{U_{1n}}{h_s}\frac{\mathrm{d}h_s}{\mathrm{d}n}u_{ds}^R\cdot\mathbf{e_s} - \frac{U_{0s}}{h_s}\frac{\mathrm{d}h_s}{\mathrm{d}n}u_{ds}^R\cdot\mathbf{e_n} + O(\epsilon^2),$$

$$\begin{aligned}(\nabla\times\mathbf{U})\times\nabla\phi &= \begin{pmatrix} 0 \\ 0 \\ -\dfrac{U_{0s}}{h_s}\dfrac{\mathrm{d}h_s}{\mathrm{d}n}\end{pmatrix}\times\begin{pmatrix}\dfrac{\epsilon}{h_s}\dfrac{\partial\phi}{\partial S} \\ \partial\phi/\partial n \\ 0\end{pmatrix} + O(\epsilon^2)\\ &= \frac{U_{0s}}{h_s^2}\frac{\mathrm{d}h_s}{\mathrm{d}n}\left(h_s\frac{\partial\phi}{\partial n}\cdot\mathbf{e_s} - \epsilon\frac{\partial\phi}{\partial S}\cdot\mathbf{e_n}\right) + O(\epsilon^2).\end{aligned}$$

This leads to the following equations for the longitudinal u_{ds}^R and transverse u_{dn}^R components:

$$\begin{aligned}&-\mathrm{i}\omega u_{ds}^R + \epsilon\frac{U_{0s}}{h_s}\frac{\partial u_{ds}^R}{\partial S} + \epsilon U_{1n}\frac{\partial u_{ds}^R}{\partial n} + \frac{U_{0s}}{h_s}\frac{\mathrm{d}h_s}{\mathrm{d}n}u_{dn}^R + \epsilon\frac{u_{ds}^R}{h_s}\frac{\partial U_{0s}}{\partial S} + \epsilon\frac{U_{1n}}{h_s}\frac{\mathrm{d}h_s}{\mathrm{d}n}u_{ds}^R\\ &= -\frac{U_{0s}}{h_s}\frac{\mathrm{d}h_s}{\mathrm{d}n}\frac{\partial\phi}{\partial n} + O(\epsilon^2),\end{aligned} \tag{5.15}$$

and

$$\begin{aligned}&-\mathrm{i}\omega u_{dn}^R + \epsilon\frac{U_{0s}}{h_s}\frac{\partial u_{dn}^R}{\partial S} + \epsilon U_{1n}\frac{\partial u_{dn}^R}{\partial n} - 2\frac{U_{0s}}{h_s}\frac{\mathrm{d}h_s}{\mathrm{d}n}u_{ds}^R + \epsilon u_{dn}^R\frac{\partial U_{1n}}{\partial n}\\ &= \epsilon\frac{U_{0s}}{h_s^2}\frac{\mathrm{d}h_s}{\mathrm{d}n}\frac{\partial\phi}{\partial S} + O(\epsilon^2).\end{aligned} \tag{5.16}$$

Then, the WKB expansion is introduced as

$$\left\{\phi, u_{ds}^R, u_{dn}^R\right\}(S,n;\epsilon) = \exp\left(-\frac{\mathrm{i}}{\epsilon}\int^S\mu(\xi)\,\mathrm{d}\xi\right)\sum_{m=0}^{\infty}\epsilon^m\left\{A_m, S_m, N_m\right\}(S,n), \tag{5.17}$$

for $0\le S\le L_c$ and $-h(S)/2\le n\le h(S)/2$. Introducing expression (5.17) into (5.15) - (5.16) and keeping only the $O(1)$ terms, yields

$$\mathrm{i}\Lambda S_0 - \frac{M}{h_s}\frac{\mathrm{d}h_s}{\mathrm{d}n}\left(N_0 + \frac{\partial A_0}{\partial n}\right)\sim 0, \tag{5.18}$$

$$\mathrm{i}\Lambda N_0 + \frac{M}{h_s}\frac{\mathrm{d}h_s}{\mathrm{d}n}\left(2S_0 + \frac{\mathrm{i}\mu}{h_s}A_0\right)\sim 0, \tag{5.19}$$

where $\Lambda = k_j - \mu M/h_s$ and $M = U_{0s}/C$. By noticing that Λ is the eigenvalue of the operator $(-\mathrm{i}\omega_j + \mathbf{U}\cdot\nabla)$, it comes out that the vortical perturbation is not purely convected because of vortical-vortical and vortical-acoustic coupling terms.

Assuming that the vortical velocity components and the acoustic velocity have the

same order of magnitude, the different couplings can all be neglected if

$$\frac{M}{k_j h_s}\frac{\mathrm{d}h_s}{\mathrm{d}n} \ll 1 \quad \Leftrightarrow \quad \mu_j^R \bar{R}_c \gg 1,$$

where the convective axial wavenumber μ_j^R is defined as

$$\mu_j^R = \frac{k_j h_s}{M}. \tag{5.20}$$

The coupling factor can be developed in terms of the design parameters, such that

$$\mu_j^R \bar{R}_c = 2\pi j \frac{B}{V}\frac{M_\Omega}{M}\left(\frac{l}{b}\frac{\cos\Psi/2}{\sin\Psi} - \frac{1+\cos\Psi}{4}\right), \tag{5.21}$$

where $M_\Omega = \Omega_R R/C$. For a scaled turbofan model such as the SDT baseline configuration composed of $B = 22$ blades and $V = 54$ vanes, taking a radius of 22.35 cm (40% of the radius of the 22-inch diameter model) and the shaft-rotation rate in approach condition of 7808 RPM ($M_\Omega \simeq 0.55$) results in an axial Mach number of $M_{-\infty} \simeq 0.45$. In such condition, the evolution of the coupling factor $\mu_j^R \bar{R}_c$, for the first BPF ($j = 1$) at $S = 0$ and $n = 0$, is plotted in Figure 5.2 for varying camber angles Ψ and solidity values l/b. For typical OGV design parameters, the vortical-vortical and

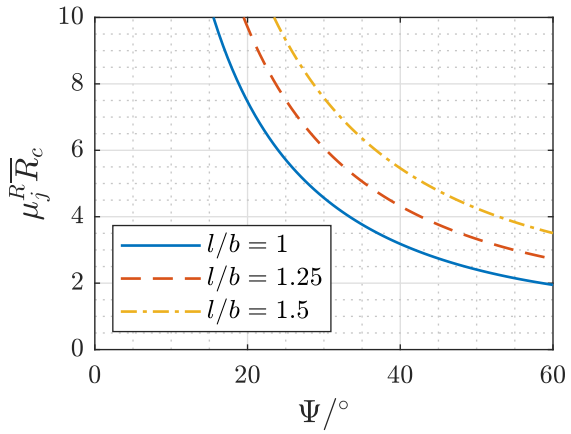

Figure 5.2: Evolution of the coupling factor $\mu_j^R \bar{R}_c$ against the camber angle Ψ for different solidity values l/b in the NASA SDT baseline configuration.

vortical-acoustic coupling can be neglected in the SDT baseline configuration. This means that both vortical velocity components u_{ds}^R and u_{dn}^R evolve independently and are simply convected by the mean flow.

The only remaining influence of curvature on the vortical velocity evolution is the scale factor $h_s = 1 - \kappa n$, in the definition of the convective axial wavenumber μ_j^R (5.20). Since the curvature is negative, this means that the wavenumber is greater in the upper part of the channel, and lower at the bottom, in order to compensate for the metric distortion induced by the curvilinear coordinates. Physically speaking, this means that the vortical perturbation is convected faster at the bottom of the channel than at the top. This curvature effect acts in a way similar to the curvature effect on the acoustic waves. With the latter, the wavefront was too drastically tilted downward when propagating through the cascade when the curvature effects were neglected (Chapter 2).

Taking the curvature into account in the model (Chapter 3) then allowed to recover a wavefront similar to the numerical results. Unfortunately, accounting for a wavenumber that varies with n would require a continuous variation of the curvature through the cascade to avoid a discontinuity at the interface BC and trailing-edge interface, as was mentioned in conclusion of Chapter 3 for the non-uniform mean flow. Such a work has not been further developed during the PhD. In the following, curvature effects are neglected as in Chapter 2, so the results are expected to be valid only at low frequencies, below the first channel cut-off.

Finally, after matching the expression of the vortical velocity field at the interface BC, between the straight (5.8) and slowly-varying (5.17) descriptions under the straight-channel assumption, the latter reads at leading order

$$\mathbf{u}_d^R \cdot \left\{ \begin{array}{c} \mathbf{e}_x \\ \mathbf{e}_y \end{array} \right. \sim \sum_{q=1}^{\infty} \begin{pmatrix} 1 \\ -\mathrm{i}\mu_j^R(X)/\theta_q(X) \end{pmatrix} A_q^R \Upsilon_{jq}^R(X) \begin{pmatrix} \cos(\theta_q(X)\,[y+h(X)/2]) \\ \sin(\theta_q(X)\,[y+h(X)/2]) \end{pmatrix} \mathrm{e}^{\mathrm{i}k_j^R a \tan\Psi}, \tag{5.22}$$

for $0 \leq X \leq L_c$ and $-h(X)/2 \leq y \leq h(X)/2$, where

$$\Upsilon_{jq}^R(X) = \frac{\theta_q(X)\left(\alpha_q^2 + (k_j^R)^2\right)}{\alpha_q\left(\theta_q^2(X) + (\mu_j^R)^2(X)\right)} \exp\left(\frac{\mathrm{i}}{\epsilon}\int_0^X \mu_j^R(\xi)\,\mathrm{d}\xi\right), \tag{5.23}$$

and

$$\alpha_q = \frac{q\pi}{a}, \quad k_j^R = \frac{k_j}{M_{-\infty}}, \quad \theta_q(X) = \frac{q\pi}{h(X)}, \quad \mu_j^R(X) = \frac{k_j(X)}{M(X)}. \tag{5.24}$$

This expression is divergence-free at leading order and fulfills the hard wall boundary condition: $u_{dy}^R = 0$, at $y = \pm h(S)/2$. The associated vorticity field $\left(\nabla \times \mathbf{u}_d^R\right) \cdot \mathbf{e}_z$ is then given by

$$\left(\nabla \times \mathbf{u}_d^R\right) \cdot \mathbf{e}_z \sim \sum_{q=1}^{\infty} \left(\frac{\theta_q^2(X) + (\mu_j^R)^2(X)}{\theta_q(X)}\right) A_q^R \Upsilon_{jq}^R(X) \sin\left(\theta_q(X)\left[y + \frac{h(X)}{2}\right]\right) \mathrm{e}^{\mathrm{i}k_j^R a \tan\Psi}, \tag{5.25}$$

for $0 \leq X \leq L_c$ and $-h(X)/2 \leq y \leq h(X)/2$. The vortical fields in the other channels are then recovered by a phase shift of $\alpha_j b$, according to the trace-velocity matching principle [97]. Notice that the vorticity amplitude (5.25) remains constant during its convection through the slowly-varying part of the channel, while its shape is slowly stretched in the transverse direction.

5.2.3 Vorticity Field Downstream of the Cascade

Due to its variation of shape through the inter-vane channels, the gust can exhibit a complex pattern downstream of the OGV. Figure 5.3 shows some numerical results of a viscous flow past the OGV in a rotor-stator configuration: (a) Mach number obtained by LES (Lewis [64]) and (b) vorticity obtained by ZDES (François et al. [33]). When looking at these numerical results, two key features of the wake evolution seem to stand out:

1. upward or downward tilting;

2. slicing by the vanes.

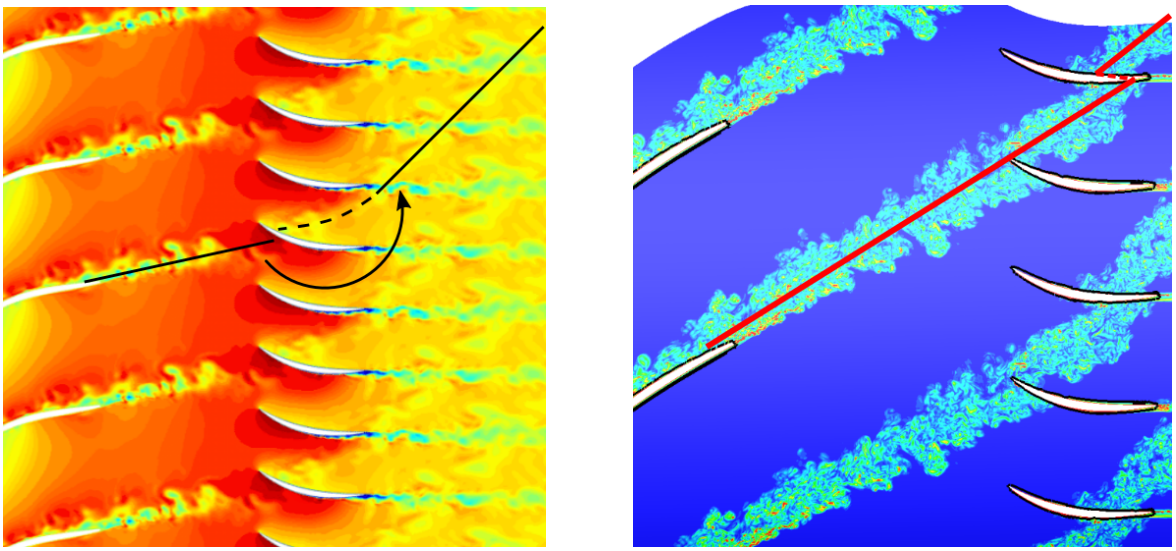

(a) (b)

Figure 5.3: Blade-to-blade visualization of fan-OGV flow simulations at mid-span: (a) Mach number obtained by LES (Lewis [64]) and (b) vorticity obtained by ZDES (François et al. [33]).

Whether the rotation/tilting is directed upward or downward seems to result mostly from the inter-vane channel geometry and the mean flow profile in it. The slicing, i.e. the horizontal shift in the wake segments between two adjacent inter-vane channels downstream of the OGV, also seems to depend on the case.

Since a vortical gust is simply a Fourier component of the wake, the same behavior should be expected. Downstream of the OGV, the transverse shape of a given gust of incident order $\alpha_j = jB/R$ can no longer be represented by a single transverse wavenumber. Furthermore, the gust profile needs to be modeled by layers in order to account for the slicing/shifting between two adjacent channels. To this end, the two following gust representations are proposed: shifted gust and smoothly shifted gust.

Shifted Gust Formulation

The shifted gust is given by

$$\mathbf{u}_t^R \cdot \begin{Bmatrix} \mathbf{e}_x \\ \mathbf{e}_y \end{Bmatrix} = \sum_{m=0}^{V-1} \sum_{p=-\infty}^{\infty} \begin{pmatrix} 1 \\ -k_{jt}^R/\alpha_p \end{pmatrix} T_p^R \mathrm{e}^{\mathrm{i}m\alpha_j b} \mathrm{e}^{\mathrm{i}\alpha_p(y'-mb)} \mathrm{e}^{\mathrm{i}k_{jt}^R x'} F_j^R, \tag{5.26}$$

with the associated vorticity field

$$(\nabla \times \mathbf{u}_t^R) \cdot \mathbf{e}_z = -\sum_{m=0}^{V-1} \sum_{p=-\infty}^{\infty} \mathrm{i} \left(\frac{\alpha_p^2 + (k_{jt}^R)^2}{\alpha_p} \right) T_p^R \mathrm{e}^{\mathrm{i}m\alpha_j b} \mathrm{e}^{\mathrm{i}\alpha_p(y'-mb)} \mathrm{e}^{\mathrm{i}k_{jt}^R x'} F_j^R, \tag{5.27}$$

for $0 \leq x' = x - l_x < \infty$ and $0 \leq y' = y - R_c(1 - \cos\Psi) < 2\pi R$, where

$$\alpha_j = \frac{jB}{R}, \quad \alpha_p = \frac{pB}{R}, \quad k_{jt}^R = \frac{k_j}{M_{+\infty}} \quad \text{and} \quad F_j^R = \exp\left(\frac{\mathrm{i}}{\epsilon} \int_0^{L_c} \mu_j^R(S)\, \mathrm{d}S \right) \mathrm{e}^{\mathrm{i}k_j^R b \sin\Psi}.$$

The T_p^R coefficients are given by the vorticity continuity at the trailing-edge interface, on a given layer $m = 0$:

$$\nabla \times \mathbf{u}_d^R = \nabla \times \mathbf{u}_t^R + \nabla \times \mathbf{u}_K^R, \quad x' = 0, \quad 0 \leq y' \leq b, \tag{5.28}$$

which yields

$$\sum_{q=1}^{\infty} \frac{\alpha_q^2 + (k_j^R)^2}{\alpha_q} A_q^R \sin\left(\frac{q\pi}{b} y'\right) = -\sum_{p=-\infty}^{\infty} \mathrm{i} \left(\frac{\alpha_p^2 + (k_{jt}^R)^2}{\alpha_p}\right) T_p^R \mathrm{e}^{\mathrm{i}\alpha_p y'} + \Omega_K \left(\delta(y') + \delta(y' - b)\right). \tag{5.29}$$

The vorticity field associated to the Kutta condition has been formulated with the Dirac delta function (see [12]) in order to simplify the following calculation. Since the ratio of B and V is usually not an integer in a fan-OGV stage [1], the gust does not have a shared periodicity with the OGV. Hence, the exponential basis $\exp(\mathrm{i}\alpha_p y')$ is not orthogonal with the inner product defined over the channel height. Equation (5.29) is then projected onto the channel modal basis by means of the operator

$$\int_0^b (\bullet) \sin\left(\alpha_\nu y'\right) \mathrm{d}y', \quad \alpha_\nu = \frac{\nu\pi}{b} \, \nu \in \mathbb{N}^*. \tag{5.30}$$

This leads to three kinds of integrals, namely $\mathfrak{J}_{q,\nu}^R$, $\mathfrak{J}_{p,\nu}^R$ and $\mathfrak{J}_{K,\nu}^R$, such that

$$\sum_{q=1}^{\infty} \frac{\alpha_q^2 + (k_j^R)^2}{\alpha_q} A_q^R \mathfrak{J}_{q,\nu}^R = -\sum_{p=-\infty}^{\infty} \mathrm{i} \left(\frac{\alpha_p^2 + (k_{jt}^R)^2}{\alpha_p}\right) T_p^R \mathfrak{J}_{p,\nu}^R + \Omega_K \mathfrak{J}_{K,\nu}^R.$$

The integral based on the channel vorticity field is expressed as

$$\mathfrak{J}_{q,\nu}^R = \int_0^b \sin\left(\frac{q\pi}{b} y'\right) \sin\left(\frac{\nu\pi}{b} y'\right) \mathrm{d}y' = \begin{cases} \frac{b}{2}(1 - \delta_{\nu,0}) & \text{if} \quad \nu = q, \\ 0 & \text{if} \quad \nu \neq q. \end{cases}$$

Hence, $\mathfrak{J}_{q,\nu}^R = b/2(1 - \delta_{\nu,0})\delta_{\nu,q}$, where δ is the Kronecker delta: $\delta_{\nu,q} = 1$ if $\nu = q$, and $\delta_{\nu,q} = 0$ otherwise. The integral associated with the vorticity field downstream of the cascade reads

$$\mathfrak{J}_{p,\nu}^R = \int_0^b \mathrm{e}^{\mathrm{i}\alpha_p y'} \sin\left(\frac{\nu\pi}{b} y'\right) \mathrm{d}y' = \begin{cases} \dfrac{\alpha_\nu}{\alpha_\nu^2 - \alpha_p^2} \left[1 - (-1)^\nu \mathrm{e}^{\mathrm{i}\alpha_p b}\right], \\ \dfrac{\mathrm{i}b}{2}(1 - \delta_{\nu,0}) \quad \text{if} \quad \alpha_\nu = |\alpha_p|. \end{cases}$$

Finally, the integral on the vorticity field associated with the Kutta condition yields

$$\mathfrak{J}_{K,\nu}^R = \int_0^b \left(\delta(y') + \delta(y' - b)\right) \sin\left(\frac{\nu\pi}{b} y'\right) \mathrm{d}y' = \sin\left(\frac{\nu\pi}{b} 0\right) + \sin\left(\frac{\nu\pi}{b} b\right) = 0.$$

This results in the the following linear system of equations on the T_p^R coefficients:

$$\sum_{p=-\infty}^{\infty} \left(\frac{\alpha_p^2 + (k_{jt}^R)^2}{\alpha_p}\right) T_p^R \mathfrak{J}_{p,\nu}^R = \frac{\mathrm{i}b}{2}(1 - \delta_{\nu,0}) \frac{\alpha_\nu^2 + (k_j^R)^2}{\alpha_\nu} A_\nu^R, \tag{5.31}$$

[1] This is done to avoid the generation of the plane-wave mode in the annular domain.

which is numerically solved after a modal truncation ($\nu \in [0, N_\nu - 1]$ and $p \in [-(N_p - 1)/2, (N_p - 1)/2]$). Note that, in order to get accurate enough results, it has been found necessary to use an iterative method with an initial guess set at $T_p^R = w_j$, if $p = j$, and $T_p^R = 0$ otherwise. However, the reliability of the result is difficult to assess with increasing camber angles. Surely this could be improved.

An example of shifted gust downstream of the OGV is represented in Figure 5.4. The modeling of the gust evolution through the cascade is able to recover both key

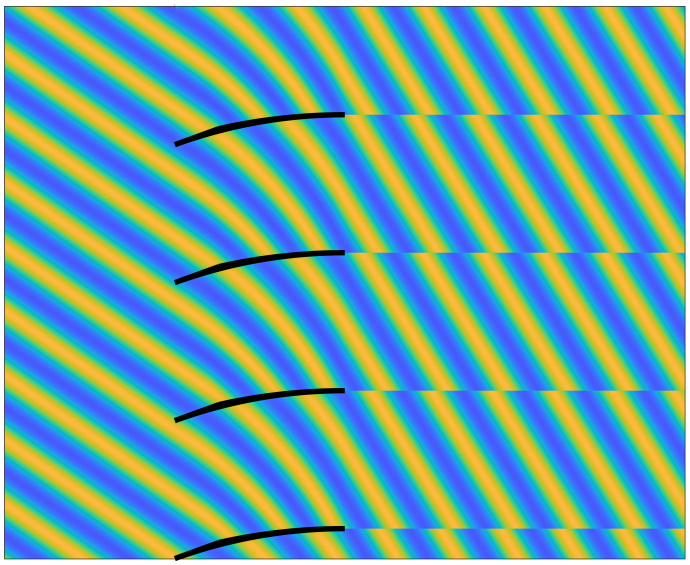

Figure 5.4: Vorticity field $\left(\nabla \times \mathbf{u}_t^R\right) \cdot \mathbf{e}_z$ with the shifted gust formulation.

features observed in the wake evolution in Figure 5.3: tilting and slicing. The different layers downstream of the OGV are discontinuous in the transverse/azimuthal direction. Even if this is not an issue in this work, another formulation of the gust is proposed, which smooths out these discontinuities.

Smoothly Shifted Gust Formulation

The smoothly shifted gust is a direct continuation of the channel gust description that allows one to smooth out the transverse discontinuity in the previous formulation. It reads

$$\mathbf{u}_t^R \cdot \left\{ \begin{array}{l} \mathbf{e}_x \\ \mathbf{e}_y \end{array} \right. = \sum_{m=0}^{V-1} \sum_{q=1}^{\infty} \begin{pmatrix} 1 \\ -\mathrm{i}k_{jt}^R/\alpha_q \end{pmatrix} T_q^R \mathrm{e}^{\mathrm{i}m\alpha_j b} \sin\left(\frac{q\pi}{b}[y' - mb]\right) \mathrm{e}^{\mathrm{i}k_{jt}^R x'} F_j^R, \tag{5.32}$$

with the associated vorticity field

$$\left(\nabla \times \mathbf{u}_t^R\right) \cdot \mathbf{e}_z = \sum_{m=0}^{V-1} \sum_{q=1}^{\infty} \left(\frac{\alpha_q^2 + (k_{jt}^R)^2}{\alpha_q}\right) T_q^R \mathrm{e}^{\mathrm{i}m\alpha_j b} \sin\left(\frac{q\pi}{b}[y' - mb]\right) \mathrm{e}^{\mathrm{i}k_{jt}^R x'} F_j^R, \tag{5.33}$$

for $0 \leq x' = x - l_x < \infty$ and $0 \leq y' = y - R_c(1 - \cos\Psi) < 2\pi R$, where

$$\alpha_j = \frac{jB}{R}, \quad \alpha_q = \frac{q\pi}{b}, \quad k_{jt}^R = \frac{k_j}{M_{+\infty}} \quad \text{and} \quad F_j^R = \exp\left(\frac{\mathrm{i}}{\epsilon}\int_0^{L_c} \mu_j^R(S)\,\mathrm{d}S\right)\mathrm{e}^{\mathrm{i}k_j^R b\sin\Psi}.$$

Using the vorticity continuity (5.28) with the same projection method (5.30) directly yields the solution

$$T_q^R = \frac{\alpha_q^2 + (k_j^R)^2}{\alpha_q^2 + (k_{jt}^R)^2} A_q^R. \tag{5.34}$$

This results in a smoothly shifted gust downstream of the OGV as represented in Figure 5.5. The latter formulation is interesting because it has a closed-form solution for

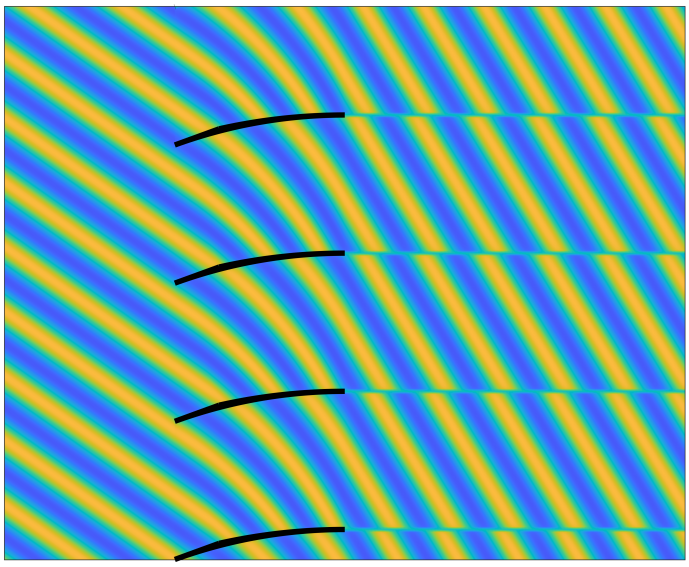

Figure 5.5: Vorticity field $\left(\nabla \times \mathbf{u}_t^R\right) \cdot \mathbf{e}_z$ with the smoothly shifted gust formulation.

the gust coefficients and allows a continuous description of the gust in the transverse direction. However, it does not tend toward the flat-vane solution of Bouley et al. [12] when $\Psi \to 0$ because of the remaining "wakes" in the gust. Therefore, this formulation is put aside for now and the shifted gust formulation (5.27) will be used in the following.

Wake Model — Summary

The vortical gust modeling has been extended to account for stagger at the leading-edge interface, and the slowly-varying cross-section across the channel. Curvature effects have been neglected in this work but a particular attention has been paid to justify the neglected effects:

1. vortical-vortical and acoustic-vortical coupling, the strength of which is given by the inverse of $\mu_j^R \bar{R}_c$;
2. curvature effect resulting in a transverse variation of the convective wavenumber $\mu_j^R \to \mu_j^R(1 - \kappa n)$: the strength of which is given by κb.

Numerical simulations available in the literature have then been used to extract the key characteristics of the wake evolution past a cascade of cambered vanes. This results in two features: slicing and tilting. Both have been incorporated into an analytical model to complete the formulation of the vortical gust evolution.

5.3 Mode-Matching Equations

5.3.1 Jump Conditions

When the fluctuating velocity field is composed of acoustic and vortical motions: $u = \nabla\phi + u^R$, the conservative variables need to be adjusted. Combining mass-flow conservation (1.13) and stagnation enthalpy conservation (1.17) as (1.17) - (1.13) yields

$$\left[\beta_x^2 \frac{p}{Z} + M_y u_y\right]_1^2 = 0,$$

where $\beta_x^2 = 1 - M_x^2$. This constitutes the first conservative variable Γ_1 as

$$\boxed{\Gamma_1 = \beta_x^2 \frac{p}{Z} + M_y u_y}. \tag{5.35}$$

Taking the combination (1.13) - M_x^2(1.17) gives

$$\left[\beta_x^2 M_x u_x - M_x^2 M_y u_y\right]_1^2 = 0,$$

which yields the same second conservative variable Γ_2 as in (2.71), when there is no vortical motion. This reads

$$\boxed{\Gamma_2 = \beta_x^2 u_x - M_x M_y u_y.} \tag{5.36}$$

Written like that, it is easy to see that the conservative variables (Γ_1, Γ_2) tend to the usual variables (p, u_x) when either $\Psi \to 0$ or $M \to 0$. The latter variables can be used at the trailing-edge interface. Furthermore, if the fluctuating velocity field is potential: $u = \nabla\phi$, then

$$\Gamma_1 = \mathrm{i}k_j\beta_x^2\phi - \beta_x^2 M_x u_x + M_x^2 M_y u_y = \mathrm{i}k\beta_x^2\phi - M_x\Gamma_2.$$

In this case, using the conservative variables (Γ_1, Γ_2) is identical to (ϕ, Γ_2), which is the set of conservative variables used for the scattering of an acoustic wave (see section 2.3.1). The conservative variables (5.35) and (5.36) are a generalized version accounting for both acoustic and vortical motions.

5.3.2 Leading-Edge Interface

Acoustic Potentials and Vortical Velocity Fields

When the incident perturbation is a vortical gust, the vortical velocity field is simply added on top of the existing scattered acoustic fields defined in the previous chapters. Both vortical and acoustic motions evolve independently in the different sub-domains

and are only connected through the matching equations at the interfaces. Figure 5.6 shows the different fluctuating fields involved at the leading-edge interface matching.

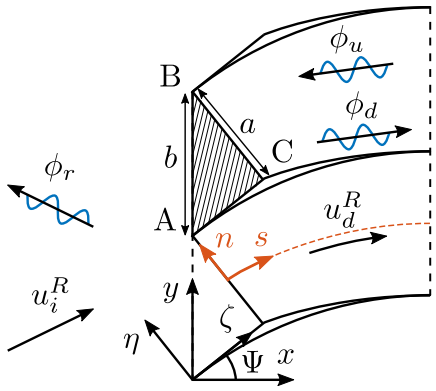

Figure 5.6: Impingement of a vortical gust on the cascade of cambered vanes at the leading-edge interface.

Since $\nabla \cdot \left(Du^R\right) = 0$ in both sub-domains joint by the leading-edge interface, the acoustic potentials are still defined by:

$$\phi_r(x,y) = \sum_{p=-\infty}^{\infty} R_p \mathrm{e}^{\mathrm{i}\alpha_p y} \mathrm{e}^{\mathrm{i}k_p^- x}, \quad -\infty < x \leq 0, \quad 0 \leq y < 2\pi R,$$

$$\hat{\phi}_d(\zeta,\eta) = \sum_{q=0}^{\infty} A_q \cos\left(\alpha_q \eta\right) \left[\mathrm{e}^{ik_q^R \zeta} + \mathcal{F}_q \mathrm{e}^{\mathrm{i}k_q^- \zeta}\right], \quad \eta \tan\Psi \leq \zeta \leq a\tan\Psi, \quad 0 \leq \eta \leq a,$$

$$\phi_u(\zeta,\eta) = \sum_{q=0}^{\infty} B_q \cos\left(\alpha_q \eta\right) \mathrm{e}^{ik_q^- (\zeta - a\tan\Psi)} \Xi_q^-(0), \quad \eta \tan\Psi \leq \zeta \leq a\tan\Psi, \quad 0 \leq \eta \leq a,$$

where

$$\alpha_p = \frac{jB + pV}{R}, \quad k_p^- = \frac{-(k - \alpha_p M_y)M_x - \sqrt{k^2 - (\beta_x^2 - M_y^2)\alpha_p^2 - 2k\alpha_p M_y}}{\beta_x^2},$$

$$\alpha_q = \frac{q\pi}{a}, \quad k_q^{\pm} = \frac{-kM \pm \sqrt{k^2 - \beta^2 \alpha_q^2}}{\beta^2}.$$

The potential $\hat{\phi}_d$ corresponds to the sum of the downstream-propagating potential ϕ_d and an eventual reflection inside the slowly-varying part of the channel, added along with its coefficient $\mathcal{F}_q$ (4.34). The potential ϕ_u is described by the general modal-evolution function Ξ_q^- (4.57) in order to account for the occurrence of transitions.

The vortical velocity fields are given by

$$\mathbf{u}_i^R \cdot \begin{Bmatrix} \mathbf{e}_x \\ \mathbf{e}_y \end{Bmatrix} = \begin{pmatrix} 1 \\ -k_{jx}^R/\alpha_j \end{pmatrix} w_j \mathrm{e}^{\mathrm{i}\alpha_j y} \mathrm{e}^{\mathrm{i}k_{jx}^R x}, \quad j \neq 0, \quad -\infty < x \leq 0, \quad 0 \leq y < 2\pi R,$$

and

$$\mathbf{u}_d^R \cdot \begin{Bmatrix} \mathbf{e}_\zeta \\ \mathbf{e}_\eta \end{Bmatrix} = \sum_{q=1}^{\infty} \begin{pmatrix} 1 \\ -\mathrm{i}k_j^R/\alpha_q \end{pmatrix} A_q^R \begin{pmatrix} \cos(\alpha_q \eta) \\ \sin(\alpha_q \eta) \end{pmatrix} \mathrm{e}^{\mathrm{i}k_j^R \zeta}, \quad \eta \tan\Psi \leq \zeta \leq a\tan\Psi, \quad 0 \leq \eta \leq a.$$

Continuity of the Stagnation Enthalpy

The first conservative variable Γ_1 is decomposed into its acoustic and vortical parts as $\Gamma_1 = \Gamma_1^a + \Gamma_1^R$. The acoustic part is equal to

$$\Gamma_1^a = \mathrm{i}k_j\beta_x^2\phi - \beta_x^2 M_x \nabla_x\phi + M_x^2 M_y \nabla_y\phi.$$

The derivative of the potential with respect to x and y has already been detailed in section 4.3.1. Thus, the conservative variable Γ_1^a of the different acoustic fields reads:

$$\Gamma_{1r}^a = \sum_{p=-\infty}^{\infty} \mathrm{i}R_p \left(k_j\beta_x^2 - \beta_x^2 M_x k_p^- + M_x^2 M_y \alpha_p\right) \mathrm{e}^{\mathrm{i}\alpha_p y}\mathrm{e}^{\mathrm{i}k_p^- x}, \tag{5.37}$$

$$\begin{aligned}\Gamma_{1d}^a = \sum_{q=0}^{\infty} \frac{\mathrm{i}}{2} A_q \Big[&\left(k_j\beta_x^2 - \beta_x^2 M_x K_q^{+-} + M_x^2 M_y A_q^{++}\right) \mathrm{e}^{\mathrm{i}A_q^{++}y}\mathrm{e}^{\mathrm{i}K_q^{+-}x} \\ &+ \left(k_j\beta_x^2 - \beta_x^2 M_x K_q^{++} + M_x^2 M_y A_q^{-+}\right) \mathrm{e}^{\mathrm{i}A_q^{-+}y}\mathrm{e}^{\mathrm{i}K_q^{++}x} \\ &+ \mathcal{F}_q \Big\{ \left(k_j\beta_x^2 - \beta_x^2 M_x K_q^{--} + M_x^2 M_y A_q^{+-}\right) \mathrm{e}^{\mathrm{i}A_q^{+-}y}\mathrm{e}^{\mathrm{i}K_q^{--}x} \\ &+ \left(k_j\beta_x^2 - \beta_x^2 M_x K_q^{-+} + M_x^2 M_y A_q^{--}\right) \mathrm{e}^{\mathrm{i}A_q^{--}y}\mathrm{e}^{\mathrm{i}K_q^{-+}x} \Big\} \Big],\end{aligned} \tag{5.38}$$

$$\begin{aligned}\Gamma_{1u}^a = \sum_{q=0}^{\infty} \frac{\mathrm{i}}{2} B_q \Big[&\left(k_j\beta_x^2 - \beta_x^2 M_x K_q^{--} + M_x^2 M_y A_q^{+-}\right) \mathrm{e}^{\mathrm{i}A_q^{+-}y}\mathrm{e}^{\mathrm{i}K_q^{--}x} \\ &+ \left(k_j\beta_x^2 - \beta_x^2 M_x K_q^{-+} + M_x^2 M_y A_q^{--}\right) \mathrm{e}^{\mathrm{i}A_q^{--}y}\mathrm{e}^{\mathrm{i}K_q^{-+}x} \Big] \Xi_q^-(0)\mathrm{e}^{-\mathrm{i}k_q^- b\sin\Psi},\end{aligned} \tag{5.39}$$

where

$$K_q^{\pm\pm} = k_q^{\pm}\cos\Psi \pm \frac{q\pi}{a}\sin\Psi, \quad A_q^{\pm\pm} = \pm\frac{q\pi}{a}\cos\Psi + k_q^{\pm}\sin\Psi.$$

On the other hand, the vortical motion being pressure-free, the conservative variable reduces to the transverse fluctuating velocity as

$$\Gamma_1^R = M_y u_y^R.$$

The latter reads:

$$\Gamma_{1i}^R = -M_y \frac{k_{jx}^R}{\alpha_j} w_j \mathrm{e}^{\mathrm{i}\alpha_j y}\mathrm{e}^{\mathrm{i}k_{jx}^R x}, \tag{5.40}$$

$$\Gamma_{1d}^R = \sum_{q=1}^{\infty} A_q^R M_y \left[\cos(\alpha_q\eta)\sin\Psi - \mathrm{i}\frac{k_j^R}{\alpha_q}\sin(\alpha_q\eta)\cos\Psi\right] \mathrm{e}^{\mathrm{i}k_j^R\zeta}. \tag{5.41}$$

The usual projection on the annular modal basis (2.13) is performed with the operator

$$\int_0^b (\bullet)\mathrm{e}^{-\mathrm{i}\alpha_\nu y}\,\mathrm{d}y, \quad \text{where} \quad \alpha_\nu = \alpha_j + \nu\frac{2\pi}{b},\ \nu\in\mathbb{Z}.$$

After some algebra, this leads to the following matching condition:

$$\boxed{\begin{aligned} b\left(R_\nu \mathfrak{K}_\nu^- + \mathrm{i}M_y \frac{k_{jx}^R}{\alpha_j} w_j \delta_{\nu,0}\right) = \sum_{q=0}^{\infty} -\mathrm{i}A_q^R \left(1-\delta_{q,0}\right) \mathfrak{I}_{j,q,\nu}^R M_y \cos\Psi \left(\tan\Psi + \frac{k_j^R \cos\Psi}{\varphi_{j,\nu}^R}\right), \\ + A_q\left(\mathfrak{K}_{q,\nu}^+ \mathfrak{I}_{q,\nu}^+ + \mathcal{F}_q \mathfrak{K}_{q,\nu}^- \mathfrak{I}_{q,\nu}^-\right) + B_q \Xi_q^-(0) \mathrm{e}^{-\mathrm{i}k_q^- b \sin\Psi} \mathfrak{K}_{q,\nu}^- \mathfrak{I}_{q,\nu}^- \end{aligned}} \tag{5.42}$$

where

$$\mathfrak{K}_\nu^- = \beta_x^2(k_j - k_\nu^- M_x) + M_x^2 M_y \alpha_\nu,$$

$$\mathfrak{K}_{q,\nu}^\pm = \beta_x^2(k_j - M_x k_q^\pm \cos\Psi) + M_x^2 M_y k_q^\pm \sin\Psi - M_x \frac{\tan\Psi}{\varphi_{q,\nu}^\pm}\left(\frac{q\pi}{b}\right)^2,$$

and

$$\mathfrak{I}_{j,q,\nu}^R(\Psi) = \begin{cases} \dfrac{-\mathrm{i}\varphi_{j,\nu}^R}{(\varphi_{j,\nu}^R)^2 - (q\pi/b)^2}\left((-1)^q \mathrm{e}^{\mathrm{i}b\varphi_{j,\nu}^R} - 1\right), \\ \dfrac{b}{2}\left(1+\delta_{q,0}\right) \quad \text{if} \quad \left|\varphi_{j,\nu}^R(\Psi)\right| = \dfrac{q\pi}{b}, \end{cases} \qquad \varphi_{j,\nu}^R = k_j^R \sin\Psi - \alpha_\nu. \tag{5.43}$$

The inner product $\mathfrak{I}_{q,\nu}^\pm(\Psi)$ is identical to the above with the adequate change of staggered wavenumber $\varphi_{q,\nu}^\pm(\Psi)$ as defined in (2.81).

Continuity of the Mass-Flow

The mass-flow reduces to $\Gamma_2 = \beta_x^2 u_x - M_x M_y u_y$ for both acoustic and vortical motions. It has already been derived for the acoustic fields as reminded below:

$$\Gamma_{2r}^a = \sum_{p=-\infty}^{\infty} \mathrm{i}R_p\left(\beta_x^2 k_p^- - M_x M_y \alpha_p\right) \mathrm{e}^{\mathrm{i}\alpha_p y} \mathrm{e}^{\mathrm{i}k_p^- x}, \tag{5.44}$$

$$\begin{aligned} \Gamma_{2d}^a = \sum_{q=0}^{\infty} \frac{\mathrm{i}}{2} A_q \Big[&\left(\beta_x^2 K_q^{+-} - M_x M_y A_q^{++}\right) \mathrm{e}^{\mathrm{i}A_q^{++} y} + \left(\beta_x^2 K_q^{++} - M_x M_y A_q^{-+}\right) \mathrm{e}^{\mathrm{i}A_q^{-+} y} \\ &+ \mathcal{F}_q \left\{ \left(\beta_x^2 K_q^{--} - M_x M_y A_q^{+-}\right) \mathrm{e}^{\mathrm{i}A_q^{+-} y} + \left(\beta_x^2 K_q^{-+} - M_x M_y A_q^{--}\right) \mathrm{e}^{\mathrm{i}A_q^{--} y} \right\} \Big], \end{aligned} \tag{5.45}$$

$$\begin{aligned} \Gamma_{2u}^a = \sum_{q=0}^{\infty} \frac{\mathrm{i}}{2} B_q \Big[&\left(\beta_x^2 K_q^{--} - M_x M_y A_q^{+-}\right) \mathrm{e}^{\mathrm{i}A_q^{+-} y} \mathrm{e}^{\mathrm{i}K_q^{--} x} \\ &+ \left(\beta_x^2 K_q^{-+} - M_x M_y A_q^{--}\right) \mathrm{e}^{\mathrm{i}A_q^{--} y} \mathrm{e}^{\mathrm{i}K_q^{-+} x} \Big] \Xi_q^-(0) \mathrm{e}^{-\mathrm{i}k_q^- b \sin\Psi}, \end{aligned} \tag{5.46}$$

where

$$K_q^{\pm\pm} = k_q^\pm \cos\Psi \pm \frac{q\pi}{a}\sin\Psi, \quad A_q^{\pm\pm} = \pm\frac{q\pi}{a}\cos\Psi + k_q^\pm \sin\Psi.$$

On the other hand, for the vortical fields, it reads

$$\Gamma_{2i}^R = \left(\beta_x^2 + M_x M_y \frac{k_{jx}^R}{\alpha_j}\right) w_j \mathrm{e}^{\mathrm{i}\alpha_j y} \mathrm{e}^{\mathrm{i}k_{jx}^R x}, \tag{5.47}$$

$$\Gamma_{2d}^R = \sum_{q=1}^{\infty} A_q^R \left[\left(\beta_x^2 \cos\Psi - M_x M_y \sin\Psi\right)\cos(\alpha_q \eta)\right. \tag{5.48}$$

$$\left. + \mathrm{i}\frac{k_j^R}{\alpha_q}\left(\beta_x^2 \sin\Psi - M_x M_y \cos\Psi\right)\sin(\alpha_q \eta)\right] \mathrm{e}^{\mathrm{i}k_j^R \zeta}. \tag{5.49}$$

The same projection is performed with the operator

$$\int_0^b (\bullet)\mathrm{e}^{-\mathrm{i}\alpha_\nu y}\,\mathrm{d}y, \quad \text{where} \quad \alpha_\nu = \alpha_j + \nu\frac{2\pi}{b},\ \nu \in \mathbb{Z}.$$

After some algebra, this leads to the second matching condition as

$$\begin{aligned} b\left(R_\nu \mathcal{K}_\nu^- - \mathrm{i}\left[\beta_x^2 + M_x M_y \frac{k_{jx}^R}{\alpha_j}\right] w_j \delta_{\nu,0}\right) &= \sum_{q=0}^{\infty} -\mathrm{i}A_q^R (1-\delta_{q,0}) \mathfrak{I}_{j,q,\nu}^R \cos\Psi \\ \times \left(\beta^2 - \frac{k_j^R \sin\Psi}{\varphi_{j,\nu}^R}\right) &+ A_q\left(\mathcal{K}_{q,\nu}^+ \mathfrak{I}_{q,\nu}^+ + \mathcal{F}_q \mathcal{K}_{q,\nu}^- \mathfrak{I}_{q,\nu}^-\right) + B_q \Xi_q^-(0)\mathrm{e}^{-\mathrm{i}k_q^- b\sin\Psi} \mathcal{K}_{q,\nu}^- \mathfrak{I}_{q,\nu}^- \end{aligned}, \tag{5.50}$$

where

$$\mathcal{K}_\nu^- = \beta_x^2 k_\nu^- - M_x M_y \alpha_\nu,$$

$$\mathcal{K}_{q,\nu}^\pm = \left(\beta_x^2 \cos\Psi - M_x M_y \sin\Psi\right) k_q^\pm + \frac{\tan\Psi}{\varphi_{q,\nu}^\pm}\left(\frac{q\pi}{b}\right)^2.$$

5.3.3 Trailing-Edge Interface

Acoustic Potentials and Vortical Velocity Fields

At the trailing-edge interface (Figure 5.7), the conservative variables (p, u_x) can be used. Since the vortical motion is pressure-free, this problem only involves two additional velocity fields compared to the problem already treated in section 4.3.2. Those velocity fields are given by

$$\mathbf{u}_d^R \cdot \mathbf{e}_s \sim \sum_{q=1}^{\infty} A_q^R \Upsilon_{jq}^R(S) \cos(\theta_q(S)\,[n + h(S)/2]) \mathrm{e}^{\mathrm{i}k_j^R a \tan\Psi},$$

for $0 \leq X \leq L_c$, $-h(X)/2 \leq y \leq h(X)/2$ and

$$\mathbf{u}_t^R \cdot \mathbf{e}_x = \sum_{m=0}^{V-1} \sum_{p=-\infty}^{\infty} T_p^R \mathrm{e}^{\mathrm{i}m\alpha_j b} \mathrm{e}^{\mathrm{i}\alpha_p (y' - mb)} \mathrm{e}^{\mathrm{i}k_{jt}^R x'} F_j^R,$$

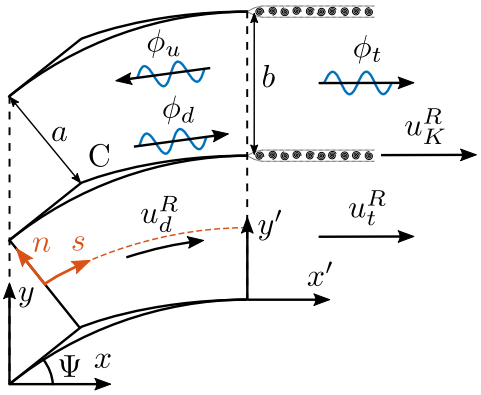

Figure 5.7: Exhaust of a vorticity gust from the cascade of cambered vanes at the trailing-edge interface.

for $0 \leq x' < \infty$, $0 \leq y' < 2\pi R$. As a reminder, the T_p^R coefficients are defined by

$$\sum_{p=-\infty}^{\infty} \left(\frac{\alpha_p^2 + (k_{jt}^R)^2}{\alpha_p} \right) T_p^R \mathfrak{I}_{p,\nu}^R = \frac{\mathrm{i}b}{2}(1-\delta_{\nu,0}) \frac{\alpha_\nu^2 + (k_j^R)^2}{\alpha_\nu} A_\nu^R .$$

Continuity Equations

The pressure continuity and axial-velocity continuity equations read, respectively,

$$\boxed{\sum_{q=0}^{\infty} \left[A_q(k_j - \tau_q^+ M)\Xi_q^+ + B_q(k_j - \tau_q^- M) \right] \mathfrak{I}_{q,\nu}^0 = bT_\nu(k_j - k_\nu^+ M)}, \tag{5.51}$$

and

$$\boxed{\begin{aligned} \sum_{q=0}^{\infty} \left[-\mathrm{i}A_q^R(1-\delta_{q,0}) \frac{\theta_q \left(\alpha_q^2 + (k_j^R)^2\right)}{\alpha_q \left(\theta_q^2 + (\mu_j^R)^2\right)} F_j^R + A_q \tau_q^+ \Xi_q^+ + B_q \tau_q^- \right] \mathfrak{I}_{q,\nu}^0 = bk_\nu^+ T_\nu \\ + \frac{\alpha_\nu}{\alpha_\nu^2 + (k_{jt}^R)^2} \Omega_K - \mathrm{i}b \sum_{p=-\infty}^{\infty} T_p^R F_j^R \mathrm{e}^{\mathrm{i}\pi([p-j]B/V-\nu)} \operatorname{sinc}\left([p-j]B/V - \nu\right), \end{aligned}} \tag{5.52}$$

where $\operatorname{sinc}(x) = \sin(\pi x)/(\pi x)$. The Kutta condition enforcing a zero pressure jump at the trailing edge is given by

$$\boxed{\sum_{q=0}^{\infty} \left[(k_j - \tau_q^+ M) A_q \Xi_q^+ + (k_j - \tau_q^- M) B_q \right] \left(1 - (-1)^q \mathrm{e}^{-\mathrm{i}\alpha_j b}\right) = 0}. \tag{5.53}$$

The acoustic modal coefficients can then be computed in an iterative procedure of leading-edge matching and trailing-edge matching until a sufficient convergence is reached. However, due to occurrences of transition near the leading edge, it has been found necessary in the previous Chapter to rely on a direct global approach.

5.3.4 Global Matching

The global problem represented on Figure 5.8 is solved by gathering all five previous matching equations in a single matrix, such that

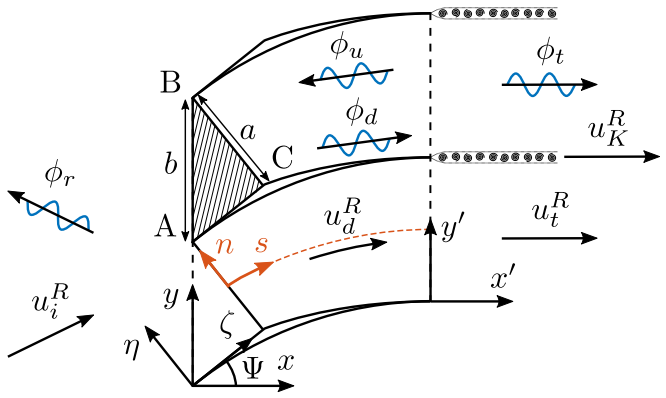

Figure 5.8: Impingement of a vorticity gust on the cascade of cambered vanes.

$$\begin{pmatrix} \mathbf{E_1^1} & \mathbf{F_1^1} & \mathbf{I_1^1} & \underline{\mathbf{0}} & \mathbf{0} \\ \mathbf{E_2^1} & \mathbf{F_2^1} & \mathbf{I_2^1} & \underline{\mathbf{0}} & \mathbf{0} \\ \underline{\mathbf{0}} & \mathbf{F_1^2} & \mathbf{I_1^2} & \mathbf{J_1^2} & \mathbf{0} \\ \underline{\mathbf{0}} & \mathbf{F_2^2} & \mathbf{I_2^2} & \mathbf{J_2^2} & \mathbf{G_2^2} \\ \mathbf{0} & \mathbf{F_K^2} & \mathbf{I_K^2} & \mathbf{0} & 0 \end{pmatrix} \begin{pmatrix} \mathbf{R} \\ \mathbf{A} \\ \mathbf{B} \\ \mathbf{T} \\ \Omega_K \end{pmatrix} = \begin{pmatrix} \mathbf{H_1^1} \\ \mathbf{H_2^1} \\ \mathbf{0} \\ \mathbf{H_2^2} \\ 0 \end{pmatrix}, \tag{5.54}$$

where

$$E_1^1(\nu,\nu) = -b\mathfrak{K}_\nu^- \delta_{\nu,\nu}, \quad F_1^1(\nu,q) = \mathfrak{K}_{q,\nu}^+ \mathfrak{I}_{q,\nu}^+ + \mathcal{F}_q \mathfrak{K}_{q,\nu}^- \mathfrak{I}_{q,\nu}^-,$$

$$I_1^1(\nu,q) = \Xi_q^-(0) \mathrm{e}^{-\mathrm{i}k_q^- b \sin\Psi} \mathfrak{K}_{q,\nu}^- \mathfrak{I}_{q,\nu}^-,$$

$$E_2^1(\nu,\nu) = -b\mathcal{K}_\nu^- \delta_{\nu,\nu}, \quad F_2^1(\nu,q) = \mathcal{K}_{q,\nu}^+ \mathfrak{I}_{q,\nu}^+ + \mathcal{F}_q \mathcal{K}_{q,\nu}^- \mathfrak{I}_{q,\nu}^-,$$

$$I_2^1(\nu,q) = \Xi_q^-(0) \mathrm{e}^{-\mathrm{i}k_q^- b \sin\Psi} \mathcal{K}_{q,\nu}^- \mathfrak{I}_{q,\nu}^-,$$

$$F_1^2(\nu,q) = (k_j - \tau_q^+ M)\Xi_q^+ \mathfrak{I}_{q,\nu}^0, \quad I_1^2(\nu,q) = (k_j - \tau_q^- M)\mathfrak{I}_{q,\nu}^0,$$

$$J_1^2(\nu,\nu) = -b(k_j - k_\nu^+ M)\delta_{\nu,\nu},$$

$$F_2^2(\nu,q) = \tau_q^+ \Xi_q^+ \mathfrak{I}_{q,\nu}^0, \quad I_2^2(\nu,q) = \tau_q^- \mathfrak{I}_{q,\nu}^0, \quad J_2^2(\nu,\nu) = -bk_\nu^+ \delta_{\nu,\nu},$$

$$G_2^2(\nu,1) = -\frac{\alpha_\nu}{\alpha_\nu^2 + (k_{jt}^R)^2},$$

$$F_K^2(1,q) = (k_j - \tau_q^+ M)(1 - (-1)^q \mathrm{e}^{-\mathrm{i}\alpha_j b})\Xi_q^+, \quad I_K^2(1,q) = (k_j - \tau_q^- M)(1 - (-1)^q \mathrm{e}^{-\mathrm{i}\alpha_j b}),$$

and

$$H_1^1(\nu,1) = \mathrm{i}bM_y \frac{k_{jx}^R}{\alpha_j} w_j \delta_{\nu,0} + \sum_{q=0}^{\infty} \mathrm{i}A_q^R \left(1 - \delta_{q,0}\right) \mathfrak{I}_{j,q,\nu}^R M_y \cos\Psi \left(\tan\Psi + \frac{k_j^R \cos\Psi}{\varphi_{j,\nu}^R}\right),$$

$$H_2^1(\nu,1) = -\mathrm{i}b \left(\beta_x^2 + M_x M_y \frac{k_{jx}^R}{\alpha_j}\right) w_j \delta_{\nu,0} + \sum_{q=0}^{\infty} \mathrm{i}A_q^R (1 - \delta_{q,0}) \mathfrak{I}_{j,q,\nu}^R \cos\Psi \left(\beta^2 - \frac{k_j^R \sin\Psi}{\varphi_{j,\nu}^R}\right),$$

$$H_2^2(\nu,1) = \sum_{q=0}^{\infty} \mathrm{i}A_q^R(1-\delta_{q,0})\frac{\theta_q\left(\alpha_q^2+(k_j^R)^2\right)}{\alpha_q\left(\theta_q^2+(\mu_j^R)^2\right)}F_j^R\mathfrak{I}_{q,\nu}^0 - \mathrm{i}b\sum_{p=-\infty}^{\infty} T_p^R F_j^R \mathrm{e}^{\mathrm{i}\pi([p-j]B/V-\nu)}\,\mathrm{sinc}\left([p-j]B/V-\nu\right).$$

Mode-Matching Equations — Summary

The mode-matching equations for the problem of sound generation by periodic wake impingement have been derived, in the assumption of an equivalent straight-channel of slowly-varying cross-section. The model is then expected of limited accuracy above the first channel cut-off frequency. An iterative approach and a direct global approach have been formulated in order to deal with cut-off/cut-on transitions of modes, occurring near the leading edge.

5.4 Comparison with Numerical and Analytical Results

5.4.1 Methodology

In the first instance, Envia's results for the fourth NASA CAA workshop, category 3, problem 2 [24] are used as reference for qualitative comparisons at the first three BPF. These results were obtained with a code called LINFLUX, which solves the frequency-domain linearized Euler equations. The first BPF is cut-off whereas the second and third are cut-on. This test case could also be interesting for studying the cut-off/cut-on transition expected at the second BPF. The dimensionless BPF is interestingly equal to $kb_{BPF} = \pi/2$. Hence, all even harmonics of the BPF are inside a transition range. Figure 5.9 illustrates the transition areas in gray in the frequency-camber domain, with dashed lines to indicate the BPF harmonics of the test case.

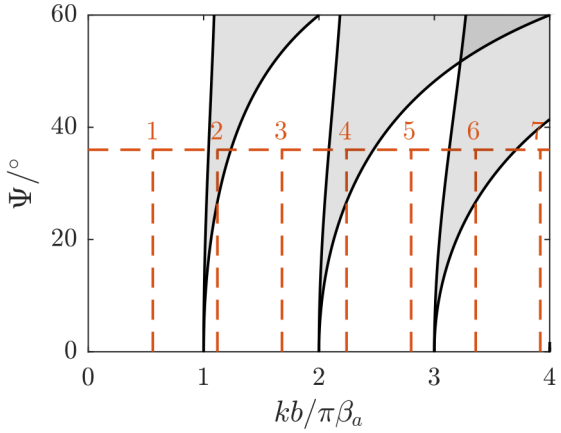

Figure 5.9: Evolution of the transition areas (painted in gray) with frequency and camber. The red dashed lines represent the first BPF harmonics of the test case of the fourth NASA CAA workshop, with an adjusted camber angle of $\Psi = 36°$.

The second and third BPF being above the first channel cut-off frequency, the MMBW model is expected to reach its limit. Limitations in terms of frequency regarding the acoustic waves modeling has already been assessed. The focus is made on the limitations regarding the vortical gust modeling here.

Quantitative results are also presented at the second and third BPF. The modal amplitudes of the annular cut-on modes predicted by different CAA solvers [24] are gathered to get a reference mean estimate. Results from the analytical model of de Laborderie et al. [25], which models vane camber by using flat vanes with different LE and TE stagger angles, are also added to the comparisons.

5.4.2 Results

Instantaneous Pressure and Axial Velocity Maps

Figure 5.10 represents the instantaneous pressure maps at the first BPF computed numerically (LINFLUX [24]) and analytically (MMBW). The cut-off BPF is correctly

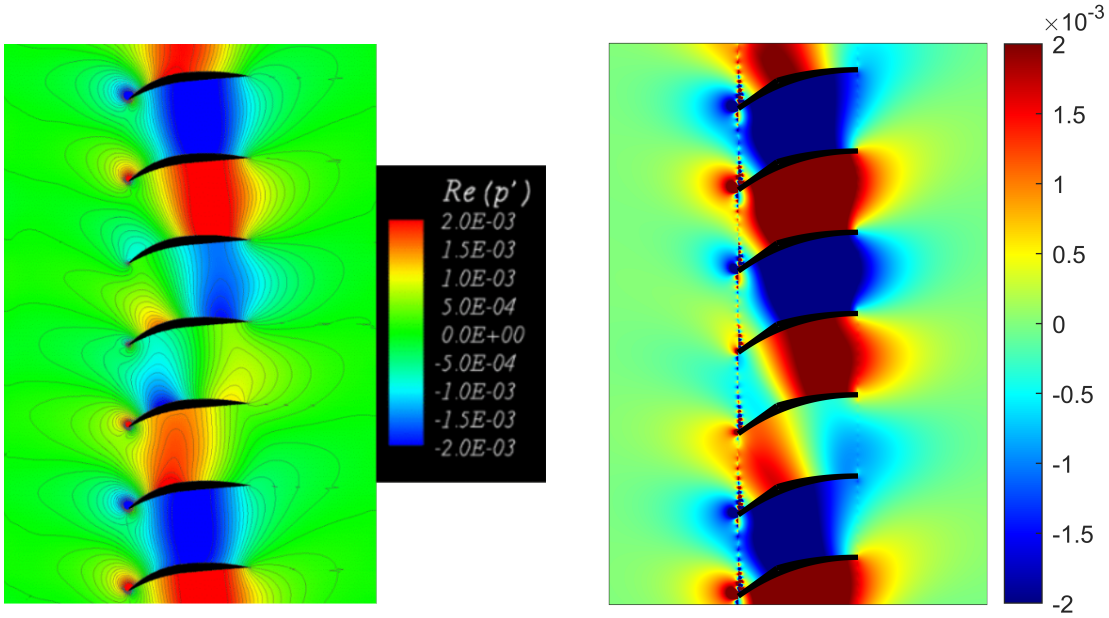

(a) (b)

Figure 5.10: Instantaneous pressure maps at the first BPF computed numerically by LINFLUX [24] (a) and analytically by MMBW (b).

predicted: similar pattern with only a phase shift between the numerical and analytical results. The amplitude is higher than what LINFLUX predicts but it stays of the same order of magnitude. Strong oscillations are present at the staggered leading-edge interface due to the low number of modes used in the modal truncation ($N = 15$). The presence of trapped modes at a cut-off frequency makes the resolution of the modal coefficients more sensitive to numerical errors. If more modes were considered, the matrix conditioning would be worse and, even if the oscillations at the LE interface would be slightly mitigated, oscillations at the TE interface would start to develop, and a pressure jump could appear at some trailing edges despite the Kutta condition.

This gives the limiting number of modes that can be used in the absence of any power balance estimation.

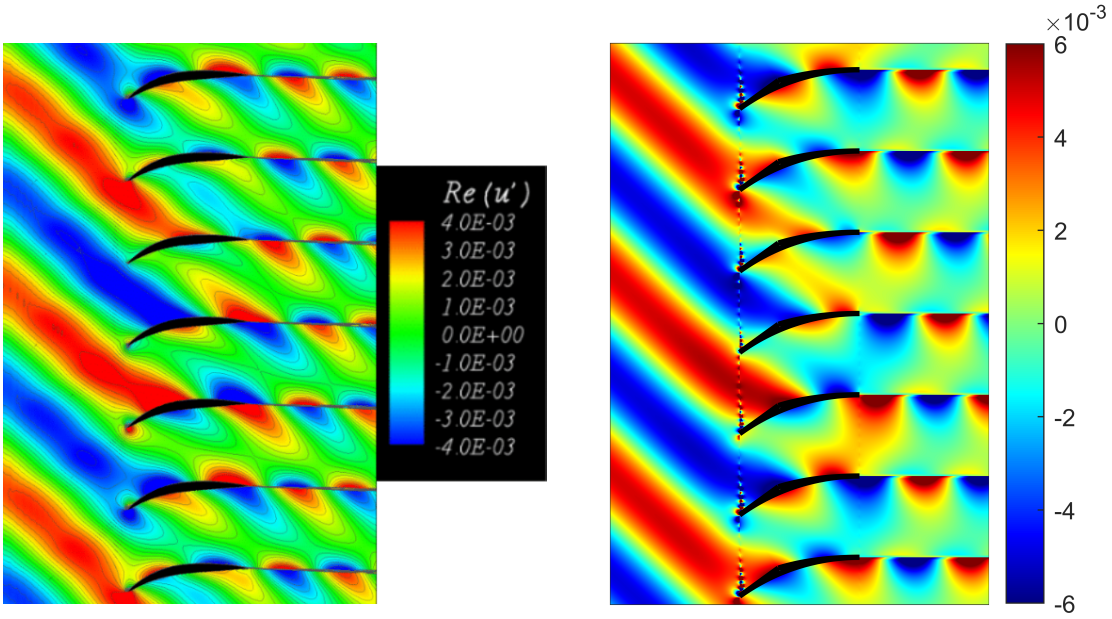

(a) (b)

Figure 5.11: Instantaneous axial velocity maps at the first BPF computed numerically by LINFLUX [24] (a) and analytically by MMBW (b).

Figure 5.11 displays the instantaneous axial velocity maps at the same first BPF. The axial velocity is composed of the acoustic and vortical motions. The latter is dominant in the plotted maps and therefore gives an insight on the accuracy of the vortical gust modeling. The shifting between two adjacent channels is in relatively good agreement with the numerical results, as well as the tilting: the mode order $pB = 22$ is dominant downstream of the OGV.

Figures 5.12 and 5.13 represent the instantaneous pressure and axial velocity maps at the second BPF. The predicted amplitude of the pressure and axial velocity is about ten times what the CAA returns. However, the overall shape of the pressure field (Figure 5.12b) is well predicted, with the correct propagation angles upstream and downstream of the OGV, emphasizing the importance of accurately modeling the evolution of the mean flow.

At this frequency, a cut-off/cut-on transition of the channel mode $q = 1$ occurs at 40% of the channel length in the approximate geometry of the MMBW model. When the transition location is far from the leading edge, the reflected cut-off mode cannot influence sound propagation. Furthermore, in this case, even the reflected cut-on mode has no significant impact. Sound propagation in the channels is dominated by the mode $q = 0$. Hence, even a computation without properly modeling the reflections gives a similar result (no change at all in the radiated powers).

Figure 5.12a indicates that either a significant cut-off acoustic mode is missing upstream of the OGV in the MMBW, or some spurious reflections are present at the inflow plane ($x = -1.5l$). Since this second BPF is above the first cut-off frequency of

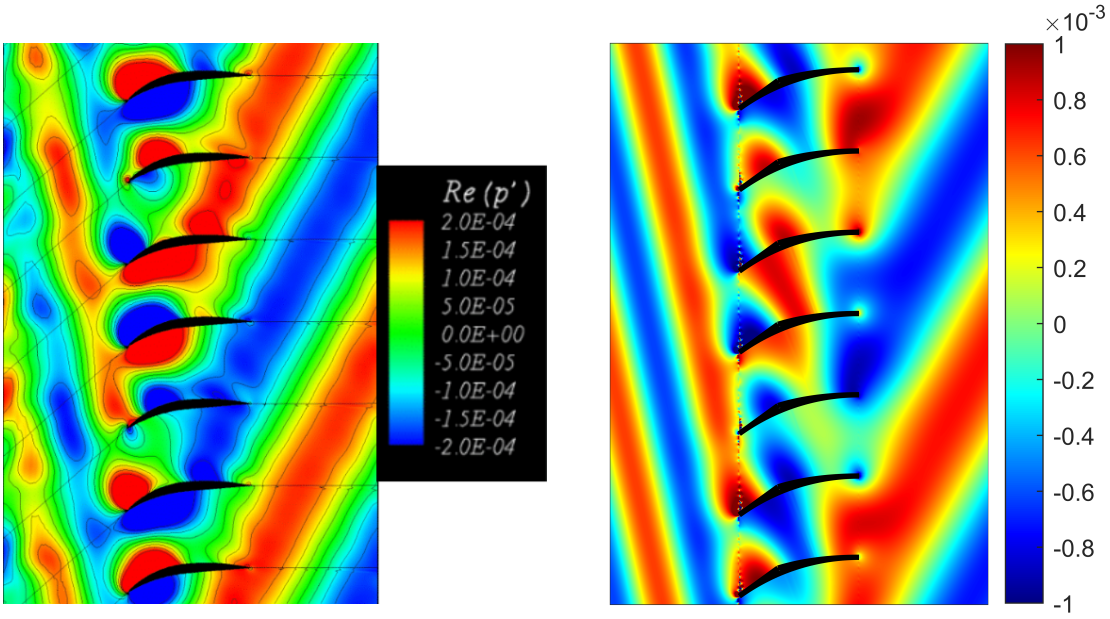

(a) (b)

Figure 5.12: Instantaneous pressure maps at the second BPF computed numerically by LINFLUX [24] (a) and analytically by MMBW (b).

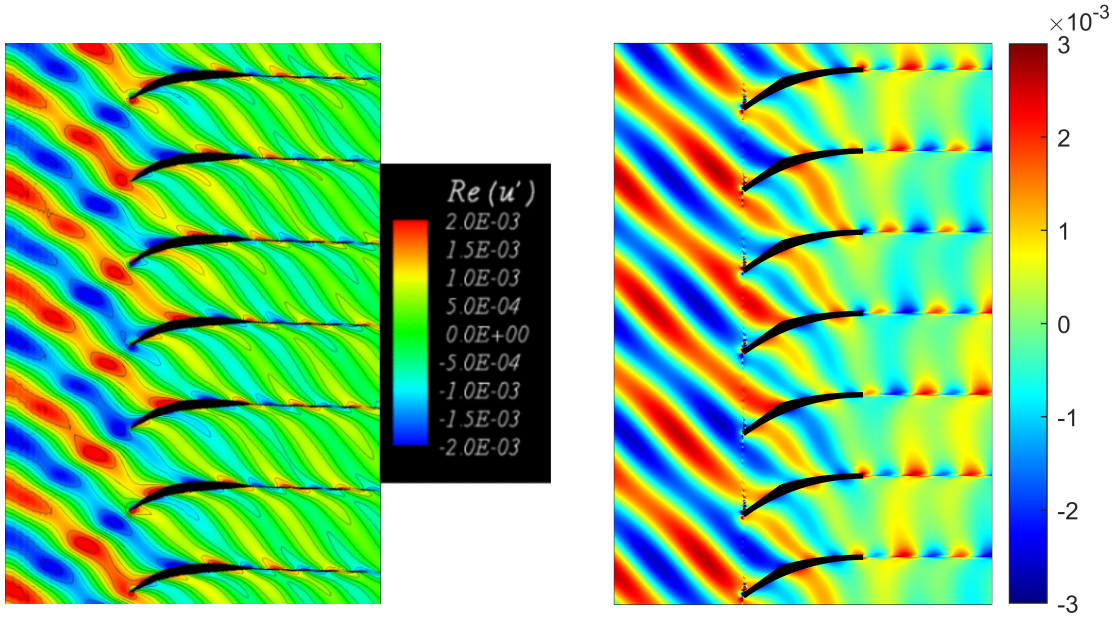

(a) (b)

Figure 5.13: Instantaneous axial velocity maps at the second BPF computed numerically by LINFLUX [24] (a) and analytically by MMBW (b).

the channels, the MMBW might be outside its validity range and could be missing a cut-off mode. The limitation is more visible on the vortical velocity field depicted in Figure 5.13b, which clearly displays an artificial downward tilting of the gust through

the inter-vane channels at this frequency. This observation proves that the vortical velocity field sensitivity to curvature is also proportional to frequency, as the acoustic pressure field, thus the proposed criterion (3.42) is useful for both.

Finally, Figures 5.14 and 5.15 display the instantaneous pressure and axial velocity maps at the third BPF, well above the theoretical validity of the MMBW. At this frequency, small oscillations start to appear at the trailing-edge interface. Caution has been taken while reducing the number of modes in the modal truncation in order to avoid any significant pressure jumps at the trailing edges, while preserving a reasonable accuracy. Surprisingly, the overall shape of the pressure field is still in good agreement

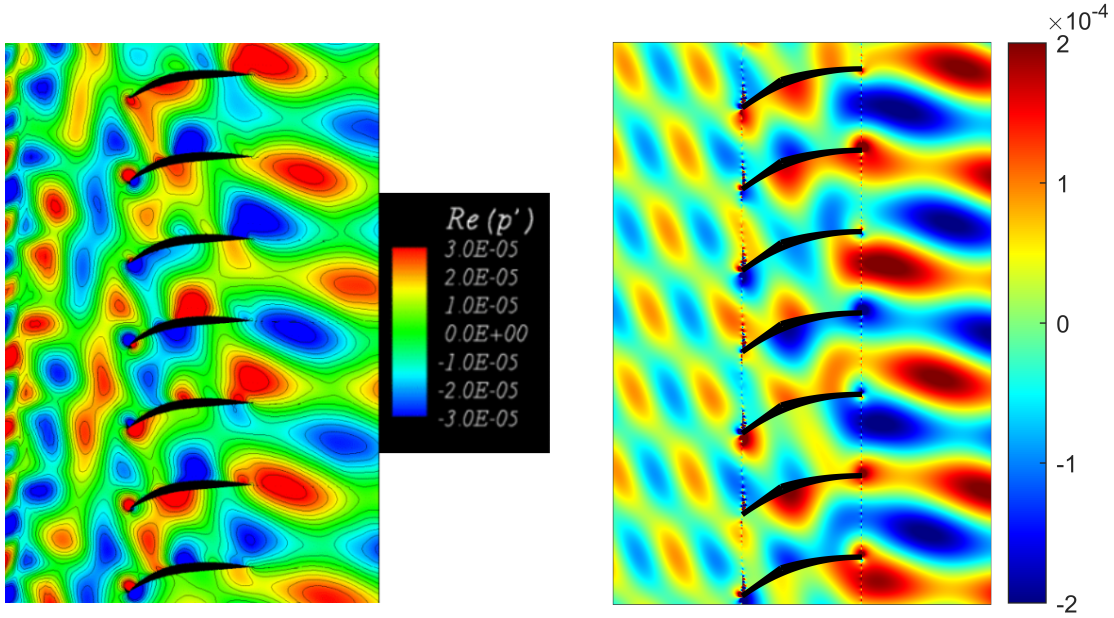

(a) (b)

Figure 5.14: Instantaneous pressure maps at the third BPF computed numerically by LINFLUX [24] (a) and analytically by MMBW (b).

downstream of the OGV, even if the amplitude is overestimated. Upstream of the OGV, the same modes are present ($m = jB + pV = -42$ and $m = 12$), but the modal distribution of energy is not correctly predicted, with too much energy in $m = -42$ (see Figure 5.16). However, when looking at the numerical axial velocity field (Figure 5.15a), the wavefront is weirdly perpendicular to the inflow interface. There should be no change in the mean flow, so this behavior might be due to the boundary condition. This rises the question of whether or not some spurious reflections are present in the upstream pressure field (Figure 5.14a), and maybe at the second BPF as well (Figure 5.12a). Extending the model of sound generation for curvature effects will allow to answer that question.

Modal Amplitudes

Figure 5.16 represents the modal amplitudes distribution of the cut-on annular modes at the second and third BPF. The amplitude is expressed by Sound Presure Levels (SPL) in dB, calculated as $\text{SPL} = 20\log_{10}(p/p_{ref})$, $p_{ref} = 20$ μPa. The different numerical

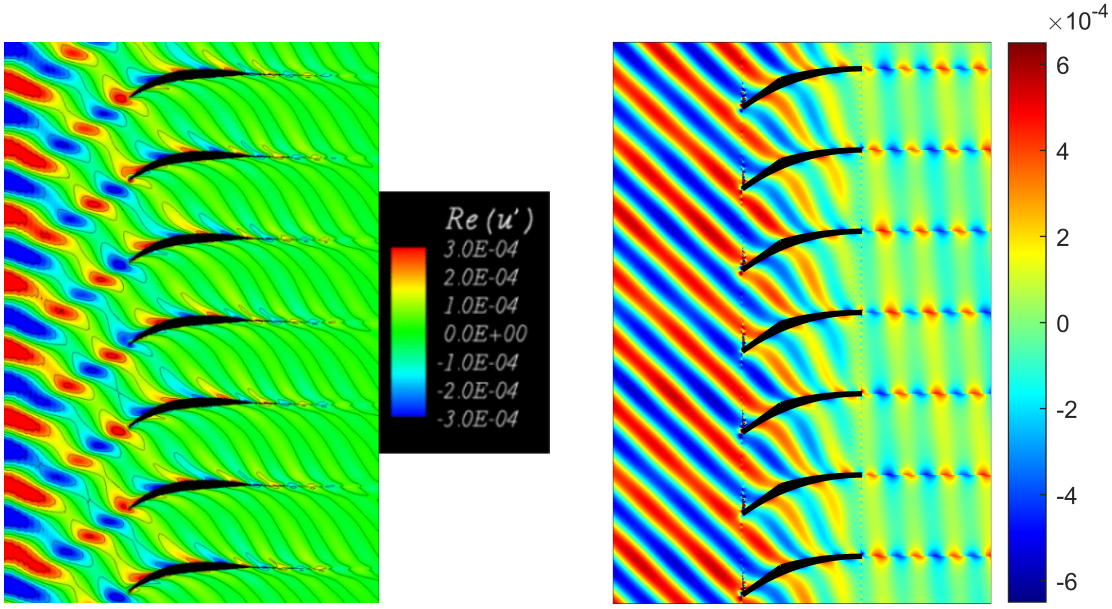

(a) (b)

Figure 5.15: Instantaneous axial velocity maps at the third BPF computed numerically by LINFLUX [24] (a) and analytically by MMBW (b).

results from the CAA codes [24] are averaged, and the mean value is displayed with an error bar delimited by the smallest and largest predictions.

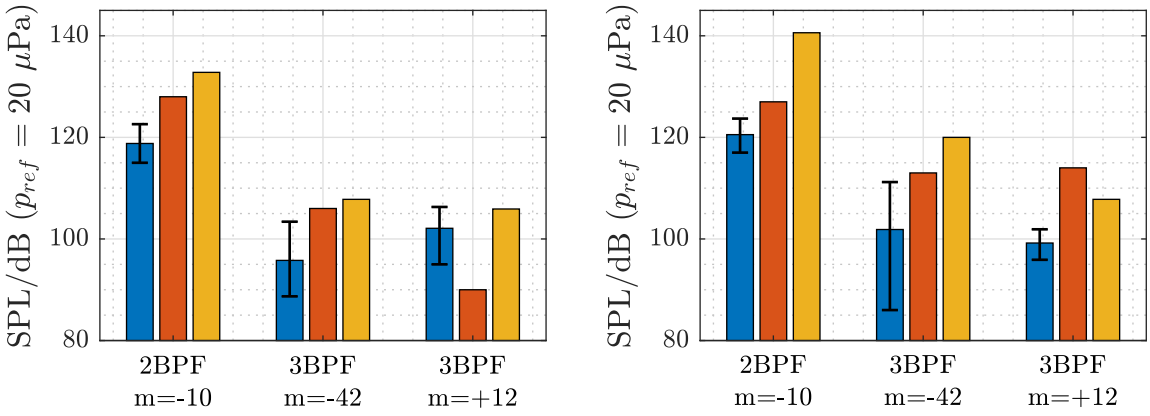

(a) (b)

Figure 5.16: Upstream (a) and downstream (b) modal amplitudes computed with: averaged CAA results [24] with error bars ( ), two-stagger angle model of de Laborderie et al. [25] ( ) and MMBW ( ).

At 2BPF, the modal amplitudes predicted by MMBW are substantially higher than the CAA mean value: 10 dB at the inflow plane, and 20 dB at the outflow plane. Even if the pressure pattern is relatively well predicted, the levels are worse than what was predicted by de Laborderie et al. [25]. The transition modeling has no impact in this case. If the reflections at the transition location are not modeled, the change in

modal amplitudes is lower than 1 dB. This shows that the MMBW is inadequate at this frequency, thus that curvature starts to have a significant effect at the 2BPF, as indicated by de Laborderie et al. [25].

At 3BPF, surprisingly, the modal amplitudes are better predicted. Upstream of the cascade, the mode $m = -42$ is predicted at the limit of the uncertainty of the CAA results, and the mode $m = +12$ is well predicted. This is a substantial improvement compared to the two-stagger angles model, which was underestimating the mode $m = +12$. Furthermore, the MMBW is able to recover a better balance between both modes. Downstream of the cascade, both analytical models give relatively the same results, with this time a more adequate balance predicted by the two-stagger angles model [25].

5.4.3 Discussion

The MMBW has been pushed to its limit in this test case. The results are promising but, indeed, it is difficult to put trust on them in such a scenario where the only BPF harmonic lying in the validity range is cut-off. However, this test case presents an excellent benchmark for the model since it provides: a cut-off BPF harmonic, a cut-on BPF harmonic with a transition, and a cut-on BPF harmonic without transition. However, a test case where the transition is closer to an edge would be needed.

Comparison with Numerical and Analytical Results ——— Summary

A test case based on the NASA SDT baseline configuration at a regime slightly higher than the approach condition has been used. The model performs surprisingly well to predict the acoustic modes and their propagation angle, except at 2BPF where the modal amplitudes are substantially overestimated. The MMBW model is able to recover a better modal distribution at 3BPF than a previous analytical model based on two different stagger angles at the LE and TE interfaces. However, the vortical gust evolution is more sensitive to the curvature effects than the acoustic waves, due to its shorter length-scale in subsonic flow condition. The vortical gust seems to be the limiting factor in terms of frequency of the developed MMBW model for sound generation.

5.5 Parametric Study

5.5.1 Methodology

A parametric study is done to assess some effects of camber and acoustic resonance on tonal noise generation by wake impingement. The base configuration used for this parametric study is the SDT low-count ($V = 26$), so that the low-order mode $m = jB + pV = -4$ is generated at the first BPF. The shaft-rotation rate Ω_R is artificially modulated in order to cover the frequency range $0.05 \leq kb/\pi \leq 2.05$, with $j = 1$. Power spectra are computed for different camber angles: $\Psi = 1°$, $12°$, $23°$ and $34°$. The fixed geometrical parameters for this test case are listed in Table 5.1.

	B	V	l/b	$M_{-\infty}$	$D_{-\infty}/D_{ref}$	$C_{-\infty}/C_{ref}$
Setup	22	26	1.5	0.4	0.90569	0.98088

Table 5.1: Input parameters of the sound generation test case, $D_{ref} = 1.2258$ kg/m^3 and $C_{ref} = 340$ m/s.

5.5.2 Results

Influence of Stagger and Camber

Figure 5.17 displays the total sound power level SWL $= 10\log_{10}([\mathcal{P}_t - \mathcal{P}_r]/\mathcal{P}_{ref})$, with $\mathcal{P}_{ref} = 1$ pW, and the upstream relative power spectrum $-\mathcal{P}_r/(\mathcal{P}_t - \mathcal{P}_r)$. Notice that, for the highest camber case ($\Psi = 34°$), the MMBW is off its validity range for $kb/\pi > 1$, so caution is required when interpreting the results.

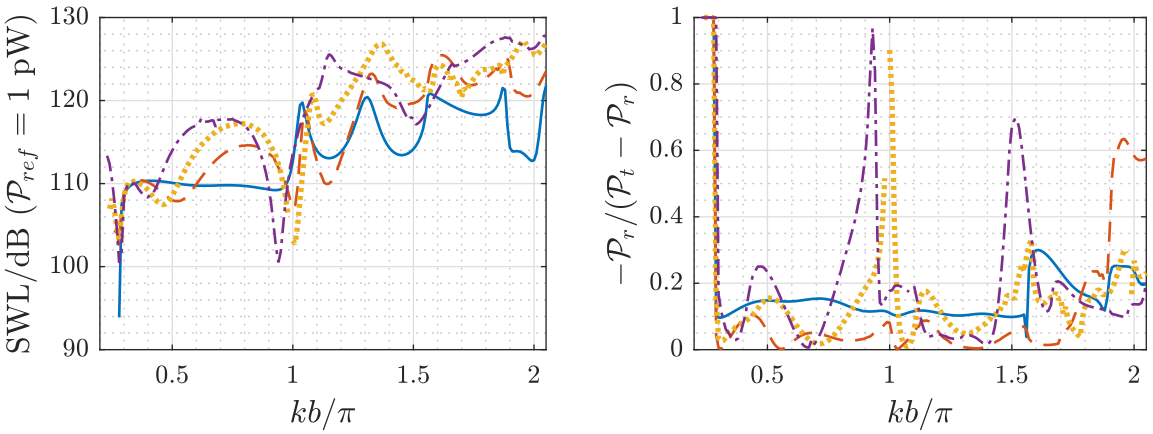

Figure 5.17: Total (a) and upstream (b) radiated acoustic powers against the frequency for varying camber angles: $\Psi = 1°$ (—), $\Psi = 12°$ (– –), $\Psi = 23°$ (····) and $\Psi = 34°$ (–·–·).

In Figure 5.17a, between the first cut-off frequency of the annular domain ($kb/\pi \simeq 0.28$) and the first cut-off frequency of the channels ($kb/\pi = \beta_b(\Psi) \in [0.95, 1]$), the total SWL remains flat for a cascade of almost flat vanes ($\Psi = 1°$). Then, above the latter frequency, regular peaks of noise emission are observed. When increasing stagger/camber, the total SWL spectra becomes more complex. In the first half of the frequency range, noise emission exhibits a large hump and multiple drops. In the second half, the pattern is similar to those of flat vanes, but flatter and with a higher mean value. This indicates that staggered and cambered vanes produce more noise than flat vanes in such conditions, except at particular frequencies.

When looking at the upstream relative power spectra (Figure 5.17b), regular peaks similar to those observed at resonant frequencies for sound transmission appear. Interestingly enough, some peaks, such as the ones at $kb/\pi \simeq 0.92$ and $kb/\pi \simeq 1.51$ for $\Psi = 34°$, correspond to a drop and a peak of noise efficiency, respectively. This phenomenon is further investigated in the following.

Influence of Acoustic Resonance

Figure 5.18 displays the instantaneous pressure maps for the two peaks observed in Figure 5.17b, at $kb/\pi \simeq 0.92$ and $kb/\pi \simeq 1.51$, for $\Psi = 34°$. Figure 5.18 displays the instantaneous pressure maps for the two peaks observed in Figure 5.17b, for $\Psi = 34°$ below $kb/\pi = 0.95$. Acoustic resonances are found at these frequencies, and more

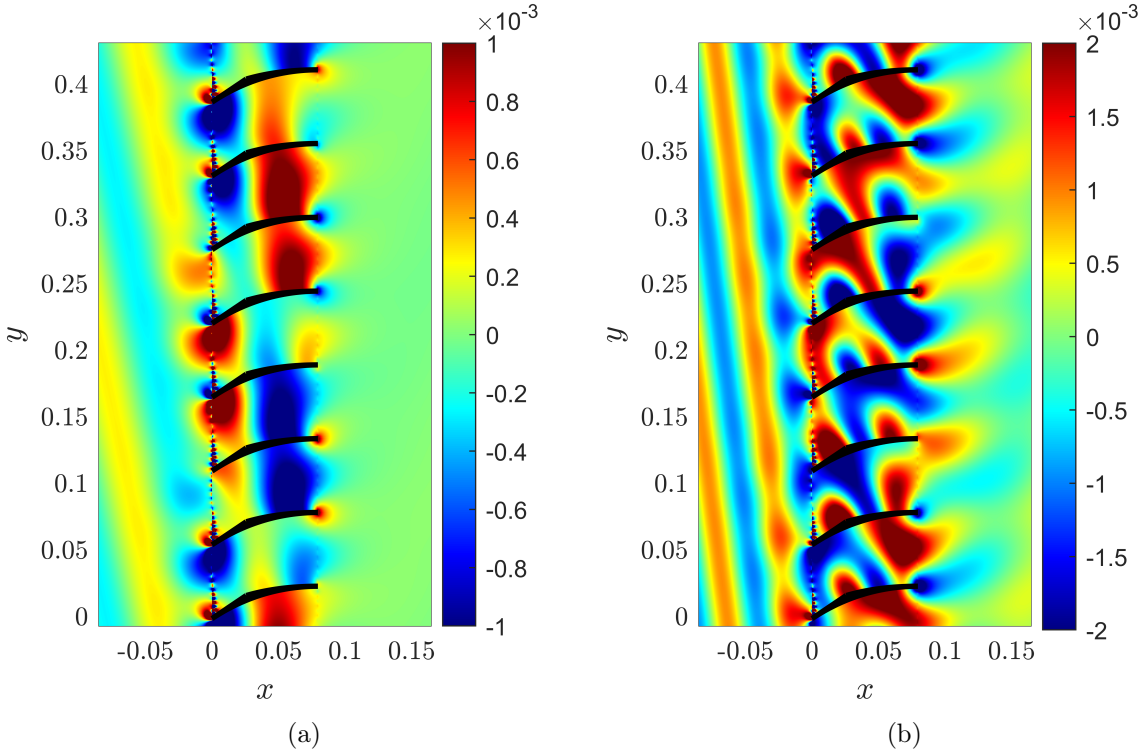

Figure 5.18: Instantaneous pressure field of the resonance (1,0) at $kb/\pi \simeq 0.92$ (a) and (2,1) at $kb/\pi \simeq 1.51$ (b), for $\Psi = 34°$.

precisely the resonances (1,0) and (2,1), respectively. The resonance phenomenon is not ideal since the periodicity of the incident gust is given by $|m| = 4$, which is different from the ideal values $V/2 = 13$ and 0, respectively. These resonances are "leaky", contrary to "trapped", in the current condition, as they radiate energy away from the cascade. An interesting characteristic of these resonances related to the channel modes $q = 0$ and $q = 1$ is that most of the vanes undergo fluctuations of nearly equal phases (Figure 5.18a) or nearly opposite phases (Figure 5.18b at each side. This seems to create adverse and favorable conditions, respectively, for noise generation by wake impingement, which consists in dipoles distributed along the vanes. This explains why these resonances were associated to either a drop or a peak in the total SWL in Figure 5.17a.

For the previous resonances, the acoustic power is mostly radiated upstream of the OGV. This reminds the results observed for acoustically triggered resonances, where it was interpreted as some sort of acoustic blockage. However, this does not hold for every wake-triggered resonances. Figure 5.19 represents the resonance (0,0) with $\Psi = 34°$ and the resonance (1,1) with $\Psi = 23°$. The acoustic power is mostly radiated downstream in these cases.

To summarize, when the resonance pattern is such that most of the vanes undergo

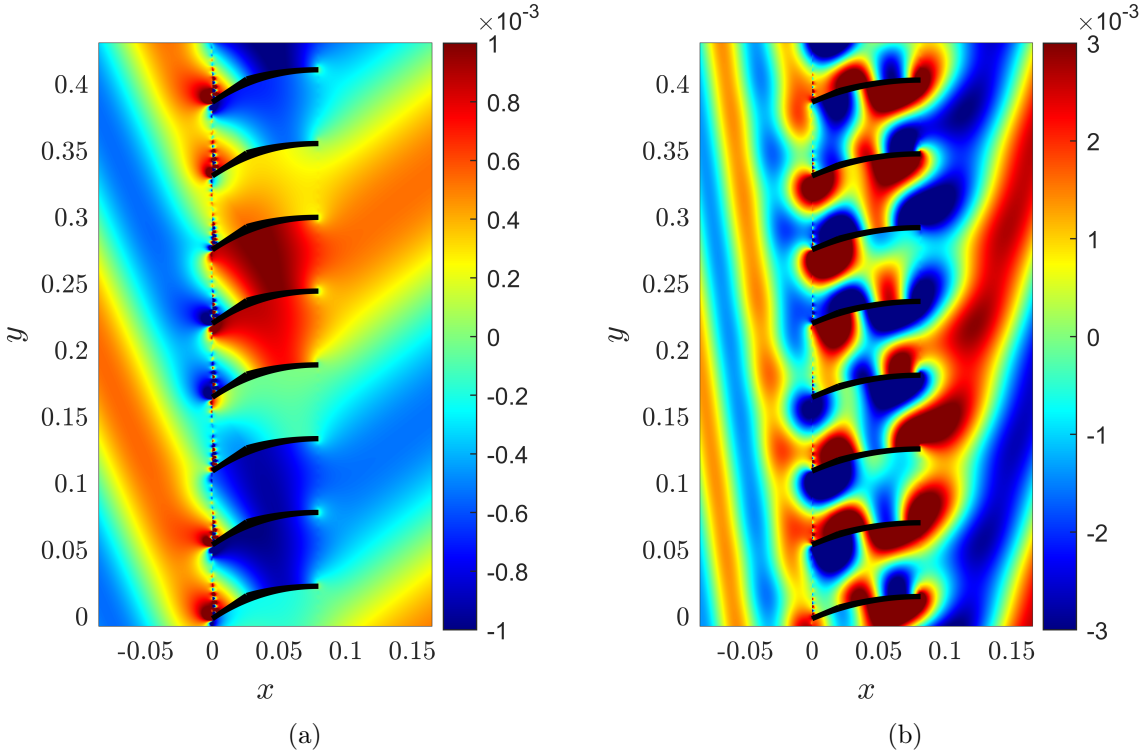

Figure 5.19: Instantaneous pressure field of the resonance (0,0) for $\Psi = 34°$ (a) and (1,1) for $\Psi = 23°$ (b).

pressure fluctuations of almost equal phases at both sides, the total sound power level drops, whereas if the pressure fluctuations at both sides are of almost opposite phases, the total sound power level peaks. The balance between upstream and downstream radiated powers then depends on the case.

5.5.3 Discussion

A short parametric study on the influence of stagger/camber on the noise produced by periodic wake impingement has been carried out. It allowed one to better understand the effects of camber and acoustic resonances on noise efficiency, and also demonstrated the possibility to trigger a resonance with an incident wake. The latter is interesting, due to the occurrence of non-ideal resonances that could be triggered at unexpected frequencies in a realistic application if only the ideal resonances are anticipated.

Because of the approximations and assumptions in the model, whether or not such resonances can occur in real turbomachinery stages remains unanswered. However, it is possible that such a resonance has been observed numerically, by means of LBM, by Sanjosé et al. [122]. Figure 5.20 represents the resonance they observed in the NASA Active Noise Control Fan rig with $B = 16$ blades and $V = 26$ vanes. Taking a close look, the alternate pattern of positive and negative lobes is seen sometimes broken, indicating that half the wavelength is not exactly equal to a channel height (characteristic of Parker's β mode). This could be explained by a non-ideal resonance triggered by the vortical gust $m = jB + sV = 1 \times 16 - 1 \times 26 = -10$, which is close to $V/2 = 13$ and can generate a resonance (0,0), trapped (Parker's β mode) or leaky as seen in Figure 5.19a. The expected resulting modulation is not inconsistent with what is seen

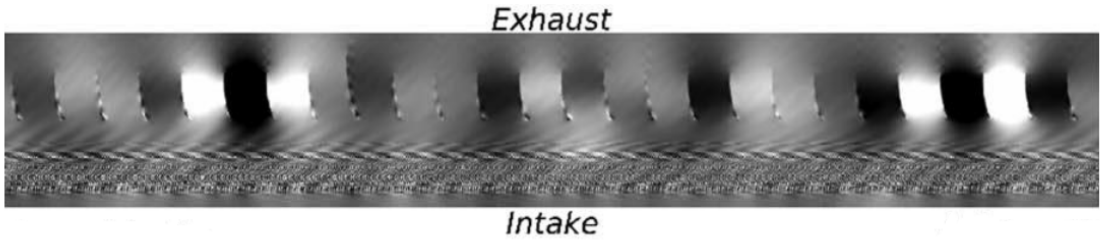

Figure 5.20: Instantaneous pressure map in the OGV frame of reference obtained by LBM [122] in the NASA Active Noise Control Fan rig.

in Figure 5.20, although at this stage it remains only a guess. The resonance could also be due to vortex shedding combined with a modulation in pressure due to another noise mechanism, as claimed by the authors, which remains the most probable scenario.

Parametric Studies — Summary

A short parametric study has been performed to get preliminary assessments on the influence of camber and acoustic resonances at low frequencies. Stagger and camber have been shown to generate more noise than flat vanes, and to have a more complex acoustic power spectra. Peaks and drops in the total sound power level have been attributed to acoustic resonances. Finally, acoustic resonances giving rise to fluctuations in phase opposition between adjacent channels proved to amplify wake-interaction tonal noise, whereas resonances resulting in fluctuations in phase between adjacent channels can mitigate noise.

5.6 Conclusion

Sound generation by periodic wake impingement has been addressed within the framework of the linearized analysis of Chu and Kovásznay [20] for small perturbations. The latter states that away from the cascade, the acoustic (potential) and wake (vortical) motions are independent. Within the inter-vane channels, it has been demonstrated that both motions stay independent in the volume, thus are linked at the leading-edge and trailing-edge interfaces only through the matching equations. This is mathematically equivalent to forcing the coupling at the vane surface, through the impermeability boundary condition, as it is usually done in other analytical models. Hence, the acoustic potentials description is the same as for an incident acoustic wave, and the wake motion is described independently.

The modeling of the fan wakes, from the rotor trailing edge to the stator leading edge, has not been addressed in this work. The assumption was made that the wake mean characteristics: velocity deficit and width, are known at the OGV location in a way that allows an expansion in Fourier series. Each resulting component, called gust, being independent. The modeling of the gust evolution through the cascade of cambered vanes relies on the method of multiple scales, and two propositions have been made for dealing with the wake slicing and tilting observed downstream of the OGV. The curvature effects were not accounted for in the vortical gust evolution.

Results obtained with the MMBW model for sound generation have been compared

with a set of numerical results on a tweaked SDT test case, from the fourth NASA CAA workshop, category 3, problem 2 [24]. Results from an alternative analytical model accounting for camber [25], by means of a two-stagger angle model, have also been added to the comparisons. Even if the MMBW model was off its validity range at the cut-on BPF harmonics, the shape and propagation angle of the acoustic waves were well predicted. However, regarding the noise power levels, they are constantly overestimated compared to the numerical results. Compared to the two-stagger model: results at the 2BPF are worse by more than 10 dB, but the modal power distribution is better reproduced at 3BPF, especially upstream. The neglected curvature effects are surely to be blamed and, more precisely, the vortical gust evolution seems to be the limiting factor. This is due to its shorter wavelength in subsonic flow condition, which makes it more sensitive to geometrical effects.

Finally, even if the MMBW model has shown its limit on a realistic test case, parametric studies have been performed on the SDT low-count configuration with varying shaft-rotation rate. This permits a continuous power spectra related to the 1BPF at different rotational speeds. This highlighted the effect of acoustic resonances on the total sound power level, which drops at resonances displaying a pattern where both sides of a vane are in phase, and peaks when the resonant pattern forces both sides to have opposite phases.

Conclusion

General Conclusions

Within a collaboration between Safran Aircraft Engines and the Laboratoire de Mécaniques des Fluides et d'Acoustique in Lyon, the aim of this PhD thesis was to improve the modeling of fan-related noise in order to better understand its origin and help engine manufacturers reducing it at its source. Focus has been placed on the periodic interaction between the fan wakes and the outlet guide vanes downstream.

A wide panel of noise simulation methods exists in the literature. The most commonly used in the context of turbomachinery have been presented, with a distinction between: methods heavily relying on numerical means for solving the fluid dynamics equations in the most accurate way, and methods trying to find analytical approximate solutions. The latter provide fast computations in exchange of a simplified geometry and flow description. These methods are well suited for early design stages, when the blade/vane geometry is not decided yet and needs to be optimized. Recently, the analytical model of Bouley et al. [12] showed promising capabilities to address rotor-stator wake-interaction tonal noise, and has even been extended to broadband noise by François et al. [34]. The model was closer to a proof of a concept than a finalized prediction tool, thus many simplifications were made on the vane geometry. In this context, the choice has been made to further improve this model by considering more realistic geometries. Hence making one step further to provide engine manufacturers with fast and accurate noise prediction tools at pre-design stage, when fast computations are needed within optimization strategies.

A review of analytical models available in the literature has highlighted that vane camber is still poorly modeled. Multiple studies have demonstrated that this parameter has a significant impact on tonal noise predictions, but almost no influence on broadband noise predictions. Furthermore, accounting for vane camber in the analytical models would allow one to remove two ambiguities: the choice of an equivalent stagger angle; the resulting uniform mean flow not representing swirl recovery through the cascade. That is why this PhD work has been focused on extending the mode-matching model to thin cambered vanes under periodic wake interactions. To do so, the modeling was restricted to two dimensions in the first instance.

The first part of this work has been dedicated to transmission and reflection phenomena within a cascade of cambered vanes. Introducing camber has a twofold impact on sound propagation in the inter-vane channels:

- curvature of the channel center line;
- expansion of the channel cross-section.

The expansion effect has been introduced, irrespective of the curvature effect, at first. It allowed one to give preliminary assessments on the overall effects of camber. Then, curvature effects have been introduced in the model and results were compared with and without accounting for them. The channel expansion also modifies the cut-off frequency along the channel. A given acoustic mode propagating in an inter-vane channel can become cut-off at some point, thus being totally reflected back, similarly to total internal reflection at an interface between two different fluids. This phenomenon has been treated apart and was introduced in the first model only, hence neglecting curvature effects on cut-on/cut-off transition.

The expansion effect on sound propagation in the inter-vane channels has been modeled by means of geometrical and flow approximations. The core geometrical assumption is that the cross-section varies slowly, allowing an analytical approximate solution based on a multiple-scale analysis. The flow is assumed to be perfectly aligned with the vane leading edge (no angle of attack), which results in a nearly uniform mean flow simply deviated by the vanes from upstream to downstream. The mean loading effects on the flow are not accounted for.

The curvature effect has then been introduced within the same mathematical framework and physical assumptions, but restating the wave equation in curvilinear coordinates. The latter was solved using a pseudo-spectral method based on Chebyshev polynomials.

Results for the scattering of an acoustic wave with both models have been compared with highly accurate numerical results, used as a reference. The Mode Matching for Bifurcated Wave-guides (MMBW), which does not account for curvature effects, proved to perform well below the first cut-off frequency of the channels, and even above it if curvature and frequency remain small. The Mode Matching for Bifurcated Curved Wave-guides (MMBCW) has been validated at relatively low and high frequencies, up to a Helmholtz number of about 12 based on the inter-vane spacing. The reliability of the model has been assessed by comparing results on the realistic vane geometry of the NASA SDT baseline configuration at mid-span. Results were in good agreement with the numerical reference, with and without flow. However, numerical results on the realistic vane geometry in the presence of flow (Mach number of about 0.45), were only available at a relatively low frequency (Helmholtz number of about 2.75). Further comparisons would be needed to assess the validity of the model in this case, using the open-source solver SU2 for example.

Parametric studies have been carried out on the different physical parameters of the MMBCW model. Apart from the vicinity of the cascade resonant frequencies, neither stagger/camber, solidity or incident mode order has a significant impact on the acoustic power balance between reflection and transmission. Although, stagger/camber and solidity do change the distribution of modal energy in the scattered fields for a given incident wave. Furthermore, camber induces reflections in the inter-vane channels even when the incident wavefront is perfectly perpendicular to the vane leading edges. For flat vanes, such a configuration is sometimes called "Venetian blind" and leads to a fully transmitted field, without any reflection or scattering. With curved vanes, reflected scattered waves appear upstream of the cascade, and a resonance can even take place in it.

Acoustic resonances occurring above the cut-off frequency of the annular domain, thus putting aside trapped modes, have also been investigated, but with the MMBW model. Within the limitations of this model, it appeared that camber has a similar effect as stagger on resonant frequencies, which consists in an increase of the frequency when solidity is large enough, depending on the resonance considered. The influence of incident mode order has also been investigated since usually left aside in the literature. A peculiar phenomenon of resonance by layers was brought to light, due to a modulation induced by the incident wave when its wavelength no longer matches the cascade periodicity.

On the other hand, cut-on/cut-off transitions have been addressed in the MMBW model by the method of matched asymptotic expansions. A uniformly valid expression of the acoustic potential in the inter-vane channels has been formulated. This allowed one to account for both: an upstream-propagating mode generated at the trailing edge being reflected back at its transition location; a cut-off mode generated at the leading edge carrying energy to the trailing edge when becoming cut-on. Both solutions were incorporated into the mode-matching equations.

The accuracy of the model within the transition frequency-ranges has been demonstrated, highlighting the significant impact a single mode can have on the overall scattering of an acoustic wave. The role of the transition in the development of certain acoustic resonances was brought to light. The standing-wave pattern formed by the upstream-propagating mode and its reflection allowing the resonance to take place even if the mode is cut-off near the leading edge area. The effect of Mach number on the transition has also been discussed.

Finally, sound generation by periodic wake impingement has been addressed. The fan wakes are expanded in Fourier series, in which each component is called a gust. The modeling of the gust evolution through the cascade of cambered vanes relied on the method of multiple scales without curvature effects, and two propositions have been made for dealing with the wake slicing and tilting observed downstream of the OGV.

The derived MMBW model for sound generation has been tested on the SDT test case and results have been compared with the literature. The model was off its validity range at the cut-on BPF of the test case but showed a good agreement with numerical results in terms of wavefront inclination outside the OGV cascade, highlighting a proper description of the mean flow deviation. The model systematically overestimated the power level of the radiated acoustic modes compared to numerical results, but showed some improvements compared to another analytical model. Introducing the curvature in the model of sound generation will give more insights on the capabilities of the developed approach.

Even if the MMBW model has shown its limit, parametric studies have been performed on the SDT low-count configuration with varying shaft-rotation rate, in order to obtain a continuous power spectra related to the 1BPF at different rotational speeds. This highlighted the effect of acoustic resonances on the total sound power level, which drops at resonances displaying a pattern where both sides of a vane are in phase, and peaks when the resonant pattern forces both sides to have opposite phases.

Perspectives

Perspectives are numerous for such a modeling work. Each part of the model has its own assumptions and limitations, which are listed in the following with possibilities for improvement.

Concerning sound propagation in slowly-varying curved ducts, the existence of an analytical solution with flow in two dimensions could be investigated to better understand the influence of Mach number. According to the website Wolfram Alpha [1], this solution is written as a combination of confluent hypergeometric functions, but its validity with hard-wall boundary conditions has not been assessed.

The next logical step is to extend the MMBCW model to the occurrence of transitions, with a new composite solution for a mode undergoing transition inside a slowly-varying bent channel. Brambley & Peake [14] already paved the way for such a work and their results could serve as a starting point. Another limit of the current model is that no energy transfer between neighboring modes at the transition location is considered, whereas it is known to occur at high frequencies, especially for large modal orders [88, 126, 127]. Detailed explanations and modeling for such scattering can be found in the work of Smith [126, 127].

Regarding the modeling of the vortical gust evolution through the OGV, an extension to account for curvature effects is necessary. This could be achieved by formulating a global system of equations in curvilinear coordinates, on both acoustic and vortical motions, and solving it by means of a pseudo-spectral method based on Chebyshev polynomials. All needed equations have been derived through this work and some tests were performed during the PhD, unfortunately without satisfying results. Such a numerical resolution could be subject to hydrodynamic instabilities, so caution would be required to resolve it properly.

Furthermore, accounting for curvature effects in the gust evolution cannot be achieved with the current description of the vane geometry due to curvature discontinuities, the gust evolution being directly proportional to it. A new description of the system with a continuous curvature through the cascade has been tested but is still under development. Notice that, such a continuous description would also enable a non-uniform description of the mean flow, thus addressing mean loading effects.

On the other hand, the model could be extended to account for any leading-edge and trailing-edge blade angles, irrespective of one another. The model is currently restricted to zero trailing-edge blade angle, which is representative of OGV. This extension would allow one to model staggered blades, with low to zero camber, representative of rotors at blade tip. Then, extending the model to a rotating cascade would enable the study of fan blades screen effect, which is still an important topic of research.

Finally, with a model of sound propagation through rotating fan blades and a model of sound generation for cambered OGV, a global model could be derived, accounting for successive reflections between the fan blades and the OGV. This would allow the study of eventual trapped modes in the inter stage, in two dimensions, which could be crucial for understanding sound emission from the fan stage.

To summarize, this PhD thesis has made one step further toward a unified modeling of sound generation and transmission in a rotor-stator stage, with realistic blade/vane geometries.

Appendix A

Slowly Varying Developments

A.1 Wave Equation and Boundary Conditions

A.1.1 Expansion of the Convected Wave Operator

Starting from the wave equation (1.11) with a change of Fourier-transform convention:

$$\mathcal{L}(\phi) = \frac{1}{D}\nabla\cdot(D\nabla\phi) - (\mathrm{i}\omega + \mathbf{U}\cdot\nabla)\left[\frac{1}{C^2}(\mathrm{i}\omega + \mathbf{U}\cdot\nabla)\phi\right] = 0, \tag{A.1}$$

the wave operator is expanded as

$$\begin{aligned}
\mathcal{L} &\equiv \frac{1}{D}\nabla\cdot(D\nabla) - (\mathrm{i}\omega + \mathbf{U}\cdot\nabla)\left[\frac{1}{C^2}(\mathrm{i}\omega + \mathbf{U}\cdot\nabla)\right] \\
&\equiv \nabla^2 + \frac{1}{D}(\nabla D)\nabla - \left[\frac{1}{C^2}\left(-\omega^2 + \mathrm{i}\omega(\mathbf{U}\cdot\nabla)\right) + (\mathbf{U}\cdot\nabla)\left(\frac{1}{C^2}(\mathrm{i}\omega + \mathbf{U}\cdot\nabla)\right)\right] \\
&\equiv \nabla^2 + \frac{1}{D}(\nabla D)\nabla + \frac{\omega^2}{C^2} - \mathrm{i}\frac{\omega}{C^2}(\mathbf{U}\cdot\nabla) - \left((\mathbf{U}\cdot\nabla)C^{-2}\right)(\mathrm{i}\omega + \mathbf{U}\cdot\nabla) \\
&\quad - \frac{1}{C^2}(\mathbf{U}\cdot\nabla)(\mathrm{i}\omega + \mathbf{U}\cdot\nabla) \\
&\equiv \partial_{xx} + \partial_{yy} + D^{-1}\left(\partial_x D\partial_x + \partial_y D\partial_y\right) + \omega^2 C^{-2} - \mathrm{i}\omega C^{-2}\left(U\partial_x + V\partial_y\right) \\
&\quad - \mathrm{i}\omega\left[U\partial_x C^{-2} + V\partial_y C^{-2}\right] - \left[U\partial_x C^{-2} + V\partial_y C^{-2}\right]\left(U\partial_x + V\partial_y\right) \\
&\quad - \mathrm{i}\omega C^{-2}\left(U\partial_x + V\partial_y\right) - C^{-2}\left[\left(U\partial_x + V\partial_y\right)^2 + \left(U\partial_x U + V\partial_y U\right)\partial_x\right. \\
&\quad \left. + \left(V\partial_y V + U\partial_x V\right)\partial_y\right].
\end{aligned} \tag{A.2}$$

Introducing the mean flow expansions from (2.49a-2.49d):

$$\mathbf{U}(X,y) = U_{0x}(X)\mathbf{e}_x + \epsilon U_{1y}(X,y)\mathbf{e}_y + \mathcal{O}(\epsilon^2), \tag{A.3a}$$

$$C(X,y) = C_0(X) + \mathcal{O}(\epsilon^2), \tag{A.3b}$$

$$D(X,y) = D_0(X) + \mathcal{O}(\epsilon^2), \tag{A.3c}$$

$$P(X,y) = P_0(X) + \mathcal{O}(\epsilon^2), \tag{A.3d}$$

equation (A.2) becomes

$$\begin{aligned}\mathcal{L} \equiv\ & \partial_{xx} + \partial_{yy} + \epsilon D_0^{-1}\partial_X D_0 \partial_x + \omega^2 C_0^{-2} - 2\mathrm{i}\omega C_0^{-2}\left(U_{0x}\partial_x + \epsilon U_{1y}\partial_y\right) - \epsilon \mathrm{i}\omega U_{0x}\partial_X C_0^{-2} \\ & - \epsilon U_{0x}^2 \partial_X C_0^{-2}\partial_x - C_0^{-2}\left[U_{0x}^2\partial_{xx} + 2\epsilon U_{0x}U_{1y}\partial_{xy} + \epsilon U_{0x}\partial_X U_{0x}\partial_x\right] + \mathcal{O}(\epsilon^2) \\ \equiv\ & \partial_{xx} + \partial_{yy} + C_0^{-2}\left[\omega^2 - 2\mathrm{i}\omega U_{0x}\partial_x - U_{0x}^2\partial_{xx}\right] \\ & + \epsilon\left\{D_0^{-1}\partial_X D_0\partial_x - \mathrm{i}\omega U_{0x}\partial_X C_0^{-2} - U_{0x}\partial_X\left(U_{0x}C_0^{-2}\right)\partial_x - 2\mathrm{i}\omega C_0^{-2}U_{1y}\partial_y\right. \\ & \left. -2C_0^{-2}U_{0x}U_{1y}\partial_{xy}\right\} \\ & + \mathcal{O}(\epsilon^2). \end{aligned} \tag{A.4}$$

This is equivalent to (2.53) and thus concludes the derivation.

A.1.2 WKB Expansion of the Acoustic Potential

From the above result, the wave equation (2.53) can be expanded as

$$\begin{aligned}& \partial_{xx}\phi + \partial_{yy}\phi - C_0^{-2}\left[-\omega^2\phi + 2\mathrm{i}\omega U_{0x}\partial_x\phi + U_{0x}^2\partial_{xx}\phi\right] \\ & + \epsilon\left\{D_0^{-1}\partial_X D_0\partial_x\phi - \mathrm{i}\omega U_{0x}\partial_X C_0^{-2}\phi - U_{0x}\partial_X\left(U_{0x}C_0^{-2}\right)\partial_x\phi - 2\mathrm{i}\omega C_0^{-2}U_{1y}\partial_y\phi\right. \\ & \left. -2C_0^{-2}U_{0x}U_{1y}\partial_{xy}\phi\right\} \\ & + \mathcal{O}(\epsilon^2) = 0. \end{aligned} \tag{A.5}$$

Introducing the WKB expansion for the acoustic potential

$$\phi(x, y; \epsilon) = \exp\left(-\frac{i}{\epsilon}\int^X \mu(\xi;\epsilon)\,\mathrm{d}\xi\right)\sum_{n=0}^{\infty}\epsilon^n\Phi_n(X, y; \epsilon), \tag{A.6}$$

where μ is the axial wavenumber, which is allowed to vary with X [83], it gives the derivatives

$$\phi_x = \exp\left(-\frac{i}{\epsilon}\int^X \mu(\xi;\epsilon)\,\mathrm{d}\xi\right)\left(-i\mu + \epsilon\partial_X\right)\sum_{n=0}^{\infty}\epsilon^n\Phi_n(X, y; \epsilon), \tag{A.7}$$

and

$$\phi_{xx} = \exp\left(-\frac{i}{\epsilon}\int^X \mu(\xi;\epsilon)\,\mathrm{d}\xi\right)\left(-\mu^2 - i\epsilon\partial_X\mu - 2i\epsilon\mu\partial_X + \epsilon^2\partial_{XX}\right)\sum_{n=0}^{\infty}\epsilon^n\Phi_n(X, y; \epsilon). \tag{A.8}$$

The wave equation (A.5) will be treated by order of magnitude and, from now on, the Einstein summation convention will be assumed for the index n. Dividing by the

common exponential term, the first line of (A.5) becomes

$$\begin{aligned}
&\left(-\mu^2 - i\epsilon\partial_X\mu - 2i\epsilon\mu\partial_X + \epsilon^2\partial_{XX}\right)\epsilon^n\Phi_n + \partial_{yy}\epsilon^n\Phi_n - C_0^{-2}\left[-\omega^2\epsilon^n\Phi_n\right.\\
&\quad\left.+2\mathrm{i}\omega U_{0x}\left(-i\mu + \epsilon\partial_X\right)\epsilon^n\Phi_n + U_{0x}^2\left(-\mu^2 - i\epsilon\partial_X\mu - 2i\epsilon\mu\partial_X + \epsilon^2\partial_{XX}\right)\epsilon^n\Phi_n\right]\\
&= -\mu^2\left(\Phi_0 + \epsilon\Phi_1\right) - \epsilon\left(i\partial_X\mu\Phi_0 + 2i\mu\partial_X\Phi_0\right) + \left(\partial_{yy}\Phi_0 + \epsilon\partial_{yy}\Phi_1\right)\\
&\quad - C_0^{-2}\left[\left(-\omega^2 + 2\omega\mu U_{0x} - \mu^2U_{0x}^2\right)\left(\Phi_0 + \epsilon\Phi_1\right) - i\epsilon\partial_X\mu U_{0x}^2\Phi_0 + 2i\epsilon(\omega U_{0x} - \mu U_{0x}^2)\partial_X\Phi_0\right]\\
&\quad + \mathcal{O}(\epsilon^2),\\
&= \partial_{yy}\Phi_0 + \left[C_0^{-2}\left(\omega - \mu U_{0x}\right)^2 - \mu^2\right]\Phi_0\\
&\quad + \epsilon\left\{\partial_{yy}\Phi_1 + \left[C_0^{-2}\left(\omega - \mu U_{0x}\right)^2 - \mu^2\right]\Phi_1 - i\partial_X\mu\left(1 - C_0^{-2}U_{0x}^2\right)\Phi_0\right.\\
&\quad\left.-2i\left[C_0^{-2}U_{0x}\left(\omega - \mu U_{0x}\right) + \mu\right]\partial_X\Phi_0\right\} + \mathcal{O}(\epsilon^2),
\end{aligned} \tag{A.9}$$

and the second line of (A.5)

$$\begin{aligned}
&\epsilon\left\{D_0^{-1}\partial_X D_0\left(-i\mu + \epsilon\partial_X\right)\epsilon^n\Phi_n - \mathrm{i}\omega U_{0x}\partial_X C_0^{-2}\epsilon^n\Phi_n - U_{0x}\partial_X\left(U_{0x}C_0^{-2}\right)\left(-i\mu + \epsilon\partial_X\right)\epsilon^n\Phi_n\right.\\
&\quad\left.-2\mathrm{i}\omega C_0^{-2}U_{1y}\partial_y\epsilon^n\Phi_n - 2C_0^{-2}U_{0x}U_{1y}\left(-i\mu\partial_y + \epsilon\partial_{Xy}\right)\epsilon^n\Phi_n\right\}\\
&= \epsilon\left\{-i\mu D_0^{-1}\partial_X D_0\Phi_0 - \mathrm{i}\omega U_{0x}\partial_X C_0^{-2}\Phi_0 + i\mu U_{0x}\partial_X\left(U_{0x}C_0^{-2}\right)\Phi_0 - 2\mathrm{i}\omega C_0^{-2}U_{1y}\partial_y\Phi_0\right.\\
&\quad\left.+2i\mu C_0^{-2}U_{0x}U_{1y}\partial_y\Phi_0\right\} + \mathcal{O}(\epsilon^2)\\
&= \epsilon\left\{-i\left[\mu D_0^{-1}\partial_X D_0 + \omega\partial_X\left(U_{0x}C_0^{-2}\right) - \mu\partial_X\left(U_{0x}^2C_0^{-2}\right) - (\omega - \mu U_{0x})C_0^{-2}\partial_X U_{0x}\right]\Phi_0\right.\\
&\quad\left.-2iC_0^{-2}(\omega - \mu U_{0x})U_{1y}\partial_y\Phi_0\right\} + \mathcal{O}(\epsilon^2)\\
&= \epsilon\left\{-i\left[\mu D_0^{-1}\partial_X D_0 + \omega\partial_X\left(U_{0x}C_0^{-2}\right) - \mu\partial_X\left(U_{0x}^2C_0^{-2}\right)\right.\right.\\
&\quad\left.\left.-(\omega - \mu U_{0x})C_0^{-2}D_0^{-1}\partial_X\left(D_0U_{0x}\right) + (\omega - \mu U_{0x})C_0^{-2}U_{0x}D_0^{-1}\partial_X D_0\right]\Phi_0\right.\\
&\quad\left.-2iC_0^{-2}(\omega - \mu U_{0x})U_{1y}\partial_y\Phi_0\right\} + \mathcal{O}(\epsilon^2).
\end{aligned} \tag{A.10}$$

Rewriting together (A.9) and (A.10), and introducing $\Omega = \omega - \mu U_{0x}$, this yields

$$\mathcal{O}(1)\quad \partial_{yy}\Phi_0 + \left(\frac{\Omega^2}{C_0^2} - \mu^2\right)\Phi_0 = 0, \tag{A.11a}$$

$$\begin{aligned}
\mathcal{O}(\epsilon)\quad &\partial_{yy}\Phi_1 + \left(\frac{\Omega^2}{C_0^2} - \mu^2\right)\Phi_1 = i\partial_X\mu\left(1 - \frac{U_{0x}^2}{C_0^2}\right)\Phi_0 + 2i\left(\frac{\Omega U_{0x}}{C_0^2} + \mu\right)\partial_X\Phi_0\\
&+ i\left[\left(\frac{\Omega U_{0x}}{C_0^2} + \mu\right)\frac{\partial_X D_0}{D_0} + \omega\partial_X\left(\frac{U_{0x}}{C_0^2}\right) - \mu\partial_X\left(\frac{U_{0x}^2}{C_0^2}\right) - \frac{\Omega}{D_0C_0^2}\partial_X\left(D_0U_{0x}\right)\right]\Phi_0\\
&+ 2i\frac{\Omega}{C_0^2}U_{1y}\partial_y\Phi_0.
\end{aligned} \tag{A.11b}$$

While equation (A.11a) has the desired shape, the right-hand side of equation (A.11b) still needs some simplifications. Using the fact that $-\partial_X\left(D_0U_{0x}\right) = \partial_y\left(D_0U_{1y}\right) =$

$D_0\partial_y U_{1y} + \mathcal{O}(\epsilon^2)$, (A.11b) is restated as

$$\begin{aligned}\mathcal{O}(\epsilon)\quad \partial_{yy}\Phi_1 + \left(\frac{\Omega^2}{C_0^2} - \mu^2\right)\Phi_1 &= i\left[\partial_X \mu\left(1 - \frac{U_{0x}^2}{C_0^2}\right) + \omega\partial_X\left(\frac{U_{0x}}{C_0^2}\right) - \mu\partial_X\left(\frac{U_{0x}^2}{C_0^2}\right)\right]\Phi_0 \\ &\quad + i\left(\frac{\Omega U_{0x}}{C_0^2} + \mu\right)\frac{\partial_X D_0}{D_0}\Phi_0 + 2i\left(\frac{\Omega U_{0x}}{C_0^2} + \mu\right)\partial_X\Phi_0 \\ &\quad + i\frac{\Omega}{C_0^2}\partial_y U_{1y}\Phi_0 + 2i\frac{\Omega}{C_0^2}U_{1y}\partial_y\Phi_0 \\ &= \frac{i}{D_0\Phi_0}\left\{\partial_X\left[\left(\frac{\Omega U_{0x}}{C_0^2} + \mu\right)D_0\Phi_0^2\right] + \frac{\Omega D_0}{C_0^2}\partial_y\left(U_{1y}\Phi_0^2\right)\right\},\end{aligned} \tag{A.12}$$

which concludes the derivations of the wave equation.

The boundary conditions in (2.54) are given by

$$(\nabla\phi\cdot\mathbf{n})|_{y=R^\pm(X)} = 0 \Leftrightarrow \partial_x\phi n_x^\pm\big|_{y=R^\pm(X)} + \partial_y\phi n_y^\pm\big|_{y=R^\pm(X)} = 0, \tag{A.13}$$

with

$$\mathbf{n}^+ = \frac{\mathbf{e}_y + \epsilon\sin\left(2\frac{\cos\Psi}{h_0}X - \Psi\right)\mathbf{e}_x}{\sqrt{1+\epsilon^2\sin^2\left(2\frac{\cos\Psi}{h_0}X - \Psi\right)}},\quad \mathbf{n}^- = -\frac{\mathbf{e}_y - \epsilon\sin\left(2\frac{\cos\Psi}{h_0}X - \Psi\right)\mathbf{e}_x}{\sqrt{1+\epsilon^2\sin^2\left(2\frac{\cos\Psi}{h_0}X - \Psi\right)}}. \tag{A.14}$$

The symbol $\pm$ is used to denote the upper $(+)$ and lower $(-)$ boundary conditions. Substituting these expressions into (A.13) and dividing by the common integral term, the result is straight-forward:

$$[(-i\mu + \epsilon\partial_X)\,\epsilon^n\Phi_n]_{y=R^\pm(X)}\frac{\epsilon\sin\left(2\frac{\cos\Psi}{h_0}X - \Psi\right)}{\sqrt{1+\epsilon^2\sin^2\left(2\frac{\cos\Psi}{h_0}X - \Psi\right)}} \pm \frac{[\partial_y\epsilon^n\Phi_n]_{y=R^\pm(X)}}{\sqrt{1+\epsilon^2\sin^2\left(2\frac{\cos\Psi}{h_0}X - \Psi\right)}} = 0,$$

$$\Rightarrow -i\mu\epsilon\sin\left(2\frac{\cos\Psi}{h_0}X - \Psi\right)\Phi_0|_{y=R^\pm(X)} \pm \left(\partial_y\Phi_0|_{y=R^\pm(X)} + \epsilon\,\partial_y\Phi_1|_{y=R^\pm(X)}\right) + \mathcal{O}(\epsilon^2) = 0,$$

which is equivalent to

$$\mathcal{O}(1)\quad \partial_y\Phi_0|_{y=R^\pm(X)} = 0, \tag{A.15a}$$

$$\mathcal{O}(\epsilon)\quad \partial_y\Phi_1|_{y=R^\pm(X)} = \pm i\mu\sin\left(2\frac{\cos\Psi}{h_0}X - \Psi\right)\Phi_0|_{y=R^\pm(X)}. \tag{A.15b}$$

A.2 Solvability Condition

The solvability condition used by Rienstra [107] is based on the Fredholm alternative as detailed with plenty of examples in Nayfeh's book [81]: Introduction to perturbation techniques, chapter 15.

It has been demonstrated, from (2.63), that the solvability condition in this case reduces to

$$\int_{R^-(X)}^{R^+(X)} \Phi_0 f_h(\Phi_0)\,\mathrm{d}y = \left[\Phi_0 \partial_y \Phi_1\right]_{R^-}^{R^+} - \left[\Phi_1 \partial_y \Phi_0\right]_{R^-}^{R^+}, \tag{A.16}$$

which is basically Green's second identity. From equations (2.56) and (2.57), this is also equal to

$$\begin{aligned} &\overbrace{\int_{R^-}^{R^+} \partial_X \left[\left(\frac{\Omega U_{0x}}{C_0^2} + \mu\right) D_0 \Phi_0^2\right] \mathrm{d}y}^{(1)} + \overbrace{\int_{R^-}^{R^+} \frac{\Omega D_0}{C_0^2} \partial_y \left(U_{1y} \Phi_0^2\right)\,\mathrm{d}y}^{(2)} \\ &\qquad = \underbrace{\mu D_0 \sin\left(2\frac{\cos\Psi}{h_0}X - \Psi\right)\left(\Phi_0^2\big|_{y=R^+} + \Phi_0^2\big|_{y=R^-}\right)}_{(3)}. \end{aligned} \tag{A.17}$$

Term (1) can be developed by application of the Leibniz's rule for differentiation under the integral sign. This gives

$$\begin{aligned} &\int_{R^-}^{R^+} \partial_X \left[\left(\frac{\Omega U_{0x}}{C_0^2} + \mu\right) D_0 \Phi_0^2\right] \mathrm{d}y \\ &= \partial_X \left[\left(\frac{\Omega U_{0x}}{C_0^2} + \mu\right) D_0 \int_{R^-}^{R^+} \Phi_0^2\,\mathrm{d}y\right] - \partial_X R^+(X) \left(\frac{\Omega U_{0x}}{C_0^2} + \mu\right) D_0\, \Phi_0^2\big|_{y=R^+} \\ &+ \partial_X R^-(X) \left(\frac{\Omega U_{0x}}{C_0^2} + \mu\right) D_0\, \Phi_0^2\big|_{y=R^-} \\ &= \partial_X \left[\left(\frac{\Omega U_{0x}}{C_0^2} + \mu\right) D_0 N^2\right] + D_0 \sin\left(2\frac{\cos\Psi}{h_0}X - \Psi\right) \left(\frac{\Omega U_{0x}}{C_0^2} + \mu\right) \left(\Phi_0^2\big|_{y=R^+} + \Phi_0^2\big|_{y=R^-}\right). \end{aligned} \tag{A.18}$$

Term (2) is derived as

$$\begin{aligned} \frac{\Omega D_0}{C_0^2} \int_{R^-}^{R^+} \mathrm{d}\left(U_{1y}\Phi_0^2\right) &= \frac{\Omega D_0}{C_0^2} \left[U_{1y}\Phi_0^2\right]_{R^-}^{R^+} \\ &= \frac{\Omega D_0}{C_0^2} \left(U_{1y}\Phi_0^2\big|_{y=R^+} - U_{1y}\Phi_0^2\big|_{y=R^-}\right) \\ &= \frac{\Omega D_0}{C_0^2}\, U_{1y}\big|_{y=R^+} \left(\Phi_0^2\big|_{y=R^+} + \Phi_0^2\big|_{y=R^-}\right). \end{aligned}$$

The last part assumed symmetry of the boundaries with respect to the channel center line in order to write $U_{1y}\big|_{y=R^+} = -\,U_{1y}\big|_{y=R^-}$. Further simplifications are obtained by using the no-slip condition of the mean flow at the boundaries:

$$\mathbf{U} \cdot \mathbf{n}^{\pm} = 0, \quad \text{at} \quad y = R^{\pm}(X). \tag{A.19}$$

Hence,

$$U_{1y}\big|_{y=R^{\pm}} = \mp U_{0x} \sin\left(2\frac{\cos\Psi}{h_0}X - \Psi\right), \tag{A.20}$$

where the $\mp$ sign on the right-hand side is chosen accordingly with the boundary

considered, respectively $y = R^+$ and $y = R^-$. Term (2) is finally rewritten as

$$- D_0 \frac{\Omega U_{0x}}{C_0^2} \sin\left(2\frac{\cos\Psi}{h_0}X - \Psi\right)\left(\Phi_0^2\big|_{y=R^+} + \Phi_0^2\big|_{y=R^-}\right). \tag{A.21}$$

Combining terms (2) and (3) cancels the second part of (1), which leaves only the following condition:

$$\partial_X\left[\left(\frac{\Omega U_{0x}}{C_0^2} + \mu\right) D_0 N^2\right] = 0. \tag{A.22}$$

Introducing

$$\sigma = \sqrt{1 - (C_0^2 - U_{0x}^2)\frac{\theta^2}{\omega^2}}, \tag{A.23}$$

the solvability condition is recast into its final form

$$\sqrt{\frac{\omega D_0(X)\sigma(X)}{C_0(X)}} N(X) = Q\,(\text{a constant}). \tag{A.24}$$

Appendix B

Orthogonal Curvilinear Coordinates

B.1 Scale Factor

This section focuses on the particular case of the two-dimensional curvilinear coordinates used in this thesis. For more general considerations on curvilinear coordinates, the book Methods of Theoretical Physics from Morse & Feshbach [78], Chapter 1.3, is recommended.

Looking at Figure B.1, a small variation $\mathrm{d}x$ or $\mathrm{d}y$ in its respective coordinate produces an equal displacement $\mathrm{d}s = \mathrm{d}x$ (segment [OA]) or $\mathrm{d}s = \mathrm{d}y$ (segment [OB]). With polar coordinates (r, θ), a change $\mathrm{d}\theta$ along the azimuthal coordinate produces

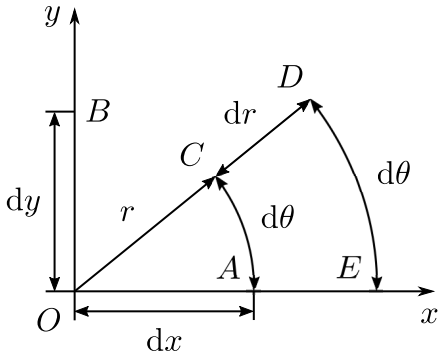

Figure B.1: Displacement produced by a small change of a coordinate.

a displacement $\mathrm{d}s = r\mathrm{d}\theta$ from point A to point C in Figure B.1. The so-called scale factor for the coordinate θ is defined by

$$h_\theta = \frac{\mathrm{d}s}{\mathrm{d}\theta} = r. \tag{B.1}$$

Note that the scale factor is usually not a constant in space. On the other side, a change $\mathrm{d}r$ along the radial coordinate, from point C to point D, produces an equal displacement $\mathrm{d}r$. Hence

$$h_r = \frac{\mathrm{d}s}{\mathrm{d}r} = 1. \tag{B.2}$$

The scale factors of each coordinate can be different !

The scale factors h_r and h_θ have been derived by simple geometrical knowledge. Noticing that the general expression of the displacement in Cartesian coordinates is

$\mathrm{d}s = \sqrt{\mathrm{d}x^2 + \mathrm{d}y^2}$, simple substitution in (B.1) and (B.2) shows that

$$h_r = \sqrt{\left(\frac{\partial x}{\partial r}\right)^2 + \left(\frac{\partial y}{\partial r}\right)^2}, \quad h_\theta = \sqrt{\left(\frac{\partial x}{\partial \theta}\right)^2 + \left(\frac{\partial y}{\partial \theta}\right)^2}. \tag{B.3}$$

Thus

$$h_r = \sqrt{\left(\frac{\partial r\cos\theta}{\partial r}\right)^2 + \left(\frac{\partial r\sin\theta}{\partial r}\right)^2} = 1, \quad h_\theta = \sqrt{\left(\frac{\partial r\cos\theta}{\partial \theta}\right)^2 + \left(\frac{\partial r\sin\theta}{\partial \theta}\right)^2} = r.$$

The scale factors are the norm of the column vectors composing the Jacobian matrix $\mathbf{J}$ of the mapping $(r, \theta) \mapsto (x, y)$. The Jacobian matrix is given by

$$\mathbf{J}(r,\theta) = \begin{pmatrix} \partial x/\partial r & \partial x/\partial \theta \\ \partial y/\partial r & \partial y/\partial \theta \end{pmatrix}.$$

It gives information about the metric distortion occurring when going from the r-θ space to the x-y space. Since the coordinates are orthogonal, the vectors $(\partial x/\partial r, \partial y/\partial r)$ and $(\partial x/\partial \theta, \partial y/\partial \theta)$ are orthogonal as well. Thus, the determinant of the Jacobian matrix is simply

$$\det(\mathbf{J}(r,\theta)) = \left\| \begin{pmatrix} \partial x/\partial r \\ \partial y/\partial r \end{pmatrix} \right\|_2 \cdot \left\| \begin{pmatrix} \partial x/\partial \theta \\ \partial y/\partial \theta \end{pmatrix} \right\|_2 = h_r h_\theta.$$

The scale factors are the eigenvalues of the Jacobian matrix ! As explained geometrically in (B.1) and (B.2), the scale factors measure how volume or surface area is scaled in each direction. This is evidently related to the property of the determinant of the Jacobian $\mathbf{J}(r,\theta)$[1]. An infinitesimal surface element in the polar reference frame, such as delimited by the points ACDE in Figure B.2, is scaled/distorted when projected into the Cartesian reference frame (Figure B.1) with a distortion factor equal to the product of the metric distortions in each direction. Its surface area is then equal to

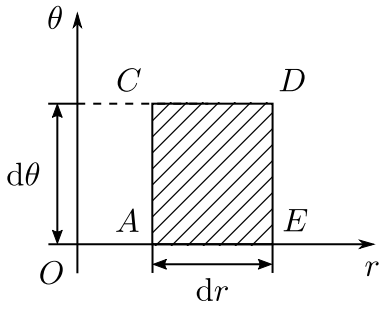

Figure B.2: Infinitesimal surface element in the polar reference frame.

$h_r h_\theta \mathrm{d}r\mathrm{d}\theta = r\mathrm{d}r\mathrm{d}\theta$. In general, the volume of an elementary rectangular parallelepiped in any orthogonal coordinate system $(\xi_1, \xi_2, ...)$ is defined by

$$\mathrm{d}v = \prod_i h_i \mathrm{d}\xi_i. \tag{B.4}$$

[1] A nice illustrative explanation can be found on 3Blue1Brown YouTube channel. [Online]. Available: https://youtu.be/Ip3X9LOh2dk

B.2 Inter-Vane Channel Coordinates

Notice that the curvilinear coordinates used in this thesis are just polar coordinates in disguise. Looking at Figure B.3, the definition of (s, n) is given by equations (B.5).

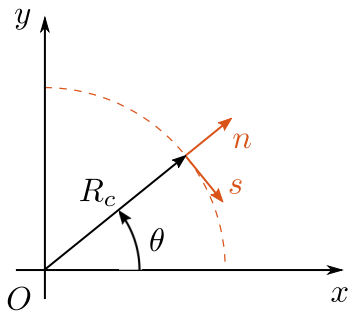

$$\begin{cases} s = -R_c\theta, \\ n = r - R_c. \end{cases} \tag{B.5}$$

Figure B.3: Curvilinear coordinates definition.

It follows that

$$\frac{\partial}{\partial s} = \frac{\partial}{\partial \theta}\frac{\partial \theta}{\partial s} = -\frac{1}{R_c}\frac{\partial}{\partial \theta}, \quad \frac{\partial}{\partial n} = \frac{\partial}{\partial r}\frac{\partial r}{\partial n} = \frac{\partial}{\partial r},$$

and so

$$\boxed{h_n = h_r = 1}, \quad \boxed{h_s = \frac{n + R_c}{R_c} = 1 + \frac{n}{R_c} = 1 - \kappa n}, \tag{B.6}$$

where $\kappa = -1/R_c$ because the curvature is negative in the chosen curvilinear reference frame.

B.3 Differential Operators

Here is a list of useful differential operators expressed in a two-dimensional orthogonal curvilinear space ξ_1-ξ_2 (except for the curl), with unit vectors $\mathbf{e}_1$ and $\mathbf{e}_2$, extracted from Morse & Feshbach [78]:

$$\nabla\phi = \frac{\mathbf{e}_1}{h_1}\frac{\partial \phi}{\partial \xi_1} + \frac{\mathbf{e}_2}{h_2}\frac{\partial \phi}{\partial \xi_2} \tag{B.7}$$

$$(\mathbf{U}\cdot\nabla)\,\phi = \frac{U_1}{h_1}\frac{\partial \phi}{\partial \xi_1} + \frac{U_2}{h_2}\frac{\partial \phi}{\partial \xi_2} \tag{B.8}$$

$$[(\mathbf{U}\cdot\nabla)\,\mathbf{V}]\cdot\mathbf{e}_1 = \frac{U_1}{h_1}\frac{\partial V_1}{\partial \xi_1} + \frac{U_2}{h_2}\frac{\partial V_1}{\partial \xi_2} + \frac{V_2}{h_1 h_2}\left[U_1\frac{\partial h_1}{\partial \xi_2} - U_2\frac{\partial h_2}{\partial \xi_1}\right] \tag{B.9}$$

$$[(\mathbf{U}\cdot\nabla)\,\mathbf{V}]\cdot\mathbf{e}_2 = \frac{U_1}{h_1}\frac{\partial V_2}{\partial \xi_1} + \frac{U_2}{h_2}\frac{\partial V_2}{\partial \xi_2} + \frac{V_1}{h_1 h_2}\left[U_2\frac{\partial h_2}{\partial \xi_1} - U_1\frac{\partial h_1}{\partial \xi_2}\right] \tag{B.10}$$

$$\nabla\cdot\mathbf{U} = \frac{1}{h_1 h_2}\left[\frac{\partial}{\partial \xi_1}(U_1 h_2) + \frac{\partial}{\partial \xi_2}(h_1 U_2)\right] \tag{B.11}$$

$$\nabla^2\phi = \frac{1}{h_1 h_2}\left[\frac{\partial}{\partial \xi_1}\left(\frac{h_2}{h_1}\frac{\partial \phi}{\partial \xi_1}\right) + \frac{\partial}{\partial \xi_2}\left(\frac{h_1}{h_2}\frac{\partial \phi}{\partial \xi_2}\right)\right] \tag{B.12}$$

$$[\nabla \times \mathbf{U}] \cdot \mathbf{e}_3 = \frac{1}{h_1 h_2} \left[\frac{\partial}{\partial \xi_1} (h_2 U_2) - \frac{\partial}{\partial \xi_2} (h_1 U_1) \right] \tag{B.13}$$

Appendix C

Transition Analysis

C.1 Airy functions

The NIST Handbook of Mathematical Functions [85] states that

$$\lim_{s\to-\infty} A_i(-s) = \frac{\exp\left(-\frac{2}{3}(-s)^{3/2}\right)}{2\sqrt{\pi}(-s)^{1/4}} + \mathcal{O}(s^{-3/2}),$$
$$\lim_{s\to-\infty} B_i(-s) = \frac{\exp\left(\frac{2}{3}(-s)^{3/2}\right)}{\sqrt{\pi}(-s)^{1/4}} + \mathcal{O}(s^{-3/2}),$$

and

$$\lim_{s\to+\infty} A_i(-s) = \frac{\cos\left(\frac{2}{3}s^{3/2} - \frac{\pi}{4}\right)}{\sqrt{\pi}s^{1/4}} + \mathcal{O}(s^{-3/2}),$$
$$\lim_{s\to+\infty} B_i(-s) = \frac{-\sin\left(\frac{2}{3}s^{3/2} - \frac{\pi}{4}\right)}{\sqrt{\pi}s^{1/4}} + \mathcal{O}(s^{-3/2}),$$

where $s \in \mathbb{C}$.

C.2 Velocity Potential

C.2.1 Downstream-Propagating Part

The acoustic potential corresponding to the downstream-propagating modes is given in the slowly-varying part of the channel by

$$\phi_d(S,n) = \sum_{q=0}^{+\infty} D_q \Xi_q^+(S) \cos\left(\theta_q(S)\left[n + \frac{h(S)}{2}\right]\right), \tag{C.1}$$

where

$$\Xi_q^+(S) = \begin{cases} \dfrac{\Gamma_q(S)}{\Gamma_q(0)} \dfrac{\mathrm{B_i}(r_q(S)) + i\mathrm{A_i}(r_q(S))}{\mathrm{B_i}(r_q(0))} e^{ik_q^+ a\tan\Psi} & \text{if} \quad \exists S_t \in [0, \epsilon L_c],\ \sigma_q^2(S_t) = 0, \\ \Upsilon_q^+(S)/\Upsilon_q^+(0)\, e^{ik_q^+ a\tan\Psi} & \text{otherwise,} \end{cases}$$

$$\Gamma_q(S) = \left| \frac{r_q(S)}{\rho^2(S)k^2(S)h^2(S)\sigma_q^2(S)} \right|^{1/4} \exp\left(-\frac{i}{\epsilon} \int_{S_t}^{S} \frac{k(\xi)M(\xi)}{\beta^2(\xi)} \,\mathrm{d}\xi \right),$$

$$r_q(S) = \begin{cases} \left(\dfrac{3}{2\epsilon} \displaystyle\int_{S}^{S_t} \frac{k|\sigma_q|}{\beta^2} \,\mathrm{d}\xi \right)^{2/3} & \text{if} \quad S < S_t, \\ -\left(\dfrac{3}{2\epsilon} \displaystyle\int_{S_t}^{S} \frac{k|\sigma_q|}{\beta^2} \,\mathrm{d}\xi \right)^{2/3} & \text{if} \quad S_t \leq S, \end{cases}$$

and

$$\Upsilon_q^+(S) = \frac{\exp\left(i/\epsilon \int_0^S \mu_q^+/\beta^2 \,\mathrm{d}\xi \right)}{\sqrt{\rho \mu_q^+ h}}, \quad \mu_q^+ = \frac{-kM + k\sigma_q}{\beta^2}.$$

The stream-wise acoustic velocity is expressed by

$$\frac{\partial \phi_d}{\partial s}(s,n) = \epsilon \frac{\partial \phi_d}{\partial S}(S,n). \tag{C.2}$$

Since $\theta_q(S) = q\pi/h(S)$ and h is a function of the slow variable S, the derivative of the cosine term in (C.1) is $\mathcal{O}(\epsilon)$. Therefore

$$\epsilon \frac{\partial \phi_d}{\partial S}(S,n) = \epsilon \sum_{q=0}^{+\infty} D_q \frac{\partial \Xi_q^+}{\partial S} \cos\left(\theta_q(S) \left[n + \frac{h(S)}{2} \right] \right) + \mathcal{O}(\epsilon). \tag{C.3}$$

In the absence of any transition, the derivative simply reads, at leading-order

$$\epsilon \frac{\partial \Xi_q^+}{\partial S} = \epsilon \frac{e^{ik_q^+ a \tan\Psi}}{\Upsilon_q^+(0)} \frac{\partial \Upsilon_q^+}{\partial S} \sim i\mu_q^+ \frac{\Upsilon_q^+(S)}{\Upsilon_q^+(0)} e^{ik_q^+ a \tan\Psi} = i \frac{-kM + k\sigma_q}{\beta^2} \Xi_q^+. \tag{C.4}$$

Otherwise, when a transition occurs, it reads

$$\epsilon \frac{\partial \Xi_q^+}{\partial S} = \epsilon \frac{e^{ik_q^+ a \tan\Psi}}{\Gamma_q(0)\mathrm{B_i}(r_q(0))} \underbrace{\frac{\partial}{\partial S} \left\{ \Gamma_q \left[\mathrm{B_i}(r_q) + i\mathrm{A_i}(r_q) \right] \right\}}_{\mathcal{D}}. \tag{C.5}$$

The derivative-term $\mathcal{D}$ can be expressed as

$$\mathcal{D} = \Gamma_q' \left[\mathrm{B_i}(r_q) + i\mathrm{A_i}(r_q) \right] + \Gamma_q r_q' \left[\mathrm{B_i}'(r_q) + i\mathrm{A_i}'(r_q) \right],$$

where at first order

$$\Gamma_q' \sim \left(\frac{1}{4} \frac{|r_q|'}{|r_q|} - \frac{i}{\epsilon} \frac{kM}{\beta^2} \right) \Gamma_q,$$

and

$$|r_q|' \sim \begin{cases} -\dfrac{1}{\epsilon} \dfrac{k|\sigma_q|}{\beta^2 |r_q|^{1/2}} & \text{if} \quad S < S_t, \\ +\dfrac{1}{\epsilon} \dfrac{k|\sigma_q|}{\beta^2 |r_q|^{1/2}} & \text{if} \quad S_t \leq S, \end{cases}$$

while

$$r_q' \sim -\frac{1}{\epsilon} \frac{k|\sigma_q|}{\beta^2 |r_q|^{1/2}}.$$

Hence the derivative of Ξ_q^+ at first order reads, in this case,

$$\epsilon\frac{\partial\Xi_q^+}{\partial S} \sim i\frac{-kM+k\varsigma_q^+}{\beta^2}\Xi_q^+, \tag{C.6}$$

where

$$\boxed{\varsigma_q^+ = i|\sigma_q| \times \begin{cases} \dfrac{1}{|r_q|^{1/2}}\dfrac{\mathrm{B_i}'(r_q)+i\mathrm{A_i}'(r_q)}{\mathrm{B_i}(r_q)+i\mathrm{A_i}(r_q)} + \dfrac{1}{4|r_q|^{3/2}} & \text{if} \quad S<S_t, \\ \dfrac{1}{|r_q|^{1/2}}\dfrac{\mathrm{B_i}'(r_q)+i\mathrm{A_i}'(r_q)}{\mathrm{B_i}(r_q)+i\mathrm{A_i}(r_q)} - \dfrac{1}{4|r_q|^{3/2}} & \text{if} \quad S_t\leq S, \end{cases}} \tag{C.7}$$

C.2.2 Upstream-Propagating Part

The acoustic potential corresponding to the upstream-propagating modes is given in the slowly-varying part of the channel by

$$\phi_u(S,n) = \sum_{q=0}^{+\infty} U_q\Xi_q^-(S)\cos\left(\theta_q(S)\left[n+\frac{h(S)}{2}\right]\right), \tag{C.8}$$

where

$$\Xi_q^-(S) = \begin{cases} \dfrac{\Gamma_q(S)}{\Gamma_q(L_c)}\dfrac{\mathrm{A_i}(r_q(S))}{\mathrm{A_i}(r_q(L_c))} & \text{if} \quad \exists S_t\in[0,\epsilon L_c],\ \sigma_q^2(S_t)=0, \\ \Upsilon_q^-(S)/\Upsilon_q^-(L_c) & \text{otherwise,} \end{cases}$$

and

$$\Upsilon_q^-(S) = \frac{\exp\left(i/\epsilon\int_{L_c}^S \mu_q^-/\beta^2\,\mathrm{d}\xi\right)}{\sqrt{\rho\mu_q^- h}}, \quad \mu_q^- = \frac{-kM-k\sigma_q}{\beta^2}.$$

When no transition occurs, the derivative of $\Xi_q^-(S)$ reads

$$\epsilon\frac{\partial\Xi_q^-}{\partial S} \sim i\frac{-kM-k\sigma_q}{\beta^2}\Xi_q^-, \tag{C.9}$$

and otherwise

$$\epsilon\frac{\partial\Xi_q^-}{\partial S} \sim i\frac{-kM-k\varsigma_q^-}{\beta^2}\Xi_q^-, \tag{C.10}$$

where

$$\boxed{\varsigma_q^- = -i|\sigma_q| \times \begin{cases} \dfrac{1}{|r_q|^{1/2}}\dfrac{\mathrm{A_i}'(r_q)}{\mathrm{A_i}(r_q)} + \dfrac{1}{4|r_q|^{3/2}} & \text{if} \quad S<S_t, \\ \dfrac{1}{|r_q|^{1/2}}\dfrac{\mathrm{A_i}'(r_q)}{\mathrm{A_i}(r_q)} - \dfrac{1}{4|r_q|^{3/2}} & \text{if} \quad S_t\leq S, \end{cases}} \tag{C.11}$$

Bibliography

[1] Wolfram Alpha. [Online]. Available: https://www.wolframalpha.com/ (Cited on pages 69, 77, 120, and 196)

[2] R. K. Amiet, "Acoustic radiation from an airfoil in a turbulent stream," *Journal of Sound and vibration*, vol. 41, pp. 407–420, 1975. (Cited on page 17)

[3] ——, "High frequency thin-airfoil theory for subsonic flow," *AIAA journal*, vol. 14, pp. 1076–1082, 1976. (Cited on page 17)

[4] ——, "Noise due to turbulent flow past a trailing edge," *Journal of sound and vibration*, vol. 47, pp. 387–393, 1976. (Cited on page 17)

[5] P. J. Baddoo and L. J. Ayton, "An analytic solution for gust–cascade interaction noise including effects of realistic aerofoil geometry," *Journal of Fluid Mechanics*, vol. 886, 2020. (Cited on pages 18, 19, 24, and 38)

[6] E. Bécache, A. S. B.-B. Dhia, and G. Legendre, "Perfectly Matched Layers for the Convected Helmholtz Equation," *SIAM Journal on Numerical Analysis*, July 2006. (Cited on pages 59 and 90)

[7] H. Bériot and G. Gabard, "Anisotropic adaptivity of the p-FEM for time-harmonic acoustic wave propagation," *Journal of Computational Physics*, vol. 378, pp. 234–256, February 2019. (Cited on pages 59 and 90)

[8] C. Bender and S. Orszag, *Advanced Mathematical Methods for Scientists and Engineers*. McGraw-Hill, 1978. (Cited on pages 42 and 46)

[9] H. Bériot, A. Prinn, and G. Gabard, "Efficient implementation of high-order finite elements for Helmholtz problems," *International Journal for Numerical Methods in Engineering*, vol. 106, no. 3, pp. 213–240, April 2016. (Cited on pages 59 and 90)

[10] S. Bouley, "Modélisations analytiques du bruit tonal d'interaction rotor / stator par la technique de raccordement modal," PhD thesis, Université de Lyon, 2017. [Online]. Available: http://www.theses.fr/2017LYSEC007 (Cited on page 19)

[11] S. Bouley, B. François, and M. Roger, "On a mode-matching technique for sound generation and transmission in a three-dimensional annular cascade of outlet guide vanes," in *22nd AIAA/CEAS Aeroacoustics Conference*, Lyon, France, May 2016. (Cited on page 19)

[12] S. Bouley, B. François, M. Roger, H. Posson, and S. Moreau, "On a two-dimensional mode-matching technique for sound generation and transmission in axial-flow outlet guide vanes," *Journal of Sound and Vibration*, vol. 403, pp. 190–213, 2017. (Cited on pages 3, 19, 25, 29, 38, 87, 170, 172, and 193)

[13] S. Bouley, M. Roger, and A. Finez, "Rotor-Stator Wake-Interaction Tonal Noise Modeling with an Edge-Dipole Approach," in *22nd AIAA/CEAS Aeroacoustics Conference*, Lyon, France, May 2016. (Cited on page 19)

[14] E. J. Brambley and N. Peake, "Sound transmission in strongly curved slowly varying cylindrical ducts with flow," *Journal of Fluid Mechanics*, vol. 596, pp. 387–412, 2008. (Cited on pages 68, 70, 123, 148, 155, 160, and 196)

[15] T. F. Brooks, D. S. Pope, and M. A. Marcolini, "Airfoil self-noise and prediction," NASA, Tech. Rep. NASA-RP-1218, July 1989. (Cited on page 9)

[16] C. Canuto, M. Y. Hussaini, A. Quarteroni, and T. A. Zang, *Spectral Methods in Fluid Dynamics*. Springer-Verlag, 1988. (Cited on page 71)

[17] M. Carazo, "Semi-analytical prediction of wake-interaction noise in counter-rotating open rotors," PhD thesis, Ecole Centrale de Lyon, 2012. (Cited on page 16)

[18] P. Chaitanya, J. Coupland, and J. P., "Airfoil geometry effects on turbulence interaction noise in cascades," in *22nd AIAA/CEAS Aeroacoustics Conference, AIAA Paper 2016-2738*, Lyon, France, June 2016. (Cited on page 24)

[19] S. Chapman and T. G. Cowling, *The mathematical theory of non-uniform gases: an account of the kinetic theory of viscosity, thermal conduction, and diffusion in gases*. Cambridge University Press, 1990. (Cited on page 13)

[20] B.-T. Chu and L. S. G. Kovásznay, "Non-linear interactions in a viscous heat-conducting compressible gas," *Journal of Fluid Mechanics*, vol. 3, no. 5, pp. 494–514, 1958. (Cited on pages 16, 21, 162, 164, and 190)

[21] T. Colonius and S. K. Lele, "Computational aeroacoustics : progress on nonlinear problems of sound generation," *Progress in Aerospace sciences*, vol. 40, pp. 345–416, 2004. (Cited on pages 13 and 14)

[22] A. J. Cooper and N. Peake, "Upstream-radiated rotor–stator interaction noise in mean swirling flow," *Journal of Fluid Mechanics*, vol. 523, pp. 219–250, 2005. (Cited on page 16)

[23] N. Curle, "The influence of solid boundaries upon aerodynamic sound," *Proceedings of the Royal Society of London. Series A. Mathematical and Physical Sciences*, vol. 231, no. 1187, pp. 505–514, 1955. (Cited on page 14)

[24] M. D. Dahl, "Fourth computational aeroacoustics (CAA) workshop on benchmark problems," in *NASA/CP-2004-212954*, 2004. (Cited on pages xiv, xviii, xix, 45, 90, 97, 100, 148, 160, 180, 181, 182, 183, 184, 185, and 191)

[25] J. de Laborderie, V. Blandeau, T. Node-Langlois, and S. Moreau, "Extension of a Fan Tonal Noise Cascade Model for Camber Effects," *AIAA Journal*, vol. 53, no. 4, pp. 863–876, 2015. (Cited on pages xix, 24, 37, 38, 39, 62, 181, 185, 186, and 191)

[26] J. de Laborderie and S. Moreau, "Evaluation of a Cascade-Based Acoustic Model for Fan Tonal Noise Prediction," *AIAA Journal*, vol. 52, no. 12, pp. 2877–2890, 2014. (Cited on pages 24 and 38)

[27] J. de Laborderie, S. Moreau, A. Berry, and H. Posson, "Several technological effects on tonal fan noise prediction," in *18th AIAA/CEAS Aeroacoustics Conference (33rd AIAA Aeroacoustics Conference), AIAA Paper 2012-2131*, Colorado Springs, CO, June 2012. (Cited on pages 24 and 38)

[28] S. L. Dixon and C. A. Hall, *Fluid Mechanics and Thermodynamics of Turbomachinery*, 7th ed. Elsevier, 2014. (Cited on pages 20, 23, 24, and 38)

[29] I. Evers and N. Peake, "On sound generation by the interaction between turbulence and a cascade of airfoils with non-uniform mean flow," *Journal of Fluid Mechanics*, vol. 463, pp. 25–52, July 2002. (Cited on pages 24 and 38)

[30] S. Felix and V. Pagneux, "Sound propagation in rigid bends: A multimodal approach," *The Journal of the Acoustical Society of America*, vol. 110, no. 3, pp. 1329–1337, 2001. (Cited on page 82)

[31] J. E. Ffowcs Williams and D. L. Hawkings, "Sound generation by turbulence and surfaces in arbitrary motion," *Philosophical Transactions of the Royal Society of London. Series A, Mathematical and Physical Sciences*, vol. 264, no. 1151, pp. 321–342, 1969. (Cited on pages 7, 14, 17, and 24)

[32] G. Floquet, "Sur les équations différentielles linéaires à coefficients périodiques," *Annales scientifiques de l'École Normale Supérieure*, vol. 12, série 2, pp. 47–88, 1883. (Cited on page 31)

[33] B. François, R. Barrier, and C. Polacsek, "Zonal detached eddy simulation of the fan-ogv stage of a modern turbofan engine," in *ASME Turbo Expo 2020: Turbomachinery Technical Conference and Exposition, Paper GT2020-1423*, September 2020. (Cited on pages xviii, 168, and 169)

[34] B. François, S. Bouley, M. Roger, and S. Moreau, "Analytical models based on a mode-matching technique for turbulence impingement noise on axial-flow outlet guide vanes," in *22nd AIAA/CEAS Aeroacoustics Conference*, Lyon, France, May 2016. (Cited on pages 3, 19, 162, and 193)

[35] F. Gea-Aguilera, J. Gill, and X. Zhang, "On the effects of fan wake modelling and vane design on cascade noise," *Journal of Sound and Vibration*, vol. 459, p. 114859, 2019. (Cited on page 24)

[36] S. A. L. Glegg, "The response of a swept blade row to a three-dimensional gust," *Journal of sound and vibration*, vol. 227, no. 1, pp. 29–64, 1999. (Cited on page 18)

[37] M. E. Goldstein, *Aeroacoustics*. New York: McGraw-Hill International Book Co., 1976. (Cited on pages 14 and 60)

[38] ——, "Unsteady vortical and entropic distortions of potential flows round arbitrary obstacles," *Journal of Fluid Mechanics*, vol. 89, no. 3, pp. 433–468, 1978. (Cited on page 22)

[39] S. M. Grace, "Fan broadband interaction noise modeling using a low-order method," *Journal of Sound and Vibration*, vol. 346, pp. 402–423, 2015. (Cited on page 24)

[40] G. Grasso, M. Roger, and S. Moreau, "Analytical model of the source and radiation of sound from the trailing edge of a swept airfoil," *Journal of sound and vibration*, vol. 493, 2021. (Cited on page 17)

[41] G. Green, "An essay on the application of mathematical analysis to the theories of electricity and magnetism," 1828. (Cited on page 41)

[42] R. W. Hamming, *Numerical Methods for Scientists and Engineers*, 1962. (Cited on page 44)

[43] D. B. Hanson, "Spectrum of rotor noise caused by atmospheric turbulence," *Journal of the Acoustical Society of America*, vol. 56, no. 1, pp. 110–126, 1974. (Cited on page 10)

[44] ——, "Acoustic reflection and transmission of rotors and stators including mode and frequency scattering | 3rd AIAA/CEAS Aeroacoustics Conference," in *3rd AIAA/CEAS Aeroacoustics Conference*, Atlanta, GA, USA, May 1997. (Cited on page 110)

[45] D. B. Hanson and K. P. Horan, "Turbulence/cascade interaction - Spectra of inflow, cascade response, and noise," in *4th AIAA/CEAS Aeroacoustics Conference*, Toulouse, France, June 1998. (Cited on page 18)

[46] R. Hixon, "Computational aeroacoustics prediction of acoustic transmission through a realistic 2d stator," in *17th AIAA/CEAS Aeroacoustics Conference, AIAA Paper 2011-2706*, Portland, Oregon, June 2011. (Cited on pages 19, 91, 98, 99, and 100)

[47] M. H. Holmes, *Introduction to perturbation methods*. Springer-Verlag, 1995. (Cited on pages 42, 46, 124, 125, and 133)

[48] M. Honjo and T. Tominaga, "Study of acoustic resonance of cascades," in *Proceedings of the Second International Symposium on Aeroelasticity in turbomachines*, Lausanne, Switzerland, September 1980. (Cited on page 114)

[49] M. S. Howe, "Attenuation of sound due to vortex shedding from a splitter plate in a mean flow duct," *Journal of Sound and Vibration*, vol. 105, no. 3, pp. 385–396, March 1986. (Cited on pages 86 and 111)

[50] J. Huber and S. Illa, "Jet noise assessment and sensitivity at aircraft level," in *13th AIAA/CEAS Aeroacoustics Conference*, Rome, Italy, May 2007. (Cited on pages xiii, 2, and 3)

[51] J. Ingenito, "Vers une modélisation d'aide à la conception acoustique d'étages de compresseurs subsoniques de turbomachines," PhD thesis, Ecole Centrale de Lyon, 2010. [Online]. Available: http://www.theses.fr/2010ECDL0015 (Cited on pages 39 and 62)

[52] J. Ingenito and M. Roger, "Analytical modelling of sound transmission through the passage of centrifugal compressors," in *13th AIAA/CEAS Aeroacoustics Conference*, Rome, Italy, May 2007. (Cited on pages 18, 70, and 157)

[53] ——, "Measurement and prediction of the tonal noise of a centrifugal compressor at inlet," in *15th AIAA/CEAS Aeroacoustics Conference*, Miami, FL, USA, May 2009. (Cited on page 18)

[54] M. C. Jacob, J. Grilliat, R. Camussi, and G. C. Gennaro, "Aeroacoustic investigation of a single airfoil tip leakage flow," *International Journal of Aeroacoustics*, vol. 9, no. 3, pp. 253–272, 2010. (Cited on page 10)

[55] J. M. Janus, H. Z. Horstman, and D. L. Whitfield, "Unsteady flowfield simulation of ducted prop-fan configurations," in *30th Aerospace Sciences Meeting and Exhibit, AIAA Paper 92-0521*, Reno, NV, USA, January 1992. (Cited on pages 97 and 100)

[56] S. Job, E. Lunéville, and J. F. Mercier, "Diffraction of an acoustic wave by a plate in a uniform flow: A numerical approach," *Journal of Computational Acoustics*, vol. 13, no. 4, pp. 689–709, 2005. (Cited on pages 86 and 111)

[57] D. S. Jones, "Aerodynamic Sound Due to a Source Near a Half-Plane," *IMA Journal of Applied Mathematics*, vol. 9, no. 1, pp. 114–122, 1972. (Cited on page 86)

[58] J. L. Kerrebrock, "Small disturbances in turbomachine annuli with swirl," *AIAA Journal*, vol. 15, no. 6, pp. 794–803, 1977. (Cited on page 16)

[59] G. R. Kirchhoff, "Zur theorie der lichtstrahlen," *Annalen der Physik*, vol. 254, no. 4, pp. 663–695, 1883. (Cited on page 41)

[60] W. Koch, "Resonant acoustic frequencies of flat plate cascades," *Journal of Sound and Vibration*, vol. 88, no. 2, pp. 233–242, 1983. (Cited on pages 111, 114, and 115)

[61] ——, "Acoustic resonances and trapped modes in annular plate cascades," *Journal of Fluid Mechanics*, vol. 628, pp. 155–180, 2009. (Cited on page 114)

[62] P. E. Krasnushkin, "On waves in curved tubes," *Uchenye Zapiski Moskovskogo Gosudarstvennogo Universiteta*, vol. 75, pp. 9–27, 1945. (Cited on page 69)

[63] R. E. Langer, "On the asymptotic solutions of ordinary differential equations, with an application to the bessel functions of large order," *Transactions of the American Mathematical Society*, vol. 33, no. 01, pp. 23–24, 1931. (Cited on pages 130 and 159)

[64] D. Lewis, "From analytical to fully numerical predictions of the broadband noise radiated by a full fan-OGV stage," PhD thesis, Université de Lyon, 2020. (Cited on pages xviii, 168, and 169)

[65] D. Lewis, J. de Laborderie, M. Sanjosé, S. Moreau, M. C. Jacob, and V. Masson, "Parametric study on state-of-the-art analytical models for fan broadband interaction noise predictions," *Journal of Sound and Vibration*, vol. 514, 2021. (Cited on page 24)

[66] M. J. Lighthill, "On sound generated aerodynamically i. general theory," *Proceedings of the Royal Society of London. Series A. Mathematical and Physical Sciences*, vol. 211, no. 1107, pp. 564–587, 1952. (Cited on pages xiii, 14, and 15)

[67] ——, "On sound generated aerodynamically ii. turbulence as a source of sound," *Proceedings of the Royal Society of London. Series A. Mathematical and Physical Sciences*, vol. 222, no. 1148, pp. 1–32, 1954. (Cited on pages xiii, 14, and 15)

[68] G. Maierhofer and N. Peake, "Acoustic and hydrodynamic power of wave scattering by an infinite cascade of plates in mean flow," *Journal of Sound and Vibration*, vol. 520, p. 116564, 2022. (Cited on pages 111 and 112)

[69] R. K. Majjigi and P. R. Gliebe, "Development of a rotor wake/vortex model," NASA, Tech. Rep. NASA-CR-174849, June 1984. (Cited on page 16)

[70] Y. Mao, A. G. Wilson, P. Joseph, C. C. Paruchuri, A. Parry, and P. Carugno, "Wave response functions for a cascade of blades with an arbitrary camber," in *25th AIAA/CEAS Aeroacoustics Conference, AIAA Paper 2019-2736*, Delft, The Netherlands, May 2019. (Cited on page 19)

[71] V. Masson, H. Posson, M. Sanjose, T. Léonard, S. Moreau, and M. Roger, "Fan-OGV interaction broadband noise prediction in a rigid annular duct with swirling and sheared mean flow," in *22nd AIAA/CEAS Aeroacoustics Conference, AIAA Paper 2016-2944*, Lyon, France, June 2016. (Cited on page 18)

[72] J. Mathews and N. Peake, "The acoustic Green's function for swirling flow in a lined duct," *Journal of Sound and Vibration*, vol. 395, pp. 294–316, 2017. (Cited on page 18)

[73] R. Mittra and S. W. Lee, *Analytical techniques in the theory of guided waves*. Macmillan, 1971. (Cited on page 18)

[74] S. Moreau, P. Badoo, H. Bériot, and M. Roger, "Two-dimensional sound transmission in realistic turbomachinery cascade," in *25th AIAA/CEAS Aeroacoustics Conference, AIAA Paper 2019-2550*, Delft, The Netherlands, May 2019. (Cited on page 19)

[75] S. Moreau and M. Roger, "Back-scattering correction and further extensions of Amiet's trailing-edge noise model. Part II: Application," *Journal of sound and vibration*, vol. 323, pp. 397–425, 2009. (Cited on page 17)

[76] ——, "Advanced noise modeling for future propulsion systems," *International Journal of Aeroacoustics*, vol. 17, no. 6–8, pp. 576–599, 2018. (Cited on page 18)

[77] S. Moreau, M. Roger, and V. Jurdic, "Effect of angle of attack and airfoil shape on turbulence-interaction noise," in *11th AIAA/CEAS Aeroacoustics Conference, AIAA Paper 2005-2973*, Monterey, CA, USA, May 2005. (Cited on page 17)

[78] P. M. Morse and H. Feshbach, *Methods of Theoretical Physics*. New York: McGraw-Hill, 1953. (Cited on pages 67, 68, 165, 205, and 207)

[79] A. H. Nayfeh and D. H. Huddleston, "Resonant acoustic frequencies of parallel plates," in *12th AIAA fluid and plasma dynamics conference, AIAA Paper 79-1522*, Williamsburg, VA, USA, July 1979. (Cited on page 114)

[80] A. H. Nayfeh, J. E. Kaiser, and D. P. Telionis, "Transmission of Sound through Annular Ducts of Varying Cross Sections," *AIAA Journal*, vol. 13, pp. 60–65, 1975. (Cited on page 43)

[81] A. H. Nayfeh, *Perturbation methods*. Wiley, 1973. (Cited on page 202)

[82] ——, *Introduction to perturbation techniques*. Wiley, 1981. (Cited on pages 42, 46, and 47)

[83] A. H. Nayfeh and D. P. Telionis, "Acoustic propagation in ducts with varying cross sections," *The Journal of the Acoustical Society of America*, vol. 54, no. 6, pp. 1654–1661, 1973. (Cited on pages 43, 130, and 200)

[84] A. H. Nayfeh, D. P. Telionis, and S. G. Lekoudis, "Acoustic propagation in ducts with varying cross sections and sheared mean flow," in *Aeroacoustics Conference*, Seattle, WA, USA, October 1973. (Cited on page 43)

[85] F. W. J. Olver, D. W. Lozier, R. F. Boisvert, and C. W. Clark, *NIST Handbook of Mathematical Functions*. Cambridge University Press, 2010. (Cited on pages 70 and 209)

[86] N. C. Ovenden, "A uniformly valid multiple scales solution for cut-on cut-off transition of sound in flow ducts," *Journal of Sound and Vibration*, vol. 286, no. 1, pp. 403–416, 2005. (Cited on pages 19, 123, 127, 130, and 159)

[87] ——, "Near cut-on/cut-off transition in lined ducts with flow," in *8th AIAA/CEAS Aeroacoustics Conference*, Breckenridge, Colorado, June 2002. (Cited on page 129)

[88] N. C. Ovenden, W. Eversman, and S. W. Rienstra, "Cut-on cut-off transition in flow ducts: Comparing multiple-scales and finite-element solutions," in *10th AIAA/CEAS Aeroacoustics Conference*, Manchester, Great Britain, May 2004. (Cited on pages 129, 130, 160, and 196)

[89] R. Parker, "Resonance effects in wake shedding from parallel plates: Some experimental observations," *Journal of Sound and Vibration*, vol. 4, no. 1, pp. 62–72, 1966. (Cited on page 114)

[90] ——, "Resonance effects in wake shedding from compressor blading," *Journal of Sound and Vibration*, vol. 6, no. 3, pp. 302–309, 1967. (Cited on page 114)

[91] R. Paterson and R. Amiet, "Acoustic radiation and surface pressure characteristics of an airfoil due to incident turbulence," in *3rd Aeroacoustics Conference*, Palo Alto,CA,U.S.A, July 1976. (Cited on page 10)

[92] N. Peake and E. J. Kerschen, "Influence of mean loading on noise generated by the interaction of gusts with a flat-plate cascade: upstream radiation," *Journal of Fluid Mechanics*, vol. 347, pp. 315–346, 1997. (Cited on pages 25 and 99)

[93] ——, "Influence of mean loading on noise generated by the interaction of gusts with a cascade: downstream radiation," *Journal of Fluid Mechanics*, vol. 515, pp. 99–133, 2004. (Cited on pages 25 and 99)

[94] N. Peake and A. B. Parry, "Modern challenges facing turbomachinery aeroacoustics," *Annual Review of Fluid Mechanics*, vol. 44, pp. 227–248, 2012. (Cited on pages 7 and 10)

[95] M. Pestana, "Impact of a heterogeneous stator on the rotor-stator interaction-noise: an analytical, experimental and numerical investigation," PhD thesis, Université de Lyon, 2020. (Cited on page 9)

[96] D. A. Philbrick and D. A. Topol, "Development of a fan noise design system. part 1: Design system and source modeling," in *15th AIAA Aeroacoustic Conference*, Long Beach, CA, USA, October 1993. (Cited on page 16)

[97] A. D. Pierce, *Acoustics: An Introduction to Its Physical Principles and Applications*. McGraw-Hill, 1981. (Cited on pages 21, 31, 32, 164, and 168)

[98] G. Podboy, M. Krupar, C. Hughes, and R. Woodward, "Fan noise source diagnostic test- ldv measured flow field results," in *8th AIAA/CEAS Aeroacoustics Conference & Exhibit, AIAA Paper 2002-2431*, Breckenridge, Colorado, USA, June 2002. (Cited on pages 89 and 100)

[99] H. Posson, M. Roger, and S. Moreau, "On a uniformly valid analytical rectilinear cascade response function," *Journal of Fluid Mechanics*, vol. 663, pp. 22–52, 2010. (Cited on page 18)

[100] H. Posson and N. Peake, "The acoustic analogy in an annular duct with swirling mean flow," *Journal of Fluid Mechanics*, vol. 726, pp. 439–475, 2013. (Cited on page 18)

[101] E. Reissner, "On the application of mathieu functions in the theory of subsonic compressible flow past oscillating airfoils," *NACA Technical Note*, no. 2363, 1951. (Cited on pages 29 and 125)

[102] B. Reynolds and B. Lakshminarayana, "Characteristics of lightly loaded fan rotor blade wakes," NASA, Tech. Rep. NASA-CR-3188, November 1979. (Cited on page 16)

[103] B. Reynolds, B. Lakshminarayana, and A. Ravindranath, "Characteristics of the near wake of a compressor of a fan rotor blade," *AIAA Journal*, vol. 17, no. 9, pp. 959–967, 1979. (Cited on page 16)

[104] S. W. Rienstra, "Sound diffraction at a trailing edge," *Journal of Fluid Mechanics*, vol. 108, pp. 443–460, 1981. (Cited on page 86)

[105] ——, "Contributions to the theory of sound propagation in ducts with bulk-reacting lining," *Journal of the Acoustical Society of America*, vol. 77, no. 5, pp. 1681–1685, 1985. (Cited on page 43)

[106] ——, "Sound transmission in a slowly varying lined flow duct," *Nieuw Archief voor Wiskunde*, vol. 4/6, no. 1–2, pp. 157–167, 1988. (Cited on page 43)

[107] ——, "Sound transmission in slowly varying circular and annular lined ducts with flow," *Journal of Fluid Mechanics*, vol. 380, pp. 279–296, 1999. (Cited on pages 43, 45, 64, 70, and 202)

[108] ——, "Cut-on, cut-off transition of sound in slowly varying flow ducts," *Aerotecnica Missili & Spazio, special issue in memory of Prof D.G. Crighton*, vol. 79, pp. 93–97, 2000. (Cited on page 129)

[109] ——, "Sound propagation in slowly varying lined flow ducts of arbitrary cross-section," *Journal of Fluid Mechanics*, vol. 495, pp. 157–173, 2003. (Cited on pages 43, 47, 123, 127, and 129)

[110] ——, "Slowly varying modes in a two-dimensional duct with shear flow and lined walls," *Journal of Fluid Mechanics*, vol. 906, no. A23, 2021. (Cited on pages 43 and 121)

[111] S. W. Rienstra and W. Eversman, "A numerical comparison between the multiple-scales and finite-element solution for sound propagation in lined flow ducts," *Journal of Fluid Mechanics*, vol. 437, pp. 367–384, 2001. (Cited on page 43)

[112] M. Roger and A. Carazo, "Blade-geometry considerations in analytical gust-airfoil interaction noise models," in *16th AIAA/CEAS Aeroacoustics conference, AIAA Paper 2010-3799*, Stockholm, SW, June 2010. (Cited on page 17)

[113] M. Roger and S. Moreau, "Back-scattering correction and further extensions of Amiet's trailing-edge noise model. Part 1: theory," *Journal of sound and vibration*, vol. 286, pp. 477–506, 2005. (Cited on page 17)

[114] M. Roger, S. Moreau, and A. Guedel, "Broadband fan noise prediction using single-airfoil theory," *Noise control engineering journal*, vol. 54, no. 1, 2006. (Cited on pages 17 and 18)

[115] M. Roger, "Analytical modelling of wake-interaction noise in centrifugal compressors with vaned diffusers," in *10th AIAA/CEAS Aeroacoustics Conference*, Manchester, Great Britain, May 2004. (Cited on page 18)

[116] M. Roger and B. François, "Combined analytical models for sound generation and transmission in cambered axial-flow outlet guide vanes," *European Journal of Mechanics - B/Fluids*, vol. 61, pp. 218–225, 2017. (Cited on pages 19, 37, 38, 41, 42, 63, and 82)

[117] M. Roger, B. François, and M. Bauerheim, "Three-dimensional modeling of annular cascade trailing-edge noise," in *22nd AIAA/CEAS Aeroacoustics Conference*, Lyon, France, May 2016. (Cited on pages 19 and 42)

[118] M. Roger, B. François, and S. Moreau, "Cascade trailing-edge noise modeling using a mode-matching technique and the edge-dipole theory," *Journal of Sound and Vibration*, vol. 382, pp. 310–327, November 2016. (Cited on page 19)

[119] M. Roger and S. Moreau, "Coupled mode-matching and slowly-varying duct formulations for predicting noise generation and transmission in axial-flow rotor-stator stages," in *MUSAF III*, Toulouse, France, September 2016. [Online]. Available: http://musaf2016.onera.fr/content/program (Cited on pages 19, 39, 62, and 76)

[120] M. Roger, S. Moreau, and A. Marsan, "Generation and transmission of spiral acoustic waves in multi-stage subsonic radial compressors," in *20th AIAA/CEAS Aeroacoustics Conference*, Atlanta, GA, USA, June 2014. (Cited on page 18)

[121] P. Sagaut, S. Deck, and M. Terracol, *Multiscale and multiresolution approaches in turbulence*. Imperial College Press, 2013. (Cited on pages xiii, 12, and 13)

[122] M. Sanjosé, S. Moreau, M. Pestana, and M. Roger, "Effect of Weak Outlet-Guide-Vane Heterogeneity on Rotor–Stator Tonal Noise," *AIAA Journal*, no. 10, 2017. (Cited on pages xix, 9, 189, and 190)

[123] M. Sanjosé, M. Daroukh, W. Magnet, J. De Laborderie, S. Moreau, and A. Mann, "Tonal fan noise prediction and validation on the ancf configuration," in *Fan 2015*, Lyon, France, April 2015. (Cited on page 24)

[124] K. Schwarzschild, "Die Beugung und Polarisation des Lichts durch einen Spalt. I," *Mathematische Annalen*, vol. 55, no. 2, pp. 177–247, 1901. (Cited on page 17)

[125] W. R. Sears, "Some aspects of non-stationary airfoil theory and its practical application," *Journal of the Aeronautical Sciences*, vol. 8, 1941. (Cited on page 17)

[126] A. F. Smith, N. C. Ovenden, and R. I. Bowles, "Flow and geometry induced scattering of high frequency acoustic duct modes," *Wave Motion*, vol. 49, no. 1, pp. 109–124, 2012. (Cited on pages 160 and 196)

[127] A. F. Smith, "Transition and flow-induced scattering of acoustic modes in ducts," PhD thesis, Department of Mathematics University College, London, 2011. [Online]. Available: http://discovery.ucl.ac.uk/1344084/ (Cited on pages 160 and 196)

[128] D. B. Stephens and S. C. Morris, "Sound generation by a rotor interacting with a casing turbulent boundary layer," *AIAA journal*, vol. 47, no. 11, pp. 2698–2708, 2009. (Cited on page 10)

[129] J. Thisse, C. Polacsek, S. Lewy, and A. Lafitte, "Generation and propagation of multiple pure tones inside turbofans at transonic regime," *AIAA Journal*, 2015. (Cited on page 8)

[130] C. S. Ventres, M. A. Theobald, and W. D. Mark, "Turbofan noise generation. Volume 1: Analysis," NASA, Tech. Rep. NASA-CR-167952, July 1982. (Cited on page 18)

[131] E. A. N. Whitehead, "The theory of parallel-plate media for microwave lenses," *Proceedings of the IEE - Part III: Radio and Communication Engineering*, vol. 98, pp. 133–140, 1951. (Cited on pages 18 and 41)

[132] J. E. F. Williams and L. H. Hall, "Aerodynamic sound generation by turbulent flow in the vicinity of a scattering half plane," *Journal of Fluid Mechanics*, vol. 40, no. 4, pp. 657–670, 1970. (Cited on page 9)

dernière page de la thèse

AUTORISATION DE SOUTENANCE

Vu les dispositions de l'arrêté du 25 mai 2016,

Vu la demande du directeur de thèse

Monsieur M. ROGER

et les rapports de

Mme S. GRACE
Professeure - Boston University - 110 Cummington Mall - Boston - MA 02215 - Etats-Unis

et de

M. C. SCHRAM
Professeur - Von Karman Institute for Fluid Dynamics - Waterloosesteenweg 72
1640 Rhode-Saint-Genèse - Belgique

Monsieur GIRIER Léo

est autorisé à soutenir une thèse pour l'obtention du grade de **DOCTEUR**

Ecole doctorale Mécanique, Energétique, Génie civil, Acoustique

Fait à Ecully, le 26 janvier 2022

Pour le directeur de l'Ecole centrale de Lyon
Le directeur des Formations

Grégory VIAL